YAP1 Signaling in Hepatobiliary Development and Oncogenesis

by

Laura Maria Molina

BS, University of Florida, 2015

Submitted to the Graduate Faculty of

School of Medicine in partial fulfillment

of the requirements for the degree of

Doctor of Philosophy

University of Pittsburgh

2021

UNIVERSITY OF PITTSBURGH

SCHOOL OF MEDICINE

This dissertation was presented

by

Laura Maria Molina

It was defended on

May 12, 2021

and approved by

Dr. Kari Nejak-Bowen, MBA, PhD, Assistant Professor, Department of Pathology

Dr. George Michalopoulos MD, PhD, Professor and Chair, Department of Pathology

Dr. Dean Yimlamai, MD, PhD, Assistant Professor, Department of Pathology

Dr. Donghun Shin, PhD, Associate Professor, Department of Developmental Biology

Dr. Lance Davidson, PhD, Professor, Department of Bioengineering

Dissertation Director: Dr. Satdarshan P. S. Monga, MD, Professor and Vice Chair, Division of Experimental Pathology, Department of Pathology

YAP1 Signaling in Hepatobiliary Development and Oncogenesis

Laura Maria Molina, PhD

University of Pittsburgh, 2021

Yes-associated protein 1 (YAP1) is critical for liver development, regeneration, and oncogenesis. In this thesis, I studied the physiological role of YAP1 in early liver development, specifically in hepatoblasts as they developed into the major liver cell types, hepatocytes and cholangiocytes. I found that YAP1 was dispensable for hepatocyte differentiation from hepatoblasts but was essential for bile duct differentiation in mice, resulting in a phenotype like Alagille syndrome. There was complete loss of intrahepatic biliary network when *Yap1* was conditionally deleted from hepatoblasts. Despite this, these mice survived long-term through genetic reprogramming of hepatocytes, favoring proliferation at the expense of metabolic function including bile acid metabolism, and reversing bile acid transport to promote excretion via the kidneys. Also, these mice did not exhibit any hepatocyte-derived biliary regeneration, in contrast to other models of bile duct paucity, showing that YAP1 is critical for hepatocyte transdifferentiation into cholangiocytes. I also developed a novel tissue clearing method for liver, which combined with ribbon-scanning confocal microscopy can be used for 3D imaging of intact tissue structures and can be adapted to understand tissue architecture of many liver pathologies.

I also studied the role of YAP1 in hepatoblastoma (HB), a pediatric tumor which arises from hepatoblasts during development, with Dr. Danielle Bell and Dr. Hong Yang. Concomitant YAP1 and β-catenin activation causes HB tumor formation in mice. Using this model, we identified that Lipocalin 2 is regulated synergistically by both YAP1 and β-catenin and can potentially be used a serum biomarker of tumor growth. Next, based on several studies

suggesting that both YAP1 and β-catenin activate mTORC1 signaling to promote tumor growth, we tested the effect of rapamycin in our HB model. We show that mTORC1 inhibition delays tumor formation and results in slower-growing tumors with more well-differentiated HB tumor cells, which tend to be less aggressive and more responsive to chemotherapy. Altogether, this thesis presents new insights into the distinct roles of YAP1 in biliary development and hepatoblastoma tumorigenesis and sets the stage for further mechanistic study to identify how YAP1 exerts such profound effects on liver formation.

Table of Contents

List of Tables

List of Figures

Preface

When I was young, I had so many questions about how the invisible, molecular world could produce something as complex and impressive as a human body. I knew I needed answers, and so began my long journey into medicine and scientific research of human pathology. Through sheer, stubborn persistence and with the help and support of many, many people for whom I am so grateful, I have reached the edge of our knowledge and begun finding answers for myself in this small corner of the vast world of science. I am surrounded by fellow scientists who share my passion for discovery, and who understand why we persist through countless obstacles of bureaucracy, publishing, grants and funding systems and "deliverables", because nothing is more gratifying than finding another little piece of the puzzle and diving into the many more questions that this opens up. I am honored to be a part of the academic community, and I could not have imagined when I first began my studies that I would feel so at home here and so fulfilled by our shared mission of discovery. I hope I can help many more people follow in these footsteps and feel empowered to make their own discoveries and keep pushing the boundaries of our knowledge, while also advocating to improve mental health, career stability, and working conditions across all ranks of academia.

First and foremost, I want to thank my parents, Dr. Jorge Molina and Dr. Patricia Felix, without whom I would not be the person I am today. Their decades of sacrifices have allowed me to live a privileged life and pursue my dreams successfully. I fondly remember my many math lessons with my dad, and learning about genetics with my mom, and from both of them learning to question what I see in the world, to be curious, and to fight hard to accomplish my goals. Thank you for always being by my side and wanting the best for me every step of the way.

I want to thank my mentors in high school and college, particularly in the chemistry department at the University of Florida. Dr. Alexander Angerhofer mentored me in my first research experience and opened many doors for me to grow professionally, together with Dr. Valeria Kleiman and Dr. Adrian Roitberg who helped me pursue a research fellowship in France, with Dr. Ludovic Carlier, and Dr. Olivier Lequin. I also want to thank my many teachers and professors who inspired me and fed my curiosity throughout my education. These opportunities not only gave me knowledge and practical experience, but helped me realize that I needed to follow a clinical direction and apply basic research to solve tangible health problems.

I want to thank my mentors in graduate school and medical school, who have been instrumental in guiding my personal growth and helping me feel confident enough to lead my own research projects. My committee members and clinical mentors have always been supportive and offered constructive advice to help me progress as both a medical and PhD student. Thanks to Dr. Kari Nejak-Bowen, Dr. Dean Yimlamai, Dr. Lance Davidson, Dr. George Michalopoulos, and Dr. Donghun Shin for our conversations over the years about science and careers. Thanks also to Dr. Ramon Bataller and Dr. Miguel Reyes-Múgica for outstanding clinical mentorship, and for helping me better understand what kind of clinical service best suits my personality and my goals. Dr. Joanne Flynn has been a great support and resource, always reminding me of the positives and also pushing me to grow in resilience and assertiveness. Many thanks to the university administrators who help our massive academic system run smoothly and without who surely we would all collapse under our weights in paperwork.

Many thanks to Dr. Jessica Zucman-Rossi, Dr. Eric Letouzé, and the whole FunGEST research team, who welcomed me to their lab and showed me a whole new way to study human disease. I learned so many skills and gained a new perspective in combining bioinformatics with

bench research to unravel mechanisms of disease, and I hope to apply these lessons carefully in my future projects. Thanks also to Dr. Frederic Lemaigre and his team, who also welcomed me into their lab and freely shared their expertise with me.

Dr. Satdarshan Monga in particular has been such an outstanding mentor and source of support through this process. From when I first joined the University of Pittsburgh in 2015 up to now, Dr. Monga has been an unwavering advocate of my career success and my own personal satisfaction in my work. He never doubted that I could be a great scientist, and he helped me take so many opportunities to explore and expand my abilities and my knowledge. I have always enjoyed our scientific discussions and our practical discussions of the realities of academia today, which have helped me better understand how to push my career forward while still doing great science. He also never wavered in supporting my varied learning goals, even helping me secure a fellowship to study abroad and learn bioinformatics. I will be forever grateful for this experience, and I can only hope that one day I will help my mentees in the same way.

I also want to thank Dr. Richard Steinman for helping me realize what a great fit our program would be for me way back when I was interviewing for MD/PhD positions. Dr. Steinman cares deeply for our cohort of students and for fostering the growth of physician scientists across the university. I have learned so much from working with Dr. Steinman, the MSTP administration, and my fellow classmates in helping our program evolve over the past few years and adapt to new challenges in physician-scientist education. I am very grateful for all the work he and our MSTP faculty have put into our program over the years.

Thank you to the whole Monga lab family, past and present! We stick together and support each other however we can, and I am so glad I got the chance to work with such amazing and brilliant individuals for the past 4-5 years. Similarly, the whole community of faculty,

students, and staff, at the University of Pittsburgh School of Medicine, has been such a great source of collaborative support. There are too many people to thank here, but know that I am glad to have crossed paths with all of you and hope to keep working with you in the future.

Finally, I want to thank my classmates, for sticking together through this long journey! In particular, I want to thank my close friends Gaelen Dwyer, Adriana Johnson, Maryanna Owoc, and Shinjini Kundu, and my partner, Trenton Tabor, for their support. Thank you for knowing me better than I know myself sometimes, and for understanding the craziness of this whole process of becoming double doctors. Thanks also for letting me share your life milestones, the happy times and the struggles. This was a much better journey for having shared it with you.

It takes a village to raise a child, and it certainly takes a whole community to mentor a physician-scientist. I am so grateful to everyone who has helped me on this journey of growth and adventure, and I can't wait to keep pursuing my dreams for many years to come.

1.0 Introduction

1.1 Overview of YAP1 Signaling

Yes-associated protein 1 (YAP1) is a transcriptional coactivator that works mostly through the TEAD family of transcription factors to regulate genes related to cell proliferation and differentiation, often by binding to enhancer regions and collaborating with AP1.[1-4] YAP1 is canonically repressed by the HIPPO kinase pathway through cytoplasmic retention and degradation (Figure 1). A variety of signaling inputs activate the kinases MST1/2, which phosphorylate LATS1/2, which phosphorylate YAP1 at various sites, including serine-127 (S127).[5-7] Phosphorylated YAP1 is sequestered in the cytoplasm, at adherens junctions through binding α-catenin, and at tight junctions through binding angiomotin [7-9]. Phosphorylated YAP1 is also sequestered and degraded through interactions with 14-3-3 proteins.[7-9]

Decreased activity of Hippo pathway kinases allows for YAP1 activation and transport into the nucleus for the regulation of gene expression. Alternatively, YAP1 can be activated through phosphorylation at tyrosine-357 (Y357) by Yes kinase, a member of the Src kinase family; this can override S127 phosphorylation and thus can activate YAP1 despite maintenance of Hippo pathway activity.[5, 10] YAP1 activity also responds to and modulates changes in cytoskeletal organization, and YAP1 becomes activated when cells interact with stiffer extracellular matrix environments.[11, 12]

Numerous inputs regulate Hippo pathway activity, including extracellular signals from growth factors and cytokines acting through membrane GPCRs and tyrosine kinase receptors, changes in actin cytoskeletal tension, and cell-cell focal adhesions and junctions.[5, 13, 14] In

particular, Merlin (Nf2), a well-known tumor suppressor, recruits Hippo pathway kinases to the plasma membrane in close proximity to YAP1, thus facilitating regulatory interactions that inactivate YAP1.[15] In addition, YAP1 can be regulated in a Hippo-independent manner through interactions with many key signaling pathways including Notch, Wnt/β-catenin, TGFβ, and mTOR pathways.[16-21] Lastly, nuclear YAP1 can be prevented from binding to TEAD through interaction with the ARID1a-containing SWI/SNF chromatin remodeling complex, which also responds to mechano-transduced signals. [22] Thus, YAP1 integrates a variety of upstream signals allowing cells to respond actively to their environment. Importantly, many of these interactions have been studied in a tissue-specific, developmental-specific, or disease-specific manner and are highly context dependent.

While the immediate upstream regulators of YAP1 have been well described, the downstream effects of YAP1 activity in the liver remain the focus of intense investigation due to the central role of YAP1 in many liver pathologies. In general, YAP1 regulates gene expression to promote cell proliferation and survival, enhanced metabolic activity, context-dependent extracellular matrix composition, all of which are critical functions that impact baseline liver size, the regenerative response to injury, and tumorigenesis.[1, 11, 23-25] Importantly, YAP1 seems to promote cell dedifferentiation in some contexts while promoting biliary differentiation in others; studies have yet to disentangle these two distinct functions in the context of liver biology and disease and identify unique YAP1 targets that mediate these processes.[5, 26, 27] Several studies have combined RNA-sequencing and ChIP-seq data to identify YAP1 transcriptional targets.[1, 28, 29] Notably, CTGF (*CCN2*) and CYR61 (*CCN1*) have been recurrently identified and used experimentally as surrogate measures of YAP1 activity.[30, 31] However, more studies are needed

to identify context-dependent transcriptional targets which regulate cell fate decisions vs. context-independent targets which are consistently activated by YAP1.

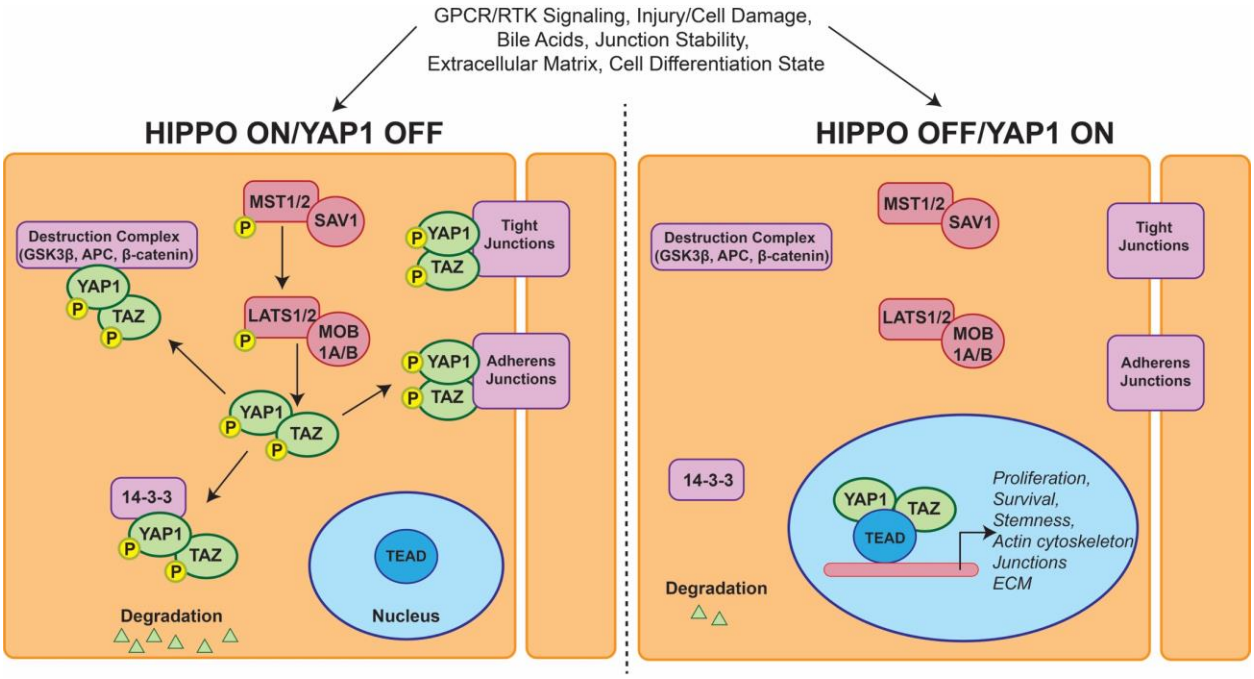

Figure 1. Overview of HIPPO/YAP Pathway.

1.1.1 YAP1 vs TAZ: Similar but not always interchangeable

TAZ (transcriptional coactivator with PDZ-binding motif, also known as WWTR1, WW-domain containing transcription regulator 1) is a paralog of YAP1 which is similarly regulated by the HIPPO pathway as well as some of the HIPPO-independent mechanisms described above.[5, 14, 32-34] YAP1 and TAZ together form a complex primarily with TEAD transcription factors as well as AP-1, TBX5, RUNX1, and SMADs2-4 in different contexts, but both YAP1 and TAZ have distinct transcriptional partners such as p73 and PPAR gamma, respectively [1, 32, 35]. Studies have shown that YAP1 can regulate transcription of TAZ, and together they can

activate expression of LATS2, forming feedback loops regulating overall HIPPO pathway activity [36].

While both YAP1 and TAZ are considered master regulators of transcription and signaling hubs that respond to most known signaling pathways, recent studies have demonstrated key differences in the structure and function of TAZ that give it distinct temporal and tissue-specific roles. Structurally, YAP1 and TAZ share most protein domains, but with several key differences. First, YAP1 contains two WW-domains while TAZ contains just one, potentially altering their ability to bind to many shared regulators such as the LATS kinases[32]. Second, while both YAP1 and TAZ carry a TEAD-binding domain to form heterodimers with TEAD proteins, TAZ has the unique ability to homodimerize and thus form a TAZ/TEAD heterotetramer, which has the potential to bind to multiple TEAD sites nearby and result in altered transcriptional regulation [37, 38]. TAZ also lacks both a proline-rich motif (used by YAP1 to interact with pre-mRNA splicing proteins) and a SCR homology 3 domain binding motif (used by YAP1 to interact with SRC and YES kinases and other kinase adaptor proteins)[32]. Finally, TAZ contains two phosphodegron regions (compared to just one in YAP1) that can be phosphorylated by glycogen synthase kinase 3α (GSK3), creating a binding site for β-TrCP ubiquitin protein ligase for protein degradation[32]. This has a notable impact on the regulation of YAP1 and TAZ along with β-catenin in the Wnt-pathway associated destruction complex[18, 39-41].

Many studies in the literature conflate YAP1 and TAZ and apply their conclusions to both proteins as a unit. Also, numerous key studies in the field have focused on double knockout models which inactivate both YAP1 and TAZ or models which delete upstream Hippo regulators MST1/2 or LATS1/2 and thus activate both YAP1 and TAZ but have additional downstream effects. Considering how often YAP1 and TAZ work as a complex, these studies are invaluable

in understanding processes that depend on both YAP1 and TAZ as a unit. However, there is mounting evidence that YAP1 and TAZ have distinct roles in many tissue types and developmental stages which may be redundant, complementary, or completely different. For instance, whole body knockout of YAP1 is embryonic lethal, with broad vasculogenetic defects, while whole body knockout of TAZ results in viable offspring with focal disease in the kidney and lung [42-44]. Studies in many organs show that YAP1 and TAZ regulate survival, proliferation, and stemness, but individual tissue-specific knockouts show additional subtle defects related to YAP1 or TAZ but not both, suggesting that beyond their core shared functions YAP1 and TAZ have unique tissue-specific roles that cannot be compensated by the other[32, 45]. For this reason, more studies are needed to dissect the individual functions of YAP1 and TAZ as well as how they regulate one another in development and disease. Specifically in the liver, several studies point to distinct roles for YAP and TAZ1 in hepatocellular carcinoma[46, 47]. In addition, while many studies have pointed to key roles for YAP1 in biliary development and homeostasis and in regulating cell plasticity between hepatocytes and cholangiocytes, TAZ is unable to fully compensate for the absence of YAP and its roles in these processes have not been clearly elucidated[30, 48-50].

1.2 Embryonic Development of the Murine Liver and Biliary System

1.2.1 Early embryonic liver development and hepatocyte differentiation

The timeline of liver development and bile duct morphogenesis has been well characterized in mouse embryos.[51-54] Foregut endoderm undergoes specification at E8.5 through

expression of Forkhead box (Fox) A1/A2/A3 and GATA4 transcription factors. Secreted bone morphogenetic proteins (BMP) and fibroblast growth factor (FGF) ligands from the growing septum transversum mesenchyme and cardiac mesoderm promote the induction of liver progenitor cells, hepatoblasts, from the foregut endoderm. Hepatoblasts begin to migrate into the septum transversum mesenchyme at E10.5, forming cords and proliferating to expand the growing liver bud.[51] Around E13.5, hepatoblasts begin to differentiate gradually into hepatocytes, which has been suggested to be the default lineage fate. Most hepatoblasts show upregulation of HNF4α and C/EBPα and downregulation of HNF1β among other factors as they differentiate into hepatocytes.[51, 55, 56] Wnt/β-catenin signaling has been shown to be essential for hepatoblast proliferation, but it is also necessary for hepatocyte differentiation at this stage.[57] The role of YAP1 in early hepatic development is unknown. From E13.5 onwards through the first few weeks of postnatal development, hepatoblasts gradually mature into hepatocytes and adopt the unique structural and metabolic features of the mature liver acini, with polarized canaliculi for bile transport and strictly zonated metabolic functions. This process involves intricate genetic reprogramming and cell-cell communication with hematopoietic progenitors, endothelial cells, stellate cells, and components of the immune system, and has been extensively reviewed elsewhere[51, 52, 58].

1.2.2 Development and maturation of the intrahepatic biliary tree

The process of intrahepatic biliary differentiation and morphogenesis is outlined in Figure 2A. Molecular studies have identified that the process of biliary differentiation starts as early as E11.5 in mice, although most morphological studies have been able to identify primitive biliary cells around E13.5.[55, 56] Mesenchymal cells surrounding the immature portal veins

express the Notch ligand Jagged1, which binds to the Notch2 receptor in neighboring hepatoblasts to induce formation of the ductal plate around E13.5[59]. Ductal plate cells and hepatoblasts also express TGF-β receptor II (TGFβRII), which allows them to respond to TGF-β ligands produced around the periportal mesenchyme.[52, 60] However, these ligands exert their activity only in a tightly controlled gradient extending outwards from the portal vein, regulated by a precise ratio of CCAAT/enhancer binding proteins C/ebpα and C/ebpβ, resulting in stimulation of a layer of hepatoblasts directly adjacent to the ductal plate.[61] Notch and TGF-β signaling form part of feedback loops that contribute to a gene regulatory network by activating the biliary transcription factors Sox9 and Sox4, which are essential for biliary morphogenesis, along with HNF6, Onecut2, and HNF1β, which also contribute to limiting TGF-β signaling to only two layers of portal hepatoblasts.[58]

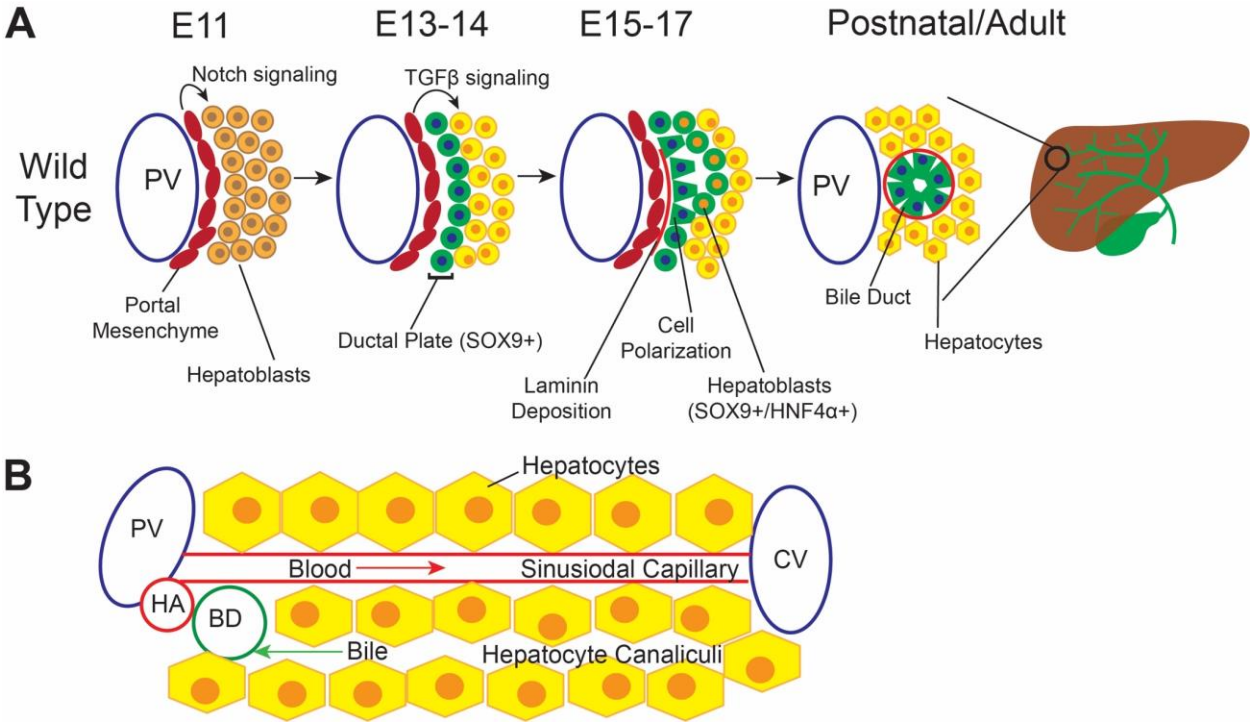

Figure 2. Overview of Biliary Development.

A) Overview of embryonic development of the intrahepatic bile ducts in the mouse. B) Schematic of the subunit structure of the mature mouse liver, showing the counter-current flow of blood and bile.

If the ductal plate is properly induced, ductal plate cells undergo a variety of changes to mature into functional biliary epithelial cells, or cholangiocytes. Cell polarity is established very early on, as visualized by polarized expression of osteopontin1 and ezrin (a junctional protein) along with the appearance of primary cilia on the apical membrane.[52] Polarization is also integral to lumen formation and apical constriction which marks the gradual morphological maturation of cholangiocytes [54, 62]. A combination of cytoskeletal mechanical forces and early bile acid flow from the nascent hepatocyte canaliculi contributes to the reorganization of plate cells to form ductal structures in parallel to the portal veins around E18.5.[52, 63] A basement membrane secreted by adjacent portal mesenchymal cells containing laminin-α1 initially supports the ductal plate, but as the cholangiocytes differentiate they secrete their own basement membrane containing

laminin-α5 which wraps around the nascent duct[64]. Ductal plate cells left out of the growing bile ducts continue to express Sox9 for some time but ultimately develop into periportal hepatocytes; a small population of hybrid Sox9+ hepatocytes remains into adulthood, with potential consequences for liver regeneration.[65, 66] At the same time, the differentiating cholangiocytes and hepatocytes secrete vasculogenic factors to regulate the formation of hepatic arteries from periportal mesenchymal cells.[67, 68] Despite our thorough understanding of the process of biliary morphogenesis from a visual point of view, there remain many gaps in our knowledge of the molecular mechanisms which underlie these subtle and coordinated changes.

Finally, at maturity, the portal veins, bile ducts, and hepatic arteries form a parallel system of vessels known as the portal triad. Blood flows from the portal vessels through the liver sinusoids (fenestrated capillary system) towards the central veins, creating an oxygen gradient, while bile produced in hepatocytes flows in a counter-current manner towards the bile ducts (Figure 2B).[69] As hepatocytes mature, they adopt different phenotypes based on their proximity to either portal triad vessels or central veins. Periportal hepatocytes perform gluconeogenesis, cholesterol biosynthesis, and urea metabolism, whereas pericentral hepatocytes responsive to Wnt/β-catenin signaling perform glycolysis, bile acid biosynthesis, and glutamine synthesis, thus creating zonation of opposing metabolic processes which is hallmark of the mature liver.[70]

1.2.3 Development and maturation of the extrahepatic biliary tree

The extrahepatic bile ducts (EHBD) consist of the common bile duct, gallbladder and cystic duct, and connect the intrahepatic bile ducts from the perihilar region of the liver to the pancreatic ductal system. The EHBDs transport bile from the liver towards the intestine, combined with the pancreatic exocrine secretions released at the Ampulla of Vater. The EHBDs

are also closely associated with peribiliary glands, a network of mucinous and serous acini connected with the bile duct lumina. The peribiliary glands have been proposed to act as a stem cell niche, although our understanding of their function remains in its infancy[54].

Although the EHBDs are thought to arise from the hepatic bud in humans, in mice the EHBDs arise from the ventral pancreatic bud as shown by recent lineage tracing studies.[71] A Sox17+/Pdx1+ progenitor population arising from the foregut endoderm and ventral pancreatic bud was shown to give rise to the pancreas and pancreatic ductal system, the duodenum, and the EHBD network.[72] Haploinsufficiency of Sox17 leads to malformation or agenesis of the gallbladder with defective contractility and function, although other parts of the EHBD network are not as strongly affected, suggesting that multiple factors play a role in specification of each component of the EHBDs.[73-76] The Notch pathway is also critical for EHBD formation. A Hes1-null mouse showed major dysgenesis of the EHBDs with expression of ectopic pancreatic cells, suggesting that Notch activity is involved in promoting and maintaining biliary differentiation while blocking pancreatic acinar differentiation from common progenitors.[72, 77] Activation of transcription factors including Hhex, Hnf6, and Hnf1β, along with BMP and FGF signals from the adjacent mesenchyme, have also been shown to play critical roles in EHBD formation.[71, 78, 79] Multiple mechanical signals regulated by Eph/Ephrin interactions regulate the formation of a continuous lumen from differentiating cholangiocytes.[80] Finally, there is some evidence that the Wnt and Hippo pathways contribute to EHBD formation, both within the biliary cells themselves and also from nearby hepatocytes[54, 71, 81].

However, the mechanisms regulating EHBD formation and the functions of each of these signaling pathways remains to be clearly elucidated, as much more work has focused on their roles in IHBD formation. Furthermore, we still do not understand how the EHBD and IHBD

networks interact during development to establish a continuous network. Some studies in animal models of EHBD dysgenesis report bile duct paucity as well, but it is unclear if this results from the genetic modification affecting both tissues or if EHBD formation is important in regulating IHBD formation. Molecular and cellular heterogeneity throughout the biliary tree remains to be fully investigated.

1.2.4 YAP1 in liver development: Knowns and Unknowns

At E10-12, Yes-associated protein 1 (YAP1) is present in both the nuclei and cytoplasm of hepatoblasts, but its function in this context is unknown.[82] Studies have identified YAP1 as a critical oncogene in hepatoblastoma, a pediatric tumor arising from hepatoblasts at various stages of development[83-85]. These studies have found YAP1 activity in patient samples, but they also have focused on a mouse model in which YAP1 contributes to dedifferentiation of adult hepatocytes into cancerous hepatoblasts[85]. This suggests that YAP1 may play a role in regulating stemness throughout embryonic development. It has been shown that YAP1 can alter the genomic binding localization of master regulators HNF4A and FOXA2, favoring an embryonic pattern of gene regulation based on enhancer binding in collaboration with YAP1/TEAD [27]. In adult tissues with decreased activity of YAP1/TEAD, HNF4A and FOXA2 bound to a different set of enhancers favoring expression of adult liver genes [27]. More studies are needed to investigate the function of YAP1 in hepatoblasts in their native context over the course of development.

Several studies have implicated YAP1 as an essential factor regulating biliary development. Deletion of YAP1 during mid-late embryonic development using Cre-recombinase driven by the Albumin promoter (*Alb*-Cre) results in a marked paucity of bile ducts postnatally,

causing long-term cholestatic injury and failed attempts by the liver to regenerate cholangiocytes.[86] On the other hand, inducing the expression of constitutively active YAP1 (S127A) in mature hepatocytes was shown to activate Notch signaling and promote the expression of biliary markers such as Sox9, and resulted in dedifferentiation of hepatocytes into oval cells, resembling liver progenitor cells.[49] Similarly, deletion of upstream regulator Merlin (Nf2) causes dramatic overgrowth of bile ducts, a phenotype which is completely ablated in the absence of YAP1.[86] Importantly, activation of YAP1 through the *Alb*-Cre-mediated knockout of the upstream inhibitory kinases Lats1/2 in mid-late embryonic development resulted in abnormal overgrowth of ductular cells expressing immature biliary markers.[48] Lats1/2-negative hepatoblasts differentiated much more efficiently into BECs than hepatocytes *in vitro*, due to YAP1-mediated direct transcriptional activation of TGF-β2 and transcriptional inhibition of HNF4α.[48] Furthermore, YAP1 may signal upstream to activate both Notch and TGF-β signaling in both embryonic cells (*in vitro*) and adult liver epithelial cells, and both of these pathways play key roles in biliary development.[48, 49, 60, 87, 88] Collectively, these studies suggest that YAP1 may be a critical driver of bile duct formation in liver development. However, the mechanistic targets of YAP1 in this process remain unknown.

Notably, deletion of both YAP1 and TAZ using the *Alb*-Cre model resulted in grossly similar biliary defects as *Alb*-Cre YAP1 single knockout.[89] However, Lee et al. examined the effect of deleting either YAP1, TAZ, or both in the context of Alb-Cre LATS1/2 deletion, and found that YAP1 and TAZ each exerted some influence on the level of biliary overgrowth, but only when both were deleted did the biliary lineage disappear altogether.[48] Furthermore, their histological analysis suggests some morphological differences in the biliary cell clusters after deletion of YAP1 and TAZ.[48] As of yet no studies have looked at embryonic TAZ knockouts to

fully differentiate the roles of YAP and TAZ in this process, which remains an open question of investigation.

Importantly, *Alb*-Cre models do not achieve complete recombination until after E18.5.[90] For instance, in the study by Lee *et al*, hepatoblasts isolated at E14.5 showed only 50% recombination, which leaves abundant YAP1+ cells at early stages of development.[48] Thus, models using *Alb*-Cre do not adequately evaluate the functions of YAP1 in early liver development and do not adequately assess the function of YAP1 in early hepatoblasts. Additional studies are needed to fully understand the role of YAP1 in early stages of liver development.

1.3 Principles of Biliary Repair and Regeneration

The biliary system is very sensitive to injury, and many acute and chronic liver injuries targeting both hepatocytes and cholangiocytes result in long-term damage to the bile ducts, with significant consequences for patients' quality of life. In this section, I will broadly discuss several ways in which the liver reacts to cholestatic injury and attempts to mount a reparative response, with varying degrees of effectiveness.

1.3.1 Overview of the cholangiocyte response to injury

Under normal conditions, mature cholangiocytes are quiescent, secretory cells which regulate the transport and composition of bile.[91] They are very sensitive to injury, and activate a variety of responses as shown in Figure 3A. Proliferation is a common injury response resulting

in a ductular reaction, which is an expansion of cholangiocytes (of varying morphology) around the portal vein and reaching into the liver parenchyma.[92-95] The ductular reaction may also consist of liver progenitor cells (LPCs), which may arise from cholangiocytes, hepatocytes, or a pre-existing stem cell compartment in the Canal of Hering, and the nature and function of LPCs remains a disputed question[95]. This ductular reaction has been thought to contribute to collecting bile from the parenchyma to prevent bile toxicity[94, 96]. The pathology of the ductular reaction varies greatly based on the disease context and has been extensively reviewed elsewhere[93, 97, 98]. Among the numerous signaling pathways activated in injured cholangiocytes, YAP1 has been shown to be critical for proliferation and ductular reaction formation in injury[99-102].

In addition, activated cholangiocytes secrete and respond to a variety of cytokines, chemokines, and neuroendocrine signals, and are closely associated with inflammatory infiltrates of neutrophils and macrophages as well as activated myofibroblasts[92, 103-105]. In chronic injury, cholangiocytes may become senescent in response to DNA damage and oxidative stress, leading to cell cycle arrest and activation of a pro-inflammatory senescence-associated secretory phenotype (SASP)[106, 107]. Senescent cholangiocytes continue secreting classic cytokines such as IL1, IL6, CXCL1/2, and IL8 in addition to matrix metalloproteinases and other ECM remodeling factors, leading to autocrine and paracrine signaling to neighboring Kupffer cells and stellate cells which respond in kind to these injury-related stimuli[106]. Chronically reactive cholangiocytes may contribute to worsening portal fibrosis and a pro-tumorigenic environment. YAP1 may contribute to inflammation and fibrosis by regulating production of cytokines such as CYR61 and CTGF, which may attract macrophages and contribute to activation of stellate cells into myofibroblasts.[31, 108, 109] This is an area of active investigation to determine how the ductular reaction can be manipulated to promote favorable repair and minimize tissue damage. Finally,

chronic severe biliary injury will often lead to duct loss through apoptosis of existing cholangiocytes and failure of proliferative regenerative mechanisms[103, 104, 106, 110].

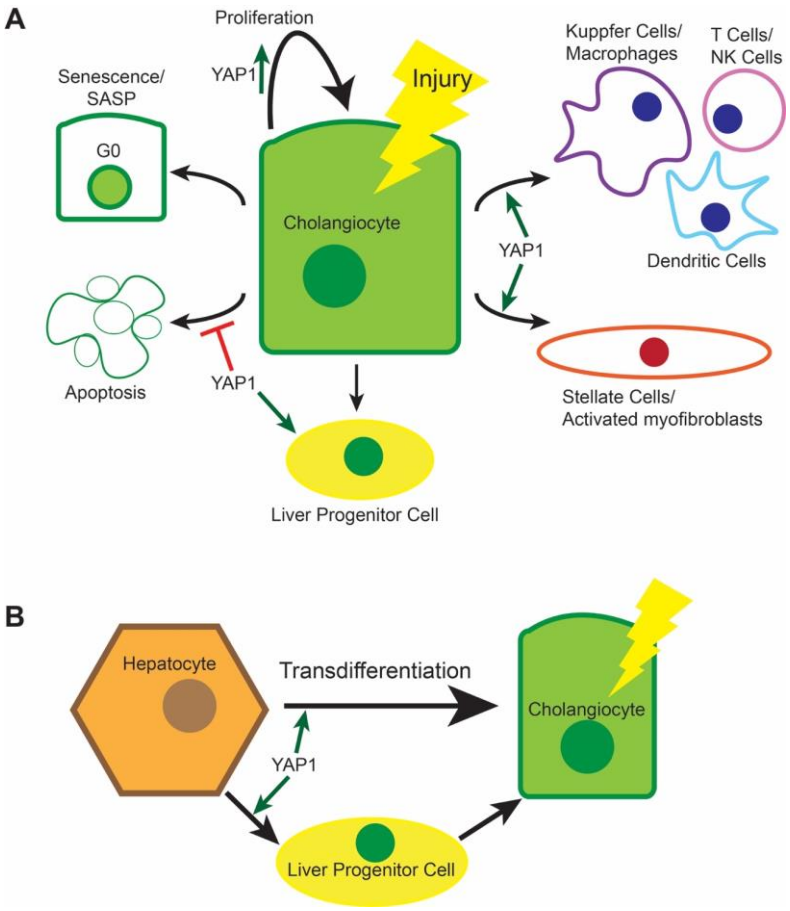

Figure 3. Overview of Cholangiocyte Response to Injury

A) Overview of various cholangiocyte responses to injury that may involve YAP1 signaling. B) Schematic of hepatocyte transdifferentiation into cholangiocytes.

1.3.2 Overview of hepatocyte-driven biliary repair via transdifferentiation

Although once a controversial idea, numerous studies in rodents have demonstrated using lineage-tracing experiments that hepatocytes have significant plasticity and are capable of

transdifferentiating into cholangiocytes to promote repair and regeneration in the setting of chronic biliary injury (Figure 3B) [88, 111-114]. Various types of injury models targeting the biliary system have been used to stimulate this response, such as the DDC-diet model, bile duct ligation, and DAPM biliary toxin. These studies have implicated pathways including Notch, Wnt-β-catenin, HIPPO/YAP1, and TGFβ pathways [30, 49, 88, 111-114]. While many studies suggest that all hepatocytes have this potential, some studies have identified specific sub-populations of hepatocytes that may have greater plasticity, such as telomerase-expressing hepatocytes or a subset of Sox9-expressing portal hepatocytes [66, 115]. Despite the clear evidence of hepatocyte-derived cholangiocytes, questions remain about whether these cells are capable of forming mature ducts or whether they regress after the injury has been resolved.[116]

Recently this regenerative response was convincingly observed in an animal model of Alagille syndrome with liver-specific developmental ablation of Notch signaling and HNF6 [88]. Intriguingly, despite the total failure of intrahepatic bile duct formation, many of these mice recovered and survived long-term due to hepatocyte-derived *de novo* generation of bile ducts forming a 3-dimensional, functional network [88]. This study further demonstrated that TGFβ-signaling through TGFβRII was necessary for transdifferentiation and regeneration to occur. Phenotypic recovery over time has also been observed in some (but not all) murine models of Alagille syndrome [117, 118], as well as in a subset of Alagille patients[119], making hepatocyte-derived biliary regeneration a likely candidate for functional repair in humans. While YAP1 can promote the expression of biliary markers in mature hepatocytes [30, 49] and is a potential regulator for Notch signaling [18, 120], it is not known whether YAP1 activation is essential or dispensable for cells to adopt a biliary phenotype or to assemble into functional ductular structures.

1.3.3 Overview of hepatocyte adaptations to cholestasis

One of the major function of the hepatocytes is the production of bile which is then channeled through first biliary canaliculi, then intrahepatic bile ducts and eventually extrahepatic biliary tree to eventually be secreted into the small intestine for fat absorption. However, imperfect flow of the bile can lead to stagnant bile flow and accumulation, a feature referred to as cholestasis. Although cholestasis can be caused by a wide variety of pathologies, the end result is an increase in hepatic bile acids (as well as bilirubin, toxins and heavy metals also excreted in bile) due to impaired bile processing and flow out from the liver through the biliary system. Since bile acids are in fact detergents essential for carrying lipids and for solubilizing lipids for absorption, these can promote cell injury and death both directly and indirectly by binding to cell death receptors and inducing oxidative damage[121, 122]. Bile acids also deplete cell membranes of cholesterol, resulting in altered lipid raft-associated signaling, and the subsequent elevated cholesterol synthesis results in hypercholesteremia and feedback effects on lipid metabolism[123, 124].

There is a complex system of feedback regulation by which hepatocytes respond to elevated bile acid levels, especially through interactions among bile acids and various nuclear receptors. One central regular is the farnesoid X Receptor (FXR) together with the Small Heterodimer Partner (SHP), which respond to elevated bile acid levels in hepatocytes by downregulating transcription of *Cyp7a1*, a key rate-limiting enzyme in bile acid synthesis[121, 122, 125, 126]. In addition, FXR/SHP, pregnane X receptor (PXR) and vitamin D receptor (VDR) among others form heterodimers with the retinoid X receptor α (RXRα) to coordinate the expression of bile acid transporters (altering influx and efflux of bile acids from hepatocytes into the canaliculi or the serum to reduce intracellular accumulation) and phase I/II metabolizing enzymes (which

conjugate bile acids to reduce their toxicity and increase hydrophilicity)[121, 122, 126, 127]. In addition, the peroxisome proliferator-activated receptor alpha (PPARα), a key regulator of lipid and glucose metabolism, regulates genes promoting bile acid conjugation and phospholipid secretion into the bile, overall decreasing bile toxicity[121, 122, 126-130]. Moreover, many of these receptors also regulate the secretion of inflammatory and pro-fibrotic cytokines as well as regulating the balance of pro- and anti-apoptotic signals[121, 122, 126, 127, 131, 132]. This complex signaling network lies at the heart of the liver's adaptive response to cholestasis and is the subject of intense investigation to develop therapeutics that amplify protective responses while reducing pro-apoptotic, pro-inflammatory, pro-fibrotic signals.

Besides managing bile acid toxicity directly, hepatocytes in the setting of cholestasis undergo a global transcriptional and functional reprogramming in response to injury. This has been described in several studies of the MDR2 knockout mouse model, which mimics human progressive intrahepatic familial cholestasis (PFIC) by impairing phosphatidylcholine secretion into the bile canaliculi, resulting in chronic obstructive cholestasis[133]. In the first few months of injury, MDR2 KO livers show an increase in oncogenic pathways, pro-survival and pro-proliferative pathways, DNA-damage response pathways, and oxidative stress response[133]. While these pathways contributed to survival in the short-term, the long-term activation of oncogenic pathways results in the development of hepatocellular carcinoma in MDR2 KO mice over 1 year of age[133-137]. Interestingly, it has been shown that bile acids can signal through the scaffold protein Iqgap1 to directly activate YAP1, which contributed to carcinoma formation in a model of severe cholestasis due to loss of FXR/SHP[138]. These models demonstrate the double-edged sword of liver adaptations to injury.

1.4 Overview of Select Pediatric Liver Diseases Arising During Development

Children are susceptible to a variety of liver diseases arising from genetic mutations and environmental insults that affect the normal course of liver development. In this section, we will focus on two disorders, Alagille syndrome and hepatoblastoma. The studies described in this thesis contribute to our understanding of the pathogenesis of these two diseases.

1.4.1 Alagille Syndrome

Alagille syndrome is an autosomal dominant disorder arising from mutations in the *JAGGED1* (<90%) or *NOTCH2* genes which causes multi-system malformations including impaired formation of bile ducts in embryonic development [119]. Children also exhibit congenital cardiovascular abnormalities, vascular anomalies, renal disease, and skeletal abnormalities among others [119]. In addition, children with Alagille exhibit marked growth deficiencies, associated with decreased caloric intake and chronic fat malabsorption due to decreased bile secretion into the gut, although there may be additional factors.[139] According to the National Organization for Rare Disorders, the incidence of Alagille Syndrome is estimated at 1 in 30,000 to 1 in 45,000 births.

One longitudinal study found that 89% of children with Alagille syndrome have cholestasis, ranging from mild to severe, and 75% exhibit bile duct paucity histologically.[140] According to a recent prospective study, only about 24% of children with bile duct paucity reach adulthood without a liver transplant, indicating the serious need for alternative therapies [141]. Interestingly, the penetrance of these mutations varies widely leading to variability in the extent of cholestasis and disease presentation, even among family members with the same mutation [119].

We lack a full understanding of the disease modifiers and relevant biomarkers that can help stratify or distinguish these patients during a critical treatment window [119, 142, 143]. Children with mild cholestasis, as measured by levels of serum bilirubin and alkaline phosphatase among others, often show improvement and resolution of disease over the first few years of life [119, 142, 143]. In contrast, persistently elevated serum total and conjugated bilirubin levels in young children with Alagille syndrome are associated with more severe liver disease and decreased likelihood of spontaneous improvement over time [144].

The disease phenotype has not been correlated with the location or type of mutation in the *JAGGED1* gene, suggesting that additional genetic or environmental modifiers greatly affect disease presentation and time course [145, 146]. Studies in mice have shown that inactivating glycosyltransferases, such as *Rumi* which directly modify JAG1 and NOTCH2 proteins, further worsens the course of disease[118, 147]. In addition, a genome-wide association study identified a single-nucleotide polymorphism in the *THROMBOSPONDIN2* gene which was associated with more severe disease[148]. Further studies are needed to identify mechanisms of action of these modifiers and determine whether they can be targeted clinically.

1.4.2 Hepatoblastoma

Hepatoblastoma (HB) is a deadly pediatric liver cancer that usually affects children in their first few years of life but may arise at any time in the first 2 decades of life.[149, 150] HB has an approximate incidence of 2 per million births, and this incidence rate has been steadily increasing over the past few decades[151]. Accounting for over 80% of pediatric liver tumors, HB has widely ranging mortality rates based on the risk category and histological subtype of HB.[149, 150, 152, 153] HB risk factors include premature birth and low birth weight, although these

associations are not understood[153]. HB is also associated with Familial Adenomatous Polyposis (FAP) and Beckwith-Wiedemann syndrome, both of which are caused by germline genetic alterations which are commonly HB tumor drivers.

The current gold standard of treatment is complete surgical resection of the tumor(s), based on the PRETEXT classification of spatial liver involvement[154]. Stratification of patients based on clinical, radiological, and pathological findings is currently critical to determine candidates for surgical resection as soon as possible and determine which patients may need neoadjuvant cytotoxic chemotherapy (often cisplatin) to reduce tumor size to facilitate removal or to treat metastatic disease[153, 154]. About 10% of children will have treatment-refractory tumors requiring a liver transplant, a costly treatment of last-resort due to the scarcity of organs.[152, 155, 156] There is a significant unmet need to develop targeted molecular therapies for children with HB, particularly to address PRETEXT 4 and metastatic disease as well as tumors which develop cisplatin resistance.

Hepatoblastoma is thought to arise from mutated hepatoblasts at various stages of development, and HB tumors consist of dedifferentiated cells that histologically resemble hepatoblasts in various embryonic stages of differentiation (Figure 4).[149] Several international studies have contributed classifications of histological and molecular subtypes reflecting the heterogeneity of HB tumors and ongoing studies aim to further improve these groupings.[152, 157, 158] Despite the existence of histological subtypes, most tumors exhibit multiple types of histology and should be treated based on the presence of the highest risk pathology. Well-differentiated fetal HB exhibits uniform fetal histology with low levels of proliferation and is the lowest risk category of HB[149, 152, 153]. Crowded fetal HB exhibits increased cell density and mitotic activity, while embryonal HB reflects immature hepatoblast morphology with high proliferation and

decreased expression of mature markers such as glutamine synthetase and glypican 3[149, 152, 153]. Finally, small-cell undifferentiated HB (anaplastic) exhibits the worst prognosis and least identifiable differentiation state[149, 152, 153]. HB tumors may also contain blastemal or mesenchymal elements as well as more specific morphological features including ductular differentiation or macrotrabecular histology, which are still under investigation[149, 152, 153].

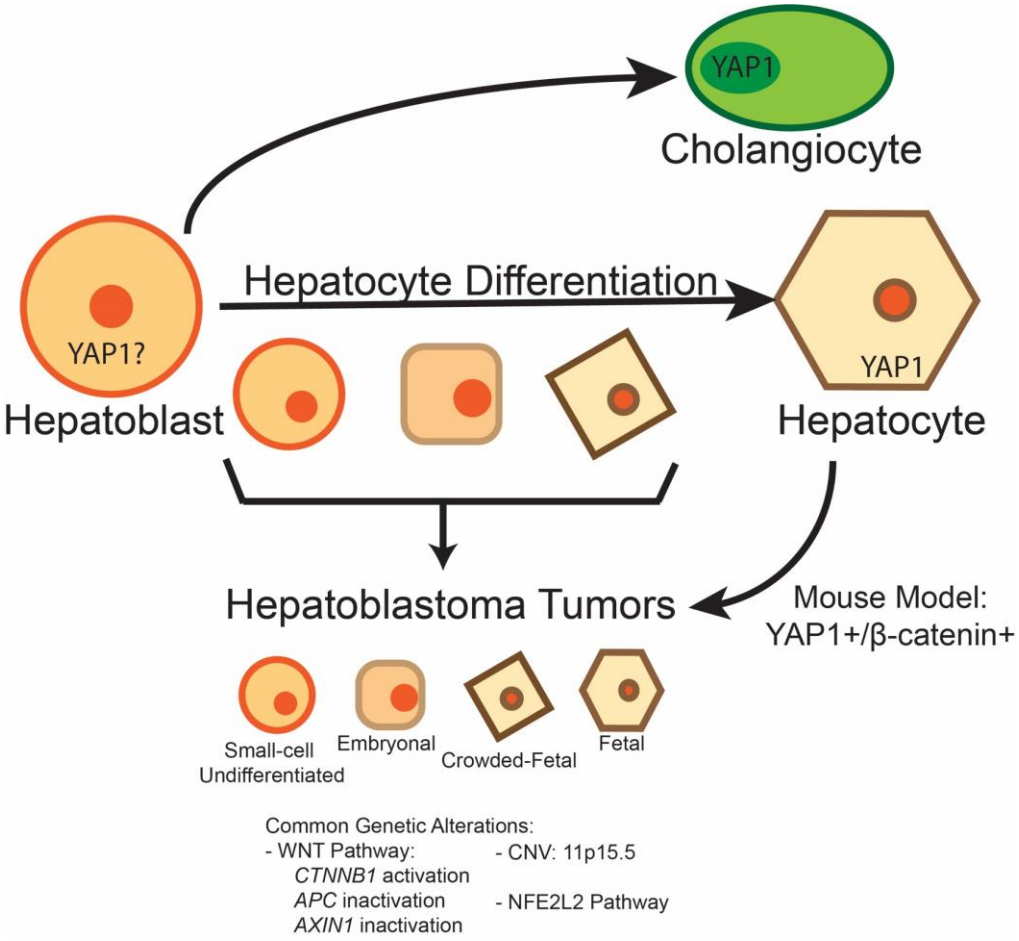

Figure 4. Overview of Hepatoblastoma Pathogenesis

Schematic of the differentiation of hepatoblasts into hepatocytes, and the origins of hepatoblastoma tumors along with common genetic alterations.

Molecular studies have shown that HB tumors generally carry a low mutational load, and the vast majority show activation of the Wnt-signaling pathway through somatic mutations in CTNNB1 (coding for β-catenin) or AXIN1 (negative Wnt regulator), or germline mutations in APC (upstream negative regulator of β-catenin).[153] Other pathways often altered included copy number alterations of imprinted locus 11p15.5 and mutations in NFE2L2 which is involved in antioxidant response. [153] Several studies have stratified tumors molecularly into high-risk categories often correlated with embryonal histology and poor prognosis and low-risk categories correlated with well-differentiated fetal histology, and new studies are taking into account mesenchymal and immune components as well.[159-163]

Our lab has shown that almost 80% of hepatoblastoma tumors from our patient cohort at Children's Hospital, Pittsburgh, demonstrated concominant activation of β-catenin and YAP1 signaling.[85] β-catenin is a transcriptional coactivator that is the major downstream effector of canonical Wnt signaling and plays key roles in liver development, regeneration, and tumorigenesis.[70] Studies have shown that β-catenin activity is essential for hepatoblast proliferation, and deletion of β-catenin in early liver development results in failure of hepatoblast differentiation and liver maturation.[57] Based on evidence of β-catenin and YAP1 activation in human samples, our lab created a mouse model of HB using Sleeping-Beauty transposase and hydrodynamic tail vein injection to force the expression of constitutively active YAP1 (S127A) and β-catenin (ΔN90 mutant).[85] We have shown that the simultaneous activation of β-catenin and YAP1 in mature hepatocytes leads to dedifferentiation into hepatoblast-like cells and causes hepatoblastoma tumor growth in mice (Figure 4).[85, 164] Both YAP1 and β-catenin are required for tumorigenesis in the mouse model of HB, but the mechanisms by which they drive HB pathogenesis and promote hepatocyte dedifferentiation remain unclear. We have shown that both

TEAD and TCF transcription factor binding partners are required for HB tumor formation in the mouse model, and activation of just YAP1 and β-catenin is insufficient to drive tumorigenesis[83, 85]. In addition, a recent study identified a critical role of mTORC1 in HB tumor development *in vitro* and *in vivo*, particularly downstream of YAP1. Multiple studies have pointed to the role of YAP1 and β-catenin in stimulating mTORC1 activity, and since mTOR can be pharmacologically targeted this may be a viable treatment option for HB tumors in patients[84, 165-167].

1.5 Overview and Rationale for Described Experiments

Several questions have emerged regarding the physiological role of YAP1 in embryonic liver and biliary development as well as its potential role in pathologies arising from developmental defects such as hepatoblastoma. To investigate the role of YAP1 in early embryonic liver development, we generated a mouse model using the *Foxa3* promoter to drive Cre-recombinase expression starting as early as E8.5. Chapter 2 focuses on the results of this investigation, which resulted in dramatic embryonic defects in bile duct formation. I also discuss subsequent adaptations to the absence of functional bile ducts in this model and demonstrate a critical role for YAP1 in hepatocyte-derived biliary regeneration. I also add some preliminary data regarding the functions of TAZ in this model, demonstrating that TAZ alone cannot compensate for the loss of YAP1 in early development but that it plays a role in the liver's adaptation to injury. I also show that loss of both YAP1 and TAZ in early foregut development results in embryonic lethality, opening the door to new questions about the cooperative and distinct functions of YAP1 and TAZ in different liver cell types.

Over the course of our studies, we aimed to visualize the biliary structures in their native context to determine their extent of growth and presence of structural defects. In collaboration with Dr. Alan Watson and the Center for Biological Imaging at the University of Pittsburgh, we designed a new method of tissue clearing specially for liver tissue, which is particularly difficult to clear, in order to achieve 3-dimensional imaging of intact biliary structures. This method is described in Chapter 3. I also demonstrate the broad applicability of this method to the study of many other liver diseases.

Chapters 4 and 5 describes investigations into the molecular mechanisms by which YAP1 regulates hepatoblastoma formation in concert with β-catenin, completed in collaboration with Dr. Junyan Tao, Dr. Danielle Bell, and Dr. Hong Yang. Using our lab's mouse model described above, we first identify lipocalin 2 as a mutual target of both tumor drivers and examine its role as a potential tumor biomarker in HB. Secondly, given the known roles of both YAP1 and β-catenin in promoting mTOR activity, we test the efficacy of general mTOR inhibition on HB tumor formation and describe a change in the differentiation state of the tumor as a result of pharmacologic mTOR inhibition. This result could have implications for treatment of aggressive embryonal tumors and reveal a close relationship between cell metabolism and hepatocyte differentiation state.

Altogether, these experiments describe important progress in our understanding of the unique roles of YAP1 in bile duct formation, hepatocyte adaptation after cholestatic injury, and hepatoblastoma tumorigenesis.

2.0 Compensatory Hepatic Adaptation Accompanies Permanent Absence of Intrahepatic Biliary Network Due To YAP1 Loss in Liver Progenitors

The following work describes my investigation of the role of YAP1 in embryonic liver development and regeneration after biliary injury. In addition, I offer preliminary insights into the roles of TAZ in this process. Part of this work is in a preprint published on BioRXiv (https://doi.org/10.1101/2020.10.21.349159). Dr. Junjie Zhu and Dr. Xiaochao Mao contributed to bile acid profiling by mass spectrometry. Dr. Qin Li and Dr. Andrew Feranchak contributed expertise in common bile duct cannulations. Dr. Tirthadipa Pradhan-Sundd, Dr. Ravi Vats, and Dr. Prithu Sundd contributed expertise in intravital imaging procedures. Dr. Khaled Sayed and Dr. Panayiotis V. Benos performed bioinformatic analysis of single-cell RNA-sequencing data. Nathanial Jenkins, Megan Smith, Dr. Alan Watson, and Dr. Simon Watkins contributed expertise and microscopy tools for 3D whole liver imaging. Yekaterina Krutsenko, Shikai Hu, Minakshi Poddar, Sucha Singh, Dr. Sungjin Ko, Dr. Junyan Tao, Dr. Aaron Bell, and Dr. Kari Nejak-Bowen contributed invaluable experimental and intellectual support. Finally, Dr. Satdarshan Monga contributed primary mentorship, funding, and intellectual input to this project.

Funding was provided by 2T32EB001026-16A1 and 1F30DK121393-01A1 to L.M.; 5R01CA204586-05, 1R01DK62277 and Endowed Chair for Experimental Pathology to S.P.M.; NIH grant 1P30DK120531-01 to Pittsburgh Liver Research Center (for services provided by the Advanced Cell and Tissue Imaging Core); and NIH grant 2P30CA047904-32 to S.W. and the Center for Biological Imaging. We would also like to extend our thanks to Dr. Frederic Lemaigre and Dr. Dean Yimlamai for numerous insightful discussions and feedback.

2.1 Summary

YAP1 regulates cell plasticity during liver injury, regeneration and cancer, but its role in early liver development is unknown. YAP1 activity was detected in biliary cells and in cells at the hepato-biliary bifurcation in single-cell RNA-sequencing analysis of developing livers. Thus, we developed a mouse model to delete YAP1 from early foregut progenitors including hepatoblasts before E13. Hepatoblast deletion of YAP1 did not impair Notch-driven SOX9+ ductal plate formation, but prevented the maturation of ductal plate cells and impaired formation of the abutting second layer of SOX9+ ductal cells, blocking the formation of a patent intrahepatic biliary tree. Intriguingly, the mice survived for 8 months with severe cholestatic injury and without any hepatocyte-to-biliary transdifferentiation. Ductular reaction in the perihilar region suggested extrahepatic biliary proliferation likely seeking the missing intrahepatic biliary network. Long-term survival of these mice occurred through hepatocyte adaptation via reduced metabolic and synthetic function including altered bile acid metabolism and transport. Furthermore, we show that deletion of both YAP1 and TAZ in early liver development results in embryonic lethality, while deletion of only one copy of TAZ from YAP1 KO mice resulted in lethality for male pups but barely affected female pups beyond the known YAP1 KO phenotype. In this case, we show that TAZ interacts with TEAD to regulate a subset of genes important in cell proliferation, inflammatory response, and apoptosis. Overall, we show YAP1 as a key regulator of bile duct development while highlighting a profound adaptive capability of hepatocytes, which is partly mediated by TAZ.

2.2 Background

The biliary tree is a delicate branching network of ducts formed of cholangiocytes which transport bile from the liver to the intestines. Alagille syndrome is an autosomal dominant disorder arising from mutations in the *JAGGED1* or *NOTCH2* genes which causes multi-system malformations including impaired formation of bile ducts in embryonic development [119]. According to a recent prospective study, only about 24% of children with bile duct paucity reach adulthood without a liver transplant, indicating the serious need for alternative therapies [141]. Interestingly, the penetrance of these mutations varies widely leading to variability in the extent of cholestasis and disease presentation, with some patients even showing spontaneous recovery. We lack an understanding of the disease modifiers and relevant biomarkers that can help stratify or distinguish these patients during a critical treatment window [119, 142, 143].

Yes-associated protein 1 (YAP1) is a transcriptional co-activator, and a mechanosensor that modulates cell differentiation, proliferation and survival among liver cells depending on the context [5]. Studies have shown that YAP1 is important for bile duct development and homeostasis, although its exact role remains poorly understood [30, 48, 49, 86]. Albumin (Alb)-Cre mediated deletion of YAP1 in late stages of murine liver development led to bile duct paucity postnatally, causing unresolved cholestatic injury [86]. Similarly, activation of YAP1 through Alb-Cre mediated deletion of upstream negative regulators LATS1/2 resulted in abnormal overgrowth of ductular cells, and *in vitro,* facilitated hepatic progenitor differentiation into BECs [48]. Other studies have shown YAP1 as a major driver of hepatoblastoma, a pediatric liver tumor, and can also dedifferentiate mature hepatocytes into hepatoblasts (HBs) in a murine model [27, 85, 168]. Thus, the role of YAP1 in hepatobiliary differentiation remains ambiguous.

Hepatobiliary plasticity is being increasingly appreciated. Chronic injury to the bile ducts in rodents induced transdifferentiation of hepatocytes into cholangiocytes to promote repair [88, 111-114]. Recently this was convincingly observed in an animal model of Alagille syndrome with liver-specific developmental ablation of Notch signaling and HNF6 [88]. Intriguingly, despite the total failure of intrahepatic bile duct formation, many of these mice recovered and survived long-term due to hepatocyte-derived *de novo* generation of bile ducts [88]. Phenotypic recovery over time has also been observed in some (but not all) murine models of Alagille syndrome [117, 118]. While YAP1 can promote the expression of biliary markers in mature hepatocytes [49] and is a potential regulator for Notch signaling [18, 120] (even in a mouse model devoid of the Notch co-factor RBPJ[169]), it is not known whether YAP1 activation is essential or dispensable for cells to adopt a biliary phenotype or to assemble into functional ductular structures.

In this study, we conclusively address the role of YAP1 during the earliest stages of embryonic liver development demonstrating its indispensable role in bile duct morphogenesis. The conditional loss of YAP1 in HBs led to a complete failure of intrahepatic biliary tree generation, reminiscent of Alagille syndrome, as demonstrated using a variety of functional studies and innovative three-dimensional (3D) imaging. Further, we characterize the compensatory metabolic and synthetic adaptations that allow mice with severe cholestatic injury to survive long-term. Finally, we show that while TAZ, a paralog of YAP1, cannot compensate for the role of YAP1 in biliary development, it plays a role in early liver development as well as in the adaptation of adult to chronic cholestatic injury by regulating gene expression independently of YAP1.

2.3 Materials and Methods

2.3.1 Animal Models

C57BL/6 *Yap1*$^{fl/fl}$ mice (Jackson Labs Stock No. 027929)[86] were bred into C57BL/6 *ROSA*-stop$^{fl/fl}$-EYFP mice. These mice were then bred into C57BL/6 *Foxa3*-Cre mice described previously[57] to create *Foxa3*-Cre *Yap1*$^{fl/fl}$ ROSA-stop$^{fl/fl}$-EYFP mice (YAP1 KO). Wild type littermate controls were compared to YAP1 KO mice for all subsequent analyses. In addition, FVB *Wwtr1*$^{fl/fl}$ *Yap*1$^{fl/fl}$ mice (Jackson Labs Stock No. 030532)[170] were bred into C57BL/6 *Foxa3*-Cre mice [57] to create *Foxa3*-Cre *Wwtr1*$^{fl/fl}$ *Yap*1$^{fl/fl}$ mice. All animal studies were performed in accordance with the guidelines of the Institutional Animal Use and Care Committee at the University of Pittsburgh School of Medicine and the National Institutes of Health. All animals were group housed in ventilated cages under 12h light/dark cycles with access to enrichment, water and standard chow diet ad libitum unless otherwise specified. Both male and female mice were used throughout the study and littermates were used as WT controls. Mice were analyzed at the following time points: E14.5, E16.5, E17.5, P9, P21, 3-4 months, and 6-8 months of age. Analysis of serum liver function tests was performed by the clinical laboratories at University of Pittsburgh Medical Center (UPMC).

2.3.2 scRNA-seq Raw Data Retrieval and Processing

The raw sequencing data files were downloaded from public dataset GEO:GSE90047 using the SRA toolkit with the “fastq-dump --split-files” command (http://ncbi.github.io/sra-tools/). The single-end reads were then quantified and aligned using kallisto algorithm with

"kallisto quant -i index_file -o output_file -t64 --pseudobam --single -l 51 -s 1 fastq_file".[171] We also used the "samtools sort" command[172] to sort the aligned bam files before we ran Velocyto[173] to create loom files with the command "velocyto run -e sample_id --onefilepercell --without-umi sorted_bam_file Mus_musculus.GRCm38.100.gtf". The loom files, which contain the data matrices, were then merged to a single file using the "loompy.combine" function on Python. Finally, the Seurat-Wrappers function "ReadVelocity()" was used to read the combined loom file and convert it to a single-cell gene expression count matrix.[174]

2.3.3 scRNA-seq Data Analysis

We used Seurat and Monocle packages to perform the single-cell and the pseudotime analyses.[174, 175] The count matrix was first converted into a Seurat object and then the data was normalized and scaled using Seurat functions NormalizeData() and ScaleData(), respectively. The top 5000 highly variable genes were then selected for the downstream analysis using the Seurat:FindVariableFeatures() function with selection.method = "disp" which selects the genes with the highest dispersion values. The top 5000 highly variable genes were used to perform principal component analysis which was conducted using the Seurat:RunPCA() function. The first 10 principal components were used for Louvain clustering and tSNE visualization (Seurat functions FindClusters() and RunTSNE(), respectively). The expression values of the genes were visualized using Seurat function VlnPlot(). The Pseudotime analysis was performed using the Monocle package following the three standard workflow steps which include choosing genes that define cells' progress (i.e., feature selection), reducing the data dimensionality using the reverse graph embedding algorithm[176], and ordering the cells in pseudotime. The Monocle function

plot_genes_in_pseudotime() was used to create Figure 5D which shows the expression levels of the genes of interest as a function of the differentiation pseudotime.

2.3.4 Immunostaining

Adult livers were harvested and fixed in 10% formalin for 48 hours, then transferred into 70% ethanol followed by paraffin embedding at the UPMC clinical laboratories. Embryonic and fetal livers were harvested and fixed in 4% paraformaldehyde (PFA) for 24 hours at 4C, followed by paraffin embedding. For immunostaining, 4μm paraffin sections were cut, deparaffinized and rehydrated. Sections underwent antigen retrieval by the following methods: 1) pressure cooker, 20 minutes, in sodium citrate buffer pH 6 (YAP1, SOX9, HNF4α, EYFP, CK8, pan-laminin, HES1, TAZ; also CK19 for IF); 2) pressure cooker, 20 minutes, in Agilent DAKO (S1699) target retrieval solution (CK19 for IHC); 3) microwave, 60% power, 12 minutes, in sodium citrate buffer pH 6 (CK8, acetylated tubulin, HNF4α); 4) steamer, 20 minutes, in sodium citrate buffer pH 6 (CD45).

At this point, for immunohistochemistry, slides were treated with 3% H_2O_2 for 10 minutes to deactivate endogenous peroxidases, washed three times with PBS, then blocked for 10 minutes with SuperBlock reagent (ScyTek Laboratories, AAA500). Slides were incubated in primary antibody diluted in PBS with 0.1% bovine serum albumin (BSA) and 0.01% sodium azide (IHC buffer), for either 1 hour at room temperature (CD45, 1:100) or overnight at 4C (YAP1 1:50, SOX9 1:2000, CK19, 1:50, TAZ 1:50). Slides were then washed three times with PBS and incubated in the appropriate biotinylated secondary antibody at 1:500 dilution for 30 minutes at room temperature. Samples were washed with PBS three times and sensitized with the Vectastain ABC kit (Vector Laboratories, PK-6101) for 30 minutes. Following three washes with

PBS color was developed with DAB Peroxidase Substrate Kit (Vector Laboratories, SK-4100), followed by quenching in distilled water for five minutes. Slides were counterstained with hematoxylin (Thermo Scientific, 7211), dehydrated to xylene and coverslips applied with Cytoseal™ XYL (Thermo Scientific, 8312-4). Images were taken on a Zeiss Axioskop 40 inverted brightfield microscope. Whole slides were scanned at 40x magnification using an Aperio AT2 slide scanner (Leica Biosystems).

For immunofluorescence staining, following deparaffinization, rehydration, and antigen retrieval as listed above, sections were permeabilized for 5 minutes with PBS/0.3% TritonX-100 and blocked for 45 minutes in PBS/0.3% TritonX-100/10% BSA. Slides were incubated at 4C overnight in primary antibody cocktails diluted in PBS/0.3% TritonX-100/10% BSA at the following concentrations: CK8, 1:8; all others, 1:100. Slides were washed three times in PBS/0.1% TritonX-100 and incubated at room temperature in secondary antibody cocktails (Invitrogen) also diluted in PBS/0.3% TritonX-100/10% BSA, for 1 hour (dilution 1:500) or 2 hours (dilution 1:800). Slides were again washed three times in PBS/0.1% TritonX-100, then washed three times in PBS, and mounted and coverslipped using VECTASHIELD Antifade Mounting Medium with DAPI (Vector Labs). Slides were imaged on a Nikon Eclipse Ti epifluorescence microscope or LSM 700 Carl Zeiss confocal microscope. Cell and nuclei quantification was performed using Fiji/ImageJ [177].

For H&E staining, samples were deparaffinized and stained with hematoxylin (Thermo Scientific, 7211) and eosin (Thermo Scientific, 71204), followed by dehydration to xylene and application of a coverslip. For Sirius Red staining, samples were deparaffinized and incubated for one hour in Picro-Sirius Red Stain (American MasterTech, STPSRPT), washed twice in 0.5%

acetic acid water, dehydrated to xylene, and coverslipped. Images were taken on a Zeiss Axioskop 40 inverted brightfield microscope.

2.3.5 Liver tissue clearing and whole liver immunostaining

Livers were washed in PBS and tissue fixation was achieved by incubating either whole livers or individual liver lobes in 4% paraformaldehyde (PFA) for 24 hours at 4C. Livers were subsequently washed in PBS and stored long-term in PBS/0.1% sodium azide (PBSA) at 4C.

Tissues were incubated in an inactive hydrogel solution overnight at 4C, consisting of 4% acrylamide (Bio-Rad 161-0140), 0.05% bis-acrylamide (Bio-Rad 161-0142), and 0.25% (wt/vol) VA-044 dissolved in PBS. The hydrogel solution was then polymerized by placing the tissues in a water bath at 37C for 3 hours.[178, 179] Excess hydrogel was removed, tissues were washed in PBS, and then tissues were placed in the X-CLARITY clearing apparatus (LogosBio C30001). Tissues were cleared using X-CLARITY-ETC Tissue Clearing Solution (LogosBio C13001) supplemented with 10-20mL of N,N,N′,N′-Tetrakis(2-Hydroxypropyl)ethylenediamine (Quadrol) for every 1.5L of clearing solution. The clearing apparatus was run at 37C with constant fluid circulation (100rpm peristaltic pump setting) and a setting of maximum current and voltage set at 1.5 Amps and 70 volts respectively. Timing of tissue clearing varied based on the size of the liver lobes and ranged from 24 hours (smallest lobes, 1000x1000x3mm) to 72 hours (large lobes, 2000x2000x5mm). Next, tissues were washed with PBSA and incubated in 3% H_2O_2 for 24 hours. At this stage, after washing with PBSA, tissue could be stored long-term in PBSA at room temperature or 4C, or they could proceed directly to immunostaining.

Tissues were stained as described by Muntifering, *et al* in 2018 with primary and secondary antibodies.[179] To ensure even staining throughout the sample, antibodies were applied

by using the SWITCH protocol.[180] All incubations took place at 30C. Briefly, tissues were incubated for 6 days in IHC buffer with 0.5 mM SDS containing CK19 antibody (1:10 dilution). Tissues were then removed from the primary antibody solution and incubated for 1 day in IHC buffer without SDS. Tissues were washed in PBS 3 times for 2 hours each, then incubated in IHC buffer with 0.5mM SDS containing the corresponding conjugated secondary antibody for 6 days. Tissues were then removed from the secondary antibody solution and incubated for 1 day in IHC buffer without SDS. Tissues were washed in PBSA 3 times for 2 hours each, fixed for 2 hours in 4% PFA, washed once more in PBSA, and finally placed in CUBIC R2 solution (50wt% sucrose, 25wt% urea, 10wt% 2,2′,2′’-nitrilotriethanol, and 0.1% (v/v) Triton X-100)[181] for imaging and long-term storage at room temperature.

All tissues were mounted in CUBIC R2 solution and imaged using an RSG4 ribbon scanning confocal microscope (Caliber, Andover, MA) as previously described by Watson *et al*.[182] The microscope was fitted with a Nikon CFI90 20x glycerol-immersion objective (Nikon, Melville, NY) with 8.3mm working distance. Volumes were captured with voxel resolution of 0.467 x 0.467 x 12.2 μm (x, y, z). Laser intensity and detector settings were specific to each sample based on the levels of staining. In all cases, the intensity of the laser was increased in a linear manner throughout deeper focal planes to compensate for absorption of excitation and emission light. RAW images acquired in this way were stitched and assembled into composites using a 24 node, 608 core cluster, then converted into the Imaris file format (Bitplane, Zurich, Switzerland). Volumes were rendered using Imaris v9.5.1.

2.3.6 Measurement of bile flow through cannulation of the common bile duct

The common bile duct was cannulated and the bile flow rate was measured in live three to four month-old, male and female, WT and YAP1 KO mice. The bile duct was cannulated with a microfil tubing according to previously described techniques.[183, 184] In brief, mice were anesthetized with Avertin 0.5 mg/g intraperitoneally (IP). The common bile duct was incised with a pair of fine iridectomy scissors about 6 mm below the hilum of the liver. A microfil tube (WPI, Sarasota, FL, MF28G-5) was passed through the incision and propelled towards the hilum for a distance of about 3 mm. Bile flow rate was recorded (μl/min/100g body weight) and bile was collected in CryoTube vials (Thermo Fisher Scientific) and immediately placed in liquid nitrogen. Animal work described in this manuscript has been approved and conducted under the oversight of the University of Pittsburgh Institutional Animal Care and Use Committee.

2.3.7 Bile acid species detection and quantification

Bile acid profiling was performed as described previously.[185] For liver tissue samples, livers were homogenized in water (100 mg tissue in 500 μL water), and then 300μL of methanol: acetonitrile (v/v, 1:1) was added to a 100 μL aliquot of liver homogenate. For serum samples, 25 μL serum was mixed with 100 μL of methanol: acetonitrile (v/v, 1:1). All the mixtures were vortexed for 2 min and centrifuged at 15,000 rpm for 10 minutes. Two microliter of the supernatants from all samples was injected into the ultra-performance liquid chromatography (UPLC) coupled with a SYNAPT G2-S quadrupole time-of-flight mass spectrometry (Waters Corporation, Milford, MA) for analysis. The column type is Acquity UPLC BEH C18 column (2.1 × 100 mm, 1.7 μm). The details of mobile phase gradient were

reported previously.[186] The QTOFMS system was operated in a negative high-resolution mode with electrospray ionization as described previously.[185] Bile acid species were quantified by measuring their relative abundance as the area under the curve for each species using standards for comparison. WT and YAP1 KO liver samples or serum samples were compared using a t-test followed by Benjamini-Hochberg correction for multiple hypothesis testing, using FDR < 0.1 as a cutoff for significance.

2.3.8 Quantitative liver intravital imaging

Surgical methods used for the intravital imaging were described previously by Pradhan-Sundd, *et al*.[187] Intravascular fluorescent dyes included 100 μg of Carboxyflurescein (CF) and 200 μg of TXR dextran. TXR dextran (MW 70,000) was used to visualize the blood flow through the liver sinusoids whereas CF (MW 377) was used to visualize uptake of the dye from blood to hepatocytes at 1-2m post-injection and then from the hepatocyte to the bile-canaliculi within 5m. Microscopy was performed using a Nikon MPE multi-photon excitation microscope. Movies were processed using Nikon's NIS Elements (Nikon Elements 3.10). Signal contrast in each channel of a multicolor image was further enhanced by adjusting the maxima and minima of the intensity histogram of that channel. A median filter with a kernel size of 3 was applied over each video frame to improve signal-to-noise ratio.

2.3.9 Immunoprecipitation and Western Blotting

Flash frozen liver tissues were homogenized in RIPA buffer with Protease Inhibitors (ThermoFisher, cat. no. 78429). The protein concentration of each sample was determined using

the bicinchoninic acid assay (Thermo Fisher). For immunoprecipitation, 1mg of protein from each sample was incubated on a rotating nutator for 1 hour at 4C with approximately 2ug of antibody (TAZ, Abcam ab242313, Mouse; or panTEAD, Cell Signaling Technology CS13295S, Rabbit). Next, 20μL of Protein A/G-PLUS Agarose Beads (Santa Cruz, sc-2003) were added to each sample and incubated at 4C on a rotating nutator from 1.5 hours to overnight. Next, samples were centrifuged at 1000xg for 5 minutes at 4C and the supernatant was removed. Samples were washed with RIPA buffer 3-4 times, each time centrifuging at 1000xg for 5 minutes at 4C and removing the supernatant. Finally, after the last wash, the beads were resuspended in 35-40μL of 2x Laemmli buffer (BioRad, cat. no. 1610737) containing 1:50 dilution of 2-mercaptoethanol (BioRad, cat. no. 1610710). Samples were heated at 95C for 10 minutes and centrifuged at 1000xg for 5 minutes at 4C.

Next, 15μL of each sample were loaded into each well of a 10% Mini-PROTEAN® TGX™ Precast Protein Gel (BioRad, cat. no. 4561036) for electrophoresis. Precision Plus Protein WesternC Standards (BioRad cat. no. 161-0376) was used as a molecular weight ladder. Proteins were then transferred onto Immobilon-FL PVDF membranes (Sigma Aldrich, cat. no. IPFL00005, pre-activated in methanol) via standard wet transfer method. Membranes were blocked for 30 minutes at room temperature (RT) in 5% Bovine Serum Albumin (BSA; Fisher, cat. no. BP1605-100) dissolved in Tris-buffered saline containing 0.1% Tween 20 (TBST). Membranes were then incubated in primary antibody dissolved in 5% BSA for either 1.5 hours at RT or overnight at 4C (YAP/TAZ, Cell Signaling Technology CS8418S Rabbit, 1:500; TAZ, Abcam ab242313, Mouse, 1:500; panTEAD, Cell Signaling Technology CS13295S, Rabbit, 1:1000). Membranes were then washed 3x in TBST and incubated in secondary antibody for 1 hour at RT (Mouse anti-Rabbit Light Chain Only HRP-conjugated, Cell Signaling Technology

CS93702, 1:5000; Goat anti-Mouse HRP-conjugated, ThermoFisher cat. no. 31430, 1:10,000). Membranes were washed 3x in TBST and bands were visualized using Super Signal West PICO Reagent (ThermoFisher cat. no. PI34580).

2.3.10 RNA extraction and RNA-sequencing analysis

Frozen liver tissue was homogenized in Trizol at 4C and RNA was extracted using QIAGEN RNeasy Mini Kit (Cat. 74104). DNA digestion and removal were performed on the column using the RNase-free DNase Set (Cat. 79254) as per manufacturer instructions. RNA quality and concentration were assessed using a Nanodrop. Purified, high quality RNA from 6 WT livers (3 male, 3 female), and 6 YAP1 KO livers (3 male, 3 female) to Novogene Co. (Sacramento, CA) for cDNA library preparation and RNA-sequencing by Illumina Novaseq 6000 of paired-end 150bp reads, with 20 million reads per end per sample. RNA-sequencing data generated from this study are available at Gene Expression Omnibus, Series GSE157777. Separately, high quality RNA was also sequenced from 3 female YAP1 KO mice with 3 female WT littermate controls (C57Bl6), and 3 female YAP1 KO/TAZ HET mice with 3 female WT littermate controls (mixed background).

Raw sequencing data was processed using CLC Genomics Workbench 20.0.3 (QIAGEN Inc., https://digitalinsights.qiagen.com) for quality control and aligned to the *Mus musculus* genome version GRCm38.p6. Reads assigned to each gene underwent TMM normalization and differential expression analysis was performed using *edgeR* within CLC Genomics to compare WT versus YAP1 KO mice. The top differentially expressed genes were filtered by adjusted p-value $q < 0.05$ and fold-change greater than 2 for subsequent downstream pathway analysis using Ingenuity Pathway Analysis (IPA; QIAGEN Inc.,

https://www.qiagenbioinformatics.com/products/ingenuity-pathway-analysis), Gene Set Enrichment Analysis (GSEA) and Molecular Signature Database (MSigDB)[188], and Enrichr[189, 190]. CLC Genomics Workbench, and IPA were all used under commercial licenses acquired by the University of Pittsburgh Health Sciences Library System.

2.3.11 Public data mining of ChIP-Sequencing data

Two public ChIP-Seq datasets were mined in this study to identify downstream genes potentially being regulated by TEAD transcription factors. The first study was downloaded from ENCODE database[191, 192] for ChIP-Seq in HepG2 cells, and peaks for TEAD1, TEAD3 and TEAD4 binding sites were called by the ENCODE website pipeline with default parameter settings (accession IDs ENCSR497JLX, ENCSR666QNP, ENCSR000BRP). The second study was downloaded from GEO data base with accession ID GSE107860.[29] Raw mouse ChIP sequencing data were collected for TEAD4. Raw reads were trimmed by Trimmomatic[193] and aligned to mouse reference genome mm10 by BWA aligner.[194] Peak calling was performed by tool MACS2[195] comparing input sample and immune-precipitation samples. For all the three studies, peak regions were annotated to genes by R/Bioconductor packages ChIPpeakAnno[196, 197] and ChIPseeker[198]. Genes involved in peaks with p-value <= 1E-7 were selected as the TEAD target genes for downstream analysis. For our final list of potential TEAD targets, we selected 3773 genes which were present in all 4 data sets as potentially targeted by TEAD genome binding.

2.3.12 Quantification and statistical analysis

Statistical details of each experiment can be found in the respective figure legends. Data are presented as mean ± standard deviation (sd). n refers to biological replicates. $p < 0.05$ was considered statistically significant, except for individual bile acid species comparisons for which an FDR of 0.1 was used. GraphPad PRISM 7.0c software was used for statistical analyses. No samples or animals were excluded from the analysis. Littermate controls of both genders were used throughout the study. Data significance was analyzed using a two-tailed unpaired Student's t test or Mann-Whitney test in cases where two groups were being compared. In cases where more than two groups were being compared, one-way or two-way ANOVA were used with Sidak's test to correct for multiple comparisons.

2.4 Results

2.4.1 Loss of YAP1 in HBs during early embryonic development impairs bile duct morphogenesis and leads to failure of intrahepatic bile duct formation

To assess the status of YAP1 activity in liver development, we analyzed single-cell sequencing data published by Yang L. *et al*, for the expression of YAP1 targets [56]. This study had previously assessed the differentiation of HBs into hepatocytes and cholangiocytes from E10.5 to E17.5. We performed Louvain clustering and tSNE visualization and identified three clusters closely matching the cell identities assigned by Yang L. *et al*, clearly distinguishing the trajectory of differentiation over pseudotime of HBs (cluster a) into hepatocytes (cluster c) and

cholangiocytes (cluster b) (Figure 5A-B). When comparing gene expression in these clusters, we observed that the expression of canonical YAP1 targets *Ccn1* and *Ccn2* was notably increased in the cholangiocyte cluster over the pseudotime axis while remaining low in the HB and hepatocyte clusters (Figure 5C-D). We also found that several cells from early time points E11.5 – E14.5 were classified differently by our methods in comparison to those previously published, and express both *Sox9* and *HNF4α*, suggesting they may be cells of intermediate differentiation (Figure 5A-B). YAP1 target gene expression in these cells (cluster d) is somewhat higher than in most HBs but lower than most cholangiocytes (Figure 5C), suggesting that YAP1 activity is increasing in these intermediate cells as they transition into cholangiocytes.

Previous studies have used *Alb*-Cre to delete YAP1 in the liver to elucidate its functions. However, in this model recombination occurs around E15-16 and is not completed until 4-6 weeks postnatally [199]. Since the process of cholangiocyte differentiation from HBs begins earlier at around E11.5 [55, 56], at which time we also observe YAP1 activation, we targeted YAP1 in HBs at the earliest stages of development. Since *Foxa3* is activated in the foregut endoderm progenitors, including HBs, starting at E8.5 and achieving complete recombination around E12-13 [57, 200], we bred *Foxa3*-Cre transgenic mice to YAP1-floxed mice and generated HB-YAP1 knockout (YAP1 KO) mice. IF imaging for YAP1 at E14.5 shows complete loss of YAP1 from HNF4α-labeled HBs (Figure 5E).

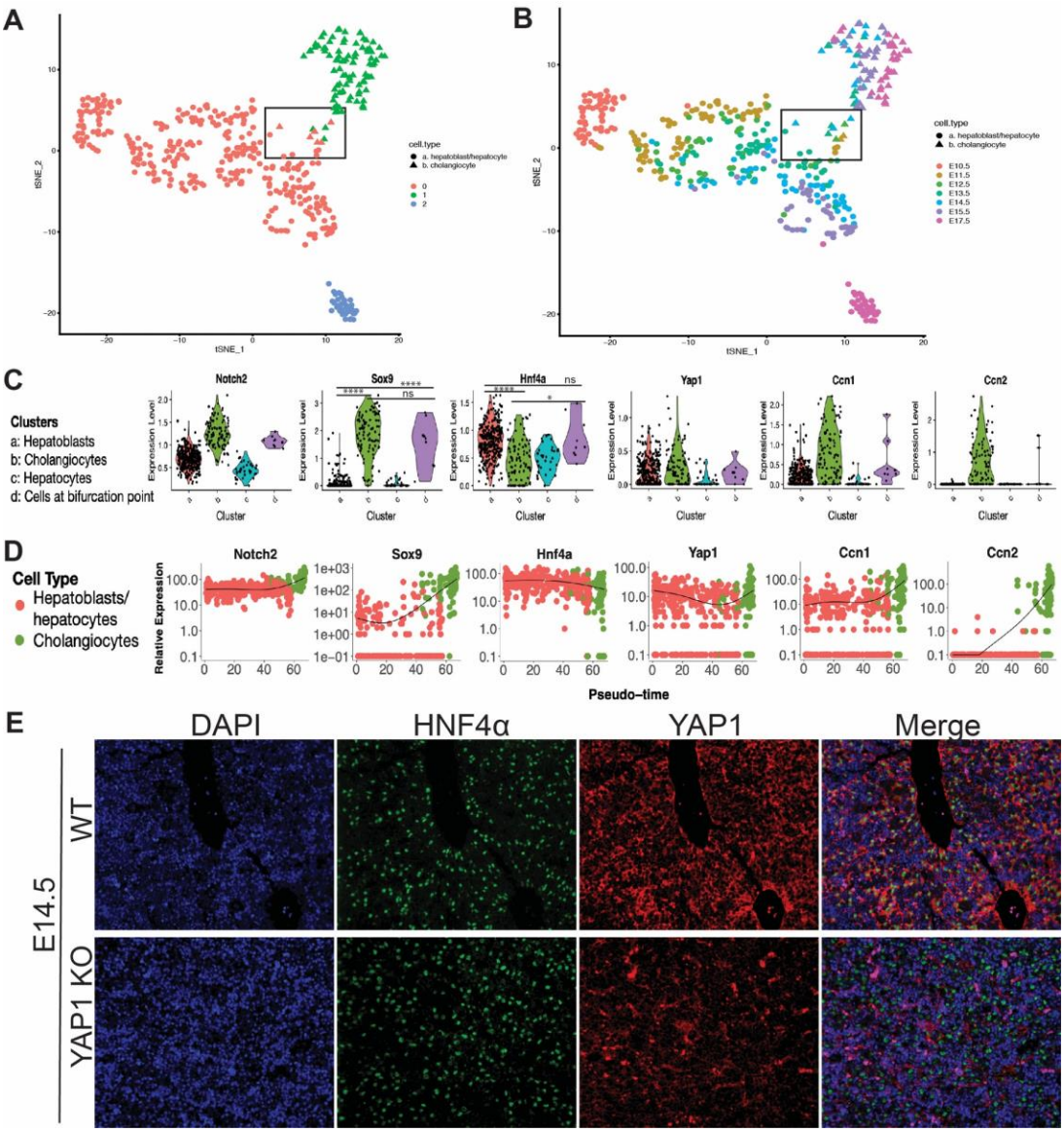

Figure 5. Characterization of YAP1 activity in early liver development

A-B) tSNE plots of single cell sequencing data from a previously published study (GSE90047) on embryonic liver epithelial cells reveals three clusters (a, b, and c) of cells roughly compatible with the original publication's classification of hepatoblasts, hepatocytes, and cholangiocytes (Cell Type) and traces the divergence of both lineages over pseudotime and developmental time from E10.5 to E17.5. Boxes highlight cells which cluster with hepatoblasts but were identified as cholangiocytes and are labeled as cluster d in panels C and D. C. Gene expression of key cell type markers and YAP1 targets by cluster. D. Gene expression of key cell type markers and YAP1 targets by cell type and pseudotime. E. IF co-staining for HNF4α and YAP1 at E14.5 in WT and YAP1 KO liver.

Although we expected to observe a more widespread effect, the YAP1 KO mice formed all foregut organs and were viable postnatally, with some mice surviving up to 8 months at which time they were sacrificed for experimental study. Over more than 3 years of breeding, we have collected embryos and adults of YAP1 KO mice, along with littermate wild-type (WT) and YAP1 heterozygous (HET) mice. We calculated the observed genotype frequencies for both harvested embryos and adult mice (P21 or later), as shown in Table 1. We found that embryos up to E18 are harvested at the expected genotype frequency of 50% WT, 25% HET, and 25% YAP1 KO. However adult mice show a significant alteration in genotype frequencies, with 59% WT, 26% HET, and 16% YAP1 KO (Chi-squared test, p-value = 0.00099). Thus, we observe a loss of YAP1 KO mice in the early postnatal period from about 74 expected to 47 observed mice, a drop of about 36%.

Table 1. Genotype Frequencies from YAP1 KO Breeding

		WT	HET	YAP1 KO	Total
Embryos	Observed	47	19	27	93
	Expected	46.5	23.25	23.25	93
Chi-squared test	p-value	0.4998			
Adult	Observed	172	75	47	294
	Expected	147	73.5	73.5	294
Chi-squared test	p-value	0.0009894			

YAP1 has previously been suggested to play a role in the formation of bile ducts in embryonic development, but an underlying mechanism has remained elusive. We first show in WT mice that YAP1 is indeed present in the nuclei of ductal plate cells and maturing bile ducts at E16.5, while YAP1 is completely absent from hepatoblasts and developing ducts in YAP1 KO mice (Figure 6A). To investigate, we closely examined previously described stages of intrahepatic bile duct formation in YAP1 KO livers using SOX9 as a marker of cells which are adopting cholangiocyte specification. SOX9-positive cells representing the initial formation of

the ductal plate were evident around the portal veins at E14.5 and E16.5, similarly in the WT and YAP1 KO (Figure 6B-C). HES1, a downstream target of Notch signaling, was also similarly expressed in the ductal plate cells of the WT and KO embryonic livers (Figure 6F), suggesting initial activation of Notch signaling in putative BECs is not affected by YAP1 loss. Furthermore, expression of JAGGED1 in ductal plate cells was not changed in YAP1 KO relative to WT, as shown in Figure 6G.

Between E16.5 and E17.5, SOX9 staining in WT livers revealed a hierarchical formation of luminal structures, lined first on one side by the above-described pre-existing SOX9-positive ductal plate cells (Figure 6D, inset 1s and 2), and on the other side by another layer of SOX9-positive cells thought to be derived from HBs, which lose HNF4α and gain SOX9 to adopt a BEC identity (Figure 6D, inset 3) [52]. At comparable time points, YAP1 KOs showed disparate ductal morphology. At E17.5, we observed formation of only a few pseudo-luminal structures in YAP1 KO closest to the largest portal vessels (Figure 6D, insets 5 and 6), that were lined by SOX9-positive cells *albeit* only on the portal side. Moreover, we failed to observe any real ducts lined completely by the second layer of SOX9-positive cells (Figure 6D). Postnatally, YAP1 KO mice continued to retain a single layer of SOX9+ cells around the portal veins showing no signs of luminal structures (Figure 6E). The parenchymal or the second layer of would-be biliary cells in nascent ducts consistently retained HNF4α in KO, while in WT these cells lose HNF4α and gain SOX9 expression as they mature into BECs (Figure 6E). This resulted in an overall increase in the number of HNF4α-positive cells in E17.5 KO livers compared to matched-WT (Figure 7A-B). HNF4α also seemed to be expressed in the nuclei of some of the YAP1 KO ductal plate cells, as can be seen in Figure 6A and 6G.

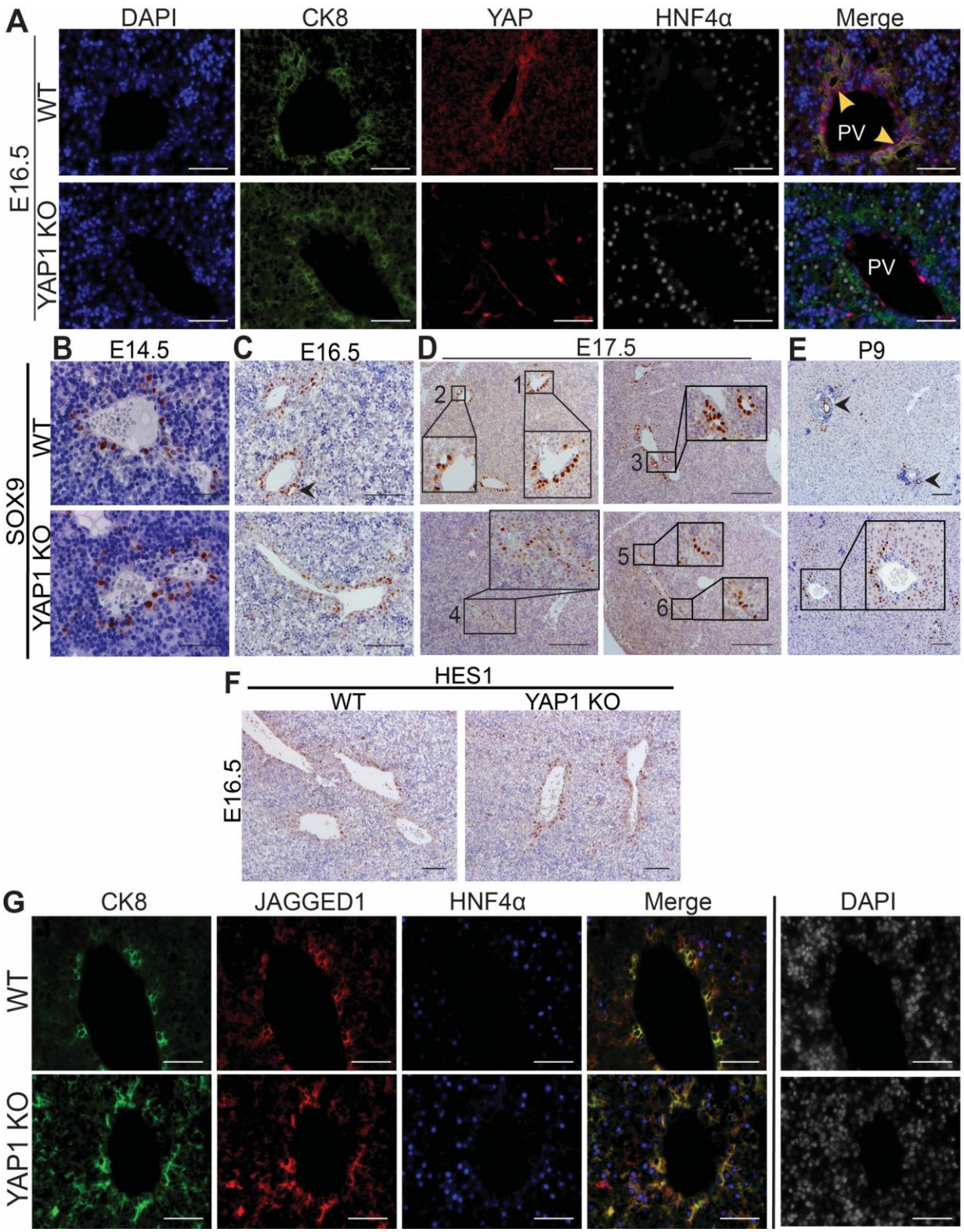

Figure 6. Biliary development is impaired in YAP1 KO mice but Notch signaling in the ductal plate is not altered.

Figure 6. A) IF co-staining for CK8, YAP1, and HNF4α at E16.5; yellow arrows highlight positive YAP1 nuclear staining in developing bile ducts in WT mice, which is absent in YAP1 KO mice. B-E) IHC for SOX9 in WT and YAP1 KO livers at (B) E14.5, (C) E16.5, (D) E17.5, and (E) P9. Arrows and insets point to various stages of bile duct development as described in the text. F) IHC for HES1 showing expression in ductal plate of WT and KO mice at E16.5. G) IF co-staining for CK8, JAGGED1, and HNF4α at E16.5 highlighting the ductal plate in WT and YAP1 KO mice. Scale bars in A, B and G are 50μm; scale bars in C-F are 100μm.

Since we observed the appearance of some pseudo-luminal biliary structures, we next queried whether primitive biliary cells in YAP1 KO mice successfully establish polarity. We used IF for acetylated α-tubulin to visualize primary cilia, which are critical for sensing bile flow and regulating numerous growth factor signaling pathways [201]. WT cholangiocytes in maturing bile ducts first displayed diffuse staining for acetylated tubulin throughout their cytoplasm, which gradually developed into precise punctate staining at the apical surface in both layers of ductal cells (Figure 7C, yellow arrows). In contrast, in YAP1 KO mice the ductal plate cells express acetylated tubulin in a diffuse pattern, with almost no puncta visible (Figure 7C). This suggests an impaired establishment of polarity in maturing portal cholangiocytes in KO mice.

Crosstalk between the ductal plate and the adjacent portal mesenchyme is also critical for bile duct morphogenesis [52]. Specifically, portal fibroblasts deposit laminins containing laminin-α1 on the portal side of the ductal plate to provide an initial foundation and later ductal cells deposit laminin-α5 in their surrounding basal lamina [52, 64]. Using a pan-laminin antibody, we show that WT ductal cells exhibit deposition of laminin first on the basolateral side closest to the portal vein and later surrounding the maturing duct (Figure 7D, yellow arrows). KO BECs showed only weak to no laminin deposition even on the portal side and failed to robustly deposit

laminin around any ductal cells (Figure 7D, white boxes), whether HNF4α positive or negative, and the only laminin observed in KO mice was lining the blood vessels.

All together, these data suggest that YAP1 loss does not alter Notch signaling in the ductal plate but rather prevents maturation of ductal plate cells and advancement of ductal morphogenesis by impairing cell polarization and laminin deposition. YAP1 loss also results in persistent HNF4α expression in hepatoblasts adjacent to the ductal plate, and even among some cells of the ductal plate.

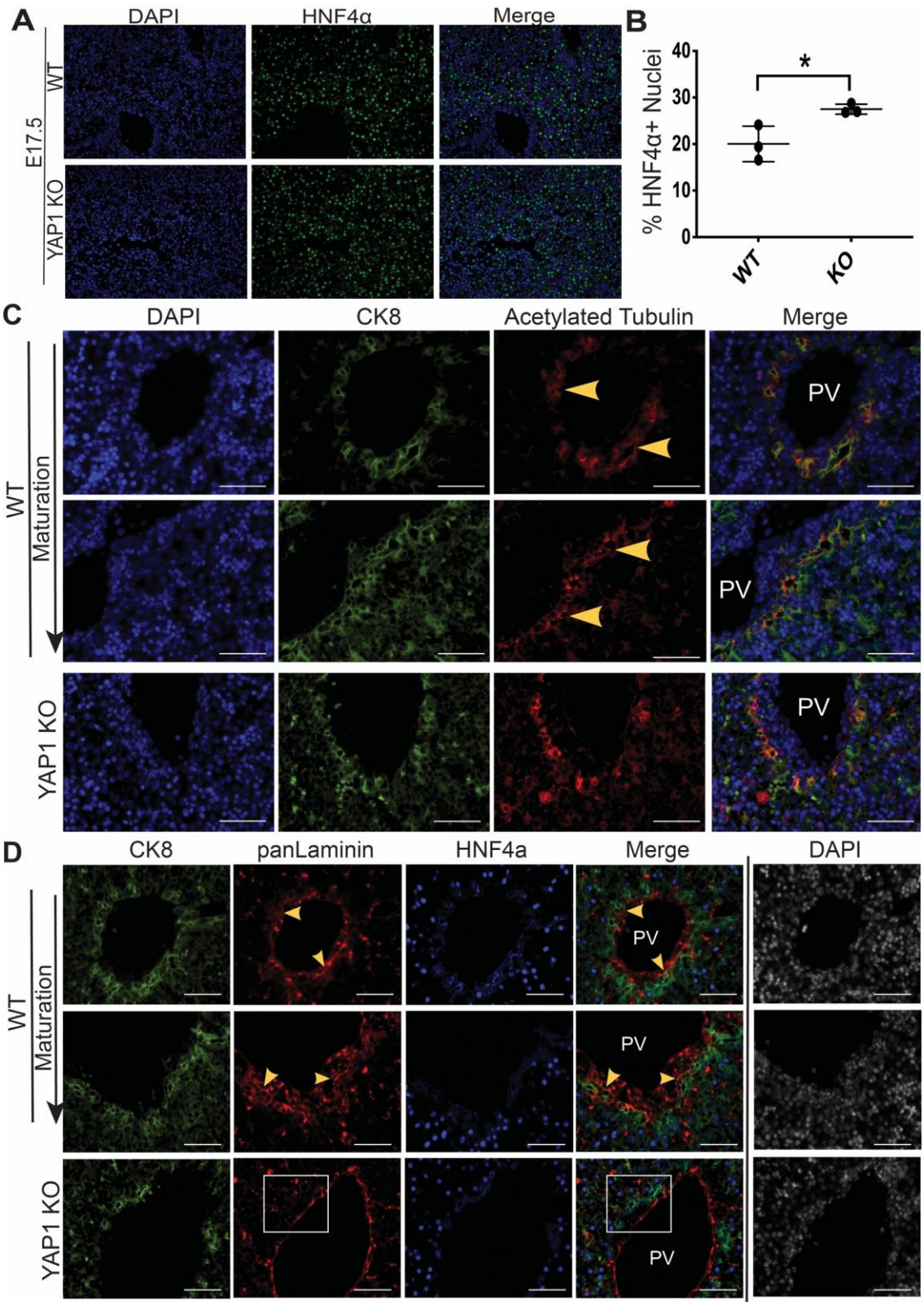

Figure 7. YAP1 KO mice exhibit defects in cell polarization and laminin deposition during biliary morphogenesis.

Figure 7. A) IF staining for HNF4α+ in WT and KO mice at E17.5. B) Quantification of HNF4α+ nuclei in KO vs WT mice (t-test, * p< 0.05). C) IF co-staining for CK8, acetylated tubulin, and HNF4α at E17.5 in WT and YAP1 KO livers showing bile ducts at intermediate stages of maturation. Yellow arrows highlight punctate acetylated tubulin staining representing primary cilia. D) IF co-staining for CK8, pan-laminin, and HNF4α at E17.5 in WT and YAP1 KO livers. Yellow arrows point to normal laminin deposition around developing ducts in the WT, which is absent around YAP1 KO ductal cells (white boxes). Scale bars in C-D are 50μm.

2.4.2 YAP1 KO mice exhibit severe chronic cholestatic injury but survive long-term

Grossly, mice displayed stunted growth and were visibly jaundiced (Figure 8A), with significantly lower body weight than WT littermates, although their liver weights were comparable to WT mice, resulting in a dramatically increased liver weight to body weight ratio (Figure 8B-D). At postnatal day 21 (P21), YAP1 KO mice showed elevated alkaline phosphatase, total bilirubin and direct bilirubin levels, and significantly elevated aspartate and alanine aminotransferases (AST and ALT), indicating severe hepatocellular and cholestatic injury (Figure 8E-H). H&E staining displayed numerous biliary infarcts (Figure 8I).

Based on the observed developmental defects in bile duct formation, we next looked for the presence of any bile duct markers. At 3 months of age, SOX9 staining in adult KO livers revealed unstructured clusters of SOX9+ cells around the portal vein, in contrast to well-formed SOX9+ patent bile ducts in WT (Figure 8J), just as we observed at P9 (Figure 6).

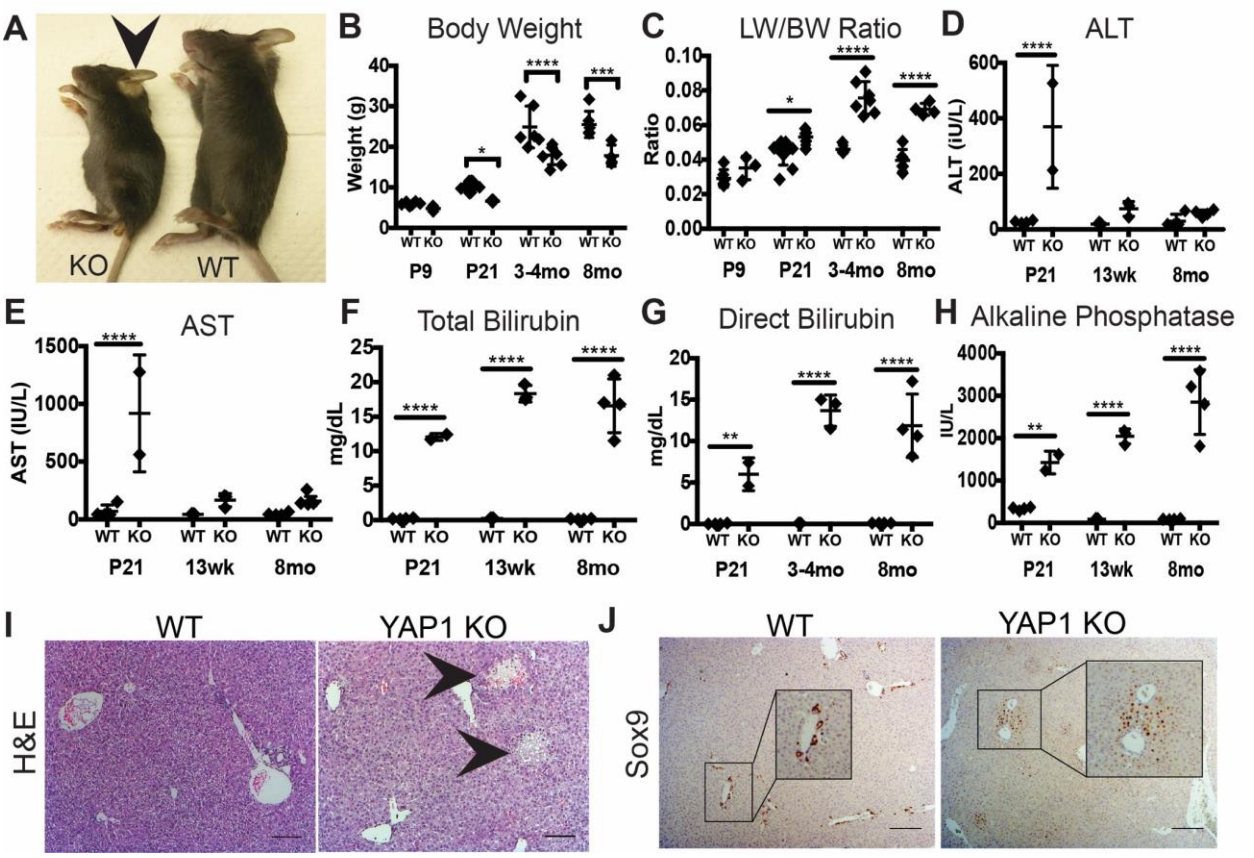

Figure 8. YAP1 KO mice exhibit severe cholestatic injury but many survive long-term.

A) Gross image of WT and YAP1 KO mouse, arrow shows jaundiced ears. B) Body weight and C) Liver weight to body weight (LW/BW) ratio of WT and KO mice over time. Serum levels of D) alanine aminotransferase (ALT), E) aspartate aminotransferase (AST), F) total bilirubin, G) direct bilirubin, and H) alkaline phosphatase in WT and KO mice over time. Graphs show mean ± sd. Data were analyzed by 2-way ANOVA with Sidak multiple comparison test, n = 2-5 mice per group (* p<0.05, ** p < 0.01, *** p<0.001, **** p<0.0001). I) H&E shows patches of necrosis in KO mice compared to healthy WT. J) SOX9 IHC shows clusters of SOX9+ hepatocytes in contrast to mature bile ducts in WT. Scale bars I-J are 100μm.

We next used whole slide scanning to demonstrate thorough loss of YAP1 and visualize the location of any bile ducts that might be found throughout the liver lobes of YAP1 KO mice to confirm total loss. IHC for YAP1 in adult KO mice showed persistent complete YAP1 loss in all liver epithelial cells but retained YAP1 staining in endothelial cells and other non-parenchymal

cells, as compared to WT which showed low levels of cytoplasmic YAP1 in most hepatocytes and strong nuclear YAP1 in mature bile ducts (Figure 9A-B). CK19 staining shows that WT livers have well-formed bile ducts surrounding the portal veins throughout the liver (Figure 9C). This type of imaging highlights the hierarchical nature of the branching bile ducts, with the smallest ducts visible in the periphery of the liver tissue (region 3), merging into larger ducts closer to the middle of the tissue (region 2), and finally coalescing into the largest ducts in the peri-hilar region (region 1) which connect to the extrahepatic ducts (Figure 9C-D). YAP1 KO mice demonstrated an absence of defined ductal structures throughout most of the liver lobes, except for a few ducts limited to the perihilar region (Figure 9E). Only the median lobes showed some ducts extending into what we have classified as region 2 (Figure 9E).

Surprisingly, YAP1 KO mice survived for over 8 months when they were euthanized due to progressive morbidity. Even though markers of cholestatic injury remained severely elevated throughout, AST and ALT returned to almost normal levels by 3 months of age, suggesting that these injured livers deployed some adaptive mechanisms to survive despite severe cholestasis (Figure 8E-H). Thus overall, YAP1 KO mice exhibited significant failure to thrive and cholestatic injury, associated with persistent lack of intrahepatic bile ducts in the postnatal liver, resembling Alagille syndrome-like phenotype.

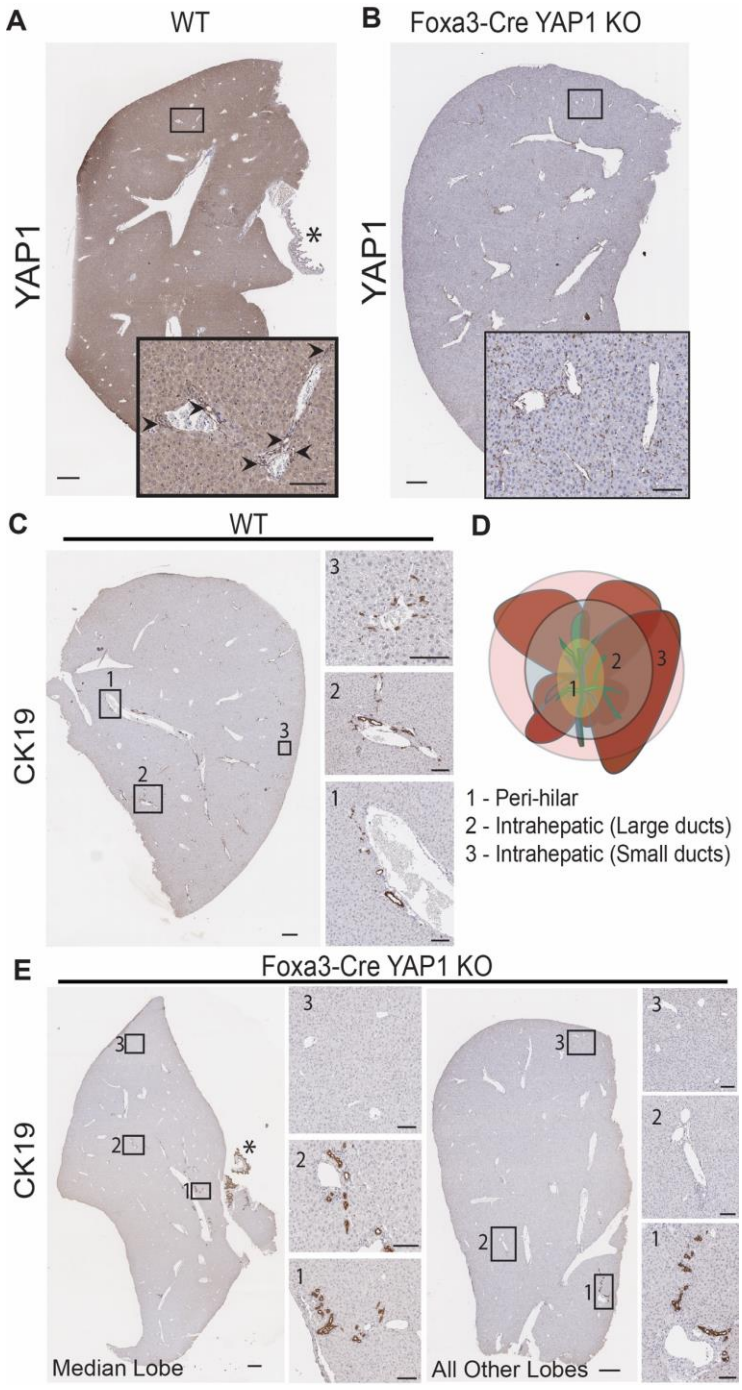

Figure 9. Adult YAP1 KO mice show persistent absence of intrahepatic bile ducts.

A) IHC for YAP1 in WT mice; arrows show nuclear YAP1 in bile ducts. B) IHC for YAP1 in KO mice. C) CK19 marks bile ducts in the liver spanning three main regions described in panel D). E) CK19 staining in various lobes of YAP1 KO mice. Asterisks mark the gallbladders. Scale bars are 500μm for whole lobes, 100μm for insets.

2.4.3 YAP1 KO mice show no hepatocyte-driven biliary regeneration, but exhibit limited DR around hilum, arising from extrahepatic bile ducts

We next investigated repair mechanisms that may be allowing YAP1 KO to survive long-term. Previous studies have convincingly demonstrated the capacity of normal hepatocytes to transdifferentiate to regenerate *de novo* bile ducts in the setting of similar developmental biliary defects *in vivo* [88]. Hence, we first evaluated whether any similar evidence of biliary regeneration occurred over time in YAP1 KO. Intriguingly, we found no YAP1-negative bile ducts even up to 8 months. In fact, the majority of the liver remained devoid of any intrahepatic ducts. To demonstrate this, we visualized the 3D structure of the bile ducts in WT and YAP1 KO mice at P21 and 8 months using a novel tissue clearing protocol combined with ribbon scanning confocal microscopy, to achieve 3D IF staining of whole liver tissue (Figure 10A-D). Staining with CK19 clearly delineated the hierarchical branching biliary network in P21 and 8-month-old WT mice, which was completely absent in YAP1 KO mice at both times except for a few ducts in the perihilar region connected to the extrahepatic biliary tree and gallbladder. Thus, we unambiguously demonstrate the gross absence of biliary regeneration in YAP1 KO mice.

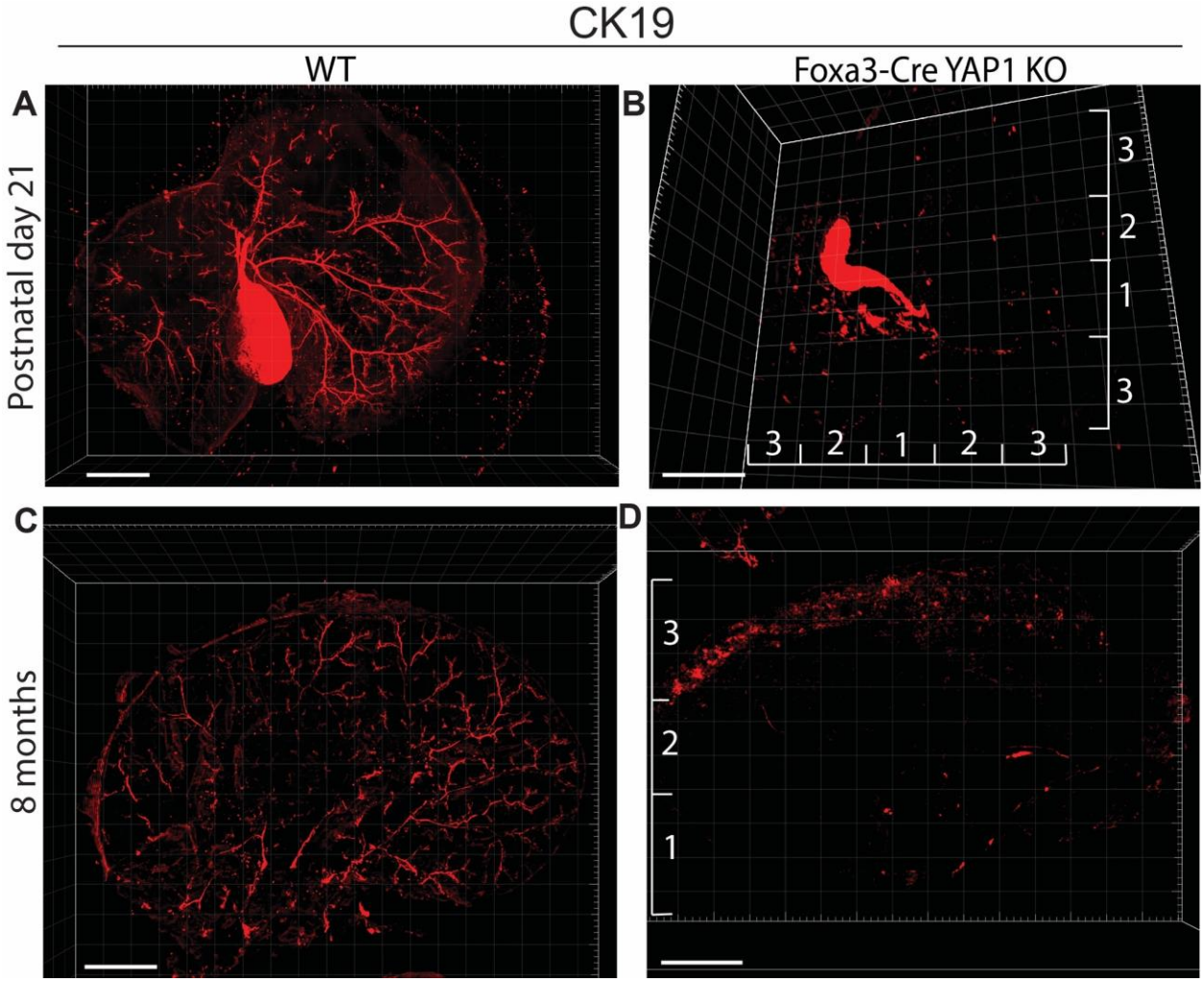

Figure 10. 3D immunostaining and whole liver imaging demonstrates lack of long-term biliary regeneration in YAP1 KO mice.

IF for CK19 followed by ribbon-confocal scanning microscopy illustrate in 3D the mature biliary tree of WT mice at (A) P21 and (C) 8 months of age and show the absence of bile ducts in YAP1 KO mice at (B) P21 and (D) 8 months of age. Scale bars are 2mm. Regions 1, 2, and 3 refer approximately to the expected positions of perihilar, intrahepatic large ducts, and intrahepatic small ducts respectively.

Interestingly, we noticed a ductular reaction (DR) *albeit* only in the perihilar region and particularly in the median lobe of the mouse liver (Figure 11A-B). This DR consisted of YAP1-positive ducts and was associated with significant inflammation and fibrosis surrounding the largest portal veins (Figure 11C-D). To assess the source of DR, we wondered whether the YAP1-positive ducts could have arisen from YAP1-positive hepatocytes that may have escaped Cre-recombination and could have then transdifferentiated into BECs. However, no YAP1-positive hepatocytes were observed by IHC as shown previously (Figure 9A-B). IF staining showed that while the DR in the hilar region was YAP1-positive, the surrounding hepatocytes were YAP1-negative (Figure 11E). Using a ROSA-stop$^{fl/fl}$-EYFP reporter, we verified that >99% of hepatocytes (HNF4α+) in YAP1 KO mice were EYFP-positive demonstrating successful Cre-recombination (Figure 11F-G). Thus, we rule out hepatocytes as a source of the DR, and also show that YAP1-negative hepatocytes are not capable of transdifferentiating into biliary cells, validating the role of YAP1 in hepatocyte transdifferentiation [28, 49].

To further substantiate the functional absence of intrahepatic biliary tree and at the same time assess if the regional DR contributed functionally, we measured the bile flow rate by cannulating the common bile duct, which is present in both WTs and YAP1 KOs. While expected bile flow at the expected normal rate in an unstimulated setting was evident in WT mice, there was no detectable bile flow in YAP1 KO mice (Figure 11H). Altogether, we show lack of intrahepatic biliary tree and a DR from extrahepatic ducts restricted mostly to the perihilar region, which was insufficient to restore function through intrahepatic biliary repair in YAP1 KO mice.

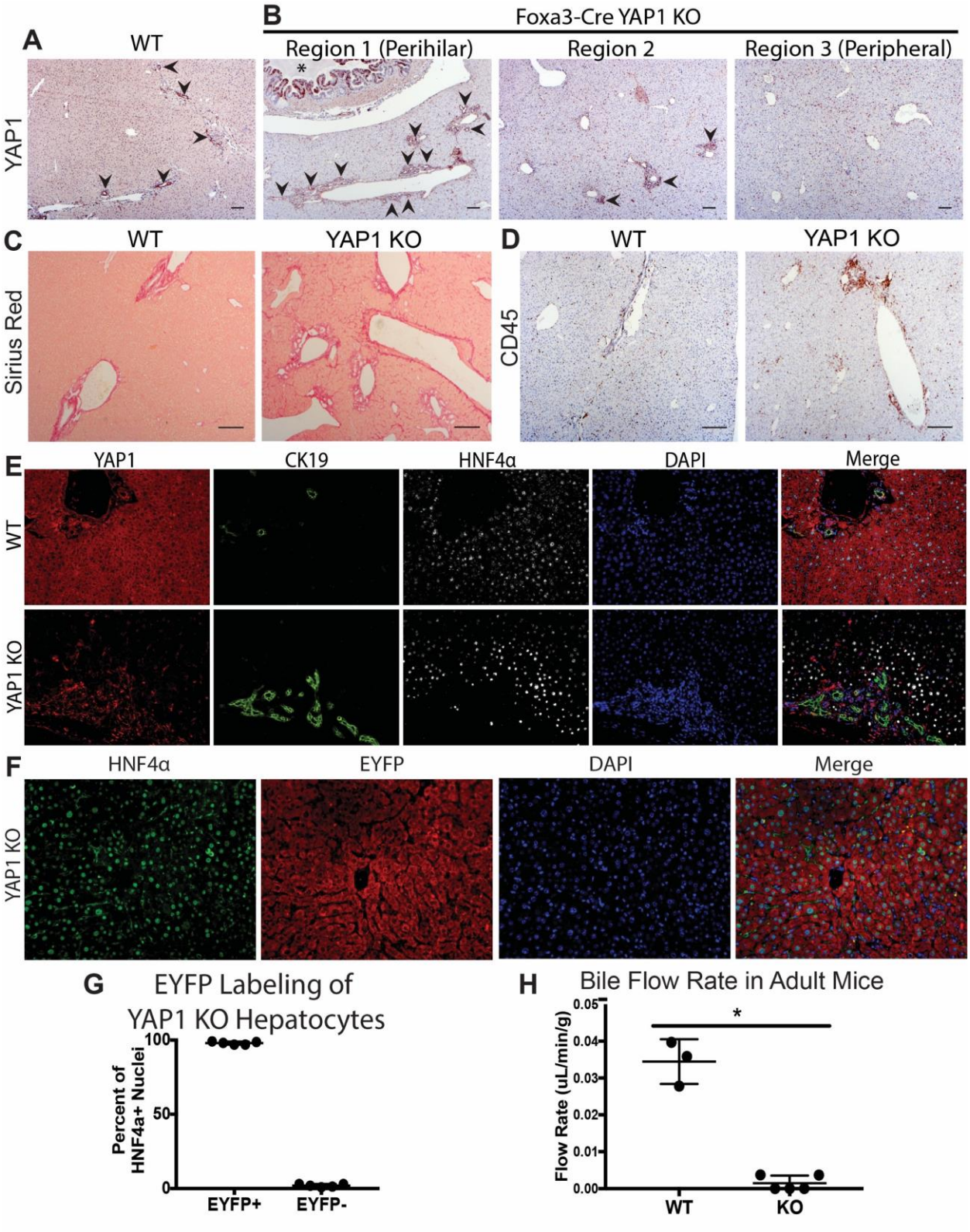

Figure 11. A ductular reaction emerging from extrahepatic bile ducts fails to provide functional biliary regeneration in YAP1 KO mice.

Figure 11. A) IHC for YAP1 in WT mice (arrows highlight bile ducts). B) IHC for YAP1 in KO mice (arrows highlight ductular reaction). C-D) KO mice show increased fibrosis (Sirius Red) and inflammation (CD45) vs WT, particularly around areas of ductular reaction. Scale bars are for A-D are 100μm. E) IF co-staining for YAP1, CK19, and HNF4α in WT and YAP1 KO mice (20x magnification). F) IF co-staining for HNF4α and EYFP in YAP1 KO mice (20x magnification). G) Quantification of EYFP-positive HNF4α-positive cells in adult YAP1 KO mice (mean ± sd, n=5 mice, representing the average of 3-5 20x fields per mouse). H) Cannulation of the common bile duct was used to measure baseline bile flow in adult WT and YAP1 KO mice (3-5 mice per group, two-tailed Mann-Whitney test, *p<0.05).

2.4.4 YAP1 KO livers undergo global gene expression reprogramming and reverse bile acid transport to favor serum and renal excretion, thus reducing hepatic injury

Since biliary reconstitution was not the basis of prolonged survival in the YAP1 KO, we posited that several adaptations to chronic cholestatic injury may be in play. We performed RNA-sequencing analysis on adult YAP1 KO mice and WT mice, using both males and females in each group for comparison. Principal component analysis showed WT and KO mice to be distinguished by the first principal component (Figure 12A). Comparison of YAP1 KO and WT livers identified 2606 differentially expressed genes (FDR<0.05, abs(FC)>2). Pathway analysis using various common software algorithms – Ingenuity Pathway Analysis (Qiagen), Gene Set Enrichment Analysis[188], and Enrichr [189], were performed and similar observations were evident. Both pathway analysis and transcription factor enrichment analysis highlighted robust activation of innate and adaptive immune responses in YAP1 KO mice, along with stellate cell activation and fibrosis (Figure 12B-C, E-F). This is consistent with histological evidence of increased pericellular fibrosis and presence of inflammatory cell clusters in adult KO (Figure 11C-D).

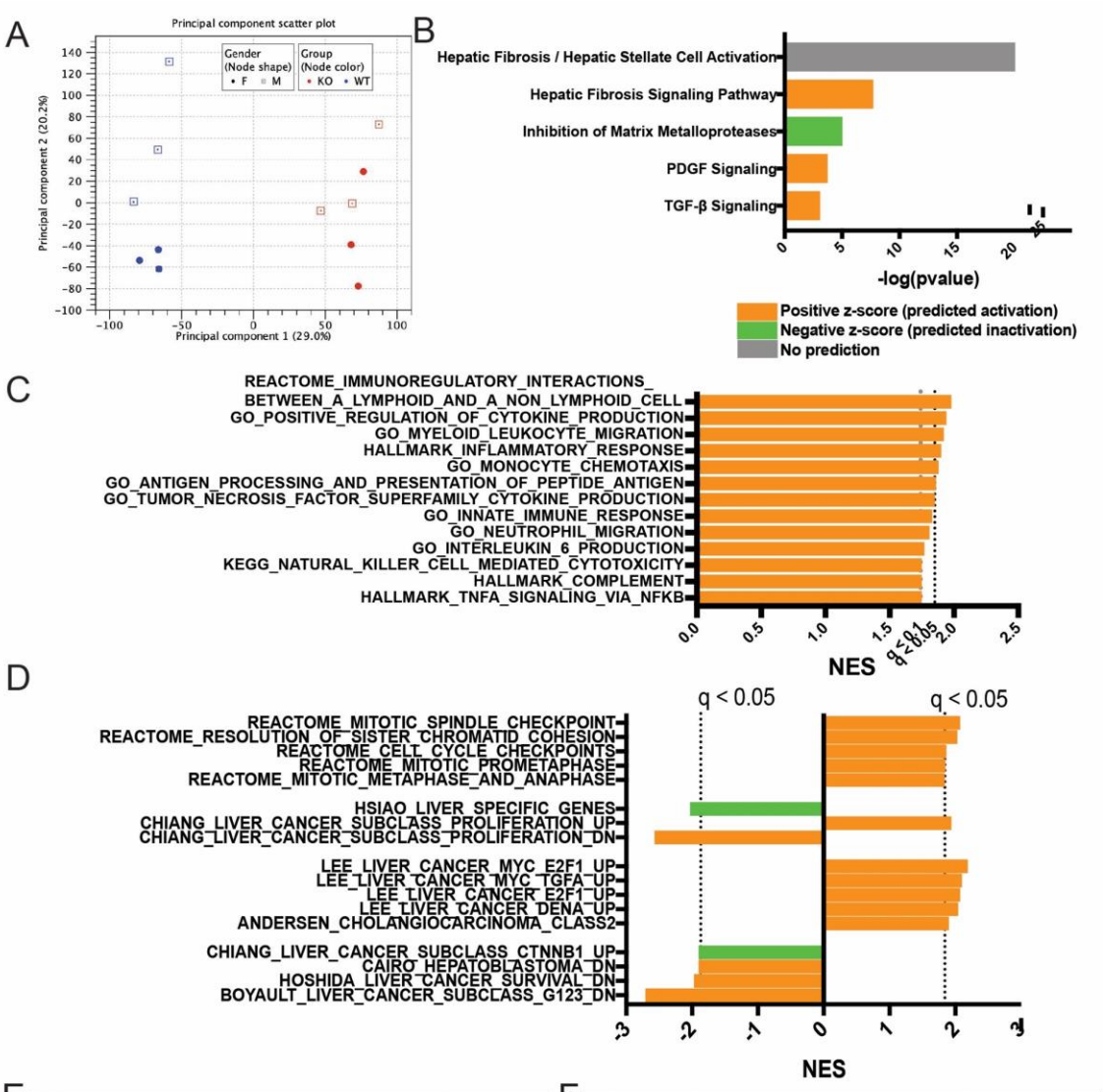

E

ENCODE and ChEA TF Consensus Regions - Enriched among regulatory regions of genes upregulated in YAP1 KO mice

Index	Name	P-value	Adjusted p-value	Odds Ratio	Combined score
1	FOXM1 ENCODE	3.45E-13	1.79E-11	4.06	116.37
2	SUZ12 CHEA	2.43E-13	2.53E-11	1.58	45.93
3	SPI1 CHEA	1.13E-10	3.91E-09	1.66	38.1
4	IRF8 CHEA	6.66E-10	1.73E-08	3.18	67.28
5	E2F4 ENCODE	3.31E-09	6.88E-08	1.76	34.28
6	RUNX1 CHEA	4.43E-09	7.68E-08	1.53	29.48
7	TP63 CHEA	4.08E-07	6.1E-06	1.43	21.09
8	TP53 CHEA	1.1E-05	0.00015	1.85	21.06
9	NFE2L2 CHEA	4.4E-05	0.00051	1.41	14.13
10	STAT3 CHEA	7.3E-05	0.00075	2.05	19.53
11	SPI1 ENCODE	0.00045	0.00428	1.27	9.8
12	SMAD4 CHEA	0.00062	0.00535	1.46	10.75
13	PPARG CHEA	0.00142	0.01133	1.44	9.45
14	SALL4 CHEA	0.00197	0.01461	1.53	9.55
15	VDR CHEA	0.00236	0.01638	2.24	13.53
16	GATA2 CHEA	0.00379	0.02464	1.32	7.36
17	FOSL2 ENCODE	0.00404	0.02472	1.68	9.24
18	GATA1 CHEA	0.00456	0.02632	1.31	7.04

F

ChEA 2016 TF Regulators - Enriched among regulatory regions of genes downregulated in YAP1 KO mice

Index	Name	P-value	Adjusted p-value	Odds Ratio	Combined score
1	LXR 22158963 ChIP-Seq LIVER Mouse	5.05E-23	3.26E-20	2.41	123.8
2	RXR 22158963 ChIP-Seq LIVER Mouse	4.50E-22	1.45E-19	2.38	116.78
3	PPARA 22158963 ChIP-Seq LIVER Mouse	5.89E-14	1.27E-11	2.04	62.12
4	ESR1 17901129 ChIP-ChIP LIVER Mouse	1.53E-08	2.5E-06	2.88	51.73
5	FOXO1 23066095 ChIP-Seq LIVER Mouse	6.85E-07	8.8E-05	2.86	40.61
6	SUZ12 20075857 ChIP-Seq MESCs Mouse	1.5E-05	0.00138	1.34	14.92
7	EGR1 23403033 ChIP-Seq LIVER Mouse	1.5E-05	0.00159	1.88	20.9
8	CLOCK 20551151 ChIP-Seq 293T Human	0.00025	0.01995	2.18	18.09
9	EED 16625203 ChIP-ChIP MESCs Mouse	0.00038	0.0245	1.75	13.8
10	PIAS1 25552417 ChIP-Seq VCAP Human	0.00037	0.02665	1.8	14.21
11	JARID2 20075857 ChIP-Seq MESCs Mouse	0.00083	0.04845	1.55	11.01
12	FOXA2 19822575 ChIP-Seq HepG2 Human	0.00093	0.04994	1.33	9.26

Figure 12. Pathway analysis of RNA-sequencing data comparing adult YAP1 KO mice to WT.

Figure 12. A) Principal component analysis of RNA-sequencing data clearly distinguishes between WT and KO mice. B) IPA analysis highlighted several altered pathways related to liver fibrosis in YAP1 KO vs WT. C-D) GSEA showed increased enrichment of numerous inflammatory and cancer-related pathways in KO vs WT mice. Enrichr analysis of regulatory regions common to genes upregulated (E) or downregulated (F) in KO mice vs WT identified key transcription factors whose activity is altered in KO mice.

In addition, we observed an increase in pathways related to proliferation, cell cycling, and cancer alongside downregulation of mature metabolic and synthetic genes normally expressed in hepatocytes (Figure 12D-F). We also observed a significant downregulation of broad metabolic and synthetic pathways related to fatty acid oxidation, oxidative phosphorylation, xenobiotic metabolism, and bile acid and sterol metabolism, all of which are hallmarks of mature liver function (Figure 13A). Decreases in fatty acid oxidation have been previously described in multiple cholestatic diseases in mice and patients and shown to be related to decreased PPARα activity, which was also supported in YAP1 KO by IPA and Enrichr analysis (Figure 12E-F) [128, 136, 202]. Decreased gene expression related to bile acid and sterol metabolism suggested inactivation of FXR, RXR, and LXR transcription factors (Figure 12F). Likewise, expression of most enzymes involved in the classic and alternative bile acid synthesis pathways were downregulated in YAP1 KO livers (Figure 13B). Interestingly, expression of most apical and basolateral transporters regulating bile acid transport in hepatocytes was altered to favor increased secretion back into the sinusoids rather than the hepatocyte apical canaliculi (Figure 13C-E).

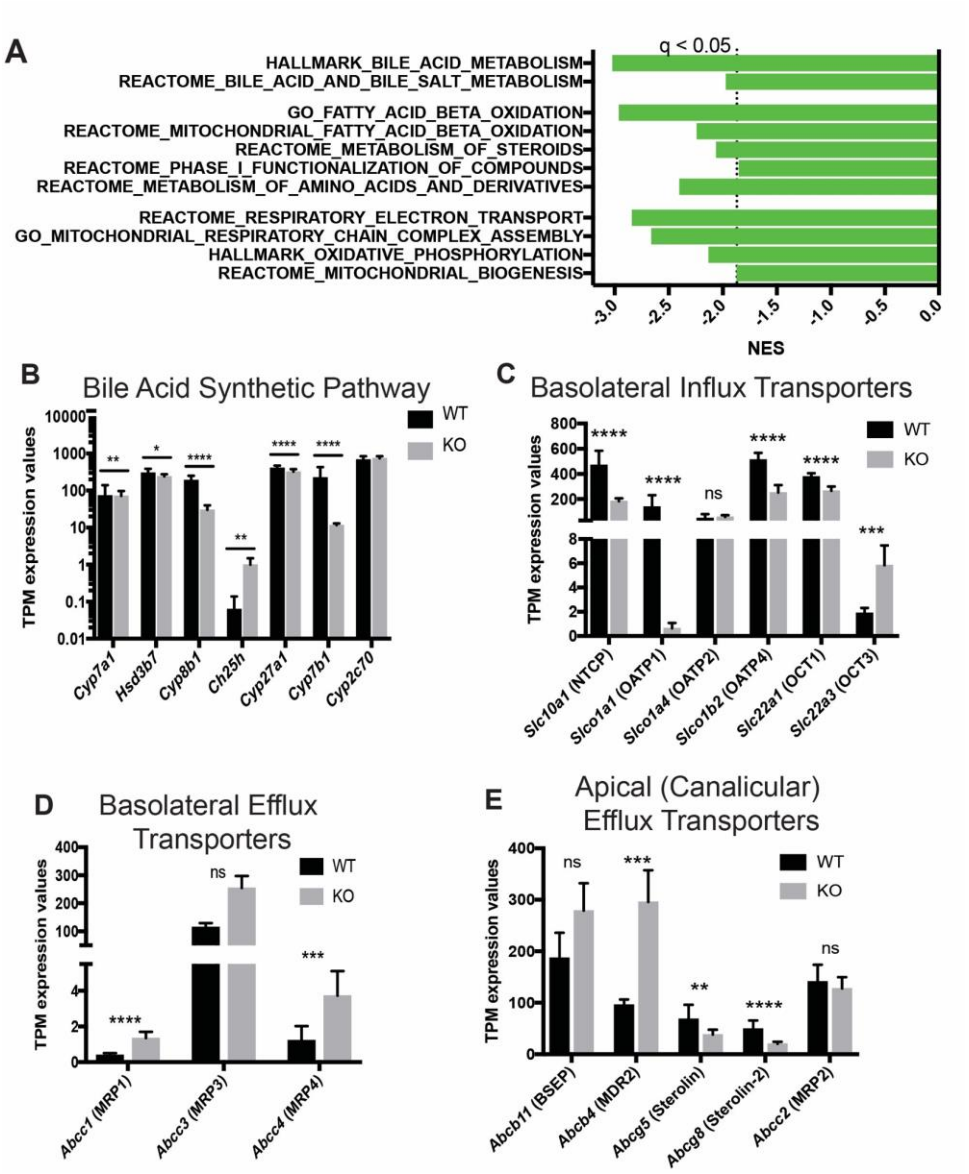

Figure 13. YAP1 KO mice alter the expression of bile acid transporters to favor serum excretion.

A) GSEA revealed several metabolic pathways negatively enriched in YAP1 KO mice vs WT. B-E) RNA-seq analysis shows altered gene expression of genes related to bile acid synthesis and excretion (*q<0.05, **q<0.01, ***q<0.001, ****q<0.0001).

To assess the functional consequences of these gene expression changes, we performed quantitative and qualitative analysis of bile acids in YAP1 KO mice compared to WT in both liver tissue and serum. The total quantity of bile acids was dramatically increased in the liver

(~6x) and in the serum (~40x) in YAP1 KO mice (Figure 14A) suggesting the general decrease in bile acid synthetic enzyme expression to be compensatory. Next, in the KOs, the diversity of species normally found in WT mice, was overwhelmingly shifted in favor of primary conjugated bile, particularly taurocholic acid (TCA) and taurobetamurocholic acid (TβMCA), which individually were increased by almost 1000-fold in the serum, while the less soluble primary unconjugated bile acids were significantly decreased in the liver tissue (Figure 14C, Figure 15A-L). Secondary bile acids derived from bacterial digestion of primary bile acids in the gut were also significantly decreased in the liver and serum of KO mice (Figure 15A-L). Using previously published data on bile acid hydrophobicity [203], we show that the bile acid pool in both liver and serum of YAP1 KO mice exhibited significantly lower hydrophobicity indices compared to WT, indicating a shift toward more soluble bile acid species to reduce their toxicity and facilitate their secretion into the blood (Figure 14B).

We next used intravital microscopy to visualize the flow of bile from hepatocytes into the canaliculi in WT and KO (Figure 14D). In WT mice, carboxy-fluorescein-di-acetate (CFDA) injected into the bloodstream was taken up by hepatocytes, metabolized into carboxyfluorescein (CF) to fluoresce green, and exported into the hepatocyte canaliculi, thus providing a clear view of the tightly sealed canalicular network completely segregated from the blood (dyed red using TXR Dextran) flow in sinusoids. In contrast, in YAP1 KO livers, none of the CF entered the canaliculi which could not be visualized. There was notable mixing of blood and bile as shown by the yellow color in sinusoids suggesting hepatocyte-metabolized CF transporting back into the blood (Figure 14D). Thus overall, these transcriptional and functional adaptations reflect a concerted effort to remove bile acids from liver by exporting them into the serum while also reducing their toxicity through conjugation, in an attempt to limit hepatocellular injury.

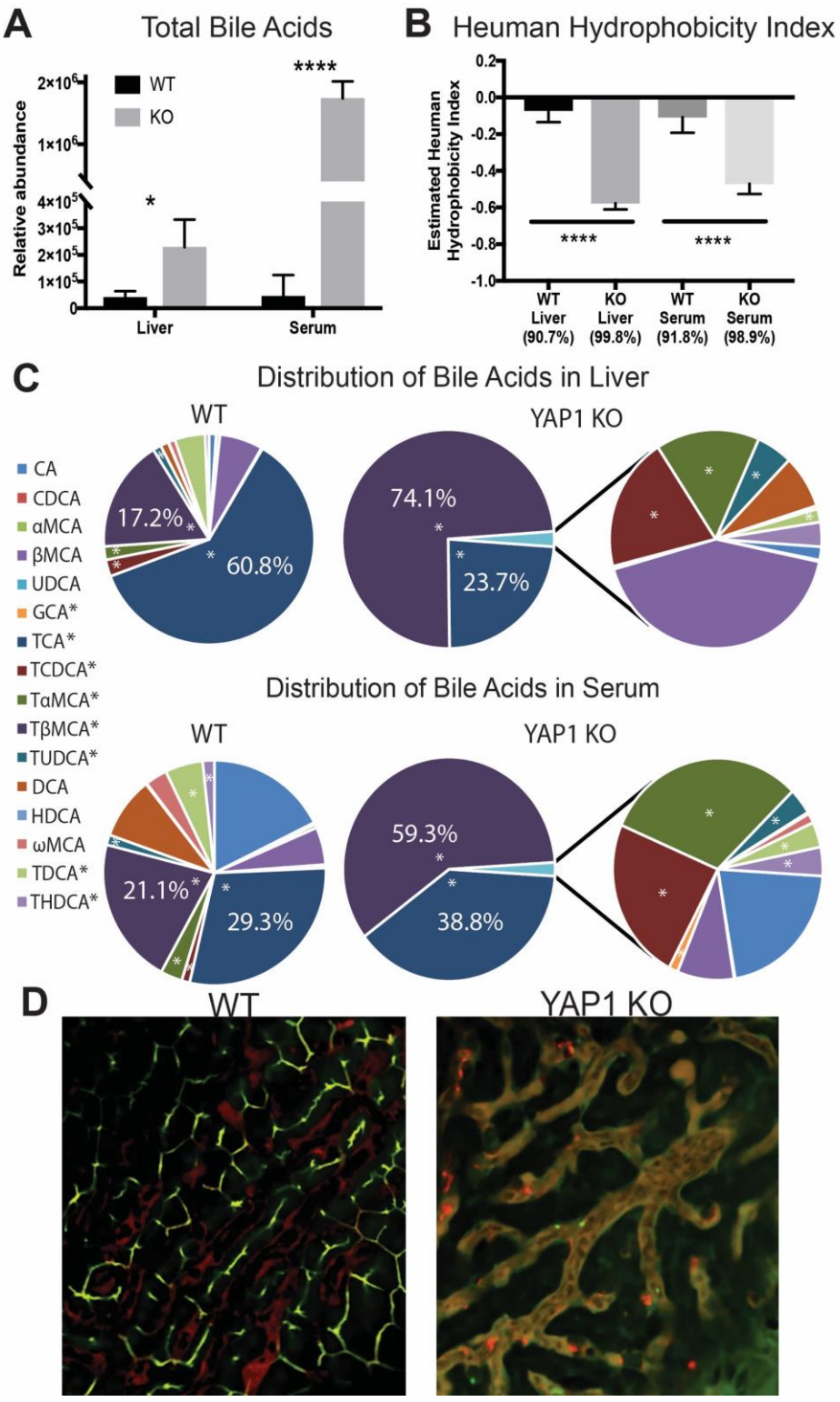

Figure 14. YAP1 KO mice show drastically elevated levels of bile acids in liver and serum with a more hydrophilic profile than WT.

Figure 14. A) Mass spectrometry was used to measure the abundance of bile acid species in liver tissue and serum from WT and YAP1 KO mice (n of 8 WT with 4 males and 4 females, and 7 KO with 4 males and 3 females; data show mean ± sd; 2-way ANOVA with Sidak multiple comparison test, * p<0.05, **** p<0.0001). B) The hydrophobicity index of the bile acid pool in liver and serum was calculated based on the Heuman index values for each bile acid species[203] (mean ± sd, t-test, **** p<0.0001). Underneath we include the percentage of total bile acids used in each calculation as the index values for certain species are unavailable. C) The average distribution and abundance of murine bile acid species is shown for WT and YAP1 mice. Asterisks (*) refer to conjugated bile acids. D) Still shots taken from live movies from intravital microscopy showing the circulation of blood (red) and bile (green) in both WT and YAP1 KO mice.

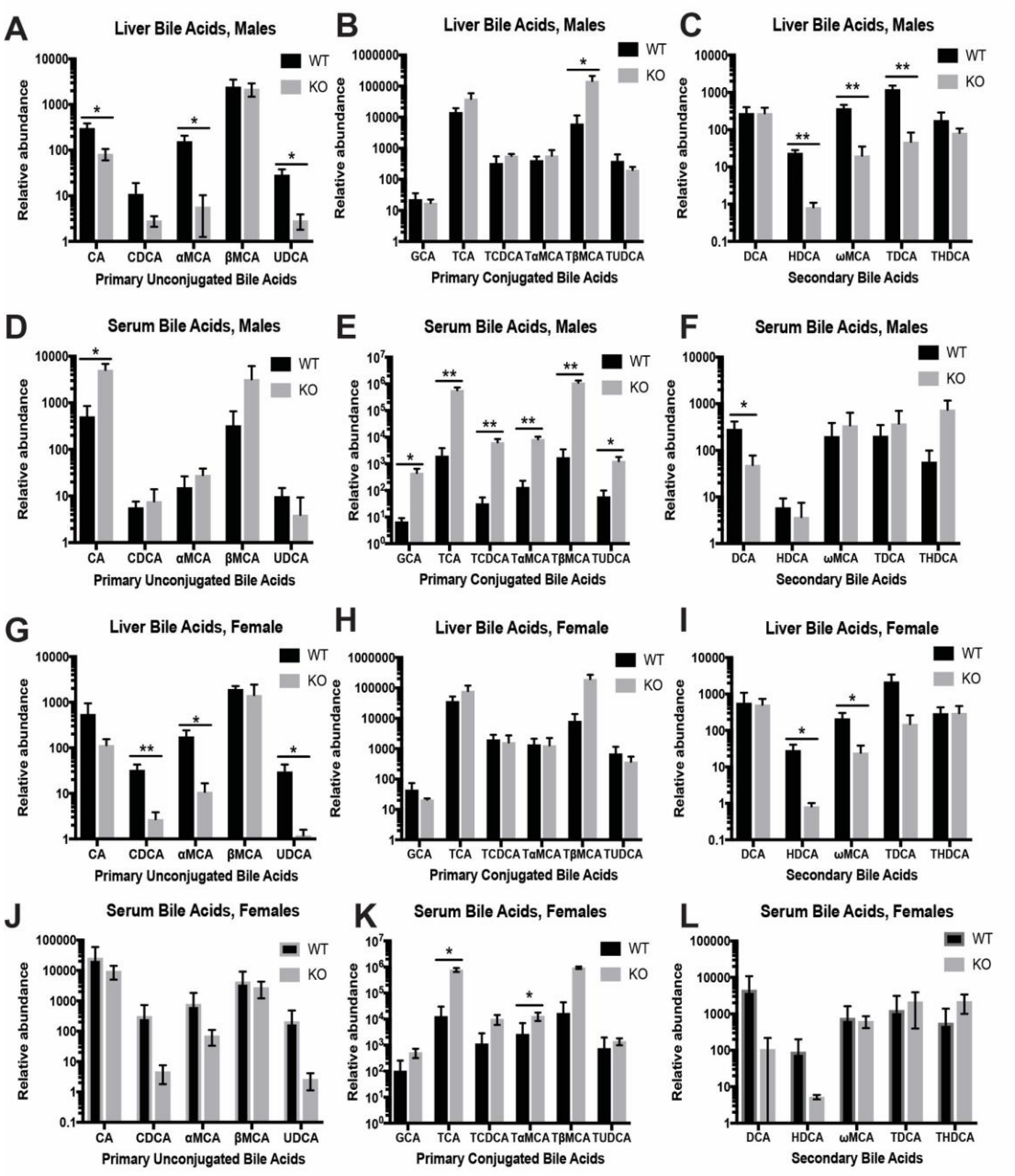

Figure 15. Quantification of bile acid species by mass spectrometry in adult liver tissue and serum of both male and female WT and YAP1 KO mice.

Primary unconjugated (A, D, G, J), primary conjugated (B, E, H, K), and secondary (C, F, I, L) bile acids in liver tissue of male mice (A-C), serum of male mice (D-F), liver tissue of female mice (G-I), and serum of female mice (J-L). WT vs KO values for each species by gender and sample type were analyzed by t-test, and all p-values were adjusted by Benjamini-Hochberg correction for multiple hypothesis testing, with an FDR of 0.1 (*p< 0.05, **p < 0.001). Data show mean ± sd.

However, protecting the liver from the toxicity of bile acids, bilirubin, and other substances normally excreted in the bile results in the exposure of the rest of the body to extremely elevated levels of these substances. The kidney is the next organ responsible for excretion of bile acids and bilirubin from the serum. We observed the development of chronic kidney disease over time in YAP1 KO mice compared to WT (Figure 16A-B). Figure 15A shows normal tissue architecture at P21, 3 months, and 6 months. While the kidneys of P21 YAP1 KO mice appears normal, by 3 months they exhibit focal tubular atrophy and cystic changes in the glomeruli, observed bilaterally. By 8 months, the kidneys were almost obliterated by cystic changes, with only small focal areas of healthy-looking tissue remaining. We observed some casts in the diseased kidney parenchyma at 3 months (Figure 16B, arrows). However, a stain for bile (Hall stain) showed no bile casts in WT or YAP1 KO kidneys as compared to a positive control from the clinical laboratory (Figure 16C). Thus, this pattern of disease cannot be classified as bile cast nephropathy. Consistent with chronic kidney disease, we observed elevated levels of blood urea nitrogen (BUN) in KO mice, although we observed only inconsistent elevations in serum creatinine (Figure 17A-B). Compared to WT kidneys at 3 months, diseased kidneys showed extensive inflammatory infiltrates as shown by CD45 staining, particularly in areas of tubular atrophy (Figure 17C), as well as increased collagen deposition (Figure 17D). Finally, to confirm that this pathology was not caused by underlying genetic ablation of YAP1 in kidney tissues during development, we show by IHC that there is no loss of YAP1 protein in the kidneys of YAP1 KO mice (Figure 17E). Overall, these data show that chronic cholestasis with extremely high serum bile acid and bilirubin levels is associated with development of severe chronic kidney disease, which has implications for patients with chronic severe cholestasis. Further investigation is needed to explore the mechanisms of injury leading to this pathology.

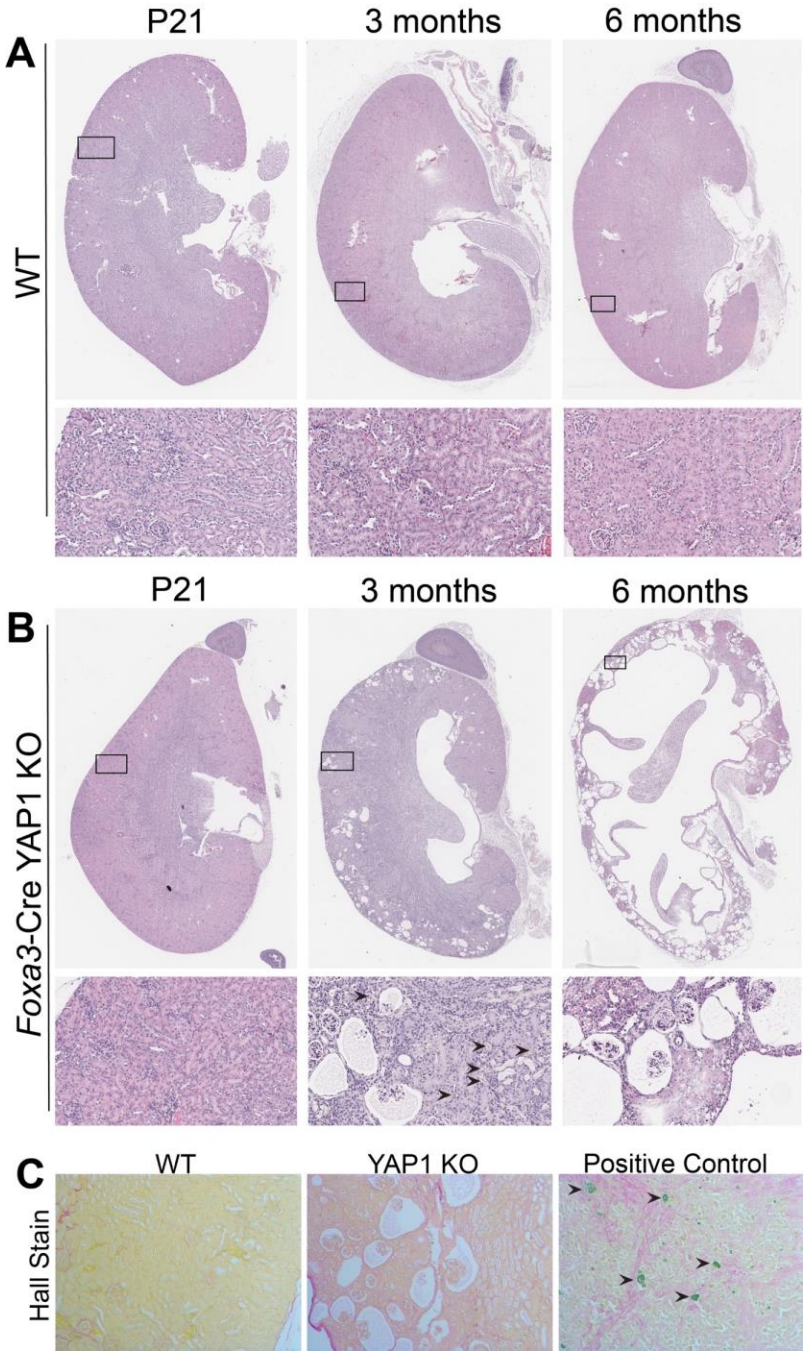

Figure 16. Characterization of chronic kidney injury over time in YAP1 KO mice.

Figure 16. A) H&E of WT kidney showing normal glomeruli and tubules at P21, 3 months, and 6 months of age (insets 10X mag). B) H&E of YAP1 KO kidney at P21, 3 months, and 6 months, showing gradual expansion of disease, with tubular atrophy and glomerulocystic changes (insets 10X mag; arrows point to tubular casts). C) Hall stain shows absence of bile casts in both WT and YAP1 KO kidneys, compared to a positive control provided by the UPMC clinical laboratories.

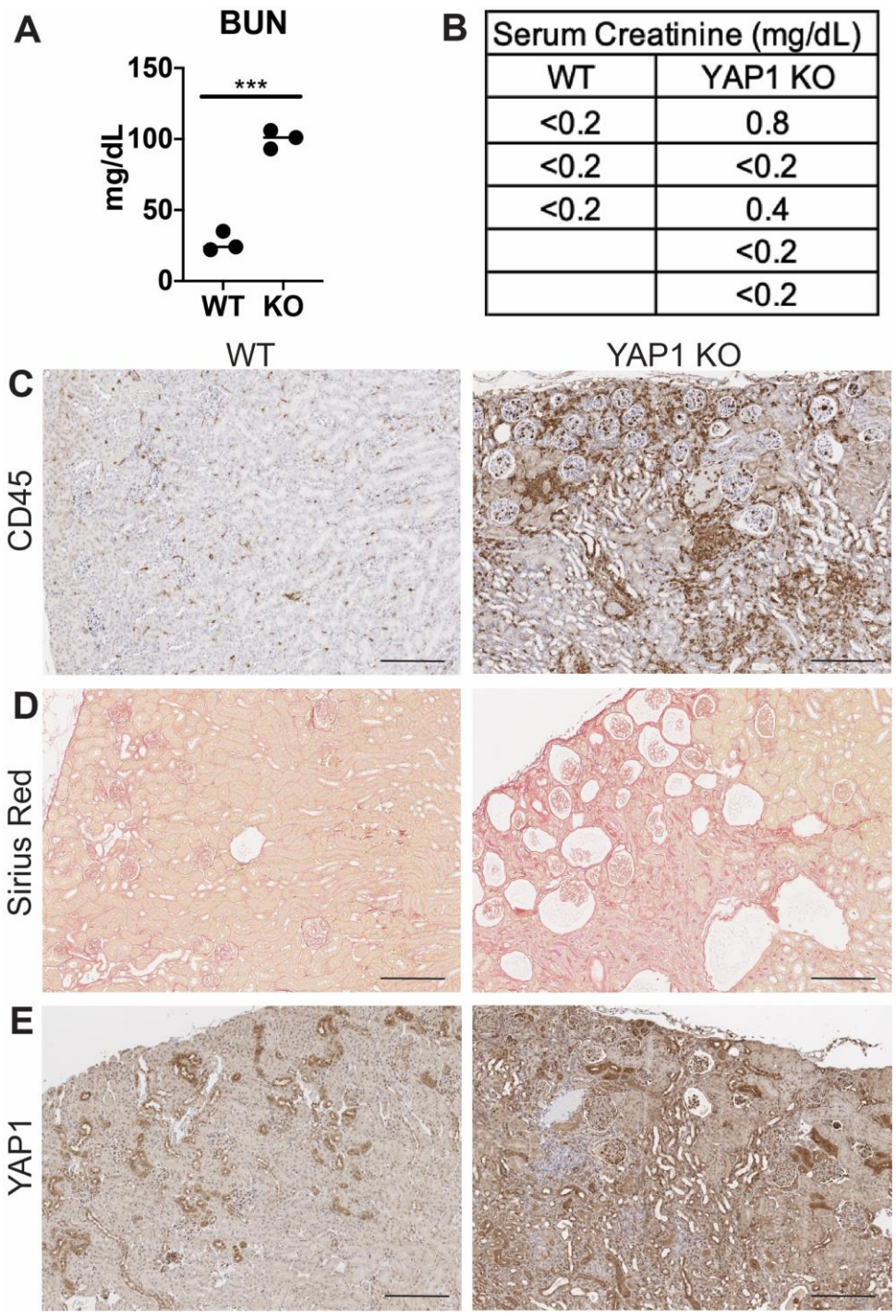

Figure 17. Kidneys of YAP1 KO mice exhibit significant fibrosis and inflammation at 4 months, and their injury is not due to genetic loss of YAP1.

A) Blood Urea Nitrogen (BUN) levels and B) serum creatinine of WT and YAP1 KO mice at 3-4 months of age. C) KO kidneys show extensive immune infiltration by CD45 IHC around areas of tubular atrophy as well as D) significant collagen deposition by Sirius Red staining. E) IHC for YAP1 in WT and KO kidneys.

2.4.5 TAZ cannot compensate for the role of YAP1 in bile duct formation but is essential in early liver development

Given the close relationship in structure and function between YAP1 and TAZ, we questioned whether TAZ could be compensating for YAP1 in some way. Based on the phenotype of YAP1 KO mice, TAZ is at least not able to compensate for the functions of YAP1 in the process of bile duct morphogenesis. We next looked at TAZ levels in our adult YAP1 KO mice. *Wwtr1* expression (the gene which encodes TAZ) was significantly upregulated in YAP1 KO mice in our RNA-seq data (Figure 18A), and we also show that TAZ protein level was significantly increased by Western blotting in YAP1 KO mice (Figure 18B). Next, using IHC, we show that in WT liver hepatocytes express very low levels of TAZ, with higher levels seen in the bile ducts (Figure 18C, red arrows). In contrast, YAP1 KO mice show increased levels of TAZ in hepatocytes, including in hepatocyte nuclei (Figure 18C, black arrows).

We next asked if TAZ may be regulating gene expression through TEAD transcription factors in YAP1 KO mice. Immunoprecipitation for TAZ indeed revealed that TAZ was binding to TEAD partners in both WT and YAP1 KO mice as shown in Figure 18D, with a clear increase in male KO vs WT mice. In addition, TAZ is also binding to YAP1 in both WT and YAP1 KO mice, which may reflect a different role in other cell types that retain YAP1 expression whether active in the nucleus or inactive sequestered in the cytoplasm. The reverse immunoprecipitation using a pan-TEAD antibody shows no binding to YAP1 in either WT and KO mice, but shows an increased level of TAZ binding in YAP1 KO mice. These results suggest that TAZ may be playing a role in regulating gene expression in YAP1 KO mice through TEAD transcription factors.

Based on this data, we decided to further examine the functions of TAZ in relation to YAP1 in this model. We developed mouse models using *Foxa3*-Cre recombinase to delete either 1 or both copies of *Yap1* and *Wwtr1*. Over the course of 2 years, we collected embryos and adult mice to examine the consequences of these genetic alterations. First, we observed significant disparities in the expected Mendelian ratios of genotypes among live births. YAP/TAZ double KO mice were never found among live births, although they are present at expected ratios among embryos harvested between E14-E17 so far (Figure 18D-E). The observed variability among embryo genotype ratios may be due to low numbers and the large number of possible genotypes and does not represent a statistically significant difference by chi-squared test. This data suggests that loss of both copies of *Yap1* and *Wwtr1* in early liver development results in embryonic lethality. Further studies are ongoing to investigate the role of YAP1 and TAZ in these early stages, which is beyond the scope of this thesis.

Interestingly, we also observed a 50% decrease in the expected birth rate of mice which have lost both copies of *Yap1* but only one copy of *Wwtr1* (YAP KO/TAZ HET). Further examination revealed that only female YAP KO/TAZ HET mice survive to adulthood. Only one male YAP KO/TAZ HET has been identified so far postnatally, and this animal died at postnatal day 1 exhibiting severe jaundice and pale skin with prominent vessels resembling earlier stage embryos. There is thus a significant sexual dimorphism in the role of TAZ in either directly compensating for YAP1 loss or in regulating adaptations to the resulting injury. Further studies are ongoing to identify the mechanisms of lethality in male YAP KO/TAZ HET mice, which is also beyond the scope of this thesis.

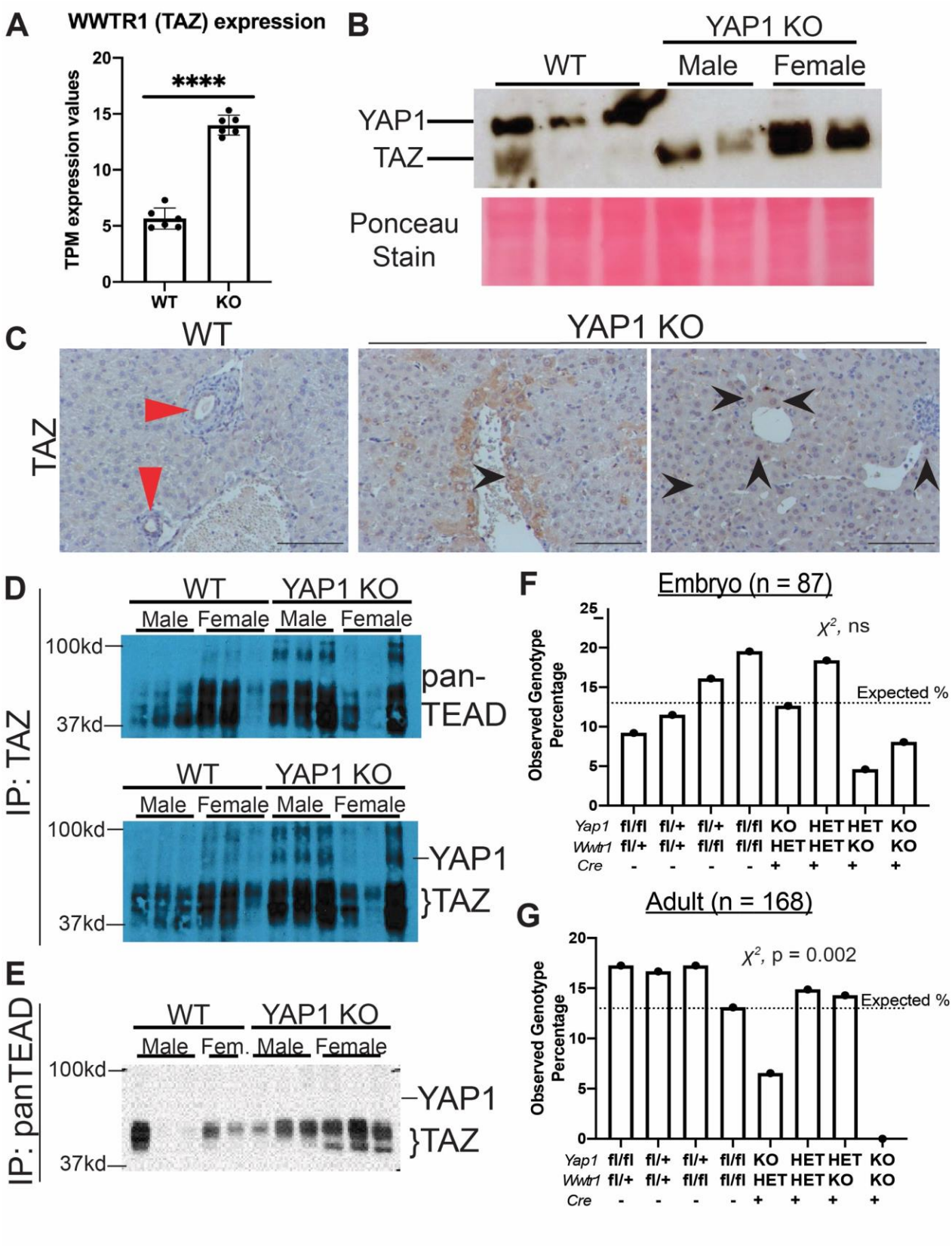

Figure 18. After YAP1 loss TAZ is upregulated and binds to TEAD factors in hepatocytes.

Figure 18. A) TPM values comparing mRNA expression of *Wwtr1* in WT and KO. B) Western blotting shows loss of YAP1 and increased levels of TAZ in KO mice compared to WT. C) IHC for TAZ in WT and KO mice; red arrows show positive bile duct staining in WT, while black arrows highlight nuclear TAZ in hepatocytes. D) Western blotting for panTEAD and YAP1/TAZ following immunoprecipitation for TAZ in WT and KO livers. E) Western blotting for YAP1/TAZ following immunoprecipitation for panTEAD in WT and KO livers. F-G) Genotype frequencies of the offspring from crossing [*Cre*$^{+/-}$, *Yap1*$^{fl/+}$, *Wwtr1*$^{fl/+}$] x [Cre$^{-/-}$ *Yap1*$^{fl/fl}$ *Wwtr1*$^{fl/fl}$], counting F) embryos from E14-17 and G) postnatal and adult mice. Dashed lines reflect the expected frequency of 1/8 for all genotypes.

2.4.6 TAZ regulates a subset of TEAD targets in the absence of YAP1 which contributes to hepatocyte adaptation to cholestatic injury

Next, we decided to explore the effect of loss of one copy of TAZ in female YAP1 KO mice (YAP KO/TAZ HET), which are able to survive postnatally, but seem to have a shorter lifespan than YAP1 KO mice of around 6 months. At 3-4 months of age, YAP KO/TAZ HET mice have similar liver weight to body weight ratii as YAP1 KO mice, but they have increased levels of ALT and AST, suggesting increased hepatocellular injury (Figure 19A-C). YAP KO/TAZ HET mice also have extremely high levels of total and direct bilirubin as well as alkaline phosphatase, similar to YAP1 KO mice (Figure 19D-F). Interestingly, YAP KO/TAZ HET mice have elevated fasting serum cholesterol levels as compared to WT mice (Figure 19G). Histologically, YAP KO/TAZ HET mice resemble YAP1 KO mice and exhibit an absence of intrahepatic ducts, with no evidence of functional biliary regeneration (data not shown). We also show that levels of proliferation are unaltered in YAP KO/TAZ HET mice as compared to YAP1 KO, although both are elevated as compared to WT (Figure 20A-B).

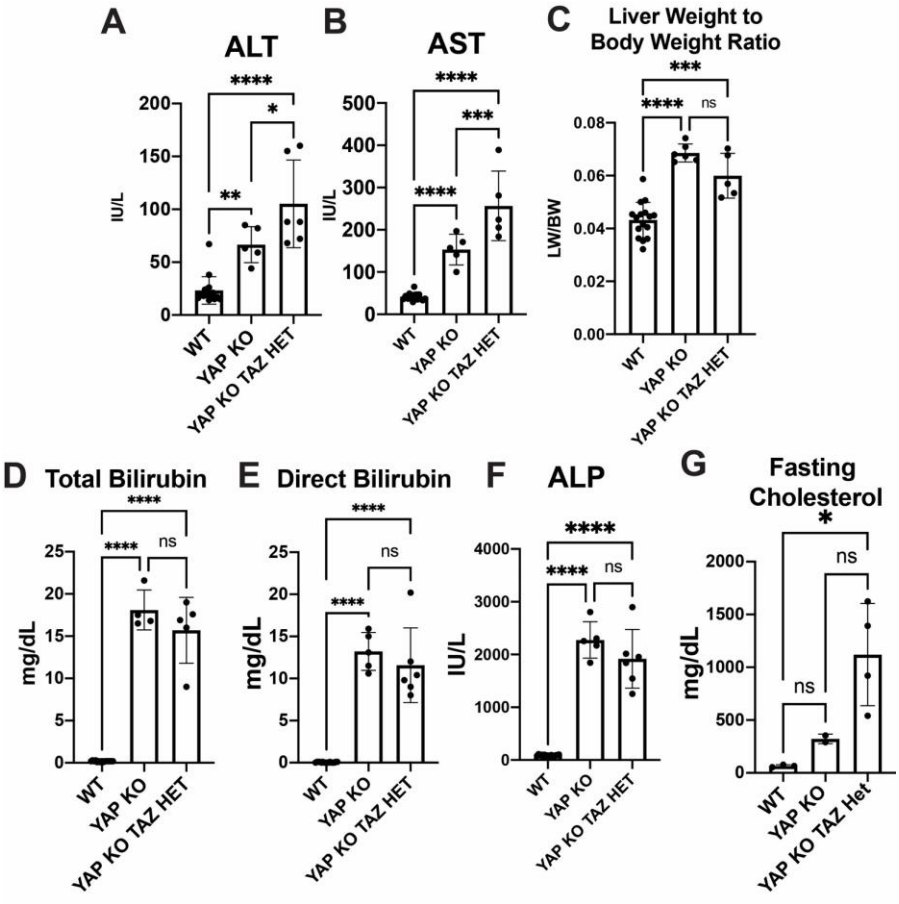

Figure 19. Serum biochemistry shows worsened hepatocellular injury in female YAP1 KO mice after loss of one copy of TAZ.

Serum levels of A) alanine aminotransferase (ALT), and B) aspartate aminotransferase (AST) in WT, YAP1 KO, and YAP KO/TAZ HET female mice at 3-4 months. C) Liver weight to body weight ratio in WT, YAP1 KO, and YAP KO/TAZ HET mice. Serum levels of D) total bilirubin, E) direct bilirubin, F) alkaline phosphatase, and G) fasting cholesterol in WT, YAP1 KO, YAP KO/TAZ HET mice at 3-4 months. Graphs show mean ± sd. Data were analyzed by 2-way ANOVA with Sidak multiple comparison test, n = 2-5 mice per group (* p<0.05, ** p < 0.01, *** p<0.001, **** p<0.0001).

We next aimed to use this model to identify specific targets that may be regulated by TAZ in the absence of YAP1 by performing RNA-sequencing analysis. Since these models have different genetic backgrounds, we compared female YAP1 KO mice to littermate controls

(C57Bl6 background), and female YAP KO/TAZ HET mice to littermate controls (mixed FVB/C57Bl6 background). A PCA plot shows that the samples are most impacted by loss of YAP1, with secondary separation based on mouse background and loss of one copy of TAZ (Figure 20C). Next, we used IPA Pathway Analysis to assess signaling changes in each model. We found 355 IPA pathways significantly altered in both YAP1 KO and YAP KO/TAZ HET mice, most of which had highly concordant z-scores, while 41 pathways were only altered in YAP1 KO mice and 40 pathways were only altered in YAP KO/TAZ HET mice (Figure 20D-E). Many of these uniquely altered pathways involve amino acid and nucleotide metabolism, calcium signaling, and MAPK signaling among others (Appendix B, Tables 4-5). However, the overall similarity of the altered pathways as well as the overall mouse phenotype in both YAP1 KO and YAP KO/TAZ HET mice suggests that TAZ is playing a more subtle role in modulating pathways rather than directing the global genetic program in these mice.

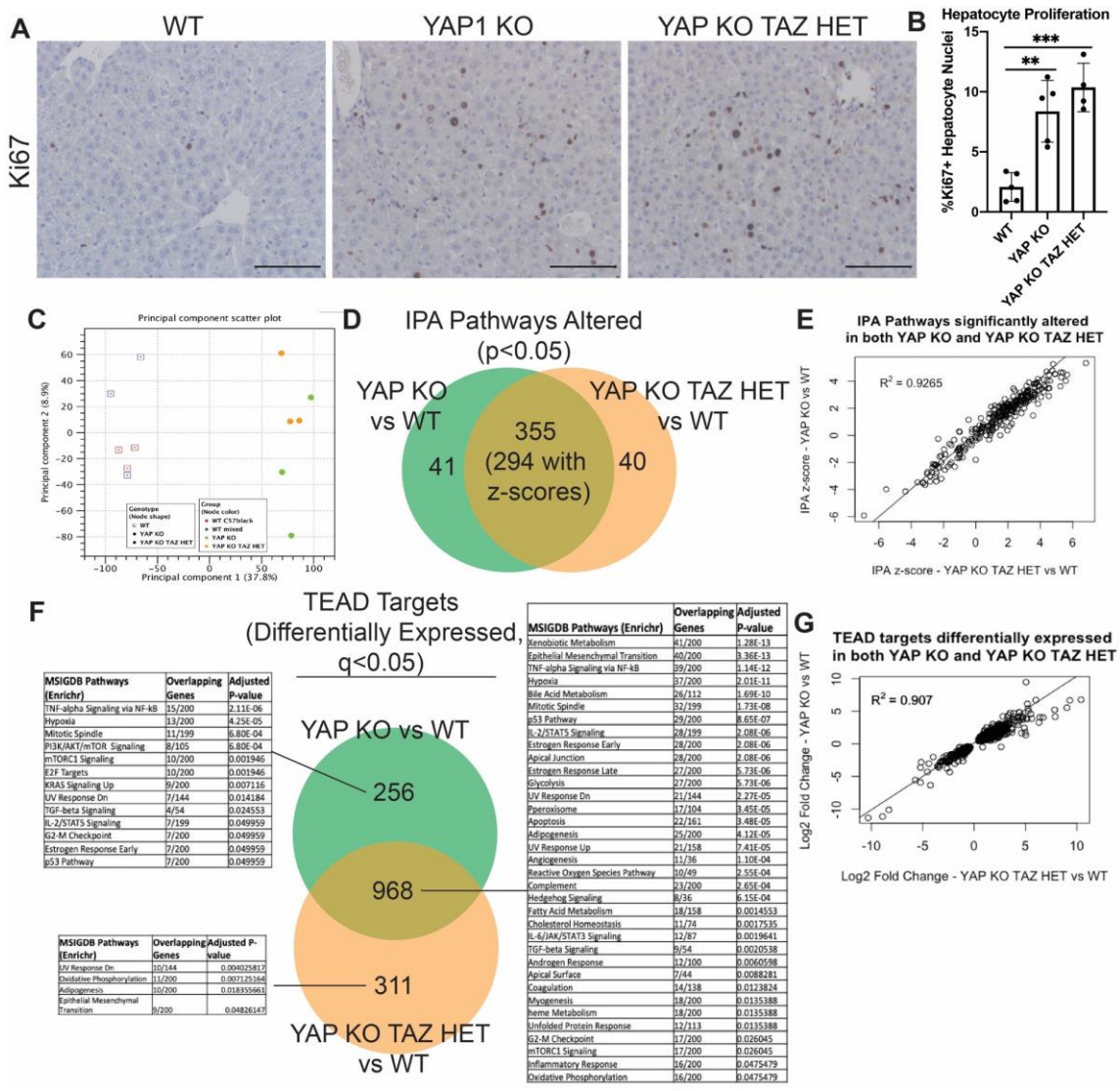

MSIGDB Pathways (Enrichr)	Overlapping Genes	Adjusted P-value
TNF-alpha Signaling via NF-kB	15/200	2.11E-06
Hypoxia	13/200	4.25E-05
Mitotic Spindle	11/199	5.80E-04
PI3K/AKT/mTOR Signaling	8/105	5.80E-04
mTORC1 Signaling	10/200	0.001946
E2F Targets	10/200	0.001946
KRAS Signaling Up	9/200	0.007116
UV Response Dn	7/144	0.014184
TGF-beta Signaling	4/54	0.024553
IL-2/STAT5 Signaling	7/199	0.049959
G2-M Checkpoint	7/200	0.049959
Estrogen Response Early	7/200	0.049959
p53 Pathway	7/200	0.049959

MSIGDB Pathways (Enrichr)	Overlapping Genes	Adjusted P-value
UV Response Dn	10/144	0.004025817
Oxidative Phosphorylation	11/200	0.007125164
Adipogenesis	10/200	0.018355661
Epithelial Mesenchymal Transition	9/200	0.04826147

MSIGDB Pathways (Enrichr)	Overlapping Genes	Adjusted P-value
Xenobiotic Metabolism	41/200	1.28E-13
Epithelial Mesenchymal Transition	40/200	3.36E-13
TNF-alpha Signaling via NF-kB	39/200	1.14E-12
Hypoxia	37/200	2.01E-11
Bile Acid Metabolism	26/112	1.69E-10
Mitotic Spindle	32/199	1.73E-08
p53 Pathway	29/200	8.65E-07
IL-2/STAT5 Signaling	28/199	2.08E-06
Estrogen Response Early	28/200	2.08E-06
Apical Junction	28/200	2.08E-06
Estrogen Response Late	27/200	5.73E-06
Glycolysis	27/200	5.73E-06
UV Response Dn	21/144	2.27E-05
Pperoxisome	17/104	3.45E-05
Apoptosis	22/161	3.48E-05
Adipogenesis	25/200	4.12E-05
UV Response Up	21/158	7.41E-05
Angiogenesis	11/36	1.10E-04
Reactive Oxygen Species Pathway	10/49	2.55E-04
Complement	23/200	2.65E-04
Hedgehog Signaling	8/36	5.15E-04
Fatty Acid Metabolism	18/158	0.0014553
Cholesterol Homeostasis	11/74	0.0017535
IL-6/JAK/STAT3 Signaling	12/87	0.0019641
TGF-beta Signaling	9/54	0.0020538
Androgen Response	12/100	0.0060598
Apical Surface	7/44	0.0088281
Coagulation	14/138	0.0123824
Myogenesis	18/200	0.0135388
heme Metabolism	18/200	0.0135388
Unfolded Protein Response	12/113	0.0135388
G2-M Checkpoint	17/200	0.026045
mTORC1 Signaling	17/200	0.026045
Inflammatory Response	16/200	0.0475479
Oxidative Phosphorylation	16/200	0.0475479

Figure 20. Bioinformatic analysis of RNA-sequencing data reveals that loss of one copy of TAZ does not grossly alter the genetic program of adult YAP1 KO mice but results in subtle signaling changes.

A) IHC for Ki67 in 3-4 month old WT, YAP1 KO, and YAP KO/TAZ HET mice. B) Quantification of Ki67+ hepatocyte nuclei. C) PCA plot comparing YAP1 KO, YAP KO/TAZ HET, and littermate control WT mice. D) Venn diagram showing overlap of IPA pathways significantly altered in YAP1 KO mice or YAP KO TAZ HET mice compared to WT. E) Scatterplot shows high correlation between IPA-calculated z-scores in either mouse model. F) Venn diagram shows overlap of potential TEAD targets differentially altered in YAP1 KO mice or YAP KO TAZ HET mice relative to corresponding WT littermates, along with the MSIGDB pathways selectively enriched in each group of genes. G) Scatterplot shows high correlation between $\log_2$ fold change of potential TEAD targets differentially expressed in both YAP1 KO and YAP KO/TAZ HET mice.

We then aimed to identify a TAZ/TEAD-regulated gene program in YAP1 KO mice, since we had shown previously that TAZ physically interacted with TEAD transcription factors in YAP1 KO mice. First, we compared the differentially expressed genes in each mouse model to publicly available ChIP-Seq data sets mapping TEAD binding sites throughout the genome in either mouse liver or the HepG2 cell line.[29, 191, 192] Out of 3,773 potential TEAD targets identified in all 4 data sets we analyzed, we found that about 26% were altered in YAP1 KO mice and 34% were altered in YAP KO/TAZ HET mice relative to WT. 968 targets were altered in both models, covering many major injury response pathways that are differentially altered as a whole in both models (Figure 20F). The $\log_2$ fold change of these genes was impressively concordant across both models, with an R^2 of 0.907 (Figure 20G). These genes were mostly not affected by the loss of one copy of TAZ and thus may be regulated by other signaling pathways which are responding to the cholestatic liver injury.

Next, we focused on the targets which are altered in one but not both mouse models. Curiously, we found that *Cyr61*, a well-known target of YAP1 and TAZ, was significantly upregulated in YAP1 KO mice relative to WT but was significantly decreased after loss of one copy of TAZ (Figure 21A). This suggests that expression of *Cyr61* in response to injury is directly regulated by TAZ in YAP1 KO mice. *Ctgf*, another YAP1/TAZ target, was similarly upregulated in YAP1 KO mice but was unchanged relative to WT after loss of one copy of TAZ (Figure 21B). We found 298 other genes (Appendix C, Table 6) whose expression followed a similar pattern of upregulation in YAP1 KO (FC>2, q<0.05) but were unaltered or downregulated in YAP KO TAZ HET mice (either q>0.05 or FC<0, q<0.05) (Figure 21C). 66 of these genes were also potential TEAD targets. These genes were enriched in GO terms and pathways associated with G1/S cell cycle transitions, E2F targets, mitosis, inflammation and

cytokine secretion, and regulation of apoptosis, reflective of a more targeted program often associated with oncogenic YAP1 signaling (Figure 21D-E).[1, 28, 29] This may reflect a specific program of genes which can be regulated by TAZ in the absence of YAP1 and are particularly sensitive to TAZ/TEAD regulation. These targets require further investigation to validate their responsiveness to both YAP1 and TAZ and investigate their role in hepatocyte-specific response to cholestatic injury.

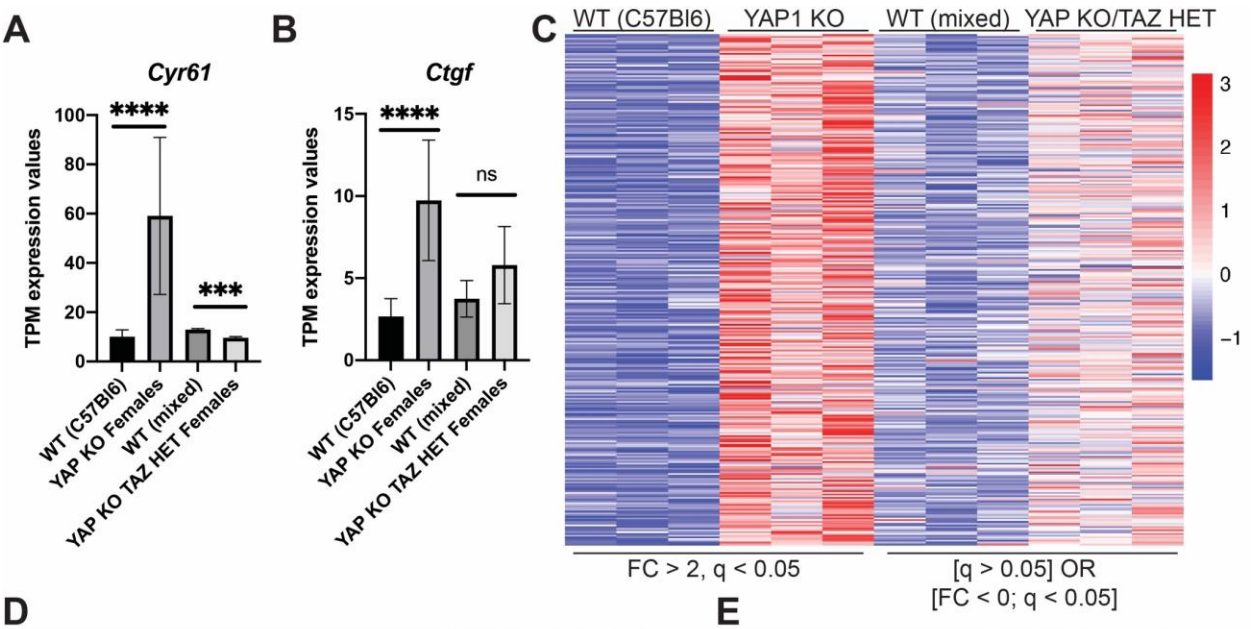

D

GO Biological Process	Overlapping Genes	Adjusted P-value
positive regulation of cell differentiation (GO:0045597)	14/194	0.00246
regulation of mitotic nuclear division (GO:0007088)	8/84	0.026396
microtubule cytoskeleton organization involved in mitosis (GO:1902850)	6/44	0.026396
mitotic chromosome condensation (GO:0007076)	4/15	0.026396
regulation of nitric oxide biosynthetic process (GO:0045428)	5/32	0.037483
negative regulation of calcium ion transmembrane transport (GO:1903170)	3/8	0.045992
G1/S transition of mitotic cell cycle (GO:0000082)	8/105	0.045992
positive regulation of fat cell differentiation (GO:0045600)	5/39	0.048337
negative regulation of myeloid cell differentiation (GO:0045638)	4/22	0.048337
regulation of tumor necrosis factor production (GO:0032680)	6/61	0.048337
negative regulation of cytokine secretion (GO:0050710)	5/40	0.048337
chromosome condensation (GO:0030261)	4/23	0.048337
negative regulation of inclusion body assembly (GO:0090084)	3/10	0.048337
positive regulation of interleukin-6 production (GO:0032755)	5/43	0.048337
cell cycle G1/S phase transition (GO:0044843)	7/92	0.048337
positive regulation of nuclear division (GO:0051785)	4/25	0.048337
positive regulation of nitric oxide biosynthetic process (GO:0045429)	4/25	0.048337
positive regulation of nitric oxide metabolic process (GO:1904407)	4/25	0.048337
cellular response to fibroblast growth factor stimulus (GO:0044344)	7/94	0.049369

E

MSIGDB Pathways (Enrichr)	Overlapping Genes	Adjusted P-value
TNF-alpha Signaling via NF-kB	23/200	1.41E-12
KRAS Signaling Up	16/200	1.20E-06
Hypoxia	15/200	3.62E-06
G2-M Checkpoint	15/200	3.62E-06
Epithelial Mesenchymal Transition	12/200	4.09E-04
E2F Targets	11/200	0.001505
Mitotic Spindle	10/199	0.004554
Inflammatory Response	10/200	0.004554
Myogenesis	8/200	0.039891
Interferon Gamma Response	8/200	0.039891
Allograft Rejection	8/200	0.039891
IL-2/STAT5 Signaling	7/199	0.091987
Apical Junction	7/200	0.091987
p53 Pathway	7/200	0.091987
Apoptosis	6/161	0.094685

Figure 21. Bioinformatic analysis reveals a subset of genes that may be regulated by TAZ and TEAD in YAP1 KO mice.

TPM gene expression values of A) *Cyr61* and B) *Ctgf* in all mouse models from RNA-sequencing data. C) Heatmap of 298 genes significantly upregulated in YAP1 KO mice but either unchanged or downregulated in YAP KO/TAZ HET mice relative to WT (FC, fold change). Enrichr analysis of these 298 genes revealed significant enrichment of several D) GO Biological Process terms and E) MSIGDB Pathways. Red text in D) highlights GO terms related to mitosis and cell proliferation.

2.5 Discussion

By directly knocking out YAP1 from HBs, we addressed the role of YAP1 in the earliest stages of liver development. We show that YAP1 is not necessary for Notch-driven initiation of biliary differentiation in the ductal plate and YAP1 loss does not impair Notch signaling in the ductal plate. However, YAP1 loss interferes with establishment of polarity in the ductal plate, laminin deposition in the basolateral side of the ductal plate, and loss of HNF4α expression in HBs adjacent to this layer. Thus, it seems that YAP1 is an essential mediator of BEC maturation in the ductal plate and is critical for the progression of BEC morphogenesis and recruitment of a second layer of HBs for incorporation into the growing ducts. [52]

There are several broad hypotheses to explain the molecular basis of this defect requiring future studies. First, YAP1 may be involved in the establishment and maintenance of cell polarization in ductal plate cells as well as adjacent HBs. A recent study showed that Anks6, a protein localized to the primary cilium of developing ductal plate cells, regulates YAP1 transcriptional activity, and loss of Anks6 also results in defects of bile duct morphogenesis[204]. While this suggests that YAP1 activity in the ductal plate is dependent on appropriate polarization, our data suggests that YAP1 loss impairs primary cilium formation and polarization, thus pointing to a positive feedback loop which may be required for maintenance of mature bile duct cell polarity.

Second, YAP1 may be involved in cell-cell communication from the portal mesenchyme to ductal plate cells as well as from ductal plate cells to adjacent HBs, which may also be dependent on the proper polarization of the ductal plate cells. This may or may not be occurring downstream of Notch signaling. A previous study suggested that overgrowth of bile ducts due to *Alb*-Cre Nf2-deletion and subsequent YAP1 activation was ablated by *Notch2* deletion,

suggesting Notch activity is downstream of YAP1 in bile duct development [205]. However, *Notch2* deletion in this model did not prevent bile duct formation and these mice exhibited limited injury. Our data, where YAP1 deletion occurs early during biliary differentiation, suggests Notch signaling to be upstream of YAP1 activation in the ductal plate, but downstream of YAP1 signaling in the second layer of HBs, which is a novel finding. In fact, YAP1 has been shown to regulate *Notch2* and *Jagged1* gene expression [48, 120].

Third, TGFβ signaling originating from the portal mesenchyme is critical for the formation of the second layer during bile duct morphogenesis [48, 60, 206], and a known driver of hepatocyte-derived biliary regeneration in a model of Alagille syndrome in which Notch signaling was impaired [88]. YAP1 may be the downstream effector of Tgfβ signaling in HBs to regulate their fate-switch to second layer of biliary cells transdifferentiation, downregulating HNF4α in second-layer HB [48]. It has been shown that YAP1 can regulate both HNF4α expression and its genome binding distribution, so YAP1 may be critical for turning off a hepatoblast/hepatocyte genetic program in favor of a Notch-driven biliary program[27, 48]. Finally, YAP1 can influence secretion of extracellular matrix components such as laminin α-5,[52, 58] which was deficient around developing ducts in YAP1 KO mice. Interrupting integrin-laminin signaling during bile duct morphogenesis results in defects similar to YAP1 KO [64]. Some or all of these molecular events may be contributing to the observed phenotypic defect.

We did not detect biliary regeneration through hepatocyte transdifferentiation in our Alagille syndrome-like model, in contrast to other studies [88, 117, 169, 207]. Our results thus demonstrate an absolute YAP1 requirement in hepatocytes to undergo transdifferentiation into cholangiocytes. Although other studies have shown YAP1 activation drives expression of biliary

markers in hepatocytes and promotes formation of hepatocyte-derived cholangiocarcinoma [17, 49, 208], we provide evidence that without YAP1 the liver cell identity shift cannot occur.

Our model also provides an opportunity to study the relationship between the intrahepatic and extrahepatic bile ducts (EHBDs), which remains poorly understood [54]. *Foxa3*-Cre did not affect *Yap1* expression in EHBDs including the gallbladder, all of which formed normally. Using tissue clearing and confocal imaging, we were able to visualize the gallbladder, cystic duct, and perihilar ducts entering the median lobe in both WT and KO mice. Our 2D and 3D imaging showed that the EHBDs extend farther into the median lobe than other liver lobes. We posit that the ductular reaction observed in adult KO mice arises from EHBDs responding to severe cholestatic injury. This response, which is accompanied by fibrosis and inflammation[105], is primarily associated with large portal vessels in KO mice, and may be an attempt of EHBDs to expand to try and locate and connect with IHBDs, which are lacking in KO. Our model demonstrates that the EHBDs are unable to regenerate IHBDs, similar to previous studies [88], although enabling such process may provide novel therapies in the future.

Despite the severity of liver disease in YAP1 KO mice, they survived long-term by adapting and reprogramming metabolic, synthetic and detoxification functions, while enhancing proliferation and survival signaling. Such adaptations have been reported in other models of liver disease such as Mdr2 KO and combined hepatic Met-EGFR loss [136, 209]. YAP1 KO mice completely invert their bile acid transport to overcome the lack of plumbing for bile excretion. While this led to elevated levels of bile acids and bilirubin in the blood, these toxic components were eliminated from hepatic parenchyma thereby reducing hepatocellular injury. Persistently elevated serum total and conjugated bilirubin levels in young children with Alagille syndrome are associated with more severe liver disease and decreased likelihood of spontaneous

improvement over time, similar to that seen in our model [144]. The same adaptive changes in bilirubin and bile acid transport observed in YAP1 KO mice may be occurring in patients with severe disease and may indicate maximal hepatocyte adaptation in the context of failed biliary regeneration. Thus, YAP1 activation may be an important disease modifier in patients with Alagille syndrome and other biliary disorders requiring further studies. Overall, the surprising capacity of the liver to survive and adapt may be harnessed therapeutically to better understand how to support patients with chronic liver injury.

In this case, our data also offers a warning for those patients who may experience kidney injury as a result of the increased serum load of bile acids and bilirubin. Our mice developed dramatic tubular atrophy and glomerulocystic changes which almost obliterated the kidneys after 6-8 months. Since we observed few casts histologically, this pathology may be due to a combination of obstruction and altered water balance in the tubules, as some studies have shown that bile acids and bilirubin can alter water and salt transporter expression and function.[210, 211] While relatively few clinical studies exist addressing a link between chronic pediatric cholestasis and subsequent chronic kidney disease, this may be a result of patients with severe injury undergoing liver transplant at an early age to restore normal biliary excretion. Most kidney injuries reported in the literature reflect acute kidney injury due to episodes of severe cholestasis in adults which resolve after normalization of liver function and may be associated with the presence of bile acid casts.[212-214] Chronic kidney disease occurring in patients with pediatric-onset cholestasis or chronic cholestatic disorders is poorly understood. Our model presents a unique opportunity to examine the consequences of long-term bile acid dysregulation on kidney function and eventually develop therapeutics targeting this method of excretion.

Finally, our data sheds light on the relationship between YAP1 and its paralog TAZ in liver development. Although some studies have shown that TAZ plays a role in biliary development, clearly TAZ is unable to compensate for the loss of YAP1 to restore bile duct morphogenesis. This suggests that either YAP1 has a unique role in this process not fulfilled by TAZ, and/or there is a delicate balance between YAP1 and TAZ activity that is disrupted upon YAP1 loss which results in aberrant HIPPO signaling and transcriptional activity in the ductal plate.

Interestingly, loss of both YAP1 and TAZ from the foregut endoderm results in embryonic lethality around E17-18. This reveals a new function for TAZ in early development. In comparison, a recent study in which YAP1 and TAZ were knocked out using *Alb*-Cre, and the resulting mice all survived[89]. *Alb*-Cre YAP1/TAZ double knockout mice exhibited bile duct paucity but still showed a significant network of bile ducts by ink injection, although their function and morphogenesis were compromised. This stands in direct contrast to our data showing a total absence of IHBDs after YAP1 loss in earlier stages of development and suggests that YAP1 plays a critical role in early development of bile ducts which may be distinct from its functions in maintenance of bile duct function and structure in postnatal development and adult homeostasis which have been addressed in other manuscripts.[30, 48, 89] In addition, this data shows that YAP1 and TAZ play a distinct role from E8.5 to E14 prior to activation of *Alb*-Cre which is essential for survival. Further studies are underway to investigate this phenomenon. In adult YAP1 KO mice, TAZ seems to partner with TEAD to regulate a subset of genes related to mitosis and cell proliferation, inflammation, and apoptosis. The clear loss of *Cyr61* and *Ctgf* upregulation following TAZ heterozygosity suggests that these genes are extremely responsive

to TAZ/TEAD regulation in hepatocytes. Further exploration of these targets may reveal specific functions of TAZ in regulated hepatocyte response to injury.

3.0 A Modified Clarity-Based Protocol for Liver Tissue Clearing and Whole Liver 3d Imaging

The following chapter describes my protocol for whole mouse liver tissue clearing and immunostaining, developed in collaboration with Dr. Alan Watson of the Center for Biological Imaging at the University of Pittsburgh. Yekaterina Krutsenko, Nathaniel Jenkins, Megan Smith, Dr. Junyan Tao, Dr. Simon Watkins, and Dr. Satdarshan Monga contributed to this work.

Funding was provided by 1F30DK121393-01A1 to L.M.; 5R01CA204586-05, 1R01DK62277 and Endowed Chair for Experimental Pathology to S.P.M.; NIH grant 1P30DK120531-01 to Pittsburgh Liver Research Center (for services provided by the Advanced Cell and Tissue Imaging Core); and NIH grant 2P30CA047904-32 to S.W. and the Center for Biological Imaging.

3.1 Summary

Over the last few decades, scientists have attempted to make organs transparent to facilitate the imaging of intact tissue structures, both healthy and diseased. Numerous tissue clearing protocols have been developed, many of which work extremely well on tissues such as the brain. However, the liver is very difficult to clear mostly due to its high iron content. In this study, we have combined and adapted several existing techniques to create a new protocol specifically for the clearing of liver tissue, combining the speed and efficiency of active X-CLARITY electrophoresis-based clearing with several depigmentation strategies derived from

the CUBIC protocol. We demonstrate the successful clearing of mouse liver tissue and subsequent immunofluorescence staining and microscopy, which allows for 3D visualization of intact structures such as bile ducts and hepatocyte canaliculi. We also show the application of this technique to visualize hepatocellular carcinoma tumors in a mouse model. Further work is necessary to adapt this protocol for human tissues. This protocol opens a new door for understanding the impact of liver disease on tissue architecture and intercellular communication and has a wide application in rodent models of liver pathology.

3.2 Background

Recent decades have seen an explosion in our ability to visualize biological structures and the architecture of organs in three dimensions. This is due to innovations in both microscopy[182, 215, 216] and tissue clearing[178, 181, 217-220], which aims to make intact organs and tissues transparent to facilitate imaging without labor-intensive sectioning and reconstruction of 2D images into a 3D composite. This has innumerable applications in basic and translational studies, allowing us to appreciate the structure-function relationships of healthy tissues and how disease processes cause and/or result from a disruption of tissue architecture and cell-cell interactions in both animal models and human tissue samples.

Numerous tissue clearing protocols have been developed in recent years, optimized first for brain tissues and subsequently expanded for application in other organs. Most of these protocols primarily focus on homogenizing the light scattering within the tissue by removing most lipids from the sample, and/or dissolving the tissue in a solution that matches the refractive index of the tissue.[220, 221] Early clearing protocols relied on organic solvents which can dissolve

membrane lipids and achieve excellent tissue clearing long-term[217, 222-224]. However, these protocols rely on toxic solvents and also require tissue dehydration, which causes samples to shrink greatly and reduces fluorescence of endogenous fluorophores.[220] Alternative approaches have been developed using aqueous-based clearing solutions, which better preserve tissue architecture, such as CLARITY, Scale, and CUBIC.[178, 181, 219]

However, the liver remains particularly difficult to clear with existing protocols, requiring weeks to months of treatment to achieve adequate tissue clearing.[66, 225-228] Faster methods may only clear tissue to a depth of 500um-1mm, whereas a mouse liver lobe can be at least 3-5mm thick.[225, 226] The liver contains a much larger quantity of porphyrin-bound iron as compared to most other organs, since the liver synthesizes heme, contributes to the recycling of red blood cells, and also has a high number of cytochrome P450 enzymes reliant on iron for their catalytic activity. Depigmentation is thus a significant problem beyond delipidation for the clearing of liver tissue.

In order to achieve consistent, rapid, and thorough clearing of liver tissue allowing imaging of whole mouse liver tissue, we developed a new protocol (LiverClear) combining the rapid delipidation and structural protein retention of CLARITY with the depigmentation and refractive index matching power of CUBIC. Our protocol is fast, easy to use, and consistently reproducible, and can be combined with commonly used immunofluorescence protocols for successful staining and imaging of complex structures.

3.2.1 Comparison with other methods

The CLARITY protocol, first published in 2013 and subsequently adapted in numerous ways, combines sodium dodecyl sulfate (SDS)-based solubilizing of lipids with an

electrophoretic gradient to drive the SDS-lipid micelles out of the tissue, resulting in rapid delipidation within a few days, which is faster than most other protocols relying on passive diffusion.[178, 218, 227, 229] Furthermore, the use of an acrylamide-based hydrogel helps preserve tissue architecture and protein content during the delipidation process, further improving the quality of subsequent protein detection and tissue imaging.[178] While this protocol works well for many organs, it does not incorporate specific depigmentation strategies and only results in moderate clearing of liver tissue.

Alternative protocols, such as Scale and CUBIC, rely on passive delipidation combined with hyperhydration of the sample using highly concentrated solutions of urea and sucrose, which further reduces the refractive index of the tissues to better approximate that of water, reducing light scattering and improving the transparency of the tissue.[181, 219, 230] The development of CUBIC in particular resulted in the discovery that certain polyhydric aminoalcohols facilitated lipid solvation when combined with traditionally used detergents.[181] Interestingly, aminoalcohols such as N,N,N′,N′-Tetrakis(2-Hydroxypropyl)ethylenediamine (Quadrol), which is a main component of one of the CUBIC clearing solutions, also contribute to decoloration of heme-based substances, possibly by interacting with heme and promoting its dissociation from associated proteins within the cell.[181, 221] In addition, treatment with substances like hydrogen peroxide can contribute to bleaching of pigments through oxidation and structural degradation.[221]

We combined features of both CLARITY and CUBIC protocols to clear liver tissue in multiple ways using aqueous-based methods which are less toxic and result in less distortion of the tissue through dehydration. We retain the efficiency of CLARITY which makes the process relatively speedy. We also add several steps to promote depigmentation using both active and passive methods. We demonstrate significant clearing of liver tissue in a matter of 2 weeks, as

compared to worse results after 4 or more weeks using either CLARITY or CUBIC alone.[181, 227, 229, 230]

3.2.2 Experimental design

The procedure can be divided into distinct stages. First, liver tissue is collected and fixed in 4% paraformaldehyde. Next, the tissue is embedded in an acrylamide-based hydrogel which crosslinks DNA and protein molecules within the tissue and holds them in place to preserve the overall tissue architecture. We then submerge the tissue in a buffered solution containing the detergent SDS and apply an electrophoretic gradient to promote the formation of lipid micelles which are then forced out of the tissue. At the same time, we add Quadrol to the actively circulating solution, which contributes to the depigmentation of iron-containing macromolecules within the liver. Next, we include a further depigmentation step using hydrogen-peroxide.[220] The final stage of clearing involves submerging the tissue in CUBIC R2 solution, a highly concentrated and viscous solution of urea and sucrose which has a refractive index much closer to that of the tissue than air or water. The CUBIC R2 further contributes to clearing the liver tissue and also is used for the final imaging to minimize differences in refractive index from the microscope lens to the tissue.

Prior to immersing the tissue in CUBIC R2, the cleared tissue can be used for immunofluorescent labeling. We have based our method on the SWITCH protocol[180] which has been shown to improve the dissolution of antibody throughout thicker tissue samples while reducing antibody aggregates which may contribute to artefacts during imaging. The antibodies used here are similar to those used in 2-dimensional immunolabeling and protocols should be optimized accordingly. After staining, the samples are fixed in paraformaldehyde once more for

a short time to keep the antibodies in place long-term while the samples are submerged in CUBIC R2.

Finally, the samples can then be imaged using a variety of microscopy techniques adapted for whole-organ imaging. We have used ribbon-scanning confocal microscopy, which has been developed at the Center for Biological Imaging at the University of Pittsburgh.[182]

3.3 Materials and Methods

3.3.1 Reagents

- Sodium phosphate monobasic monohydrate (Sigma-Aldrich, cat. no. S9638)
- Sodium phosphate dibasic (anhydrous) (Sigma-Aldrich, cat. no. S9763)
- Distilled water
- Sodium azide (Sigma-Aldrich, cat. no. S2002)
- 16% w/v Paraformaldehyde (Fisher, cat. no. 50-980-487) **CAUTION**
- 2% bio-acrylamide (Bio-Rad, cat. no. 161-0142)
- 40% acrylamide (Bio-Rad, cat. no. 161-0140)
- VA-044 (Wako Chemicals, Fisher, cat. no. NC0632395) **CAUTION**
- X-CLARITY™ Electrophoretic Tissue Clearing Solution (Logos Bio, C13001)
- N,N,N′,N′-Tetrakis(2-Hydroxypropyl)ethylenediamine (Quadrol) (Sigma-Aldrich, cat. no. 122262) **CAUTION**
- Bovine serum albumin (BSA) (Fisher, cat. no. BP1605-100)
- Sodium dodecyl sulfate (SDS) (Sigma-Aldrich, cat. no. L3771) **CAUTION**

- Triton X-100 (Fisher, cat. no. BP151-500)
- Urea (Sigma-Aldrich, cat. no. U5378)
- Sucrose (Sigma-Aldrich, cat. no. S9378)
- Triethanolamine (TEA) (Sigma-Aldrich, cat. no. T58300)

3.3.2 Reagent and equipment setup

- Phosphate buffered saline: Add 3.1g NaH_2PO_4 (monohydrate) and 10.9g Na_2HPO_4 (anhydrous) to 500 mL dH_2O. Adjust the pH to 7.4, and bring to 1 liter with dH_2O. Store indefinitely at room temperature.
    - Alternatively, you can use pre-mixed pouches from Fisher (cat. no. PI28374)
- PBS/0.1% sodium azide: Add 0.5 grams of sodium azide (Sigma) to 500mL of PBS for a final concentration of 0.1% w/v sodium azide.
- 4% w/v PFA: Dilute 10mL of 16% PFA (Fisher) into 30mL of PBS. Store at 4°C for 1-2 weeks.
- Hydrogel solution: Add 1.25 mL of cold 2% bio-acrylamide (BioRad) and 5mL of cold 40% acrylamide (BioRad) to 43.75 mL PBS. Then add 0.175g of VA-044 (Wako Chemicals) and dissolve without vortexing. Store at 4°C for 1 week.
- IHC buffer: Add 0.05 grams of sodium azide (Sigma) and 2.5 grams of BSA (Fisher) into 500mL of PBS for a final concentration of 0.01% w/v sodium azide and 0.5% BSA. Mix by stirring.

- IHC buffer with SDS: Add 0.072g of SDS into 500mL of IHC buffer for a final concentration of 0.5mM SDS.
- CUBIC R2 solution: Mix 125g urea (Sigma) and 75mL dH_2O in a glass beaker. Stir on a hot plate over low heat until the urea dissolves. Slowly add 250g sucrose (Sigma) and continue stirring on low heat until dissolved. Turn off heat and add 44.5 mL TEA (Sigma) and 380μL TritonX-100 (Fisher), stirring until well-mixed. Store up to 1 month at room temperature.
- X-CLARITY™ Electrophoretic Tissue Clearing System: Set up according to manufacturer specifications. Ensure there are no leaks in any of the tubing connecting the main system, the sample holder, and the buffer reservoir. Run distilled water through the system passively to ensure that the temperature is stable and there are no leaks.

3.3.3 Procedure

3.3.3.1 Tissue Fixation (Timing: 2 days)

1. Mice were housed, fed, and monitored in accordance with the protocols approved by the Institutional Animal Care and Use Committee at the University of Pittsburgh School of Medicine. Wild type healthy C57BL/6J mice were euthanized and their livers removed.
2. (Optional) Perfusion of the liver (as described previously[231, 232]) may be performed if desired, first with PBS followed by 4% PFA.
3. Fix fresh tissue (whole liver or individual lobes, 5mm thickness or less) in 4% PFA for 24 hours.
4. Wash tissue with PBS/0.1% sodium azide.

PAUSE POINT: Fixed tissues can be stored at 4℃ in PBS/0.1% sodium azide for up to a year. It is imperative to include the azide as a preservative to prevent growth of mold or bacteria in the tissues.

3.3.3.2 Tissue Clearing (Timing: 5-9 days depending on the size and composition of the tissue)

5. Incubate the tissue in hydrogel solution for 24 hours at 4°C in a 50mL Falcon container. This solution should be made fresh each time and can be stored at 4°C for about a week. Make sure the tissue is fully submerged.
6. Polymerize the hydrogel by placing the 50mL container with tissue and hydrogel solution into a water bath at 37°C for 3 hours. The hydrogel should be neither firm nor runny, with a gelatin-like texture.
7. Remove polymerized hydrogel containing the tissue from the container and rub off excess hydrogel surrounding the tissue. Wash the tissue with PBS.
8. Turn on the X-CLARITY™ Tissue Clearing System (set up as per manufacturer specifications). Add 2L of X-CLARITY™ Electrophoretic Tissue Clearing Solution to the reservoir. Then add 10-20mL of Quadrol to the reservoir. Do not try to dissolve the Quadrol manually, it will gradually dissolve over time when the buffer begins to circulate.
9. Place the tissue into the desired sample holder and place it into the ETC chamber of the X-CLARITY™ system

CRITICAL STEP: Make sure the sample holder is not free floating as this could block the buffer from circulating freely and raise the pressure inside the chamber which may cause it to crack and leak. Also make sure the chamber lid and reservoir lids are sealed securely to prevent leaks.

10. Adjust the settings on the X-CLARITY™ system to set the temperature at 37°C, voltage at 70V, pump speed at 100 rpm, and current at ~1.2 Amps (this will vary as the buffer is consumed). Begin the run by starting the X-CLARITY™ system and selecting ETC Active Clearing.

CRITICAL STEP: How long the tissue will take to clear depends on the dimensions of the tissue. A small chunk of liver 2mm in thickness may clear in 48-72 hours, while a whole median lobe, left lobe, or right lobe of murine liver may clear in 72-96 hours, after which it will reach a steady state and is unlikely to clear any further. The tissue clearing solution will turn yellow over time and should be changed every 24-48 hours as it changes color to encourage continuous dissolution and removal of lipids from the tissue into circulation. The tissue can be cleared for up to 1 week/10 days if needed. You may pause the run at any time to check on the state of the sample. Different sample holders may hold 1-6 tissues at a time. If clearing multiple tissues at a time you may need to change the buffer more frequently.

11. When you decide to stop clearing the tissue, stop the run and turn off the X-CLARITY™ system. Remove the sample from the sample holder and wash the tissue in PBS/0.1% sodium azide.

PAUSE POINT: The tissue can be stored at this point in PBS/0.1% sodium azide at 4℃ long term.

12. Place the tissue in a solution of 3% vol/vol hydrogen peroxide for 24-48 hours.
13. Wash the tissue in PBS/0.1% sodium azide for 2 hours on a shaker.

PAUSE POINT: The tissue can be stored at this point in PBS/0.1% sodium azide at 4℃ long term.

3.3.3.3 Immunofluorescence Staining (Timing: 2-3 weeks)

14. Incubate tissue in IHC/SDS buffer as well as any primary antibodies of choice for 4-7 days depending on the size of the tissue. The tissue should be kept on a shaker at a temperature ranging from 25-30°C. Multiple primary antibodies can be added at the same time, similar to 2-dimensional immunofluorescence staining protocols.

CRITICAL STEP: Tissues should be incubated in wide-bottom tubes (at least 50mL Falcon containers) to allow for free circulation of the solution containing antibodies all around the tissue. The tissue should be fully submerged.

15. Incubate tissue in IHC buffer (without SDS or primary antibodies) for 24 hours, on a shaker at a temperature ranging from 25-30°C.
16. Wash the tissue in IHC buffer or PBS/0.1% sodium azide 3 times for 2 hours each, on a shaker at a temperature ranging from 25-30°C.
17. Incubate tissue in IHC/SDS buffer as well as secondary antibodies conjugated to fluorophores of choice for 4-7 days depending on the size of the tissue. The tissue should be kept on a shaker at a temperature ranging from 25-30°C. Keep the tissue shielded from light by covering the container in aluminum foil.
18. Incubate tissue in IHC buffer (without SDS or secondary antibodies) for 24 hours, on a shaker at a temperature ranging from 25-30°C.
19. Wash the tissue in IHC buffer or PBS/0.1% sodium azide 3 times for 2 hours each, on a shaker at a temperature ranging from 25-30°C.

20. Incubate the tissue in 4% PFA for 2 hours on a shaker at a temperature ranging from 25-30°C.

21. Wash tissue in PBS/0.1% sodium azide for 1 hour.

22. Place tissue in CUBIC R2 solution at room temperature in the dark for at least 24 hours.

PAUSE POINT: The tissue can be stored at this point in CUBIC R2 at room temperature in the dark long term (months – years).

TROUBLESHOOTING: The concentrations of primary and secondary antibodies may need to be higher than for 2-dimensional staining and may need to be adjusted. The time of incubation may also vary based on the size of the tissue. Finally, we recommend using 50mL Falcon (Corning) tubes for incubation of tissues to ensure that the tissues are free floating at all times with ample room for the buffer to circulate.

3.3.3.4 Microscopy and Image Processing

This process may vary based on the systems available at your institution. To acquire the images described in the Results section, all tissues were mounted in CUBIC R2 solution and imaged using an RSG4 ribbon scanning confocal microscope (Caliber, Andover, MA) as previously described by Watson *et al*.[182] The microscope was fitted with a Nikon CFI90 20x glycerol-immersion objective (Nikon, Melville, NY) with 8.3mm working distance. Volumes were captured with voxel resolution of 0.467 x 0.467 x 12.2 µm (x, y, z). Laser intensity and detector settings were specific to each sample based on the levels of staining. In all cases, the intensity of the laser was increased in a linear manner throughout deeper focal planes to compensate for absorption of excitation and emission light. RAW images acquired in this way were stitched and assembled into composites using a 24 node, 608 core cluster, then converted

into the Imaris file format (Bitplane, Zurich, Switzerland). Volumes were rendered using Imaris v9.5.1.

3.4 Results

3.4.1 LiverClear protocol results in rapid, simple, and effective clearing of mouse liver tissue

Figure 22A shows the step-by-step progression of clearing of a single lobe of liver tissue after each step of the clearing protocol. Figure 22B shows fresh fixed liver tissue consisting of one large lobe of mouse liver, of about 4mm thickness (each square in the grid beneath the tissue is 5mm x 5mm). Figure 22C shows the same tissue after 6 days of active clearing using the X-CLARITY™ system with Quadrol added to the circulating buffer. This process alone produces significant clearing of the liver tissue but for a large lobe is not sufficient to achieve translucency. Figure 22D shows improved clearing after 2 days of incubation in 3% hydrogen peroxide. Figure 22E shows the appearance of the liver after 1 day of incubation in CUBIC R2 solution, and we can see that the grid lines are visible beneath a large part of the liver tissue except for the very middle which is the thickest part. Finally, Figure 22F shows further clearing of the liver tissue after incubation in CUBIC R2 for 12 days. The tissue can be left in CUBIC R2 solution indefinitely at room temperature and continues clearing over time. However, satisfactory immunostaining and imaging can be achieved without extended incubation times, as demonstrated by Figures 23-25.

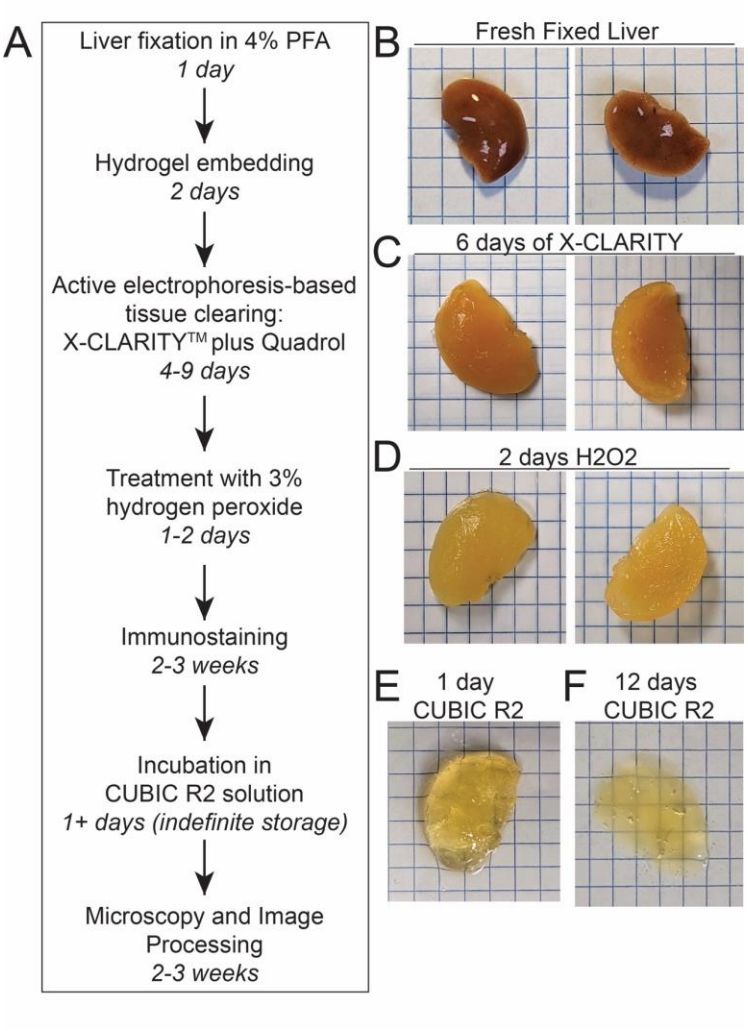

Figure 22. Diagram of tissue clearing and staining protocol with example images.

A) Outline of the tissue clearing and staining process. B-E) Photographs of the same liver tissue going through the tissue clearing process, starting with B) fresh fixed murine liver, C) liver tissue embedded in hydrogel and subjected to 6 days of active X-CLARITY, D) 2 subsequent days of hydrogen peroxide treatment, E) 1 day of incubation in CUBIC R2 solution, and F) 12 days of incubation in CUBIC R2 solution.

3.4.2 Immunostaining and ribbon-scanning confocal microscopy on cleared liver tissue can produce high-resolution images of micron-level tissue structures

Figures 23 and 24 demonstrate the results of 3D immunostaining to visualize the biliary transport structures, namely the bile ducts labeled with cytokeratin 19 (CK19) and the hepatocyte canaliculi labeled with CEACAM1. In healthy adult liver (Fig23A and 24A-C), bile is produced by hepatocytes and secreted into the canaliculi, which are small channels between hepatocytes that push the bile towards the larger bile ducts, which form a branching network that dumps bile into the common bile duct exiting the liver. After clearing and immunostaining, we were able to visualize the biliary tree throughout a whole liver lobe of 3-4mm thickness (CK19) and also visualize the fine network of canaliculi which are normally 1-2 μm wide (CEACAM1). Figure 24 offers a higher magnification illustrating the level of detail, specificity, and precision that can be achieved with this immunostaining method. Figures 23C-D and 24B-C also show the 2-dimensional histological correlates which are the standard imaging techniques used in the field. Traditional immunostaining allows CK19-labeled bile ducts to be seen mostly in cross-section, whereas 3D-imaging allows us to appreciate the precise branching structure and interconnectedness of the ducts. This is critical to our understanding of bile duct formation, how structure changes in the setting of injury, and how duct repair take place at an organ level, not just a cellular level. To highlight the utility of this technique, we show results of imaging with the same markers on murine liver in which YAP1 was deleted in early development, resulting in a congenital absence of bile ducts (YAP1 KO) [see Chapter 2 of this thesis; manuscript under review]. Figure 23 grossly shows the absence of CK19-labeled ductal structures throughout the liver (consistent with the absence of CK19-positive ducts illustrated with 2D histology in Figure 24E). Figure 23 also shows that the hepatocyte canaliculi are present but much more

disorganized than in normal liver. Figure 24D highlights this structural change, showing dropout of some canaliculi and swelling of others, which is consistent with a loss of an outflow tract and thus impaired fluid flow through these structures. 2D histology shows the presence of canaliculi marked by CEACAM1 and also reveals some structural dilatation (arrows), but it does not convey the level of disorganization that can be clearly understood from Figure 24D.

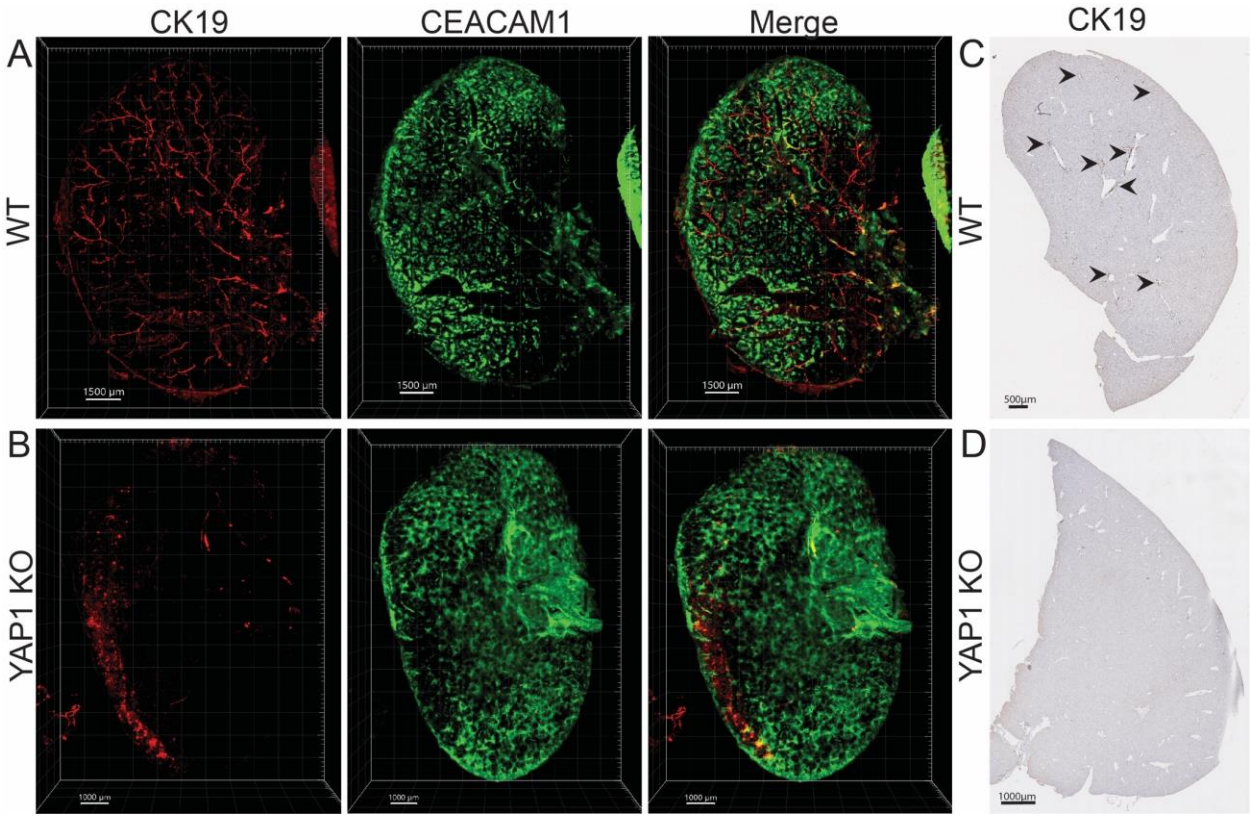

Figure 23. 3D imaging of biliary transport structures in healthy and diseased livers with a genetic absence of bile ducts from birth.

A-B) 3D imaging of whole liver lobes from A) WT and B) YAP1 KO stained for CK19 and CEACAM1. C-D) Slide scan of a 5µm thick section of a whole liver lobe from C) WT and D) YAP1 KO stained for CK19. Arrows point to CK19-positive bile ducts.

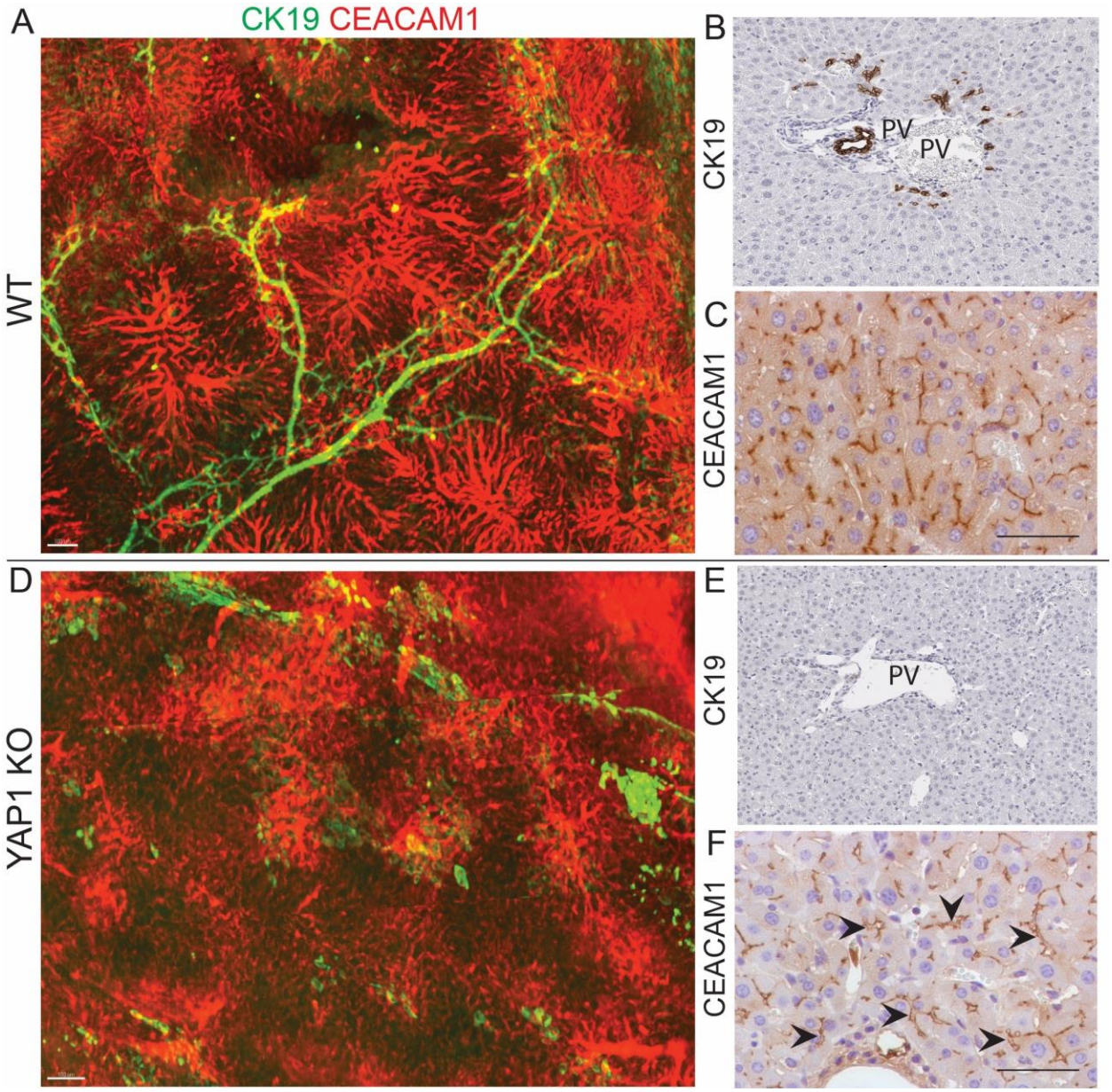

Figure 24. Higher magnification of 3D imaging of biliary transport structures in healthy and diseased livers along with 2D imaging of structural correlates.

A) Higher magnification from 3D imaging of WT liver lobe stained for CK19 and CEACAM1. B) IHC of WT liver showing CK19 positive bile ducts (PV, portal vein). C) IHC for WT liver showing CEACAM1 positive hepatocyte canaliculi. D) Higher magnification from 3D imaging of KO liver lobe stained for CK19 and CEACAM1. E) IHC of KO liver showing CK19 positive bile ducts (PV, portal vein). F) IHC for KO liver showing CEACAM1 positive hepatocyte canaliculi. Arrows point to areas of canalicular dilatation.

3.4.3 LiverClear protocol allows for the clearing and imaging of murine hepatocellular carcinoma tumors

Figure 25A-B shows an example of a liver tissue from a murine model of hepatocellular carcinoma driven by constitutively activated forms of β-catenin and Met receptor.[233-235] In this case, we have labeled the tumors using glutamine synthetase (GS), a canonical target of β-catenin signaling which is strongly expressed in β-catenin-activated HCC tumors, as can be seen by immunohistochemical staining of tumors from the same mouse model in Figure 25C. We can visualize clumps of GS-positive tumor cells which resemble sheets and aggregates matching the clusters seen by IHC, and we can even resolve individual cells within the tumor areas as seen in Figure 25B. In this case, we saw less antibody penetration than in other samples, which requires further troubleshooting. Nevertheless, this is a promising start and shows the potential of visualizing complex disease structures.

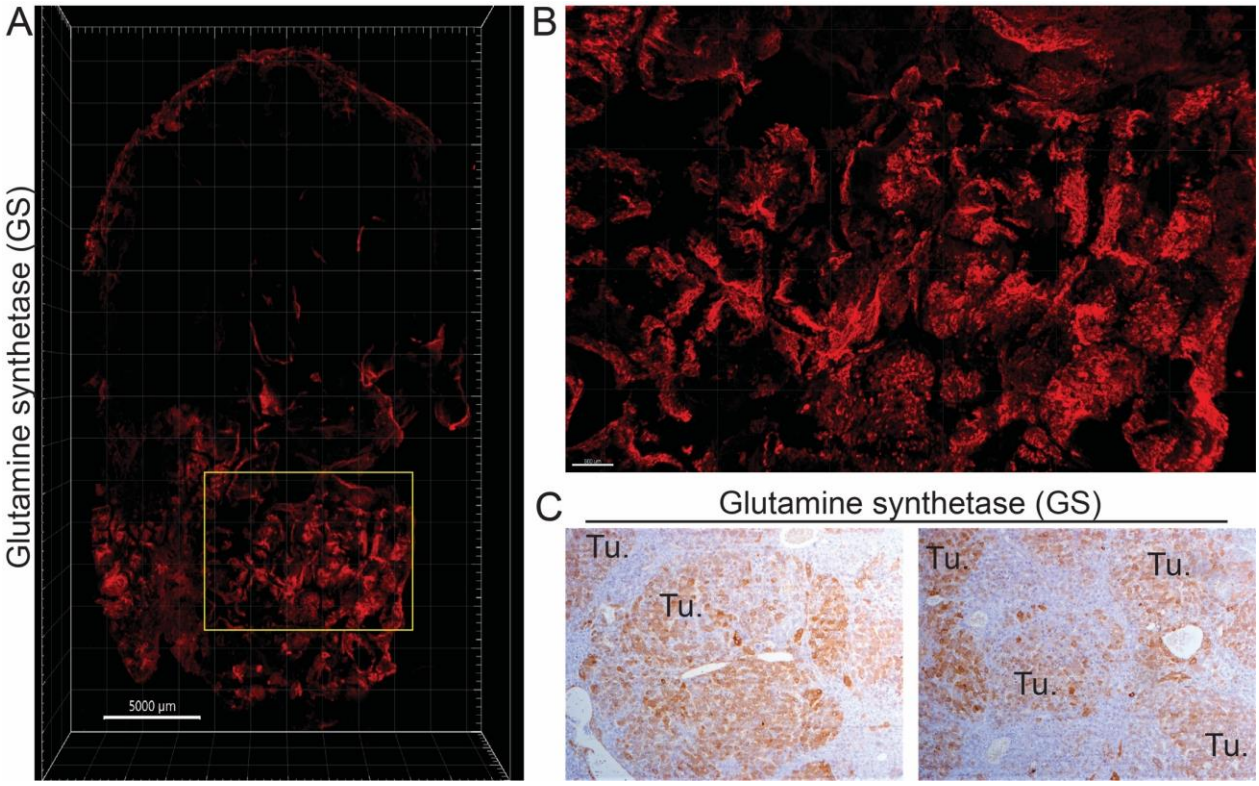

Figure 25. 3D imaging of hepatocellular carcinoma liver cancer model with 2D histological correlate.

A) 3D imaging of whole liver lobe containing HCC liver tumors, stained for glutamine synthetase (GS). Yellow box marks inset shown in B). C) IHC for GS on 5µm thick section of a whole liver lobe bearing GS-positive HCC tumors.

3.5 Discussion

3.5.1 Application of the method

This protocol can be applied to examine the tissue architecture of both normal and diseased liver of mice or similarly sized animal models. This protocol is simple and flexible enough that it can be applied to answer numerous questions in almost category of disease affecting the liver, in particular to visualize changes that alter the 3-dimensional organization of

cells and correlate these with functional changes in metabolism, transport, proliferation, or fibrous deposition. For example, it can be used to examine liver zonation of metabolic processes and how zonated markers may be altered in regeneration or disease. It can also be used to visualize the biliary ductal system and how it integrates with hepatocytes, as well as how the ductular reaction may or may not be connected with existing liver structure. Furthermore, in the setting of liver tumors this technique could be used to assess heterogeneity within tumors and visualize the relationship between tumors and the liver vasculature. This protocol can be adapted to the study of a variety of liver diseases and experiments examining liver injury and repair, making it a highly promising and versatile tool.

3.5.2 Limitations

We have tested this protocol with liver tissue up to 4-5mm thick and do not recommend trying to visualize thicker tissues due to limitations in both clearing and available microscopy techniques. Further work is needed to investigate whether nuclei can be distinguished at nuclear-level resolution, which is technically achievable based on the microscopy parameters but is limited by our computational capacity for processing terabytes of data. This protocol is excellent for visualization of protein-based markers, but as with most clearing techniques cannot be used to visualize lipids or phospholipid membranes. In addition, this protocol cannot remove precipitates of bilirubin, bile acids, and/or porphyrins, such as those modeled in animals treated with DDC diet. When clearing livers with very advanced hepatocellular carcinoma, we have observed some tissue swelling so the user should use photographs to track tissue changes and ensure that they do not cause excessive distortion of the liver tissue as a whole. Finally, we have

not yet been able to use this protocol to clear small pieces of human liver tissue, so more testing will be needed to further adapt this protocol to study patient samples.

4.0 MTOR Inhibition Affects YAP1-β-Catenin-Induced Hepatoblastoma Growth and Development

In this section, Dr. Hong Yang and I collaborated to investigate the role of mTOR signaling in regulating hepatoblastoma tumor growth in a mouse model. Dr. Adeola Michael, Dr. Aaron Bell, and Dr. Junyan Tao were involved in experimental design and data collection. Dr. Michael Oertel and Sucha Singh provided technical support for data collection. Dr. Xin Chen and Dr. Satdarshan Monga provided funding and intellectual input, and Dr. Monga directed the project.

This work was published in *Oncotarget* in 2019 (PMID: 30863496), and I am co-first author on this manuscript along with Dr. Hong Yang. As Oncotarget is an open access journal, written permission for re-use in this dissertation was not required.

This work was supported by NIH grants R01CA204586 to S.P.M and X.C. and 1R01DK62277, 1R01DK100287, 1R01DK116993 and Endowed Chair for Experimental Pathology to S.P.M. This work was also supported by T32EB0010216 to LM.

4.1 Summary

Hepatoblastoma (HB) is the most common pediatric liver malignancy. Almost 80% of HB demonstrate simultaneous activation of β -catenin and Yes-associated protein 1 (YAP1). Recently, mTORC1 activation was reported in human HB cell lines and a murine HB model driven by mutant β -catenin and YAP1. Here, we directly investigate the impact of mTORC1

inhibition on HB development. Tumors were established by hydrodynamic tail vein injection (HTVI) of Sleeping Beauty transposase and plasmids containing ΔN90-β-catenin and S127A-YAP1. Using Affymetrix microarray, we validated the clinical relevance of our mouse model by showing a strong correlation of gene expression between murine HB and two HB patient cohorts. We then treated mice with rapamycin-containing diet starting at five weeks post-HTVI. Control and treatment groups were monitored weekly with ultrasound imaging until sacrifice at 10 weeks post-HTVI. Ultrasound and gross pathology showed that Rapamycin treatment dramatically decreased HB burden, almost normalizing liver weight to body weight ratio. Immunohistochemistry confirmed successful inhibition of mTORC1 activity and showed that Rapamycin-treated HB exhibited more well-differentiated histology compared to control HB tumors. Our results support the use of mTORC1 inhibitors in HB treatment and demonstrate the utility of standard and 3D ultrasound imaging for monitoring liver tumors in mice.

4.2 Background

Hepatoblastoma (HB) is the most common pediatric liver cancer and is commonly diagnosed in the first few years of life [150]. Despite being a rare cancer, the annual incidence of HB has gradually increased over the past three decades [236]. Most cases of HB appear to be sporadic, but some are associated with genetic abnormalities and malformations, such as in cases with Beckwith-Wiedemann syndrome and familial adenomatous polyposis [237, 238]. Premature babies with low birth weight are also at a greater risk of developing HB [149, 150]. At present, surgical resection along with chemotherapy remains the curative strategy for HB and offers the only realistic chance of long-term disease-free survival [239]. Investigating the genetic and

molecular origins of HB will provide better understanding of the disease and identify novel therapeutic approaches.

HBs arise from hepatoblasts, fetal progenitor cells of the liver, and are categorized by histological subtyping based on the level of cell differentiation [152]. Despite the rarity of these tumors, several studies have used small patient cohorts to characterize genomic and transcriptomic alterations to identify tumor drivers, of which the most common is β-catenin. β-catenin is a downstream effector of the Wnt pathway and plays a critical role in hepatoblast proliferation and hepatocyte differentiation in normal hepatic development [70]. In about 60-70% cases of HB, deletion or missense mutations have been identified in the CTNNB1 gene encoding for β-catenin [240, 241]. These mutations impair the phosphorylation and degradation of β-catenin, leading to constitutively active β-catenin [242].

We recently showed many cases of sporadic HBs to exhibit nuclear localization of β-catenin and Yes-associated protein 1 (YAP1), which is a major effector of the Hippo signaling pathway playing a key role in regulating liver size and liver cell differentiation [5, 85]. Based on this evidence, we developed a unique mouse model of HB driven by co-activation of YAP1 and β-catenin [85]. Upon co-delivery of Sleeping-Beauty (SB) transposase and plasmids containing mutant ΔN90-β-catenin and S127A-YAP1 to the liver by hydrodynamic tail vein injection (HTVI), a small fraction of hepatocytes stably co-express the two oncogenes, which resulted in permanent transformation. This YAP1-β-catenin model results in rapid development of HB in mice allowing investigation of biology, mechanisms and therapies.

Several studies have also shown the importance of mammalian target of Rapamycin complex 1 (mTORC1) activation in HB tumor growth [84, 243, 244]. Based on this evidence, we hypothesized that pharmacologic mTORC1 inhibition using Rapamycin (Sirolimus), an FDA-

approved agent indicated for prevention of transplant rejection, oncology and orphan conditions like lymphangioleiomyomatosis, would significantly impair HB tumor growth *in vivo* [245, 246]. Five weeks after establishing YAP1-β-catenin driven HB using SB-HTVI, we monitored tumor growth and development using non-invasive 2D and 3D ultrasound (US) imaging to evaluate changes in tumor burden in the same mice over time, producing a more accurate representation of the effects of Rapamycin while reducing the number of animals used for the study. Additional analysis and validation of US imaging was done after 5-week treatment with Rapamycin. Our results show that Rapamycin significantly reduces HB burden *in vivo*, by reducing mTORC1 activation, affecting proliferation, and altering histology of HB from an embryonal to a well-differentiated fetal subtype. This study supports the clinical use of Rapamycin for a subset of HB driven by YAP1-β-catenin co-activation.

4.3 Materials and Methods

4.3.1 Microarray Data Analysis

Mice were sacrificed at 7, 9, or 10 weeks after YAP1-β-catenin SB-HTVI for extraction of livers with significant HB tumor burden. Tumor-bearing livers (n=3) and normal livers from non-injected mice (n=3) were utilized for mRNA isolation and analyzed using Affymetrix gene array chip R430 2.0. The full data set is available at Gene Expression Omnibus (http://www.ncbi.nlm.nih.gov/geo, accession number GSE112485). The raw CEL files were imported into R (version 3.5.0) using the *affy* package [247]. Probes were mapped to genes using the custom brain array CDF.[248] The *gcrma* package was used to perform GCRMA (Guanine

Cytosine Robust Multi-Array Analysis) normalization [249]. Low expressed genes were then filtered out using *genefilter* by selecting only genes with an expression value of 3 or more in at least 3 samples [250]. Gene annotation information was added using the *annotate* and *mouse4302.db* packages [251, 252]. Principal component analysis was performed in base R and the results were plotted using ggplot2 and ggfortify [253, 254]. Next, the *limma* package was used to apply an empirical Bayes statistical model to calculate a moderated t-statistic and p-value for each gene comparing its log-fold expression in HB samples relative to the WT samples [255]. Using an adjusted p-value cutoff of 0.05, 3263 differentially expressed genes were identified. The processed gene data set was then uploaded into BaseSpace Correlation Engine (which correctly identified 3106 genes for further analysis) and compared with a large database of previously published and curated gene expression data sets to identify sets with significant overlap [256]. In addition, the processed gene expression values for all genes were uploaded into Gene Set Enrichment Analysis (GSEA) software (version 3.0) for comparison with curated gene sets using 1000 gene-set permutations; for genes associated with multiple probe sets, the median of the expression values was used for analysis [257, 258].

4.3.2 Animals, Plasmids, and Treatment

All animal experiments were approved by the Institutional Animal Use and Care Committee at the University of Pittsburgh, School of Medicine. FVB/N mice were purchased from Jackson Laboratory (Bar Harbor, ME). Hydrodynamic tail vein injections (HTVI) were performed as described before [85]. A mix of 10μg pt3-EF1α-YAPs127a, 10μg pt3-EF1α-ΔN90-β-catenin together with 4μg pcmv/SB was injected into the mice. 16 mice were randomized into two groups. The control group was kept on normal diet for 10 weeks post-HTVI (n=8), while the

treated group was fed normal diet for 5 weeks post-HTVI, then treated with diet containing 19 mg/kg Rapamycin (Research Diets, Inc.) for another 5 weeks (n=8). All 16 mice were sacrificed at 10 weeks post HTVI. An additional two mice kept on normal diet were sacrificed 8 weeks post-HTVI to compare US imaging with gross pathology.

4.3.3 Sonographic Examination

Ultrasound (US) scans were performed for each mouse at 4, 7, 8, 9, and 10 weeks using a Visual Sonics Vivo 3100 scanner (Fujifilm, Japan) and a transducer (MX250S) with 20MHz central frequency. Mice were stabilized on a warmed operating table and sedated using an inhalation anesthesia system loaded with a mixture of isoflurane and oxygen. The transducer mounting system was employed to fix the transducer in a longitudinal position perpendicular to the mouse body. First, the liver was thoroughly observed and pictures were taken using standard 2D-US imaging. Next, a 3D-US scan was obtained for each mouse; the transducer starting position was directly to the left of the gall bladder, and the following parameters were used for the 3D-scan: transducer frequency 21MHz, output power 100%, gain 23~27dB, dynamic range 60dB, depth 18 mm, 3D range 27~35mm, and 3D step size 0.1 mm.

US scan and imaging analysis was performed by a trained radiologist with experience in diagnosis and treatment of human liver tumors (H.Y.). VisualSonics Vivo LAB 3.0.0 software (Fujifilm, Japan) was used to measure liver volume and tumor diameter. Multi-slice method was employed to measure the total liver volume; the boundary of liver on each sectional slice was delineated and the 3D liver image was reconstructed to calculate liver volume by software analysis. Liver tumors were then identified on sequential sectional images frame by frame, and the maximum tumor diameter for each lesion was measured on the largest cross-sectional slice of

the targeted lesion. The volume of each tumor was then approximated as the volume of a sphere using the maximum tumor diameter for each lesion. Based on the high correlation of measured total tumor volumes with liver weight to body weight ratio, this approximation was deemed sufficient for the present study.

4.3.4 Immunohistochemistry

Livers were harvested and fixed in 10% formalin for 48 hours, followed by paraffin embedding. For H&E, 4μm paraffin sections were deparaffinized and rehydrated, stained with Shandon's Hematoxylin (Thermo-Fisher, 7211) for 45 seconds and Eosin (Thermo-Fisher, 71204) for 15 seconds, dehydrated, and mounted using Cytoseal XYL (Thermo-Fisher, 8312-4). For immunohistochemistry, deparaffinized sections were either microwaved for 12 minutes in pH6 sodium citrate buffer (Myc-tag, Cyp2E1, Cyclin D1, phospho-mTOR Serine-2448 or S2448, phospho-S6 ribosomal protein S235/236, phospho-S6 ribosomal protein S240/244, and phospho-4EBP1 Threonine 70 or T70), microwaved for 8 minutes in 1% zinc sulfate buffer (PCNA), or were pressure cooked for 20 minutes in pH 6 sodium citrate buffer (YAP1, Sox9) for antigen retrieval. Next, slides were treated with 3% hydrogen peroxide to inactivate endogenous peroxidases, and blocked with Superblock (Scytek Laboratories, AAA500). Sections were incubated overnight at 4C in the following primary antibodies: YAP1 (1:50; Cell Signaling CS14074), Sox9 (1:2000, EMD Millipore ab5535). Alternatively, sections were incubated for one hour at room temperature in the following primary antibodies: Myc-tag (1:100; Maine Medical Center Research Institute Vli01), PCNA (1:100; Santa Cruz Biotechnology sc-56), Cyclin D1 (1:200; Abcam 134175), GS (1:2000; Sigma G2781), Cyp2E1 (1:100; Sigma HPA-0009128), phospho-mTOR Ser 2448 (1:100; Cell Signaling, 2976), phospho-S6 ribosomal

protein Ser 235/236 (1:50; Cell Signaling, CS4858), phospho-S6 ribosomal protein Ser 240/244 (1:50, Cell Signaling, CS5364), and phospho-4EBP1 Thr 70 (1:50; Cell Signaling CS9455). Sections were then incubated for 30 minutes at room temperature with biotin-conjugated secondary anti-mouse, -rabbit or -goat antibodies (Vector Laboratories), and developed using the VECTASTAIN ABC HRP kit (Vector Laboratories, PK-6101) and Vector DAB kits (Vector Laboratories, SK-4100). Sections were counterstained in Shandon's Hematoxylin, dehydrated, and mounted in DPX. Images were taken on a Zeiss Axioskop 40 inverted brightfield microscope. Images for tiling were taken on a Zeiss Axio Observer.Z1 microscope and assembled utilizing ZEN Imaging software.

4.4 Results

4.4.1 S127A-YAP1-ΔN90-β-catenin driven murine hepatoblastoma tumors show significant correlation of gene expression to independent cohorts of patient hepatoblastoma tumors and are associated with more proliferative HB subtypes.

We first aimed to determine the clinical relevance of our mouse model of HB driven by YAP1 and β-catenin activation by comparing gene expression patterns in murine HB to available gene expression data sets derived from human HB tumors. To do this, we used Affymetrix microarray to compare gene expression of livers with late-stage HB tumors (n = 3) induced by YAP1-β-catenin SB-HTVI to WT murine liver (n = 3). Principal component analysis shows that the HB tumors mostly cluster together and distantly from the WT liver tissue, as expected (Figure 26A). We then compared our data set with previously published gene expression data of

human HB patient cohorts using two different methods. Using Gene Set Enrichment Analysis (GSEA) software, we determined that mouse HB tumors showed a significant enrichment of genes upregulated in a cohort of 25 human HB tumors studied by Cairo *et al*, as well as a significant negative correlation with genes downregulated in human HB tumors (Figure 26B) [162, 258]. We next identified differentially expressed genes using a false discovery rate of 0.05, and uploaded our gene set into BaseSpace Correlation Engine, which compares the dataset with a large library of curated gene sets from the literature [256]. Notably, we identified highly significant overlap between our HB data set and human HB tumor data sets from both the Cairo *et al* patient cohort (Figure 26C) as well as an independent HB patient cohort profiled by Hooks *et al* (Figure 26D) [162, 259]. The results show a strong positive correlation among upregulated and downregulated genes in all three data sets. This data further strengthens the correlation in gene expression patterns between our HB mouse model and patient HB tumors, supporting our use of this model for further preclinical investigation.

Through GSEA analysis, we also identified a significant enrichment of genes expressed in early liver development (embryonic days 11.5-12.5) as compared to later developmental stages, while genes characteristically expressed in mature adult hepatocytes were significantly enriched in WT samples as opposed to HB tumors (Figure 26E) [162, 260]. Previously, Cairo *et al* had distinguished two classes of HB tumors based on a 16 gene signature correlated with tumor differentiation state and patient prognosis, and identified a subclass of more highly proliferative tumors associated with less well-differentiated tumor types and overall decreased survival [162]. Notably, we identified that genes significantly upregulated in this subclass of proliferative patient HB tumors relative to more well-differentiated HB tumors were also significantly enriched in our mouse model of HB (Figure 26E). This data is consistent with the enrichment of

poorly differentiated hepatoblast-like tumor cells in the mouse HB liver samples and suggests that our tumor model exhibits features of more aggressive HB tumors.

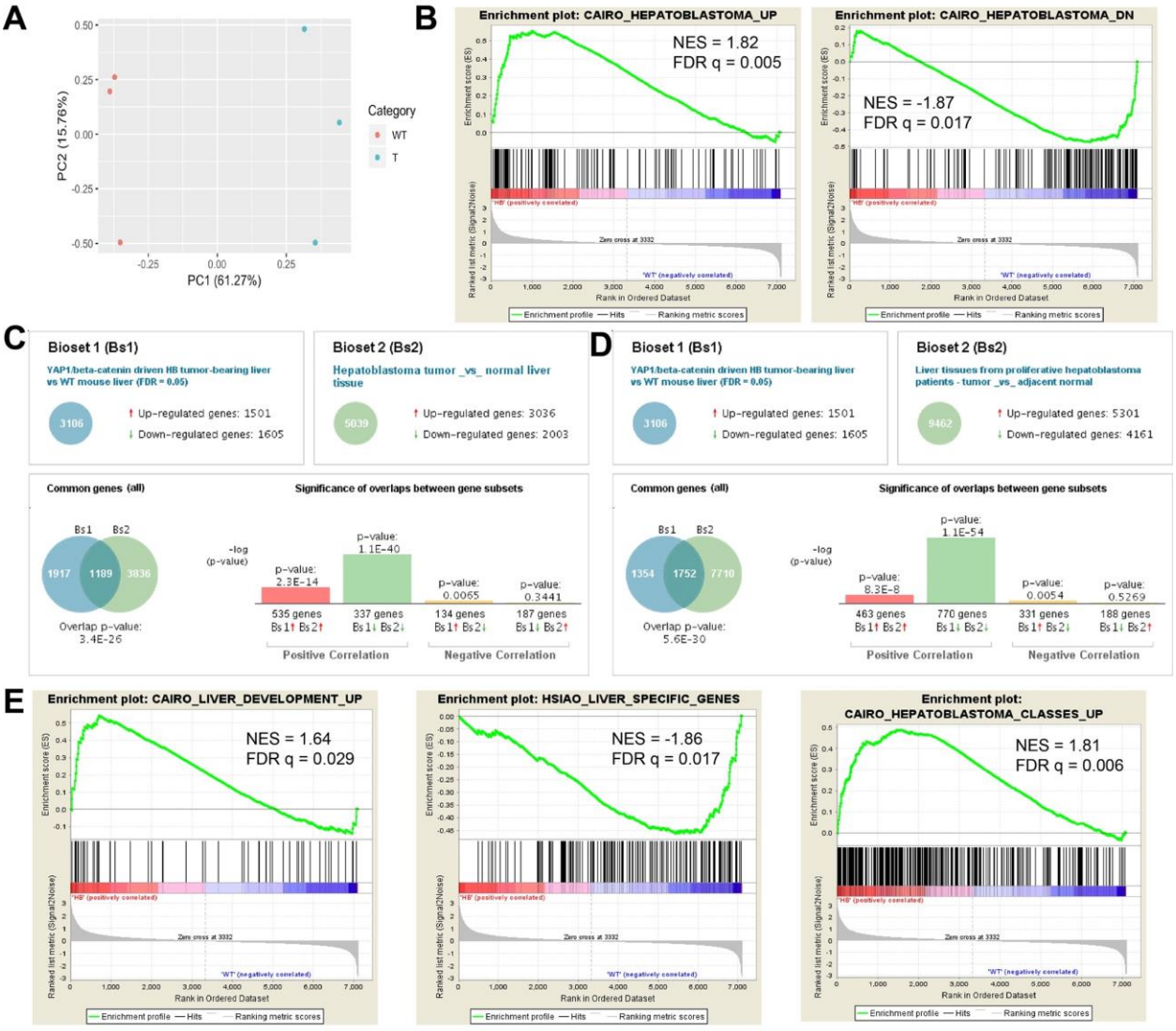

Figure 26. HB occurring in the YAP1-β-catenin model show similarity to HB in patients by transcriptomic analysis.

A. Principal component analysis (PCA) plot derived from Affymetrix microarray gene expression analysis shows that wildtype (WT) and HB tumor-laden (T) liver samples cluster separately along the PC1 axis, with PC1 explaining 61.27% of the variance in the data. B. Gene Set Enrichment Analysis for gene sets upregulated (Cairo_Hepatoblastoma_Up) or downregulated (Cairo_Hepatoblastoma_Down) in patient hepatoblastoma tumors shows significant enrichment of HB genes in our mouse model [162]. C-D. BaseSpace Correlation Engine software was used to determine the overlap in the set of differentially expressed genes in

our HB tumors relative to WT liver (Bioset 1) with gene expression data sets enriched in HB tumors from independent patient cohorts published by Cairo *et al* (C, Bioset 2) and Hooks *et al* (D, Bioset 2) [162, 259]. E. GSEA analysis shows significant enrichment in murine HB tumors for genes expressed in early liver development (Cairo_Liver_Development_Up) and for genes expressed in a proliferative subclass of HB patient tumors (Cairo_Hepatoblastoma_Classes_Up), while genes enriched in mature adult liver tissue are significantly enriched in WT over HB samples (Hsiao_Liver_Specific_Genes). NES, normalized enrichment score. FDR, false discovery rate.

4.4.2 Mice treated with rapamycin show significantly decreased hepatoblastoma tumor burden.

We next used our clinically relevant HB model to address the potential therapeutic efficacy of mTORC1 inhibition to decrease HB tumor growth. We used the SB-HTVI system to induce hepatoblastoma tumor formation driven by mutant YAP1-S127A and β-catenin-ΔN90 in 5-week old FVB mice. As reported previously, at 5 weeks post-HTVI small tumors are already present [85]. At this stage, we began treating half of the mice with Rapamycin through diet as described in the Methods, and we used ultrasound (US) imaging to monitor tumor growth in control and treatment groups (Figure 27A). By 10 weeks post-HTVI, control mice exhibited severe abdominal distension reflecting extensive tumor burden, requiring euthanasia. At this time-point, liver weight to body weight ratio (LW/BW) showed a dramatic increase in control mice (around 25%) versus around 5% in normal wild-type (WT) mice reflecting a profound tumor burden (Figure 27B). In contrast, mice treated with 5 weeks of Rapamycin diet showed a significant decrease in LW/BW (around 5.5%) compared to the control group, and showed no significant difference in LW/BW compared to WT mice, thus displaying a dramatically lower

tumor burden compared to the control mice (Figure 27B). Indeed tumor-laden livers were clearly visible in the abdomens of controls but not in Rapamycin-treated group (Figure 27C). Representative gross pathology images showed an abundance of large and small tumors in the control group, while Rapamycin treated livers showed very few and notably smaller nodules, and largely normal appearance (Figure 27D). We next performed immunohistochemistry against Myc-tag, which labels exogenous ΔN90-β-catenin, to compare the distribution of transformed cells in control vs Rapamycin treated groups. Figure 27E shows representative tiled images of control and Rapamycin treated mice. Control mice 10 weeks post-HTVI showed abundant large and small Myc-tag positive HB tumor nodules occupying the majority of the liver lobe, while Rapamycin treated group showed predominantly normal liver parenchyma with occasional small tumor nodules and small clusters of transformed cells. In addition, nuclear YAP1 was evident in all HB in the control group by immunohistochemistry while Rapamycin treatment led to notably smaller HB which still showed nuclear YAP1 (Figure 27F). Altogether, this data showed Rapamycin treatment led to a dramatic decrease on growth and development of HB in the YAP1-β-catenin mice.

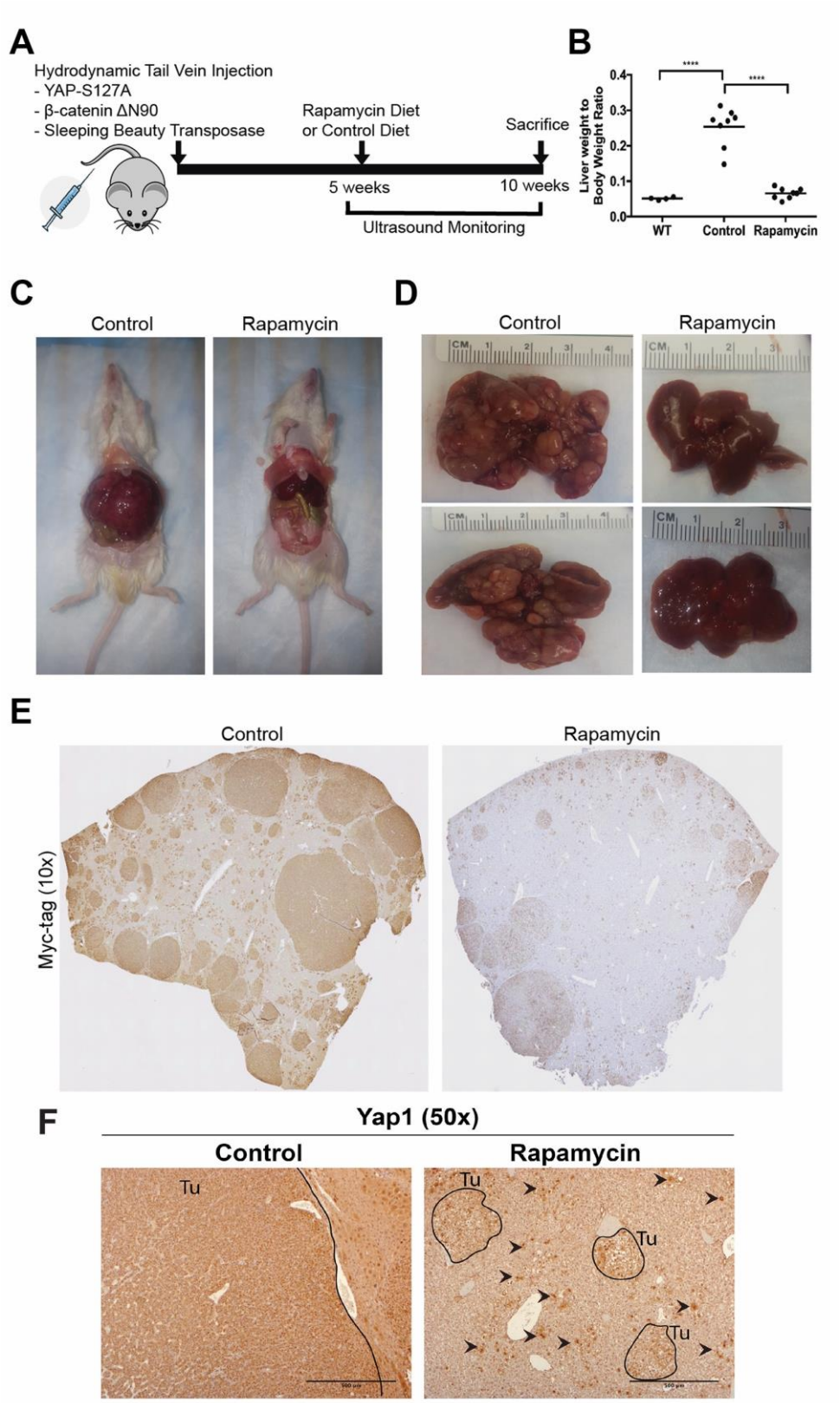

Figure 27. Tumor burden decreased in the YAP1-β-catenin HB mouse model following Rapamycin treatment.

Figure 27. A. Schematic detailing the generation of YAP1-β-catenin HB mouse model and randomization to Rapamycin or control diet. B. Liver weight to body weight ratio of wild type (WT) mice which are historical controls, mice 10 weeks post-HTVI on control diet (Control), and mice 10 weeks post-HTVI treated with 5 weeks of Rapamycin diet (Rapamycin). C. Gross images showing excessive liver growth due to tumor formation in control mice post-HTVI, which does not occur in Rapamycin treated mice. D. Gross pathology images show that control mice have significant tumor burden, while Rapamycin-treated mice show few, small tumors and appear mostly normal. E. Representative tiled images of one liver lobe comparing tumor burden in control (160 tiles) and Rapamycin treated (110 tiles) mice using immunohistochemistry to target Myc-tag (representing exogenous, mutant β-catenin). F. Representive immunohistochemistry for YAP1 showing strong nuclear staining in HB tumors in both control and Rapamycin-treated mice.

4.4.3 3D ultrasound verifies a reduction in tumor burden by rapamycin in the YAP1-β-catenin model.

We also used standard and 3D ultrasound monitoring to quantify tumor growth over time in both groups, as described in the Methods, and address effect of Rapamycin on tumor growth. The goal was to determine whether US monitoring could effectively quantify liver tumor burden in mice over time and hence limit the number of mice needed for studies. A notable tumor burden in the form of multiple hypo- or hyperechoic, round, well-circumscribed, focal lesions, was clearly evident in a representative US image of a control mouse liver, 10 weeks post SB-HTVI, with the largest lesions showing areas of necrosis (Figure 28A). As a proof of concept, the US image could be matched with gross pathology showing pale, round lesions distinct from the surrounding liver as shown in examples from two control mice 10 weeks post-HTVI (Figure 28B). Additionally, the largest tumors also showed a non-echoic acoustic halo on US (Figure 28B, lower panels).

While standard US imaging can detect the presence of tumors with diameter of at least 0.5 mm, it lacks a cohesive view of the whole liver as opposed to CT or MRI scans to directly compare tumor burden from mouse to mouse. To address this limitation, we used 3D-US imaging to measure quantitative volumetric parameters for each mouse weekly, starting at 4 weeks post-HTVI for both the control and Rapamycin treated group. With a 20MHz probe stabilized on a mechanical arm, successive transverse images of the whole liver were obtained and compiled to create a 3D-scan of the liver. Prior to Rapamycin treatment, at 4 weeks after HTVI of plasmids, livers appeared comparable in both groups, as the tumors present at this time point were small and dispersed throughout the liver (Figure 28C). At this time, most tumors were smaller than the limit of detection of standard US imaging. At 7 weeks, control livers began to appear larger than the Rapamycin treatment group, and by 10 weeks, control livers showed a dramatic loss of the normal liver shape due to the irregular expansion of the tumors also visible as an irregular surface contour (Figure 28C). The livers in the mice treated with Rapamycin showed normal liver size and shape with only a few surface irregularities, if at all (Figure 28C).

Next, a radiologist (H.Y.) evaluated each scan frame-by-frame to quantify tumor number, tumor diameter, total tumor volume, and total liver volume for each mouse to compare the time course of tumor growth in both controls and Rapamycin-treated groups. Some representative frames used to assess such parameters are included (Figure 28D). A detailed recording of these parameters is included in Table 2.

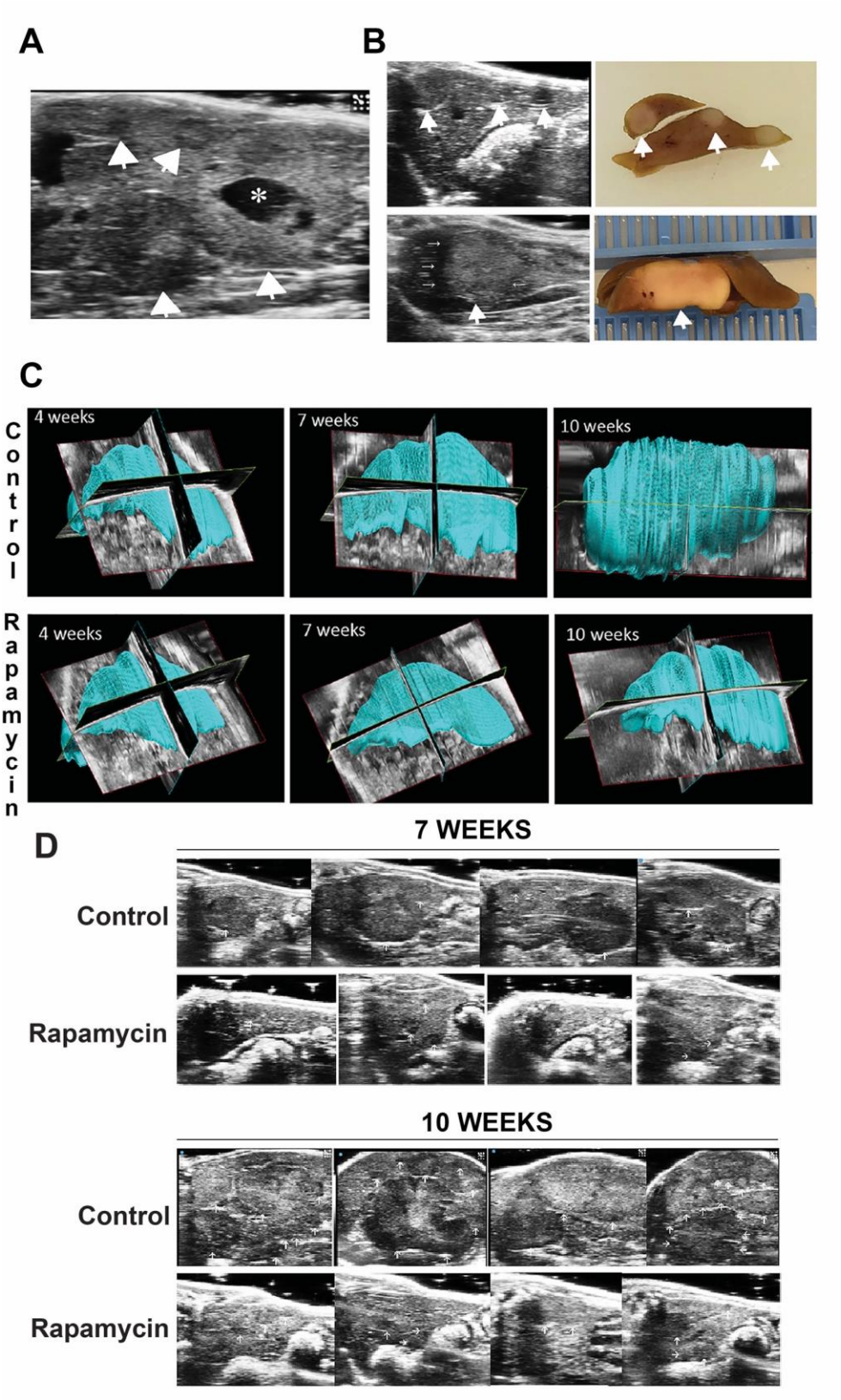

Figure 28. Ultrasound and US-based 3D modeling to detect tumor and liver volume in YAP1-β-catenin model.

Figure 28. A. Representative ultrasound image of a control mouse showing multiple large, focal, well-circumscribed HB tumors (arrowheads) as well as a large area of necrosis (asterisk). B. Representative ultrasound images are shown alongside the gross pathology images of the same liver. Both pairs of images represent control mice 10 weeks post-HTVI showing multiple HB tumors (arrowheads). Small arrows highlight an acoustic halo around the largest tumor. C. Representative reconstructed 3D liver images used to calculate total liver volume for control and Rapamycin-treated mice at multiple time points including 4, 7, and 10 weeks post-HTVI. D. Representative ultrasound panels for control and Rapamycin-treated mice at 7 and 10 weeks.

Arrows point to identified tumors in each panel.

Table 2. Liver volume, HB tumor number, total HB tumor diameter, and total HB tumor volume in control and treated groups at 4, 7, 8, 9, and 10 weeks after SB-HTVI injection.

	Liver volume (mm^3)		Tumor number		Total tumor diameter (mm)		Total tumor volume (mm^3)	
	control	treated	control	treated	control	treated	control	treated
4w	799.8±51.3	829.3±51.6	0	0	0	0	0	0
7w	1492.9±416.5	930.9±74.1	6±3	4±2	20.3±9.2	7.9±4.6	218.7±185.7	22.1±23.2
8w	2816±664.1	1104.4±236.3	16±5	8±4	56.5±17.5	21.3±16.4	901.9±477.9	79.2±58.7
9w	4386.1±1305.3	1371.2±289.1	33±5	11±6	125.7±23.0	29.2±14.9	2759.0±1006.6	178.7±107.3
10w	5893.2±1661.6	1475.9±441.3	40±9	19±11	178.5±39.8	47.6±27.7	5093.8±1525.1	330.4±208.3

Control mice showed a steady increase in liver volume starting at 7 weeks post-HTVI (Figure 29A), and the combined increase in the tumor numbers (Figure 29B) and tumor diameter (Figure 29C) over time resulted in an exponential increase in total tumor volume (Figure 29D). In contrast, mice treated with Rapamycin showed only a small increase in total liver volume (Figure 29A) and these parameters diverge significantly from control mice after just 3 weeks of Rapamycin treatment (Figure 29A). Significant decreases in tumor number and tumor diameter were also visible in Rapamycin-treated versus control mice at all tested times (Figure 29B, 29C).

Thus, the final tumor volume in Rapamycin treated mice was extremely small and significantly lower than controls, showing its efficacy in reducing overall tumor burden in the YAP1-β-catenin model of HB (Figure 29D). Intriguingly, the 3D-US data showed an upward trend in tumor number and size over time in the Rapamycin treated group, showing that Rapamycin delayed but did not completely abolish HB tumor growth in this model.

To evaluate the sensitivity and accuracy of 3D-US scans, we next determined the correlation between the four volumetric US parameters measured at 10 weeks post-HTVI and the liver weight to body weight ratio of each mouse, which is the standard and surrogate for representing the liver tumor burden in a mouse model. Indeed, total liver volume and total tumor volume determined by 3D-US, showed a very strong correlation with liver weight to body weight ratio across a broad dynamic range and hence could have an application as a surrogate measure to compare tumor burden in mice prior to sacrifice (Figure 29E, 29F). Total tumor diameter showed a strong correlation but with increased variability, while total tumor number showed only a moderate correlation, most likely due to the wide range of tumor sizes in both the control and Rapamycin-treated groups (Figure 29G, 29H). This data shows that 3D-US parameters can be used to measure tumor burden and can reduce the number of mice used for experiments while providing important temporal information about tumor growth *in vivo*.

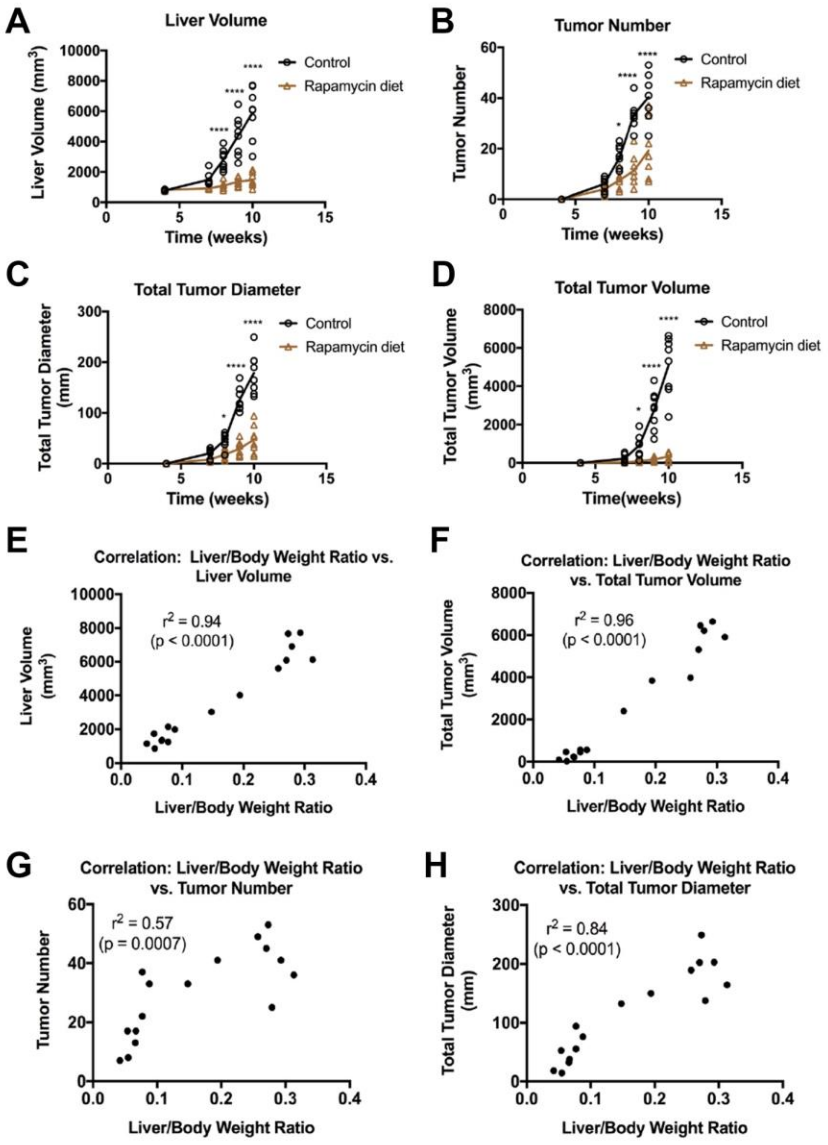

Figure 29. Effect of Rapamycin on liver volume and tumor number, volume and diameter in the YAP1-β-catenin HB mouse model.

A-D. 3D-US imaging was used to approximate the total liver volume (A), number of tumors in each liver (B), total tumor diameter (C), and total tumor volume (D) of each mouse from 4 to 10 weeks post-HTVI, showing a dramatic increase in tumor burden in control mice, which is significantly stunted in mice fed Rapamycin from weeks 5-10 post-HTVI (*, $p < 0.05$; ****, $p < 0.0001$). E-H. At 10 weeks post-HTVI, the liver weight to body weight ratio (LW/BW) was compared with the 3D-US parameters from the same time point including liver volume (E), total tumor volume (F), tumor number (G), and total tumor diameter (H). Pearson's r^2 correlation coefficients are shown on each graph.

4.4.4 Rapamycin treatment profoundly affects HB development and decreases tumor cell proliferation.

While the overall tumor burden was notably decreased in the Rapamycin-treated group, we next wanted to address if Rapamycin treatment also led to any differences in tumor histology. Hematoxylin and Eosin (H&E) staining was performed on liver samples from both groups (Figure 30). At 10 weeks after HTVI, the histology of the tumors occurring in the control group was that of crowded fetal or embryonal HB (Figure 30). In the Rapamycin treated group, the overall tumor burden was dramatically lower but none of the remnant tumors showed any embryonal or crowded fetal histology. Instead, the small tumors evident in this group were composed of well-differentiated cells and histology was reminiscent of well-differentiated fetal HB (Figure 30). The tumor cells were composed of hepatocytes with clear cytoplasm.

We next performed immunohistochemistry for Myc-tag that represents the exogenous β-catenin since Myc-tag is linked to the ΔN90-β-catenin plasmid. Using the historical control mice, we show that at 5 weeks post-HTVI mice develop small tumor nodules with diameters of around 0.5 mm containing clusters of transformed cells (Figure 31). The predominant histology of cells clustering as microscopic tumor foci was reminiscent of HB, as published previously [85]. At 10 weeks post-HTVI, the livers in the control group are packed with abundant HB exhibiting embryonal or crowded fetal histology (Figure 31). Rapamycin-treated mice showed an overall dramatic reduction in numbers and size of tumors, with tumor size and distribution almost similar to that observed in control mice at 5 weeks post-HTVI, suggesting a notable cytostatic role of Rapamycin (Figure 31). Importantly, the remnant tumors in the Rapamycin-treated group were still composed of Myc-tag-positive cells but the histology was indicative more of a well-

differentiated HB which were smaller and composed of clear but small hepatocytes (Figure 31). Likewise, as shown previously, nuclear YAP1 was evident in all HB in the control group by immunohistochemistry while Rapamycin treatment led to notably smaller HB which still showed nuclear YAP1 (Figure 27F). Thus, Rapamycin treatment differentially diminished the growth and survival of the HB with predominant crowded fetal or embryonal-like histology, while the smaller foci composed of more differentiated HB resembling fetal form persisted [85].

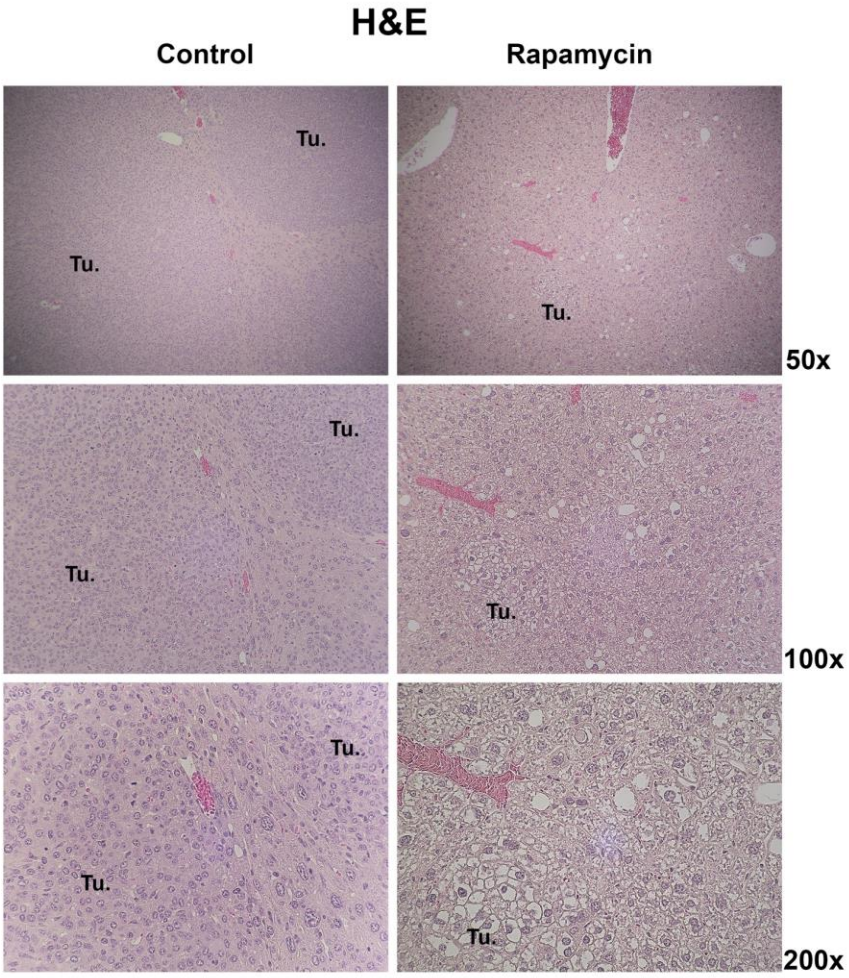

Figure 30. Histology of HB tumors with and without Rapamycin treatment.

Representative images of H&E staining showing the predominant histological features of HB tumors in control mice and Rapamycin-treated mice 10 weeks post-HTVI. (Tu. – Tumor foci)

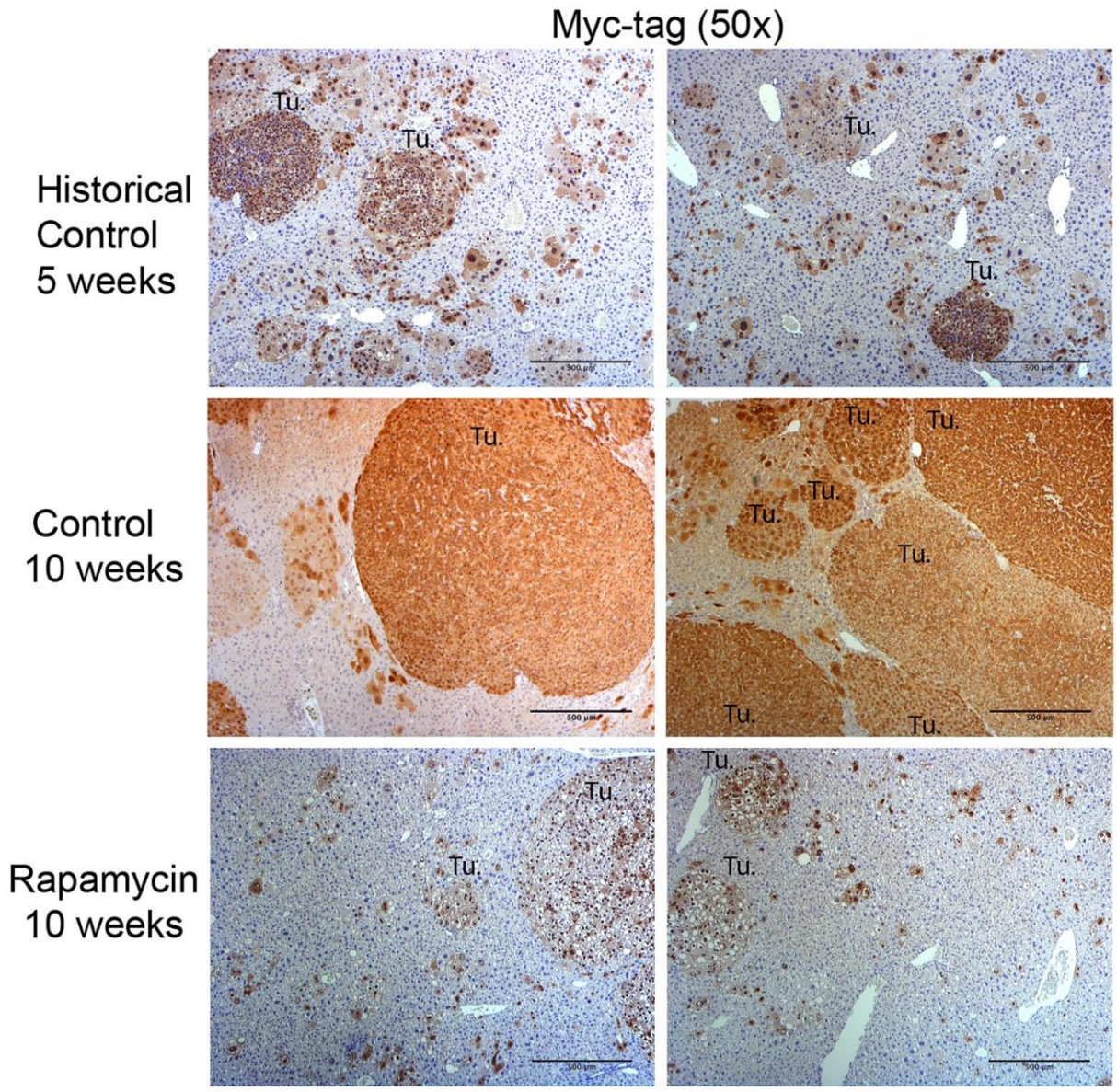

Figure 31. Immunohistochemistry for Myc-tag in HB tumors with and without Rapamycin treatment. **Immunohistochemistry for Myc-tag (representing exogenous, mutant β-catenin) was used to distinguish tumor cells in mice 5 weeks post-HTVI (historical controls), 10 weeks post-HTVI (control), and 10 weeks post-HTVI treated with 5 weeks of Rapamycin diet (Rapamycin). Representative images from control mice show abundant HB tumors at 10 weeks, most of which demonstrated embryonal histology. While Rapamycin treated mice show a tumor burden similar to that observed in historical control mice at 5 weeks after HTVI, the histology of Rapamycin-treated tumors is notably altered and represents mostly well-differentiated fetal HB. (Tu.- Tumor foci; Scale bar: 500 μm)**

Glutamine synthetase (GS) has been used to distinguish a more differentiated fetal from an undifferentiated embryonal HB [240]. We have also reported previously that HB that occur in YAP1-β-catenin model are only transiently GS-positive at the earliest stages of tumorigenesis [85]. Indeed, HB in the control group after 10 weeks of HTVI were GS-negative (Figure 32). Most of the tumors in the Rapamycin-treated group also continued to show GS-negative nodules despite the resemblance to a fetal HB like morphology (Figure 32). However, while HB tumors in the control group showed a mixed expression pattern of Cyp2E1 (a pericentrally zonated gene associated with well-differentiated tumors), Rapamycin-treated tumors were strongly positive for Cyp2E1 (Figure 32) [162]. We also evaluated the expression of biliary marker Sox9; expression of biliary markers has been associated with less differentiated tumor types [162, 240]. Consistent with histological observations, the crowded fetal and embryonal tumors in the control group were strongly positive for Sox9, but Rapamycin-treated tumors showed significantly decreased expression of Sox9 and several remnant HB were often Sox9 negative (Figure 32). Altogether, these observations suggest that alterations in cell morphology following Rapamycin treatment are also associated with increases in some molecular hallmarks of tumor cell differentiation.

We next assessed tumor proliferation in both control and experimental group. Cyclin-D1, an important regulator of G1 to S phase cell cycle transition, was tested by immunohistochemistry. In both control and Rapamycin treated groups, tumor cells continued to be positive for cyclin-D1 irrespective of the size of the tumor foci (Figure 32). Proliferation was next assessed by PCNA immunohistochemistry. Like Cyclin-D1, tumor cells in both the control as well as the Rapamycin-treated groups were positive for PCNA (Figure 32). Thus, while a clear decrease in tumor numbers, size and histology was apparent after 5 weeks of Rapamycin treatment, the remnant tumor foci still had PCNA staining even in the Rapamycin-treated group.

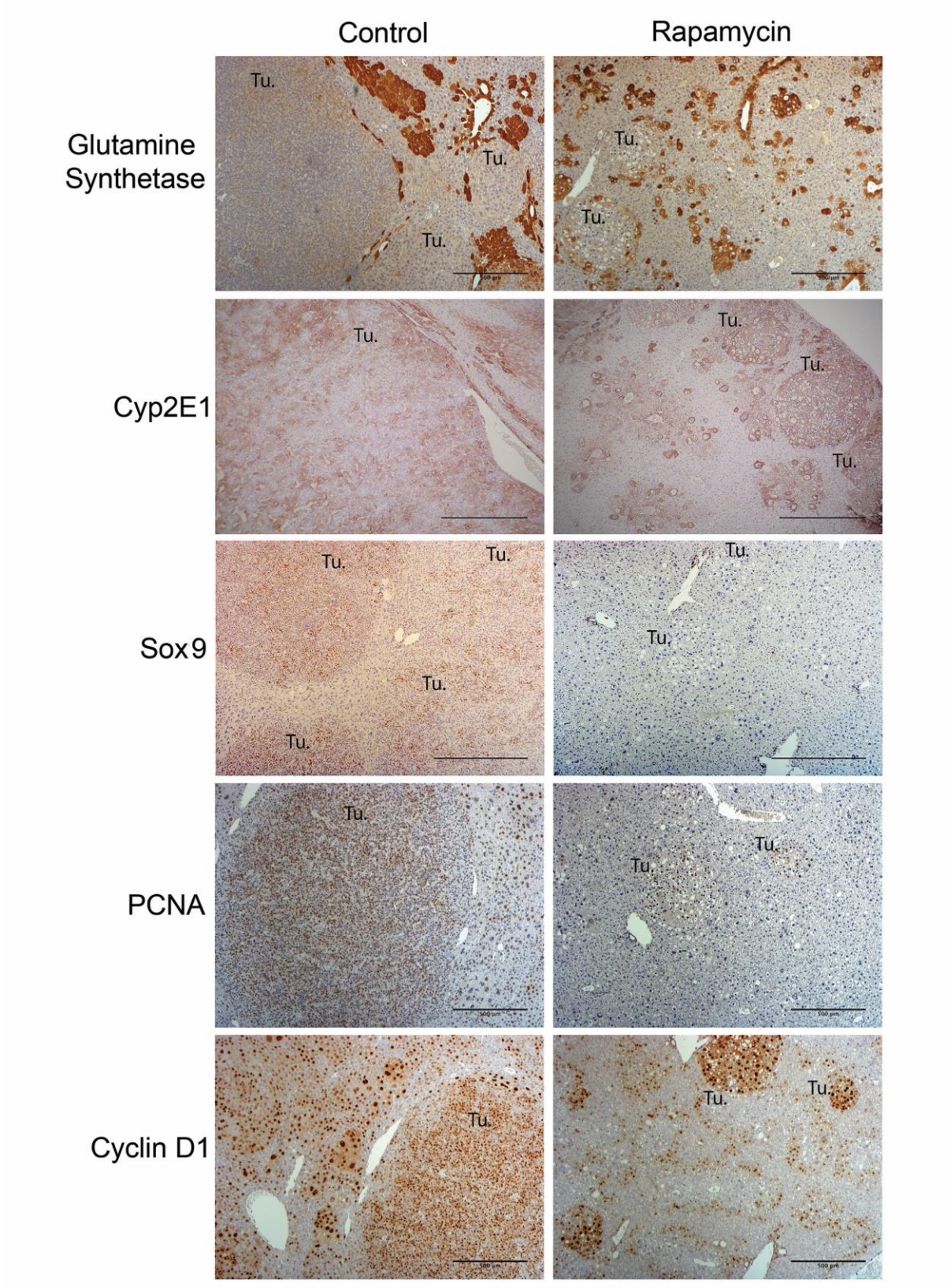

Figure 32. Molecular characterization of HB tumors untreated vs treated with Rapamycin.

Figure 32. Representative immunohistochemistry images (50x) assessing differentiation and proliferation of HB with and without Rapamycin treatment. Representative immunostaining for Glutamine Synthetase (GS) shows that HB tumors in both the control and Rapamycin treatment group are negative for this marker (50x). Immunostaining for Cyp2E1 (50x) shows mixed expression levels in control HB tumors but high levels of expression in Rapamycin-treated tumors. Immunostaining for Sox9 (50x) shows that control HB tumors are strongly positive while Rapamycin treated tumors are mostly negative. Representative immunohistochemistry images (50x) for cyclin-D1 and PCNA staining compare control versus Rapamycin treatment group showing comparable intratumoral proliferation despite a dramatic difference in tumor sizes between the two groups. (Tu.- Tumor foci; Scale bar: 500 μm)

4.4.5 Rapamycin treatment affects mTORC1 signaling in the YAP1-β-catenin model of HB development.

To address if Rapamycin effectively reduced signaling in HB, we next performed immunohistochemistry on the livers from the control and treatment group for downstream effectors of mTORC1. Intriguingly the HBs observed in the control mice at 10 weeks did not show any notable staining for phospho-mTOR-S2448, an indicator of active-mTORC1, by immunohistochemistry (Figure 33). Remnant tumors in the Rapamycin-treated group also stained negative for p-mTOR-S2448 (Figure 33). Only occasional small foci composed of a cluster of a few cells were p-mTOR-S2448-positive in both control and Rapamycin group (Figure 33).

We next examined indicators of mTORC1 signaling, including changes in the levels of phospho-S6-ribosomal protein (S6)-Ser235-236 (pS6-S235-236) and pS6-S240-244, as well as phosphorylated form of elongation repressor eukaryotic translation initiation factor 4E-binding protein 1 (4EBP1) at Threonine-70 (p-4EBP1-T70). Despite absence of frank p-mTOR-S2448

staining, all HB in controls showed staining for all three downstream effectors of mTORC1 signaling, which ranged from intensively positive subpopulation of cells within tumor nodules to a more uniform staining of the entire foci (Figure 33). Rapamycin treatment completely abolished the presence of any of these downstream markers of mTORC1 in any of the remnant foci observed after 5 weeks of treatment (Figure 33). This shows that Rapamycin successfully decreased mTORC1 activation and hence may have decreased HB burden by affecting protein synthesis and ribosomal biogenesis, thus affecting tumor cell proliferation.

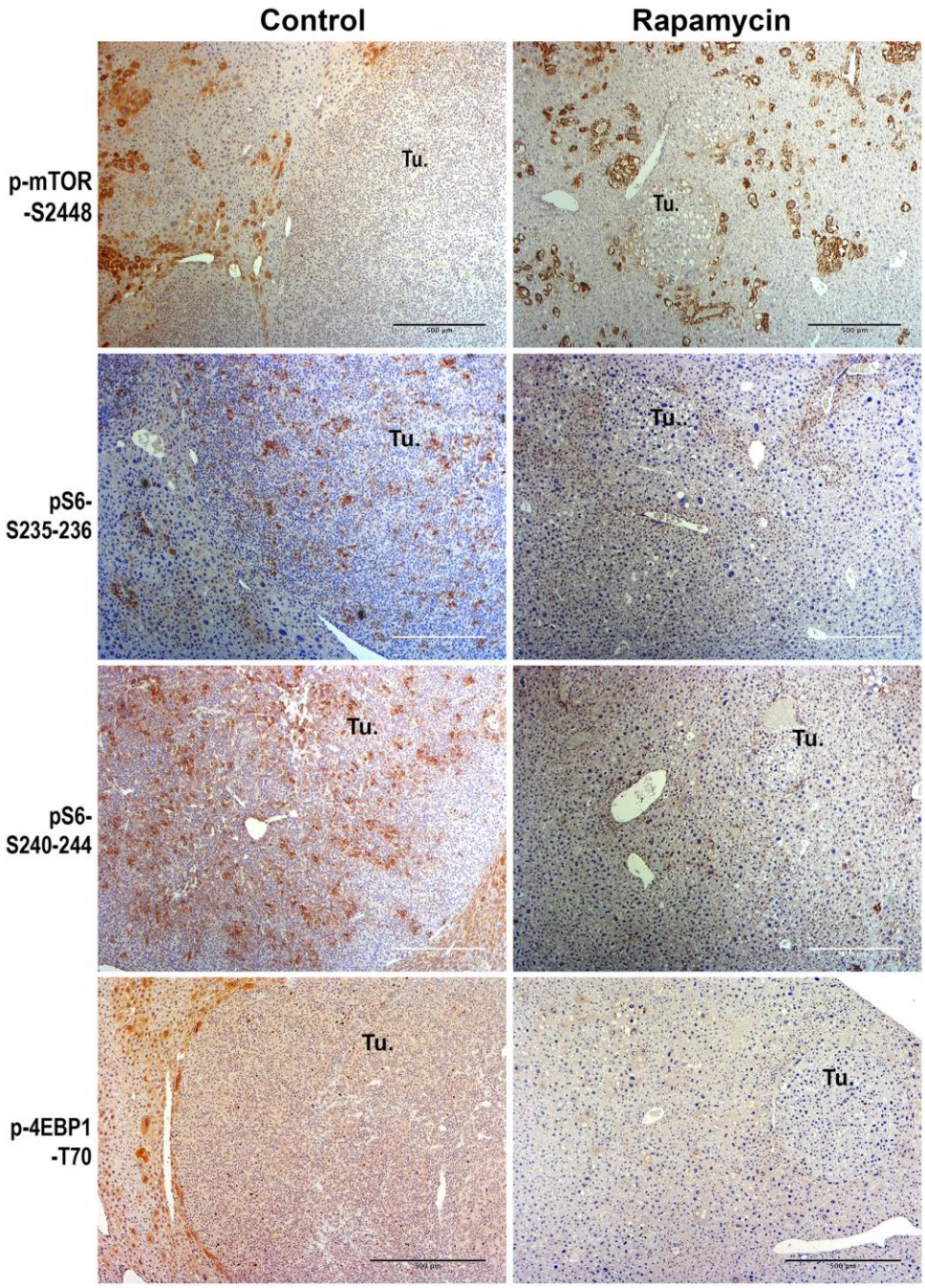

Figure 33. Immunohistochemical analysis of mTORC1 signaling in HB tumors treated with Rapamycin vs no treatment.

Representative immunohistochemistry images (50x) assessing mTORC1 signaling in HB in the control versus Rapamycin treatment group. Both groups were negative for p-mTOR-S2448. HB tumors were positive for p-S6 ribosomal protein (pS6)-S235-236, pS6-S240-244, and p-4EBP1-T70 in the control group but Rapamycin-treated remnant tumors were negative for all these markers. (Tu.- Tumor foci; Scale bar: 500 μm)

4.5 Discussion

In this study, we show that our murine model of HB using SB-HTVI delivery of mutant YAP1 and β-catenin shows a strong correlation in gene expression patterns with two independent patient HB cohorts, and also shows an enrichment in genes associated with less well-differentiated, more proliferative HB. This genetic analysis matches the mixed histological features observed in control HB tumors, which range from embryonal to crowded fetal histology based on expression of specific molecular markers like Sox9 and Cyp2e1 [162, 240]. Importantly our data supports the clinical relevance of our mouse model as a tool to study HB pathogenesis, particularly among more aggressive tumors that may be more difficult to treat [152, 162, 259].

We also show that Rapamycin treatment reduced HB and overall tumor burden in the YAP1-β-catenin model by dramatically affecting their growth, supporting its relevance for HB clinical therapy. This study validates the activation of mTORC1 in HB as was reported recently [84]. Liu and colleagues showed that mTORC1 is activated in HB cell lines and in the HB occurring in the YAP1-β-catenin model. They demonstrated that an mTOR inhibitor MLN0128 significantly inhibited human HB cell growth *in vitro*. The *in vivo* relevance of the mTOR signaling pathway was shown by disruption of Raptor, a positive regulator and component of the mTORC1 complex, which resulted in delayed YAP1-β-catenin-induced HB development in mice. Our study used a clinically relevant therapeutic agent to inhibit mTOR signaling in the YAP1-β-catenin HB model and showed directly its efficacy to notably reduce the HB burden following 5 weeks of treatment, which was well tolerated by the mice.

The mechanism of mTORC1 activation in HB development may be multifactorial. Liu and colleagues showed increased expression of an amino acid transporter SLC38A1 in HB, and

amino acid deprivation led to mTORC1 suppression in HB cell lines.[84] Silencing of YAP1 or its paralog, the transcriptional co-activator with PDZ binding motif (TAZ), decreased SLC38A1 expression as well as mTORC1 activation in HB cells [84]. In this study, in the YAP1-β-catenin model specifically, YAP1 was shown to upregulate expression of the glutamine transporter SLC38A1, contributing to mTORC1 activation by altering glutamine levels. YAP1 has also been shown to activate mTOR signaling by downregulating PTEN, a negative regulator of mTOR [167]. Our lab has also identified that β-catenin, through its regulation of GS expression, can regulate intracellular glutamine levels and in turn induce mTORC1 activation.[165] Although established tumors in the YAP1-β-catenin HB tumor model are GS-negative, earliest nodules in this model are GS-positive and hence mTORC1 activation may be contributed to by the presence of GS during early stages of tumorigenesis. Nevertheless, mTORC1 activation seems to be critical in HB sustenance and growth, downstream of YAP1 and β-catenin.

Multiple mTOR inhibitors are currently approved for clinical use as immunosuppressants and have proven effective for certain solid tumors. Although most solid tumors have been shown to be sensitive to mTOR inhibition in vitro or in preclinical models, the clinical utility of mTOR inhibition has proven limited due to the complexity of mTOR signaling and the development of resistance [261, 262]. Rapamycin and its analogs are mostly cytostatic, significantly decreasing proliferation but not promoting tumor cell death, and as such they have shown more promise in combination with cytotoxic chemotherapies [261]. We have observed similar effects in our study, as mice 10 weeks post-HTVI treated with 5 weeks of Rapamycin diet show a similar tumor burden histologically as mice 5 weeks post-HTVI, which corresponds to the time point when Rapamycin treatment was begun. Our results show that Rapamycin had a powerful effect in slowing down HB tumor growth and significantly reducing cell proliferation, which could prove useful to

potentiate the effects of other chemotherapies. Notably, most of the Rapamycin-resistant HB tumors which persist in treated mice display a more well-differentiated HB-like histology. Indeed, these tumors were negative for Sox9 and positive for Cyp2e1. Two possibilities can explain the presence of remnant disease. One is that by slowing tumor proliferation by altering cell metabolism, Rapamycin promoted differentiation of embryonal or crowded fetal HB to a more differentiated HB which are relatively indolent. The second possibility is that due to some pre-existing heterogeneity in subtypes of HB in the YAP1-β-catenin model, which displays predominantly crowded and embryonal and occasional fetal HB, Rapamycin abolishes growth and development of only embryonal and crowded fetal HB over time, whereas a more fetal HB subset persists during the course of treatment. The mechanism of differential response of more undifferentiated HB to mTORC1 suppression and more resistance of differentiated HB to Rapamycin remains under investigation.

Finally, our study also underscores the utility of US imaging for studies of liver cancer especially in the relevant animal models. While standard US imaging offers an overview of tumor burden, 3D-US provides more detailed and accurate measures of tumor burden that correlate well with the standard pathology measure of liver weight to body weight ratio. Monitoring tumor growth in the same mice over time not only reduces the number of animals needed for each experiment but also provides a better understanding of how treatments can alter the kinetics of tumor growth. Indeed, endpoint LW/BW measurements would have shown only a significant decrease in tumor burden between control and Rapamycin-treated groups. However, US data along with histological analysis demonstrated that tumors are not completely absent, but in fact small foci of a different histology in fact persist following Rapamycin in the YAP1-β-catenin HB model. One caveat remains the sensitivity of detection for very small tumors, which

is evident when performing US on mice at 5 weeks post-HTVI. At this time, the gross tumor burden appears to be negligible, but histopathology shows that the liver is littered with very small nodules below the threshold of US detection. Thus, US is best used in combination with histopathology and can offer an excellent view of tumor development once tumors have grown to greater than 0.5 mm in diameter, which is small enough to provide excellent detail in the mouse liver.

5.0 Hepatocyte-Derived Lipocalin 2 Is a Potential Serum Biomarker Reflecting Tumor Burden in Hepatoblastoma

In this work, Dr. Danielle Bell and I collaborated to identify novel targets upregulated in hepatoblastoma as a result of synergistic activity of YAP1 and β-catenin. Dr. Junyan Tao, Dr. Morgan Preziosi, Dr. Tirthadipa Pradhan-Sundd, Dr. Jianhua Luo, and Dr. Sarangarajan Ranganathan contributed to experimental design, data collection, and provided intellectual input. Sucha Singha and Minakshi Poddar provided invaluable technical support for data collection. Dr. Maria Chikina performed bioinformatic analysis. Dr. Satdarshan Monga was the principal investigator on the project, providing funding and intellectual direction at all stages.

This work was published in the *American Journal of Pathology* in 2018 (PMID: 29920228), and I was a co-first author on this manuscript along with Dr. Bell. The publisher, Elsevier, has granted full permission to reuse the manuscript in this dissertation.

This work was supported by NIH grants 1R01DK62277, 1R01DK100287, 1R01CA204586 and Endowed Chair for Experimental Pathology (S.P.M.) and in part by CATER T32 EB001026 to L.M.

5.1 Summary

Hepatoblastoma (HB) is the most common pediatric liver malignancy. Previously, we reported co-activation of β-catenin and YAP1 in 80% of HB. Hepatic co-expression of active β-catenin and YAP1 via sleeping beauty transposon/transposase and hydrodynamic tail vein

injection (SB-HTVI) led to HB development in mice. Here, we identify lipocalin 2 (LCN2) as a target of β-catenin and YAP1 in HB and show that serum LCN2 values positively correlated with tumor burden. LCN2 was strongly expressed in HB tumor cells in our mouse model. A tissue-array of 62 HB cases showed highest LCN2 expression in embryonal and lowest in fetal, blastemal and small cell undifferentiated forms of HB. Knockdown of LCN2 in HB cells had no effect on cell proliferation but reduced NF-κB reporter activity. Next, we generated liver-specific LCN2 knockout mice (LCN2 KO). We show no difference in tumor burden between LCN2 KO and wildtype littermate controls (WT) after SB-HTVI delivery of active YAP1 and β-catenin, although LCN2 KO mice with HB lacked any serum LCN2 elevation, demonstrating that transformed hepatocytes are the source of serum LCN2. We observed more blastemal areas and inflammation within HB in LCN2 KO compared to WT tumors. In conclusion, LCN2 expressed in hepatocytes appears to be dispensable for the pathogenesis of HB. However, transformed hepatocytes secrete serum LCN2, making LCN2 a valuable biomarker for HB.

5.2 Background

Hepatoblastoma (HB) is the most common pediatric liver malignancy, comprising about 1% of all pediatric cancers and accounting for 80% of pediatric liver cancer[263, 264]. Twenty percent of children will present with lung metastasis at diagnosis, and for this subset of patients, the prognosis is poor[158, 265, 266]. Treatment is dependent on staging, which is derived from a combination of radiographic and histological findings. While well-differentiated fetal HB can be cured with resection alone, less differentiated histology, such as embryonal or crowded fetal, require more aggressive treatment with cytotoxic chemotherapy followed by surgical resection,

or liver transplantation[158]. HB is unique in that multiple different histological subtypes can exist within a single tumor[267]. These histologic differences may be due to mutations occurring at various stages of hepatoblast development[268]. The most well-known mutations in HB are in *CTNNB1* (β-catenin gene) and are seen in around 90% of human HB[241, 269-271]. Recently, overactivation of Yes-associated protein-1 (YAP1) has also been found in a majority of HB. In fact, co-activation of β-catenin and YAP1 was reported in 80% of human HB[272]. It is presumed that β-catenin and YAP1 activation results in nuclear translocation and binding to transcription factors TCF4 and TEAD, respectively, to initiate cell proliferation, growth, and differentiation[273-275].

Previously we developed a murine model of HB using sleeping beauty transposon/transposase and hydrodynamic tail vein injection (SB-HTVI) to overexpress constitutively active forms of β-catenin (N90-β-catenin) and YAP1 (YAPS127A) in hepatocytes[276]. Co-expression of these two proto-oncogenes but not singly led to HB development in YAP1-β-catenin mouse model with 100% penetrance[272, 276]. This finding suggests that an oncogenic promoter downstream of β-catenin and YAP1 may be involved in HB development. In the current study, we identify Lipocalin 2 (LCN2) as one gene regulated by both β-catenin and YAP1 and upregulated in HB in mice and patients.

LCN2, also known as neutrophil-gelatinase-associated lipocalin (NGAL), is a small protein that has been implicated in a variety of human cancers, including breast, pancreatic, gastric, colon, ovarian and hepatocellular carcinomas (HCC)[277-280]. It was first discovered less than a decade ago as a component of the innate immune system, present in neutrophils and other inflammatory cells as well as the epithelial lining of the respiratory and gastrointestinal tracts. LCN2 participates in iron metabolism by binding siderophores and moving iron intracellularly

and can deprive bacteria of iron, causing decreased bacterial growth[281]. It is also a secretory protein present in both serum and urine of humans and animals, and has been studied as a potential biomarker for acute kidney injury[282-284]. The role of LCN2 in cancer has recently been under close scrutiny. LCN2 is overexpressed in breast cancer and even more so in metastatic disease, directly correlating with worse patient outcomes[285-287]. Conversely, overexpression of LCN2 in pancreatic cancer is associated with anti-tumorigenic effect[288, 289]. The mechanisms by which LCN2 may be involved in oncogenesis have yet to be determined. LCN2 can bind to matrix metalloprotease 9 (MMP9) and stabilize it to aid in tumor invasion and metastasis[278, 286]. LCN2 induction may trigger inflammation within the tumor environment via the NF-κB pathway[290-292]. LCN2 may also regulate iron dependent pathways that are essential for cancer growth[293]. Increasingly, LCN2 has been identified as a non-specific biomarker of inflammation and organ injury that could be useful in disease monitoring, or even predictive of prognosis[280].

While LCN2 has been found to be overexpressed in HCC, it has not been studied in HB and not known to be associated with either β-catenin or YAP1 signaling. Based on our analysis depicting marked upregulation of LCN2 in the mouse model of HB, we hypothesized LCN2 to be overexpressed in murine and human HB samples. We also sought to determine if LCN2 was contributing to β-catenin-YAP1-induced HB. Our results show that LCN2 expression in human HB tumors correlates with tumor differentiation, with increased expression in less differentiated tumors. We also show LCN2 to be secreted from hepatocytes in murine HB, and serum LCN2 correlates strongly with tumor burden. While knocking out LCN2 from hepatocytes in mice did not affect HB initiation or progression, it did effect overall tumor inflammation and led to areas of distinct histology. Our work offers strong support for the applicability of serum LCN2 as a biomarker for HB burden and histology.

5.3 Materials And Methods

5.3.1 Microarray, genome wide scan and identification of commonly upregulated genes.

Macroscopic tumor nodules <7 weeks after YAP1-β-catenin injection (n=3/mouse; 3 mice) and normal livers from non-injected mice (n=3) were utilized for mRNA isolation and subjected to Affymetrix gene array using chip R430 2.0. The full data set is available at Gene Expression Omnibus (http://www.ncbi.nlm.nih.gov/geo, accession number GSE112485). Microarray data was normalized using the expresso function from the "affy" Bioconductor package[247]. Probes were mapped to genes using the custom brain array CDF[248]. Differential expression was determined using the "limma" Bioconductor package, with robust linear models[255]. We compiled a list of genes that were significantly (q.value <0.1) up-regulated (at least 1.5-fold) in tumor samples relative to control livers. Genome-wide scan for TCF4-TEAD target genes was performed to identify genes containing both TEAD and TCF4 binding sites in their promoters. Potential TCF4 targets were taken from a combination of genome-wide TCF4 ChIP experiments as compiled by the CHEA database[294]. Since the CHEA database does not contain any data for TEAD, potential TEAD targets were extracted from a genome wide scan of TEAD consensus sites as provided by Homer "Known Motifs" genome track[295]. We considered genes that had a TEAD consensus site within 2000 upstream-500 downstream of the TSS. Using the above 2 approaches, we found a significant overlap of genes (hypergeometric p-value = 0.01) resulting in 5 top candidates, of which LCN2 was one and was chosen for additional, in-depth analysis.

5.3.2 *In vivo* studies.

All mouse studies were performed in accordance with NIH's Guide for the Care and Use of Laboratory Animals and under an approved animal protocol by the Institutional Animal Use and Care Committee at the University of Pittsburgh. LCN2-floxed mice were used with permission by Dr. Jack Cowland and generously supplied by Dr. Grace Gao from Rutgers University, New Brunswick, NJ. LCN2-floxed mice were crossed with Albumin-Cre mice to generate liver-specific LCN2 knockout or LCN2 KO mice. LCN2 KO or wildtype littermate controls (WT) were injected with plasmids for both N90-β-catenin, and YAP S127A at 7-8 weeks of age using the concentrations and HTVI described in our original publication[276]. At 6-7-weeks post injection, the mice were sacrificed. Serum and livers were harvested from all animals and stored at -80°. Liver sections were placed in 10% formalin for 48 hours and then transferred to 70% ethanol. Sections were processed and embedded into paraffin blocks.

5.3.3 Protein extraction and Western blotting.

After transfection, the cell media was aspirated, RIPA buffer containing Protease Inhibitor Cocktail (Thermo Scientific) was added to each well. HepG2 cells were lysed in RIPA buffer and three wells of each sample were pooled for optimal protein concentration, which was determined by bicinchoninic acid assay (Thermo Fisher). Aliquots of 40μg were denatured by boiling for 9 minutes in 2x Laemmli Sample Buffer (Bio-Rad, Hercules, CA, USA), and loaded in pre-cast 4-15% gradient gels (Bio-Rad) for electrophoresis. Protein was transferred onto a nitrocellulose membrane via a semi-dry transfer method using the Trans-Blot Turbo transfer system (Bio-Rad). Membranes were blocked in 5% non-fat dry milk in blotto (Tris-buffered

saline containing 0.1% Tween 20) overnight at 4°C. The primary antibodies used were: rabbit monoclonal anti-LCN2 (Abcam, ab125075, Cambridge, MA, 1:1000), rabbit monoclonal anti-Yap (Abcam, ab52771 1:1000), mouse monoclonal anti-β-catenin (BD Biosciences, San Jose, CA; 1:1000), rabbit polyclonal anti-p65 (1:200, Santa Cruz Biotechnology, Dallas, TX), rabbit polyclonal phosphor-Ser536-p65 (1:1000, Cell Signaling, Danvers, MA) and mouse monoclonal anti-GAPDH (Sigma-Aldrich, St. Louis, MO; 1:1000). Each primary antibody was incubated overnight at 4°C, except anti-GAPDH, which was added for 2 hours at room temperature. Membranes were washed with blotto and incubated with either rabbit (1:15,000) or mouse (1:50,000) horseradish peroxidase-secondary antibody for 2 hours. Bands were visualized by Super Signal West Femto kit (Thermo Fisher).

5.3.4 RNA extraction and Real-Time Polymerase Chain Reaction.

We used frozen livers from our previously published Yap-β-catenin model[276]. RNA was extracted with Trizol (Ambion, Carlsbad, CA). A DNAse kit (Ambion, Carlsbad, CA) was used to remove contaminating genomic DNA and cDNA synthesis kit (Invitrogen) was used for reverse transcription. Real Time Polymerase Chain Reaction (RT-PCR) was performed on cDNA using SybrGreen. Primers were purchased from Integrated DNA Technologies. Mouse-specific LCN2 primers used were: 5'-TTTCACCCGCTTTGCCAACT-3', 5'-GTCTCTGCGCATCCCAFTCA-3'. Additional primers used include: iNOS- 5'-TCACGCTTGGGTCTTGTTCA-3' and 5'-GGGGAGCCATTTTGGTGACT-3'; MYC- 5'-CCTAGTGCTGCATGAGGAGA-3' and 5'-TCCACAGACACCACATCAATTT-3'; IL-6- 5'-ATCAGGAAATTTGCCTATTGAAA-3' and 5'-CCAGGTAGCTATGGTACTCCAGA-3';

IFNγ- 5’-ATCTGGAGGAACTGGCAAAA-3’ and 5’-TTCAAGACTTCAAAGAGTCTGAGGTA-3’; IL-1B- 5’-AGTTGACGGACCCCAAAAG-3’ and 5’-AGCTGGATGCTCTCATCAGG-3’. Mouse-specific GAPDH primers used were: 5’-AACTTTGGCATTGTGGAAGG-3’ and 5’-ACACATTGGGGGTAGGAACA-3’.

5.3.5 Serum ELISA analysis.

Blood from all mice was collected at time of sacrifice. Serum was then used for ELISA for LCN2 using the Mouse Lipocal-2/NGAL Quantikine ELISA kit (R&D Systems catalogue# MLCN20). Assays were performed as per manufacturer’s instructions.

5.3.6 Immunohistochemistry

All patient sample analysis was performed under an exempt protocol by the Institutional Review Board at the Children’s Hospital, Pittsburgh. A tissue array of 69 de-identified HB cases collected from the Children’s Hospital, Pittsburgh was assessed for LCN2 expression using immunohistochemistry. Slides were deparaffinized by passing through xylene, graded alcohol and deionized water[276]. Slides were rinsed with PBS, immersed in citrate buffer at a pH of 6.0 and microwaved at 60% power. Three percent hydrogen peroxide was applied for 10 minutes, and slides were rinsed with PBS. Samples were blocked for 30 minutes using Superblock (ScyTek Laboratories Inc) and incubated with LCN2 antibody (Sigma HPA002695, 1:100) at room temperature for 60 minutes. Slides were rinsed and incubated with biotin-conjugated secondary rabbit antibody (Chemicon, Temecula, CA) for 30 minutes. Signal was detected using Vectastain ABC Elite kit (Vector Laboratories, Inc., Burlingame, CA) and developed with DAB

(Vector Laboratories). All slides were then counterstained with Shandon hematoxylin solution (ThermoFisher, Pittsburgh, PA). Slides were dehydrated using graded alcohol (95%, 100%) and xylene before being cover-slipped.

The tissue-array was reviewed by a pediatric pathologist and signal positivity determined using a 0-3 grading scale, with zero indicating no expression, and 3 being highest expression. Samples of normal liver included on the same tissue-array were used as baseline controls. The histological subgroup of each sample was determined by cell morphology and arrangement. LCN2 cytoplasmic and nuclear immunoreactivity was recorded for each histological component of each sample.

The same immunohistochemistry protocol was used to analyze the expression of several markers in paraffin-embedded mouse liver samples. The following antibodies were used: Myc-tag (Cell Signaling, CS2276S, 1:1000, Danvers, MA), PCNA (Santa Cruz Biotechnology, sc-56, 1:4000, Santa Cruz, CA), Cyclin-D1 (Abcam, ab134175, 1:200, Cambridge, MA), glutamine synthetase (Sigma, G2781, 1:4000, St. Louis, MO), CD45 (Santa Cruz Biotechnology, sc-53665, 1:100, Santa Cruz, CA), F4/80 (Serotech, MCA497GA, 1:100, Hercules, CA), neutrophil elastase (Abcam, ab68672, 1:1500, Cambridge, MA).

5.3.7 Cell culture, transfection, and *in vitro* assays.

HepG2 cells, a human HB cell line with a known 116-amino acid deletion in β-catenin, were grown in Eagle's Minimum Essential Media, supplemented with 10% fetal bovine serum. 50% confluent HepG2 cells plated in 6-well plates (200,000 cells/well) were transfected with small interfering RNA (siRNA) against LCN2 (Ambion, Catalogue # AM51331, ID #121013), β-catenin (Cell Signaling Technology, # 6225s) Yap1 (Ambion, Catalogue #4392420, ID #

s20368) or scrambled RNA (Ambion catalogue # AM4611) using INTERFERin siRNA Transfection Reagent (Polyplus Transfection, Catalogue # 409-10, France) as recommended by the manufacturer and incubated for 72 hours. All knock-downs were done in triplicate.

A tritium-labeled thymidine incorporation assay was performed on transfected HepG2 cells. 200,000 cells/well in 6-well plates in triplicate were transfected with si-RNA against LCN2 or scrambled control. 24 hours later, 1ml/well of EMEM containing 2.5 μCi ^{3}H-thymidine (Perkin Elmer) was added to the plate. After 24 or 48 hours, cells were washed with cold 5% trichloroacetic acid, washed with cold running tap water, and dried. 1mL of 0.33M NaOH was added next for 30 minutes. 300μL of cell solution was added to scintillation vial. mixed with 3ml of Universal Scintillation Fluid (Perkin Elmer), placed in dark for 30 minutes and radioactivity measured with a scintillation counter.

To assess p65 transcriptional regulatory activity, HepG2 cells were seeded in 6-well plates and transiently transfected with plasmids or siRNA combined with reporters. Validated LCN2 siRNA or negative control siRNA (Ambion, Inc., Austin, TX) was used at a final concentration of 25nM in the presence of Lipofectamine 3000 reagent (Invitrogen, Carlsbad, CA), as per the manufacturer's instructions. Simultaneously, 0.4μg of p65 luciferase reporter plasmid (provided by Dr. Kari Nejak-Bowen) was co-transfected with 0.1μg of *Renilla* plasmid, also in the presence of Lipofectamine 3000[296]. Cells were harvested 48 hours after transfection for protein extraction and luciferase assay. Luciferase assay was performed using Dual Luciferase Assay System kit (Promega, Madison, WI). Relative luciferase activity (in arbitrary units) was reported as fold-induction after normalization for transfection efficiency. All studies were done in triplicate.

5.4 Results

5.4.1 Genome-wide scan for TCF4-TEAD target genes and mouse HB analysis reveals LCN2 as a candidate target of YAP1 and β-catenin in this tumor type.

In a previous study, SB-HTVI was used to co-express constitutively active β-catenin (ΔN90β-catenin) and YAP1 (YAPS127A) in mouse liver to generate the YAP1-β-catenin model, which resulted in rapid development of HB in these mice[276]. Since both proto-oncogenes regulate target gene expression via binding to their respective transcription factors, we were interested in identifying candidate targets commonly regulated by the two pathways, which may have a role in HB pathogenesis. We first performed *in silico* analysis to identify such genes. Potential TCF4 targets were taken from a combination of genome-wide TCF4 ChIP experiments as compiled by the CHEA database[294]. We identified 3045 genes as TCF4 targets (Figure 34A). Since the CHEA database does not contain any data for TEAD, potential TEAD targets were extracted from a genome wide scan of TEAD consensus sites; 2422 genes were identified as potential TEAD targets (Figure 34A)[295]. Next, we used tumor-bearing livers from the YAP1-β-catenin and age-matched wild-type FVB livers for mRNA isolation and Affymetrix genearray using chip R430 2.0 as described in methods. We identified 59 genes that were upregulated more than 1.5-fold in expression in YAP1-β-catenin livers as compared to the controls (Figure 34A).

Then, we combined information obtained from the above approaches to identify overlap between genes having β-catenin-TCF and YAP1-TEAD binding in their promoter regions and were also upregulated in the YAP1-β-catenin model. We found a significant overlap of genes

(hypergeometric p-value = 0.01) resulting in 5 top candidates (Figure 33A). One of these genes was lipocalin 2 (*Lcn2*).

To verify that *Lcn2* was indeed over-expressed in the YAP1-β-catenin model, three additional tumor-bearing livers and three WT livers were used for mRNA isolation for RT-PCR analysis. A significant upregulation (~600-fold) in *Lcn2* expression was observed in HB-bearing livers in the YAP1-β-catenin mice (Figure 34B).

Since LCN2 is a secreted protein, we next queried its levels in the serum of control and YAP1-β-catenin mice. Control FVB mice showed around 100ng/ml of LCN2 in serum (Figure 34C). Serum from YAP1-β-catenin mice collected at time of sacrifice over a period of 5-10-weeks post-injection showed a dramatic increase with progressive tumorigenesis with some animals showing around 5000ng/ml of LCN2 (Figure 34C). Since YAP1-β-catenin mice had significantly increased liver weight to body weight (LW/BW) ratios representing increased tumor burden, we next asked if serum LCN2 levels in these mice correlated with tumor burden. Indeed, serum LCN2 values were directly proportional to the LW/BW ratio of the animals with a coefficient of determination (R^2) of 0.82 (Figure 34C). Thus, our results demonstrate a strong correlation between serum LCN2 levels and tumor burden in our mouse model of HB.

5.4.2 YAP1 and β-catenin regulate expression of LCN2 in HB cells.

To further confirm that LCN2 expression is regulated by both β-catenin and YAP1, we analyzed changes in LCN2 protein levels after siRNA-mediated knockdown of either β-catenin or YAP1 in the human HepG2 HB cell line as shown in the schematic (Figure 34D). Western blot analysis utilizing HepG2 cells transfected with control, YAP1 or β-catenin siRNA showed

that knockdown of either β-catenin or YAP1 independently caused a notable decrease in total LCN2 levels (Figure 34E). Interestingly, a more pronounced effect of β-catenin suppression than YAP1 suppression was evident on LCN2 levels. To address if LCN2 silencing in HepG2 cells would have any impact on either YAP1 or β-catenin levels, we also transfected these cells with siRNA against LCN2 (Figure 34E). While LCN2 suppression was evident, its knockdown did not affect the levels of β-catenin or YAP1 in the HepG2 cells (Figure 34E). Thus, β-catenin and YAP1 both regulate LCN2 expression in the HB cells.

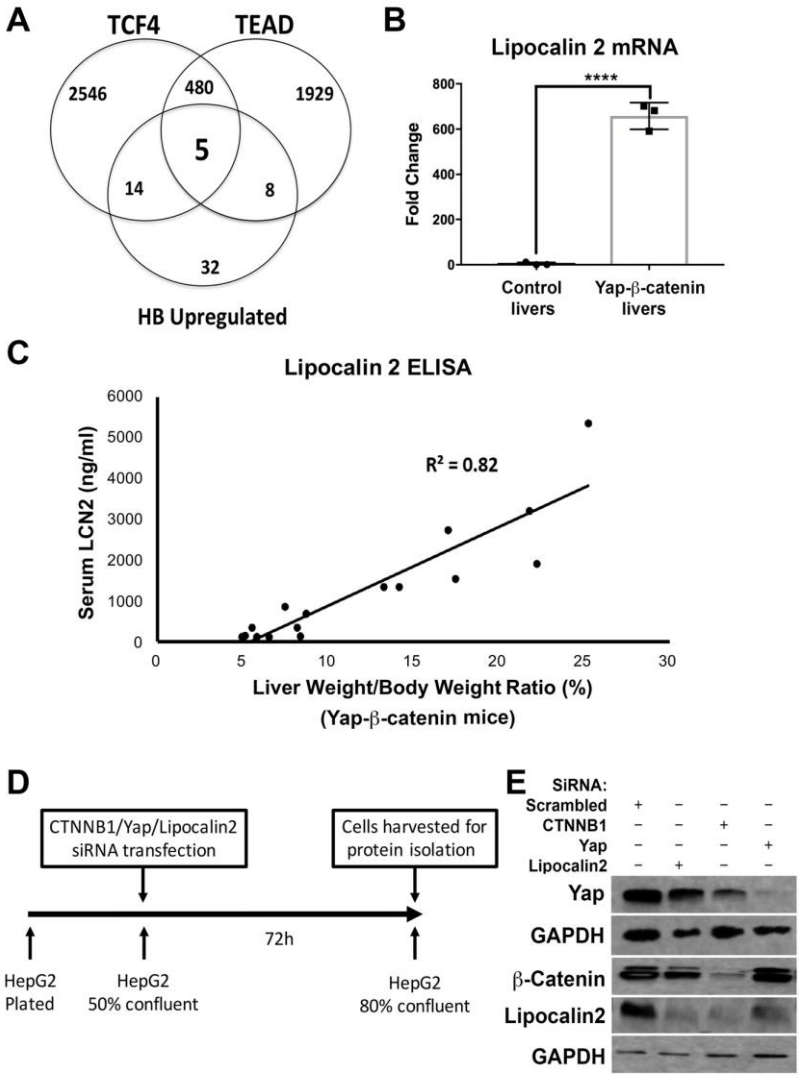

Figure 34. Lipocalin2 expression and protein levels are regulated by YAP1 and β-catenin in HB.

Figure 34. A. Venn diagram of upregulated genes in a mouse genome analysis illustrating that 5 gene loci containing binding sites for both TCF4 and TEAD also had upregulated expression in murine HB. B. RT-PCR of liver lysates from control mouse livers and β-catenin-YAP1 induced HB tumor-laden livers, showing significantly increased expression of LCN2 (Student's t test, ****p < 0.0001). C. Serum ELISA for LCN2 was performed on mice with HB tumors and varying degrees of tumor burden, approximated by liver weight to body weight ratio (%), showing a positive and significant correlation between serum LCN2 level and disease burden in mice (R2=0.82). D. Schematic representation of the timeline for HepG2 cell transfection with silencing RNA targeting β-catenin, YAP1, LCN2 or scrambled siRNA. E. Western blot shows decreased levels

of LCN2 after transfection of HepG2 cells with siRNA to LCN2, β-catenin or YAP1. Efficacy of each of the siRNA is shown by decrease in their respective protein levels. GAPDH was used as loading control.

5.4.3 LCN2 is aberrantly expressed in HB in patients and correlates with tumor histology.

Since ~80% of HB show concomitant nuclear β-catenin and YAP1, as we previously reported[276], and LCN2 is regulated by both of these oncoproteins, we next performed immunohistochemistry for LCN2 on a tissue-array of HB samples collected from Children's Hospital of Pittsburgh. Of the 69 patient samples that were stained for LCN2, 7 were excluded due to loss of tissue during the staining process, leaving 62 patient samples for analysis. Each sample was classified as having one or more of the 8 different histological components by an experienced pediatric pathologist based on the classification parameters described in proceedings from the Children's Oncology Group International Pathology Symposium in 2014[297]. In fact, within our tissue-array, 69% of tumors exhibited more than 1 histological subtype and some tumor samples had up to 5 subtypes. We have included de-identified patient demographic information and the full list of histological classifications found in each patient's tumor in Appendix C, Table 7. To account for differences in LCN2 positivity based on histological classification, we quantified the expression of LCN2 in all histological subtypes independently identified within each tumor. Although the total number of patients was 69, the total number of distinct histological samples identified for analysis was 160, broken down into 43 (27%) embryonal, 53 (33%) crowded fetal, 20 (12.5%) fetal, 18 (11%) blastema, 11 (7%) small cell undifferentiated (SCU), 8 (5%) mesenchymal-epithelial transitional (EMT), 4 (2.5%) teratoid, and 3 (2%) giant cell (Figure 35A). Each sample was then graded based on the nuclear and cytoplasmic expression of LCN2 as observed by immunohistochemistry, ranging from absent

(0), mild (1), moderate (2) to strong (3). Within the tissue array, several samples of normal pediatric liver adjacent to tumor sections were used as a negative control (grade 0) as LCN2 is not expressed in epithelium in the normal liver tissue (Figure 35B). Within each sample, we used Kupffer cells, which are inflammatory cells that innately express LCN2, as a positive control (grade 3). In fact, in normal human liver, Kupffer cells did express LCN2 at baseline by immunohistochemistry (Figure 35B).

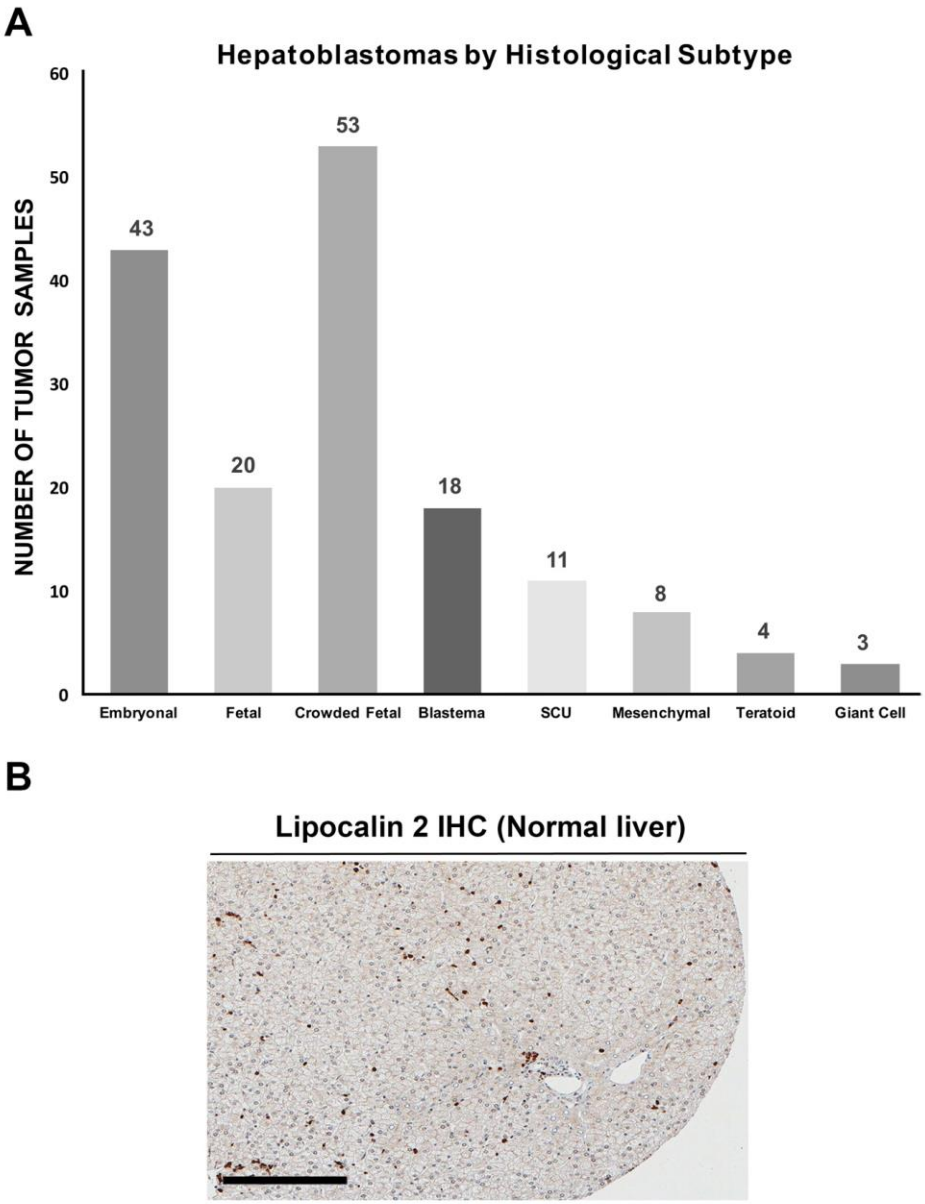

Figure 35. Distribution of HB tumor types within our patient cohort, and baseline IHC for LCN2 in normal liver control

A: Distribution of hepatoblastoma histologic subtypes in patients from the Children's Hospital of Pittsburgh assessed in the current study. B: Immunohistochemistry (IHC) of LCN2 in normal liver shows localization in only macrophages, whereas hepatocytes are completely absent for this marker. Scale bar = 100 µm. SCU, small cell undifferentiated.

Upon analysis of HB cases, all embryonal components of HB across various cases had either nuclear or cytoplasmic staining with typical intensity of 2-3 (Figure 36, 37A, 37B). Ninety-five percent of the crowded fetal tumor samples also showed positive staining for LCN2, but with a lower intensity of 1-2. In contrast, only 50% of the most differentiated, or fetal, HB were positive for LCN2, with absent nuclear LCN2 and a typical cytoplasmic stain intensity of 1-2 (Figure 36, 37A, 37B). Notably, all blastemal tumor samples, which have a stromal cell origin[297], were negative for LCN2. Similarly, small cell undifferentiated tumors, which show neither epithelial nor mesenchymal differentiation [297], had the second lowest expression levels of LCN2, with only 18% of samples staining positive for LCN2 (Figure 36, 37A, 37B). Interestingly, teratoid tumors, which are rare tumors that often contain heterologous cellular elements from multiple germ layers, showed 100% positive staining for LCN2 (Figure 36, 37A, 37B).

Our results demonstrate that LCN2 expression differs greatly based on the histological subtype of HB and correlates with the level of tumor cell differentiation. Figure 37A shows the proportion of tumors of each histological subtype that exhibited positive staining for LCN2. Figure 37B further breaks down the data to show the distribution of scores of LCN2 stain intensity, showing cytoplasmic expression in the outer circle and nuclear expression in the inner circle. Taken together, these results reveal a dramatic correlation between the expression of LCN2 and the tumor grade of HB with the highest LCN2 expression in embryonal and crowded fetal tumor samples as well as teratoid and giant cell tumors.

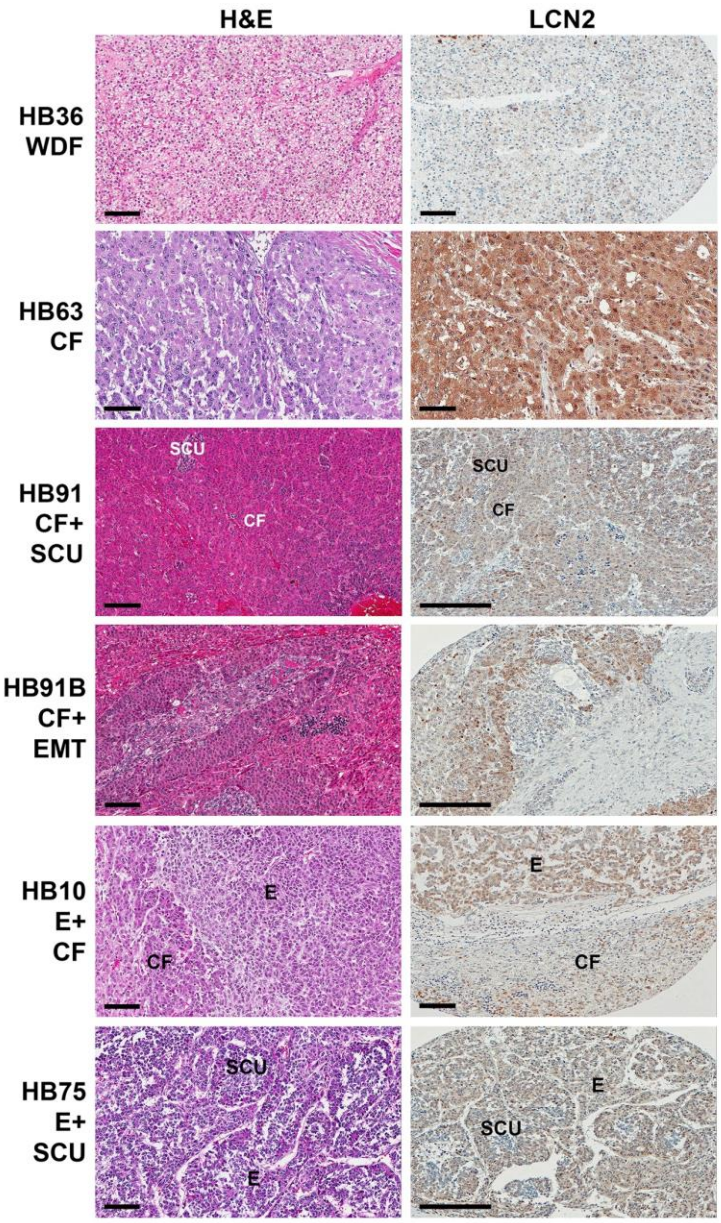

Figure 36. Immunohistochemical analysis of LCN2 expression in HB cases

Representative images from human HB samples with H&E staining (left) and LCN2 immunohistochemistry (right). Note that the intensity of staining is dependent on histologic subtype, which is exemplified in HB75, were SCU islands of hepatoblasts have no LCN2 expression, compared to the surrounding embryonal hepatoblasts which were positive for LCN2. LCN2 was negative in the well differentiated fetal histology of HB36 and the EMT subtype of HB91B. CF, crowded fetal, E, embryonal; EMT, mesenchymal-epithelial transitional; SCU, small-cell undifferentiated; WDF, well-differentiated fetal. Small scale bar represents 100μm and large scale bar represents 200μm.

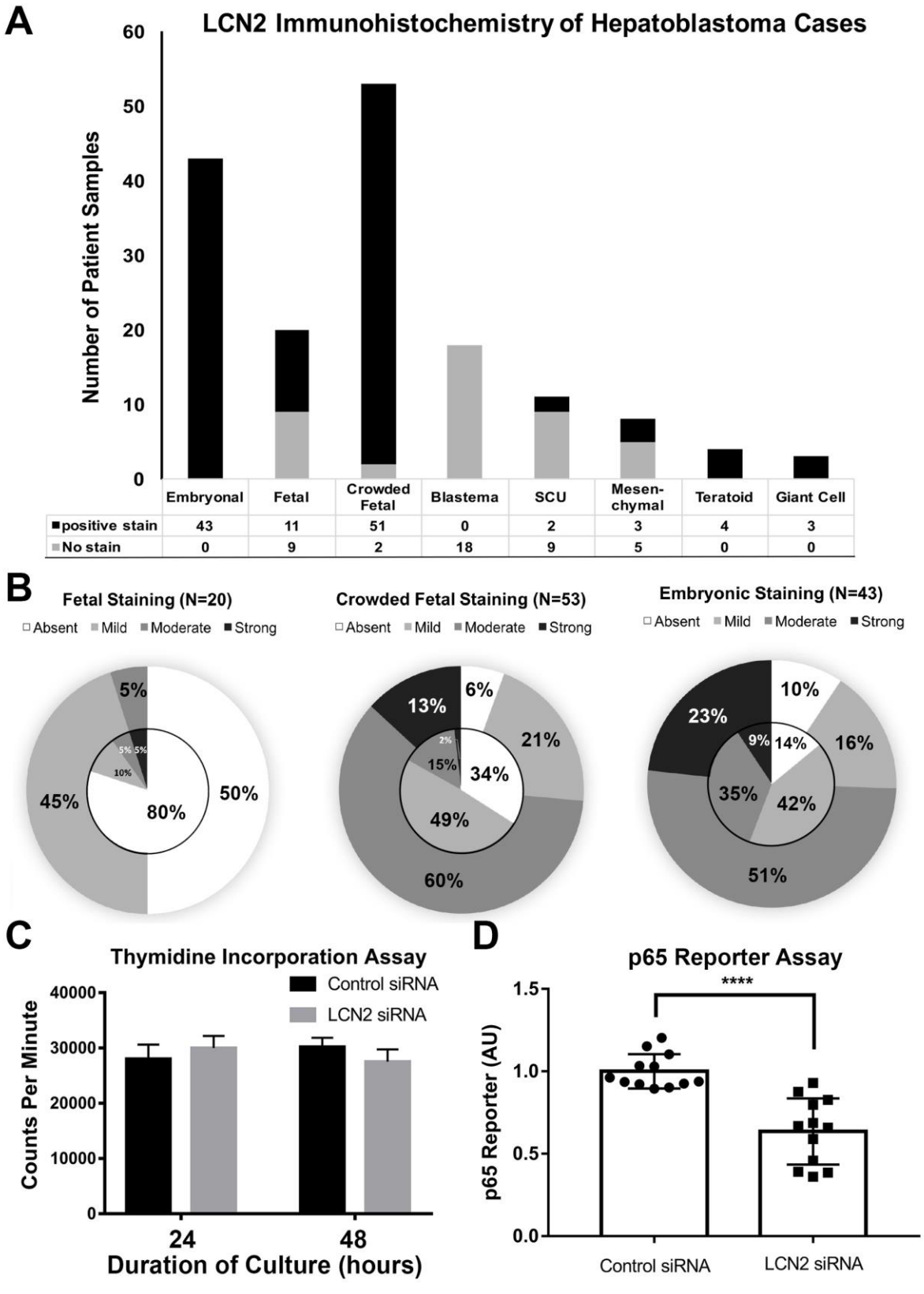

Figure 37. Expression of LCN2 in HB cases and its role in HB cells.

Figure 37. A. Graphical representation of tumor samples with positive staining (including grades 1-3) for each different histological subtype found in the collection of HB samples from Children's Hospital of Pittsburgh. B. Graphical distribution of nuclear LCN2 staining (inner circle) and cytoplasmic LCN2 staining (outer circle) among the three most common subtypes of HB, including absent (0), mild (1), moderate (2), and strong (3) staining intensity. Embryonal, which is the least differentiated, has the most nuclear staining, and the highest intensity of LCN2 expression. Fetal Histology is well differentiated, and has only 50% cytoplasmic staining, very little nuclear staining, and less intense LCN2 expression. Crowded fetal histology is less differentiated than fetal tumors, but more so than embryonal tumors, and it shows intermediate staining intensity. C. Thymidine incorporation assay was performed 24 to 48 hours after treatment of HepG2 cells with scrambled siRNA or siRNA targeting LCN2, showing no difference between the two groups. D. Results of a luciferase reporter assay to detect the transcriptional regulatory activity of p65 show a significance decrease in luciferase activity in HepG2 cells after 48-hour treatment with LCN2 siRNA as compared to scrambled siRNA (Student's t-test, ****p<0.0001).

5.4.4 Impact of LCN2 silencing on HepG2 cell proliferation and p65 reporter activity.

Since LCN2 was strongly expressed in tumor cells within HB, we next wanted to address its biological role. First, we silenced LCN2 in a HB cell line and queried its impact on cell proliferation using thymidine incorporation. Interestingly, at either 24- or 48-hours, no difference in thymidine incorporation was observed in HepG2 cells transfected with either control of LCN2-specific siRNA (Figure 37C). This suggests that LCN2 does not play a direct role in regulating HB cell proliferation.

We next sought to explore whether LCN2 had any effect on gene expression regulation in HepG2 cells, since we observed LCN2 to be present in the nucleus of tumor cells in patients. Studies have shown that LCN2 is involved in a regulatory feedback loop with NF-κB to control the level of inflammation in chronic injury [298]. We used a p65 luciferase reporter plasmid to

assess the activity of NF-κB. Treatment of HepG2 cells with siRNA targeting *Lcn2* mRNA led to a significant decrease in p65 luciferase reporter activity, suggesting that LCN2 may be inducing NF-κB activity in HB cells (Figure 37D).

Thus, LCN2 does not directly regulate cell proliferation. However, it does positively regulate NF-κB signaling in HB cells.

5.4.5 Liver-specific LCN2 conditional knockout mice lack any overt phenotype.

To more conclusively address the role of LCN2 in YAP1-β-catenin driven HB and examine its potential role as a secreted biomarker that represents tumor burden in this model, we generated a LCN2 liver-specific knockout (LCN2 KO) using *Lcn2*-floxed and Albumin-Cre transgenic mice as described in methods. These mice were verified as LCN2 KO by the presence of both the homozygous LCN2-floxed alleles, and Cre-recombinase in PCR analysis of genomic DNA (Figure 38A). For all studies, littermates with homozygous *Lcn2*-floxed alleles and absent Cre were used as controls and henceforth referred to as wild-type mice (WT). The LCN2 KO mice were born in normal Mendelian ratio and lacked any overt phenotype. Real-time PCR using RNA isolated from WT and LCN2 KO livers showed a significant decrease in *Lcn2* expression in the LCN2 KO although variable expression was observed in WT (Figure 38B). LW/BW ratio was comparable between the two groups (Figure 38C). Serum analysis showed no abnormalities in alanine aminotransferase (ALT), total bilirubin (BR) or alkaline phosphatase (ALP) (Figure 38D-F). H&E of liver sections was unremarkable for both LCN2 KO and WT (Figure 38G).

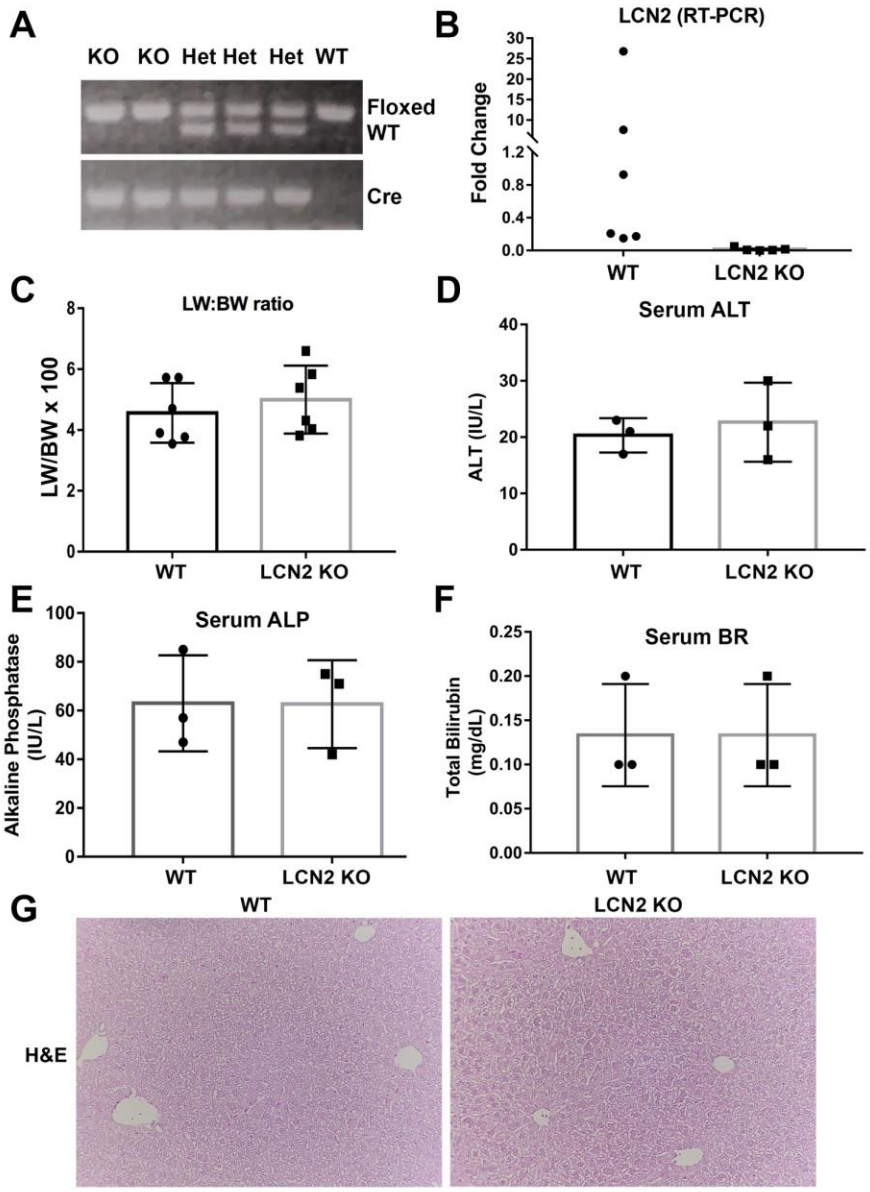

Figure 38. Generation and characterization of liver-specific LCN2 knockout mice.

A. Genotyping of mouse litter mates distinguishes between WT mice lacking Cre expression, mice heterozygous for the LCN2 floxed allele (Het), and LCN2 KO mice homozygous for the LCN2 floxed allele and positive for Cre expression (KO). B. RT-PCR for LCN2 confirms decreased LCN2 expression in LCN2 KO mouse livers as compared to WT livers. C. Liver weight to body weight ratios of control and liver-specific LCN2 KO mice at baseline. Liver function tests including serum alanine aminotransferase (D), alkaline phosphatase (E), and total serum bilirubin (F) show no difference between WT and LCN2 KO mice. G. Representative H&E of WT and LCN2 KO mice.

5.4.6 Co-expression of constitutively active YAP1 and β-catenin in LCN2-KO mice via SB-HTVI does not alter the growth and development of HB.

To address if LCN2 is playing a role in HB development in the YAP1-β-catenin model, we next co-expressed YAP1 and β-catenin via SB-HTVI in the LCN2 KO and WT mice. By 6-7-weeks post injection, both LCN2 KO and WT mice had large and grossly comparable tumors (Figure 39A). This was also reflected by the lack of any significant difference in the LW/BW ratio between the LCN2 KO and WT administered YAP1-β-catenin through SB-HTVI (Figure 39B). H&E of representative sections show tumors occurring in both LCN2 KO and controls after YAP1-β-catenin, which were reminiscent of crowded fetal or fetal HB as in the original YAP1-β-catenin model (Figure 39C). While no major differences were evident, there was evidence of more crowded fetal histology and more pronounced areas of blastemal cells within tumors in the LCN2 KO as compared to the WT (Figure 39C). To confirm that tumors in both groups were composed of cells expressing exogenous YAP1 and β-catenin, we stained the sections for Myc-tag, which represents exogenous β-catenin SB plasmid. As expected, the tumors were strongly positive for Myc-tag in both WT and KO mice (Figure 39D).

5.4.7 Serum LCN2 is derived from hepatocytes in YAP1-β-catenin HB murine model.

Since serum LCN2 correlated strongly with tumor burden in the YAP1-β-catenin HB model but tumor burden was comparable between YAP1-β-catenin injected LCN2 KO and WT mice, this gave us an opportunity to conclusively ask if the elevated serum LCN2 in this model was indeed being secreted by the transformed hepatocytes, especially since only inflammatory

cells are the known source of LCN2. ELISA for LCN2 was performed on serum from baseline LCN2 KO, littermate WT controls, YAP1-β-catenin injected tumor harboring LCN2 KO mice along with WT as well as YAP1-β-catenin historical controls with advanced HB. Serum LCN2 were very low in WT and LCN2 KO mice at baseline with insignificant differences (Figure 39E). The low levels of serum LCN2 (<200ng/ml) at baseline and absence of differences in serum LCN2 in WT versus LCN2 KO indicates that hepatocytes are not the source of basal serum LCN2. A marked and significant reduction in serum LCN2 levels was observed in LCN2 KO mice at 6-7 weeks (average=150ng/ml) after YAP1-β-catenin as compared to the time-matched, YAP1-β-catenin injected WT which showed around 700 ng/ml of LCN2 (Figure 39E). The highest levels of LCN2 (average=2500ng/ml) were observed in historical controls, which represent advanced stages of HB development and greatest tumor burden as reflected by >10% LW/BW (Figure 39E). The marked reduction in serum LCN2 in the LCN2 KO mice after YAP1-β-catenin injection clearly establishes that tumor cells in the HB are the source of serum LCN2 supporting its potential as a biomarker for HB disease burden.

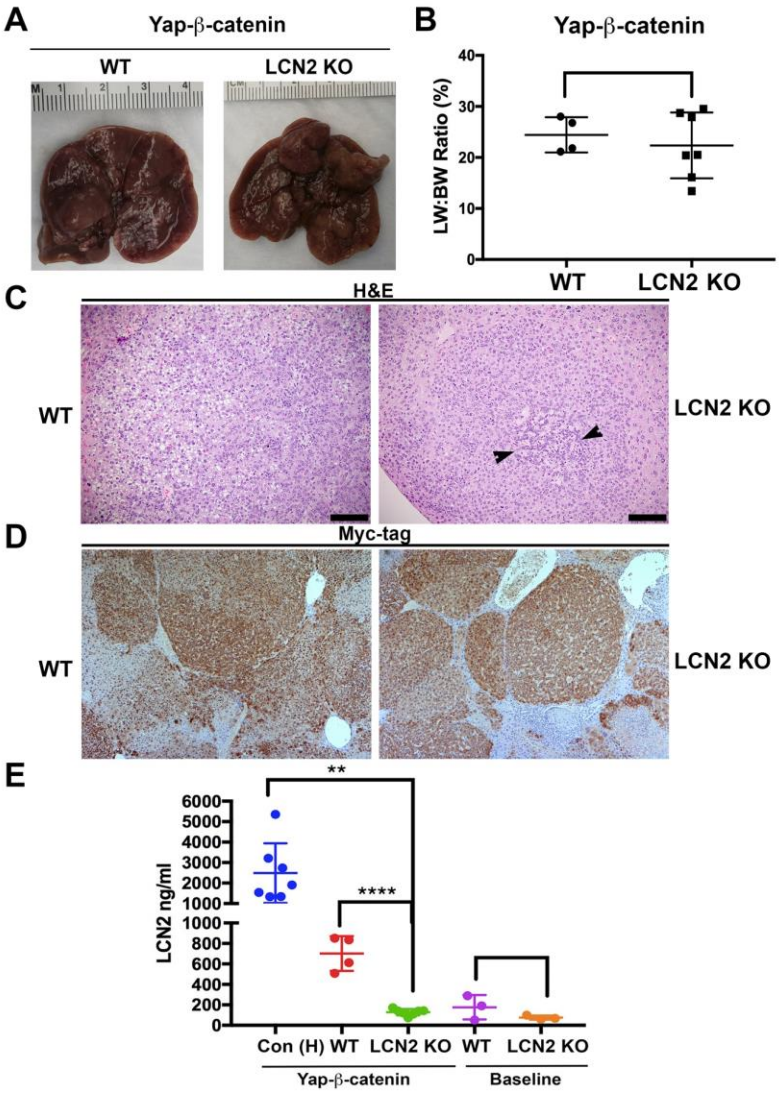

Figure 39. HB development in LCN2 KO versus WT after YAP1-β-catenin expression.

A. Representative gross images of WT and LCN2 KO livers 6-7 weeks after HB induction. B. Liver weight to body weight ratios of control and LCN2 KO mice at 6-7 weeks after induction of HB. C.Representative H&E of murine HB in control and LCN2 KO mice showing relatively more blastemal component (arrowhead). Scale bar, 100μm. D. Immunohistochemistry for Myc-Tag shows strongly positive tumor nodules in both WT and LCN2 KO mice treated with YAP1/β-catenin by SB-HTVI. E. Serum LCN2 levels detected by ELISA of control mice at baseline (C57BL/6J background; purple), LCN2 KO mice at baseline (orange), littermate WT mice 6-7 weeks after HB induction (liver weight to body weight ratios <10%; red) and historical controls or Con (H) after 8-10-weeks of SB-HTVI injection and liver weight to body weight ratios >10% (blue). (p<0.01; ****p<0.0001).**

5.4.8 Differences in histology, inflammation and p65 activity in YAP1-β-catenin HB model in LCN2 KO versus WT.

To further address the role of LCN2 in vivo in HB pathogenesis, we next assessed YAP1-β-catenin induced HB in LCN2 KO and WT for cell proliferation. No difference in between the two groups was observed as shown by immunohistochemistry for PCNA (Figure 40A). Likewise, tumors occurring in both groups were strongly positive for cyclin-D1 (Figure 40A). We next assessed the expression of the β-catenin target Glutamine synthetase (GS). Previously, we reported YAP1-β-catenin-induced HB to be GS-negative[276]. HB occurring in both LCN2 KO and WT continued to be GS-negative (Figure 40A).

Based on our *in vitro* evidence showing that knocking down LCN2 decreased p65 transcriptional activity, we next assessed if LCN2 may be modulating inflammatory response during HB development. We evaluated the presence of inflammation by performing immunohistochemistry for CD45, a pan-leukocyte marker. LCN2 KO tumors exhibited a modest increase in the overall numbers of CD45-positive cells as compared to WT tumors (Figure 40B). We also observed that both WT and LCN2 KO tumors showed increased presence of CD45-positive cells in areas of blastemal histology (Figure 40B), which were more profound and frequent in LCN2 KO.

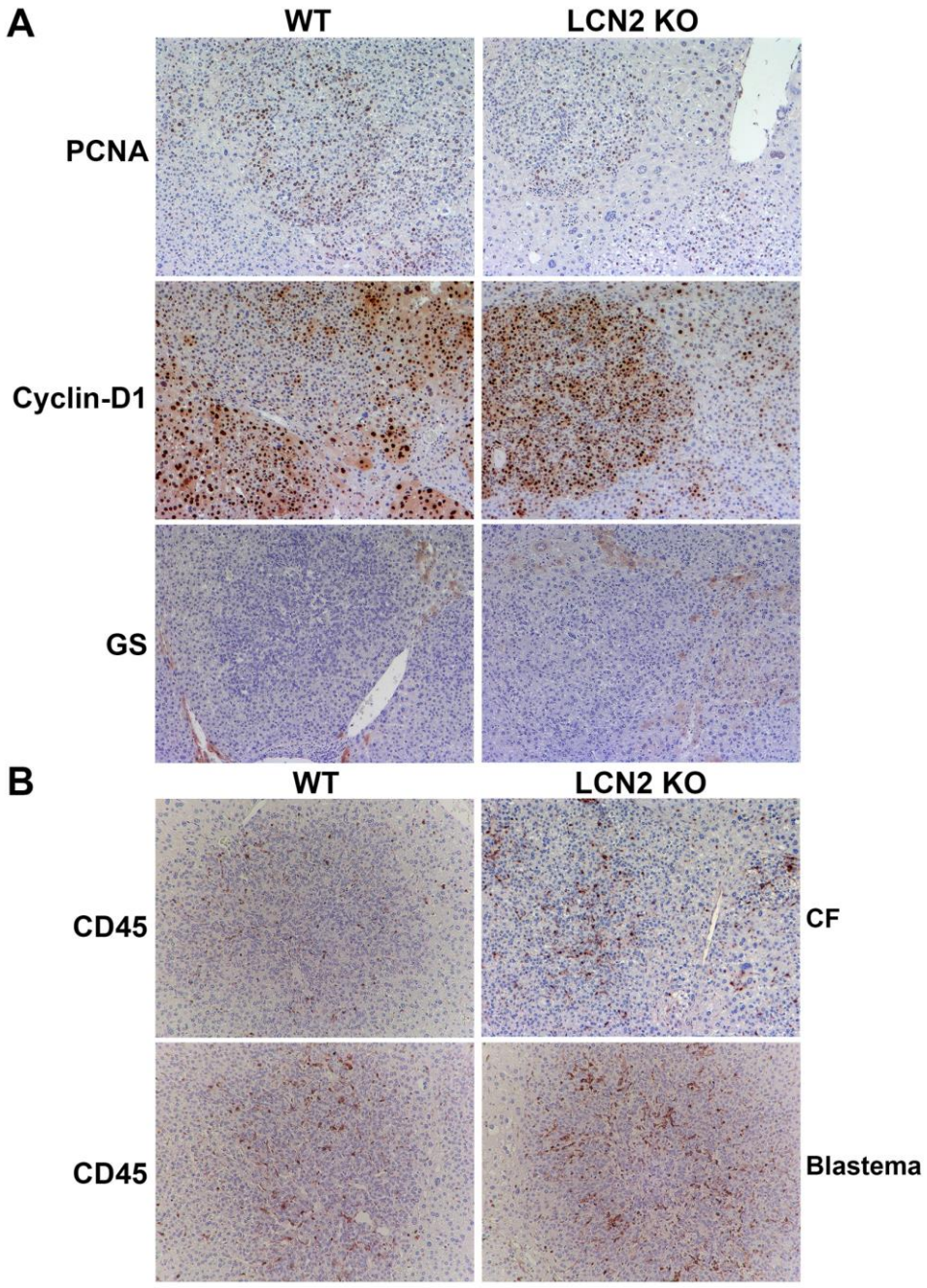

Figure 40. Differences in HB occurring in WT vs LCN2 KO mice after YAP1-β-catenin activation.

A. Representative immunohistochemistry for PCNA, Cyclin D1, and glutamine synthetase in WT and LCN2 KO livers 6-7 weeks after HB induction. B. Representative immunohistochemistry for CD45 in WT and LCN2 KO livers 6-7 weeks after HB induction showing modest increase in overall inflammation in LCN2 KO. Blastemal areas in both WT and LCN2 KO HB showed an increase in CD45-positive cells in these areas, but numbers were more pronounced in LCN2 KO.

We next performed immunohistochemistry for the macrophage marker F4/80 and the neutrophil marker neutrophil elastase to determine the distribution of innate immune cell types in the tumor microenvironment. Our results show that macrophages are abundant in the tumor microenvironment in both WT and LCN2 KO tumors (Figure 41A). A comparison of the abundance and distribution of F4/80 and CD45 staining suggests that macrophages comprise the majority of immune cells in our HB tumor model. Very few neutrophils were detected in both WT and LCN2 KO tumors, except in areas of necrosis within large tumors (Figure 41B and not shown). No notable differences were seen in the overall numbers of macrophages or neutrophils between the WT and LCN2 KO tumors despite marginal increase in overall CD45-positive cells in LCN2-KO. Likewise, variable expression of various inflammatory markers including IL-6, IL-1b and IFNγ was also observed in the two groups, both at baseline as well as in the tumor-bearing bearing livers from Yap-β-catenin WT and LCN2 KO mice (Figure 42A).

We then investigated the *in vivo* activity of p65 in the WT and LCN2 KO tumors, using whole liver samples. Interestingly, the protein levels of p65 trended downward in the LCN2 KO tumors, as did the levels of the activated phospho-Ser536-p65, although the quantified results are not statistically significant (Figure 42B). We also determined expression of various cytokines that are known targets of NF-κB signaling. However, a high variability in the expression of various such targets including Fas, iNOS and Myc was observed by qRT-PCR analysis using mRNA from tumor-bearing bearing livers from Yap-β-catenin WT and LCN2 KO mice (Figure 42C). We also did not observe any differences in the expression of NF-κB targets at baseline between the WT and LCN2 KO (Figure 42C).

Thus overall, SB-HTVI injection of mutated YAP1-β-catenin led to the induction of similar HB tumors with mostly crowded fetal histology in both WT and Alb-Cre LCN2 KO

mice, but LCN2 KO tumors showed a modest increase in intratumoral inflammation and more frequent areas of blastemal histology.

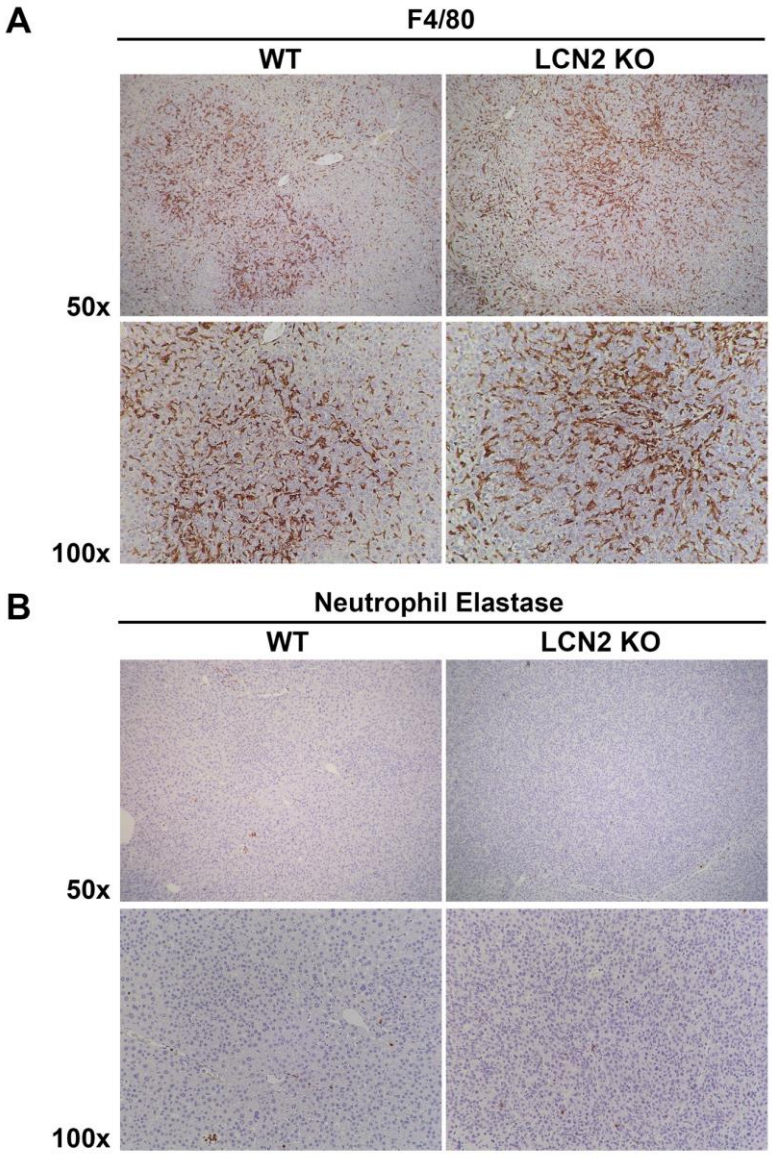

Figure 41. Differences in macrophage and neutrophil infiltration in HB occurring in LCN2 KO vs WT after YAP1-β-catenin activation.

A. Representative immunohistochemistry for the macrophage marker F4/80 showing large numbers of macrophages infiltrating HB tumors in both Yap1-β-catenin driven tumors in WT and LCN2 KO livers. B. Representative immunohistochemistry for the neutrophil marker Neutrophil Elastase showing a few neutrophils infiltrating the Yap1-β-catenin driven HB tumors in both WT and LCN2 KO livers.

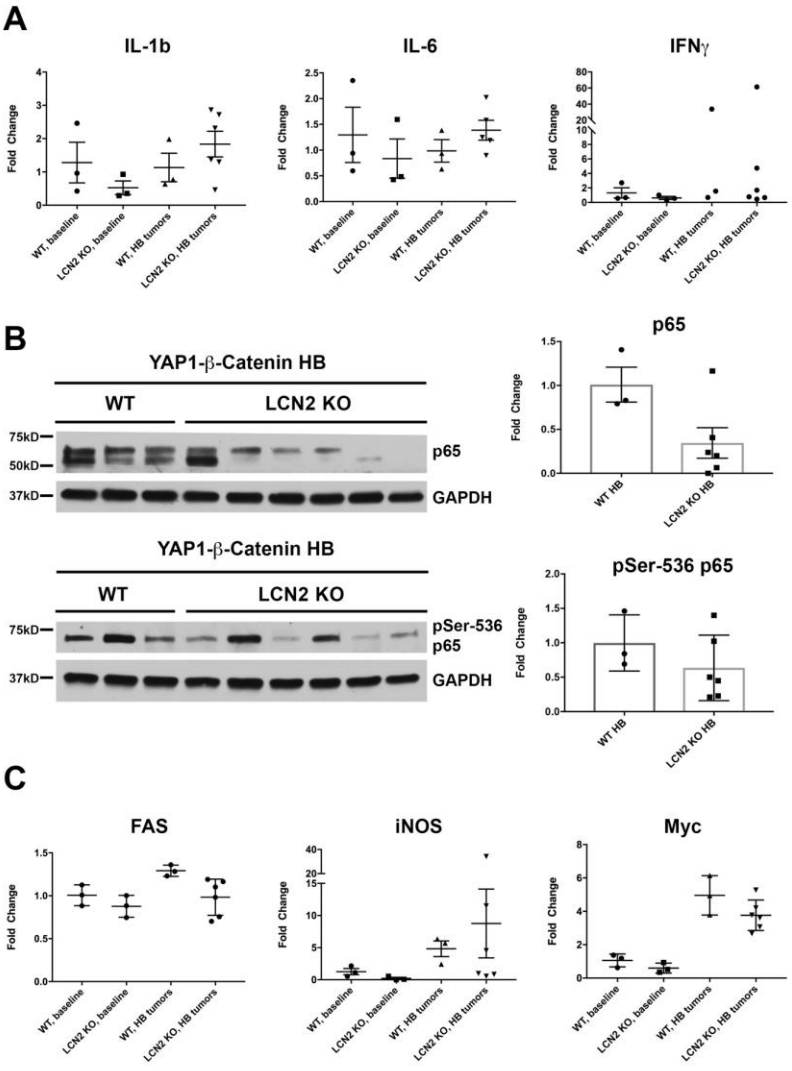

Figure 42. Evaluating inflammatory cytokines and NF-κB signaling in HB occurring in LCN2-KO versus WT after YAP1-β-catenin co-expression.

A. Gene expression of inflammtory cytokines IL-1b, IL-6, and IFNgamma was detected using RT-PCR, showing high levels of variability within tumor-laden livers of both WT and LCN2 KO HB. No significant difference in cytokine expression was detected in baseline WT and LCN2 KO livers. B. LCN2 KO HB shows decreased total levels of p65 as well as the activated phospho-Ser536 p65 by Western blot. Protein levels were quantified using densitometry and are she in in the panels to the right. There is no statistically significant difference between WT and LCN2 KO HB. C. Gene expression of p65 targets FAS, iNOS, and Myc was

detected using RT-PCR, showing high levels of variability within tumor-laden livers of both WT and LCN2 KO HB. No significant difference in gene expression was detected in baseline WT and LCN2 KO livers.

5.5 Discussion

Our current study offers novel insight into the role of LCN2 in HB. We have shown that *Lcn2* expression is driven by both YAP1and β-catenin, the primary tumor drivers in mouse model of HB as well as a majority of HB cases. Serum levels of LCN2 correlated strongly with tumor burden, and we show conclusively that serum LCN2 is derived from tumor cells within murine HB. Notably, our work demonstrates that LCN2 is present in a majority of human HB, and levels of LCN2 expression show an intriguing correlation with the histological subtypes within individual tumors. Together, this evidence presents LCN2 as a clinically relevant biomarker of HB tumor burden.

LCN2 is already under investigation in clinical trials as a biomarker for a variety of solid tumors, and assays for serum and urine LCN2 are readily available for use in clinical laboratories. Recent studies have shown that serum and urine LCN2 concentrations may have diagnostic and prognostic utility in colorectal, pancreatic, and thyroid cancer[280, 299, 300]. Future studies using patient serum samples will be important to assess LCN2 expression and whether LCN2 can be used in conjunction with α-fetoprotein to aid in the diagnosis, surveillance, prognosis and even therapeutic response of HB. Serum and urine LCN2 levels have also been shown to be elevated in a variety of liver diseases, mirroring the progression of inflammatory and oxidative damage to the liver[301]. Clinical trials using LCN2 as a serum biomarker for acute kidney injury have also found that serum LCN2 levels are strongly influenced by underlying

inflammatory processes, pre-existing kidney injury, and other comorbidities in severely ill patients, which may confound its use as a biomarker in patients receiving toxic chemotherapy[302]. Nevertheless, the same studies have shown an increased predictive capacity in neonates and pediatric patients, who are more likely to have few comorbidities and normal renal function. Thus, serum LCN2 holds promise as a clinical tool to improve detection and monitoring of HB in children.

It should be noted that the majority of the human tissue samples used in our study were taken from patients who had already received some form of chemotherapy and who were referred to Children's Hospital, Pittsburgh with late stage disease because of its status as a major tertiary care and transplant center. Our results showing a strong correlation of LCN2 nuclear and cytoplasmic staining with tumor differentiation status are thus most applicable to late-stage HB tumors. It is unclear how chemotherapy may affect LCN2 expression in HB tumors, and further studies are needed to expand these results to a larger group of pre-treatment HB tumors in order to account for this confounding variable. A larger, prospective patient cohort would also be needed to query whether LCN2 expression in early stage disease may be correlated to measures of prognosis and survival in children with HB.

Despite these limitations, our study sheds some light on the role of LCN2 in HB pathobiology. Within our patient cohort, all embryonal cases and most crowded fetal cases of HB showed the highest level of expression of LCN2. However, loss of LCN2 in hepatocytes did not affect HB proliferation *in vitro* or *in vivo*. This suggests that LCN2 may not directly influence cell proliferation, and that the more undifferentiated cases of HB may just have the highest activity of YAP1 and β-catenin[303]. While there are conflicting reports in the literature regarding the potential role of LCN2 in regulating hepatocyte proliferation after liver injury, our results are

consistent with reports showing no difference in proliferation between WT and LCN2 KO hepatocytes during liver regeneration. [304, 305] Both YAP1 and β-catenin promote hepatocyte proliferation through a variety of downstream targets independently of LCN2, so it is not surprising that loss of LCN2 alone in hepatocytes may not alter the level of proliferation in tumor cells. We also observed increased frequency of blastemal (stromal) areas in the HB derived from LCN2-deficient hepatocytes, which may be due to yet unknown role of LCN2 in regulating stem cell differentiation, which requires additional studies. Also, epithelial-mesenchymal transition (EMT) could contribute to blastemal like phenotype. However, there is conflicting evidence suggesting that LCN2 inhibits EMT in hepatocellular carcinoma and colorectal cancer while promoting tumor invasion, metastasis and EMT in prostate and breast cancer[279, 289, 306-308]. Again, addditional studies will be necessary to address any role of LCN2 in EMT in HB.

LCN2 silencing in HB cells *in vitro* affected NF-κB transcriptional activity, which is consistent with prior studies[298]. However, the results *in vivo* were ambiguous although downward trend in total and active-p65 were noted. We believe that the heterogeneity in amounts of tumors in lysates from tumor-bearing livers and the presence of LCN2-expressing inflammatory cells in the tumor microenvironment in both WT and LCN2-KO may be contributing to the high level of variability in p65 levels and activity in whole liver lysates in both protein and mRNA expression analysis. It is likely though that LCN2 in HB may be regulating NF-κB to in turn regulate inflammation in HB. Indeed, we observed a marginal increase in overall infiltrating immune cells in LCN2 KO HB, especially in blastemal areas, despite comparably higher macrophage numbers and low neutrophils in both experimental groups. A complex relationship between p65 and β-catenin, upstream effector of LCN2 has also been noted[296]. Future studies will address how LCN2 may be influencing specific immune response and impact overall histology of HB.

6.0 Concluding Remarks and Clinical Significance

The role of YAP1 in liver depends on the context, the ability of normal cellular mechanisms to turn YAP1 off, and the transcriptional partners active in the same cell. In general, YAP1 regulates gene targets that promote stemness, proliferation, and cell survival, programs essential for normal tissue regeneration.[5, 11, 309] This program seems to be permissive for cells to achieve a less differentiated state, which in general is associated with increased repair capacity. When turned off under normal repair mechanisms, these cells can regain their original quiescent state and resume their normal functions.[30, 310] When dysregulated, this program quickly becomes oncogenic, explaining the active role of YAP1 in many liver cancers.[5, 16, 311]

However, beyond this function, YAP1 has the additional ability to promote expression of biliary program in both hepatoblasts and hepatocytes. This has been demonstrated in normal liver development, in adult biliary homeostasis, in several studies artificially upregulating YAP1 in hepatocytes, leading to a range of biliary-like outcomes from oval cells to cholangiocarcinoma cells.[30, 49, 86, 204, 312, 313] In the adult liver, Dr. Sungjin Ko from our lab has recently shown that YAP1 transforms adult hepatocytes into cholangiocytes by downregulating HNF4α expression and activating DNMT1, a DNA methyl-transferase.[313] This suggests that YAP1 partly promotes cell plasticity by altering the global methylation landscape in a TEAD dependent manner, in addition to its known role as master regulator of enhancer activity.[1-3, 314] Further studies are needed to determine if this mechanism also plays a role in liver development. This function of YAP1 may also be promoted by combined activation of Notch, Tgfβ, MAPK, and other signaling pathways, all of which are critical for bile duct development.[54] However, more work is required to delineate these gene regulatory networks. Future studies will combine single-cell

RNA-sequencing with imaging and *in vitro* experimentation to elucidate this mechanism. To complete our understanding of this process, we must investigate how YAP1 is activated in the ductal plate, what signaling partners it works with, and what are the primary downstream targets that activate the biliary phenotype. This has important therapeutic impact on our understanding of Alagille syndrome and modifiers that can alter severity of disease, as well as mechanisms that can be targeted to reverse or prevent developmental damage.

We will continue to use the *Foxa3*-Cre YAP1 KO model for these studies. One interesting feature is that in this model YAP1 is deleted from all foregut endoderm organs, but curiously not the extrahepatic biliary tree. This means we cannot rule out non-cell autonomous functions from other epithelial cell populations which may be impacting the phenotype, and thus additional models may be necessary to identify the functions of YAP1 in these other cell types, particularly the EHBDs. At the same time, this may prove to be advantageous in studying the response of EHBDs to intrahepatic injury and artificially promoting EHBD-derived regeneration.

We will also continue to study the role of TAZ in both early embryonic foregut development and in biliary development. Although YAP1 loss alone did not impact early development overall, YAP1/TAZ combined loss resulted in embryonic lethality, suggesting that in this context YAP1 and TAZ may have redundant functions critical for survival. However, almost nothing is known about the role of TAZ in bile duct formation. Preliminary data not shown in this thesis suggests that TAZ loss results in bile duct paucity, but not complete absence of IHBDs like YAP1 loss. We also show significant gender dimorphism in survival depending on how many alleles of YAP1 and TAZ are lost. This opens up many questions about the co-dependent functions of YAP1/TAZ which may rely on total copy number as opposed to unique functions of either protein. We also cannot ignore potential physical interactions that may lead to

mutual activation and/or mutual inhibition, as shown previously.[32] This is a fertile area of study which promises to reveal much about the specific roles of YAP1 and TAZ in biliary differentiation, and thus has implications for developmental disorders as well as cholangiocarcinomas.

We also highlight the extraordinary capacity for the liver to adapt and survive under conditions of severe injury. The liver has many mechanisms for repair and regeneration, and many studies have shown that losing one pathway may delay or hamper repair but rarely stop it altogether.[309, 315, 316] Although loss of YAP1 caused the primary injury, it does not seem that YAP1 loss prevented the liver from adapting quite successfully to cholestatic injury. While TAZ seems to contribute to repair in absence of YAP1, the liver was still able to undergo a dramatic global reprogramming independent of YAP1/TAZ signaling in hepatocytes to preserve liver function and reduce bile acid toxicity. This lays bare the extreme resilience of the liver in the face of chronic severe injury. More work is needed to explore the key signals regulating this adaptation, as this may hold important insights for promoting this adaptation in patients with cholestatic disease. Importantly, the chronic damage done to the kidney in this model also highlights the terrible risk of cholestatic disease on the whole body, not just the liver. These adaptations must be regulated to preserve liver function but prevent serious damage to the kidney, which can be equally fatal to patients. Future work using our model will shed light on these mechanisms.

This thesis also focused on the dysregulation of YAP1 in development of hepatoblasts, specifically focusing on the pathogenesis of hepatoblastoma (HB). We still do not know how YAP1 is activated in hepatoblastoma, since no activating mutations in YAP1 or HIPPO pathway components have been found to date in various whole genome and whole exome sequencing

studies of patient HB tumors. One hypothesis is that YAP1 is already active in hepatoblasts over the course of normal development. This may be the case in early stages, as demonstrated by the fact that Foxa3-Cre YAP/TAZ DKO mice are embryonic lethal. However, our IF staining suggests that YAP1 is cytoplasmic is most hepatoblasts during the course of liver development, and loss of YAP1 alone in hepatoblasts did not prevent liver formation. It may be active in a subset of hepatoblasts and/or its activity may change temporally over the phases of hepatoblast differentiation into hepatocytes.[82] Alternatively, YAP1 activation in HB may simply be a consequence of oncogenic transformation of hepatoblasts and may not be the result of a specific driver mutation. Further study is needed to better understand whether common HB driver mutations specifically regulate YAP1 activation or whether YAP1 is just an oncogene co-opted by cancer cells and going along for the ride.

Along these lines, one major limitation of our studies involves the fundamental nature of the mouse model we use to mimic HB. In our mice, activation of YAP1 and beta-catenin leads to dedifferentiation of adult hepatocytes into hepatoblast-like tumor cells. However, this may not reflect the normal ontology of HB tumor cells in patients, which are more likely to originate from hepatoblasts during fetal and early postnatal stages of liver development. Some studies have tried to examine tumorigenesis arising from early developmental stages[317, 318], but the lack of a truly developmental HB tumor model remains a serious gap in the field. Nevertheless, our model is still useful to identify therapeutic strategies for HB since its transcriptional signature resembles that of human HB tumors. Our model is also useful for better understanding the relationship between YAP1 and β-catenin in this context.

While numerous studies have uncovered links between YAP1 and β-catenin activity, the relationship between these two transcriptional coactivators is complex and context-dependent,

and the interactions between YAP1 and β-catenin throughout liver development have not been clearly elucidated. Several studies have shown that phosphorylated YAP1 and β-catenin physically associate together at the "destruction complex" consisting of APC, GSK-3β, and others, resulting in mutual inhibition.[40, 319] β-catenin and YAP1 also seem to antagonize one another in the context of adult liver homeostasis. Overactivation of YAP1 in hepatocytes expands the gradient of periportal cells at the expense of β-catenin positive peri-central cells, while deletion of YAP1 resulted in the expansion of β-catenin positive hepatocytes.[28, 49] This antagonistic relationship is further supported in the context of liver tumorigenesis. A broad examination of patient liver tumors shows that while β-catenin and YAP1 both play important roles of hepatocellular carcinoma (HCC) pathogenesis, their activation is generally mutually exclusive in this setting.[85] Indeed, Fitamant *et al* showed that the HCC signature induced by YAP1 activation best correlates with patient HCC tumors that do not exhibit enhanced β-catenin activity.[28] Similarly, YAP1 is highly active in a large fraction of intrahepatic cholangiocarcinomas (ICC), a finding that is consistent with its general activation in BECs and promotion of biliary differentiation, while β-catenin is generally not active in ICC patient tumors.[85] In light of this evidence, hepatoblastoma stands out as a unique example of a liver tumor in which YAP1 and β-catenin collaborate to drive tumorigenesis. Both YAP1 and β-catenin are required for tumorigenesis in the mouse model of HB, but the mechanisms by which they drive HB pathogenesis and promote hepatocyte dedifferentiation remain unclear.

While many labs are studying methods to block the YAP1/TEAD interaction or WNT/β-catenin activation as a way to target these factors therapeutically, we aimed to identify downstream targets unique to HB that could be targeted more easily for therapy with less off-target effects. Our first approach was to identify genes regulated by both YAP1 and β-catenin

which may be unique to HB, and this led to our discovery of lipocalin 2 as a tumor biomarker. Our study combined microarray analysis of our HB tumors with publicly available data sets showing binding patterns of TCF and TEAD. However, further studies are needed to refine our understanding of how YAP1 and beta-catenin actually interact in HB tumors. It is not known if YAP1 and β-catenin physically interact in the nucleus to jointly regulate gene expression via the associated TEAD and TCF transcription factors respectively. Alternatively, YAP1 and β-catenin may mostly regulate gene expression independently, and it is the unique combination of downstream targets that promotes the development of HB tumors specifically. Further, this relationship may change based on the stage of tumor growth and differentiation. Thus, more detailed ChIP-seq and molecular experiments are needed to understand the unique interaction of YAP1 and beta-catenin in HB.

Our second approach was to study the metabolic effects of mTORC1 activation, which has been shown by our lab and others to be activated by both YAP1 and beta-catenin in many contexts.[84, 165, 167, 208, 320] mTORC1 has long been targeted therapeutically for many purposes, including cancer chemotherapy and immunosuppression, an ever-growing family of drugs descended from rapamycin is in clinical use today. Despite the risk of side-effects on other tissues, these medications are relatively well-tolerated by many patients. Our study treated HB tumors with rapamycin from an early stage and showed significant impact in slowing the growth of HB tumors, further confirming that mTORC1 activation drives HB tumor growth at least in small nodules. However, tumors eventually resumed the pace of growth seen in the control group, suggesting that they activated mechanisms of resistance that allowed mTORC1 independent unrestrained growth. Further experimentation is needed to treat HB tumors at a late

stage to determine whether mTORC1 inhibition can be cytostatic or cytotoxic to large tumors, more like what would be seen in patients.

Interestingly, tumors which grew despite rapamycin treatment showed completely different cellular morphology from the control group HB tumors, ranging from fetal to HCC-type cell morphology. This highlights the delicate balance between cell differentiation and cell growth or proliferation, long seen as a push-pull dichotomy, and shows how little we understand about the relationship between metabolic activity and differentiation in hepatoblasts. HB tumors with fetal histology tend to be less aggressive and more susceptible to treatment with chemotherapeutics like cisplatin. Indeed, a recent study in Cancer Discovery (in press) from Jessica Zucman-Rossi's lab shows that HB tumors which develop resistance to cisplatin are more likely to be embryonic rather than fetal HB tumors.[321] Furthermore, fetal HB tumors which develop cisplatin resistance tend to produce less differentiated recurrent or metastatic tumors.[321] This may be linked to the mutational load caused by cisplatin therapy, which may facilitate accumulation of oncogenic hits. This fascinating observation deserves much further study to learn about resistance mechanisms in HB tumors. However, combined with the observations of our study, it may be possible to take advantage of mTORC1 inhibition to potentiate cisplatin therapy, alter tumor differentiation state to reduce risk of developing resistance, or slow tumor growth rate to reduce chances of expansion of cells with high mutation number from cisplatin exposure. These and other mechanisms are worth studying to examine whether mTORC1 inhibition should be tested as adjuvant therapy in clinical trials for HB therapeutics.

Appendix A : Table of Antibodies Used in this Thesis

Table 3. List of Antibodies Used in this Thesis

ANTIBODY TARGET	ANTIBODY SPECIES	SOURCE	IDENTIFIER
YAP1	Rabbit	Cell Signaling Technology	Cat#CS14074
CK19 (Cytokeratin 19)	Rat	Developmental Studies Hybridoma Bank (DSHB)	Cat#TROMAIII
SOX9	Rabbit	EMD Millipore	Cat#ab5535
CD45	Rat	Santa Cruz Biotechnology	Cat#sc-53665
HNF4α	Mouse	R&D Systems	Cat#PP-H1415-00
HNF4α	Rabbit	Cell Signaling Technology	Cat#CS3113
GFP/EYFP	Chicken	Abcam	Cat#ab13970
CK8 (Cytokeratin 8)	Rat	DSHB	Cat#TROMAI
Acetylated α-tubulin	Mouse	Sigma Aldrich	Cat#T6793
pan-laminin	Rabbit	Sigma Aldrich	Cat#L9393
JAGGED1	Mouse	Santa Cruz Biotechnology	Cat# sc-390177
CEACAM1	Mouse	LSBio	Cat# LS-C106710
EpCAM	Rat	BioLegend	Cat# 118201
HES1	Mouse	Santa Cruz Biotechnology	Cat# sc-166410
Myc-tag	Rabbit	Maine Medical Center Research Institute	Cat# Vli01
PCNA	Mouse	Santa Cruz Biotechnology	Cat# sc-56
Ki67	Rabbit	Sigma	Cat# NM-SP6
CyclinD1		Abcam	Cat# 134175
Glutamine Synthetase	Rabbit	Sigma	Cat# G2781
Cyp2E1	Rabbit	Sigma	Cat# HPA-0009128
p-mTOR Ser2448	Rabbit	Cell Signaling	Cat# CS2976
p-S6 Ser235/236	Rabbit	Cell Signaling	Cat# CS4858
p-S6 Ser240/244	Rabbit	Cell Signaling	Cat# CS5364
p-4EBP1 Thr70	Rabbit	Cell Signaling	Cat# CS9455
Lipocalin 2 (IHC)	Rabbit	Sigma	Cat# HPA002695
Lipocalin 2 (WB)	Rabbit	Abcam	Cat# ab125075
F4/80	Rat	Serotech	Cat# MCA497GA
Neutrophil Elastase	Rabbit	Abcam	Cat# ab68672
Pan-TEAD	Rabbit	Cell Signaling	Cat# CS13295S
YAP/TAZ	Rabbit	Cell Signaling	Cat# 8418S
TAZ	Mouse	Abcam	Cat# ab242313
GAPDH	Mouse	Protein-Tech	Cat# 60004-1
P65	Mouse	Santa Cruz Biotechnology	Cat# sc-8008
p-p65 Ser536	Rabbit	Cell Signaling	Cat# CS3033S
β-catenin	Mouse	BD Biosciences	Cat# BD610154

Table 3 continued

Donkey anti-Rat IgG (H+L) Highly Cross-Adsorbed Secondary Antibody, Alexa Fluor 488		Invitrogen	Cat#A-21208
Donkey anti-Rabbit IgG (H+L) Highly Cross-Adsorbed Secondary Antibody, Alexa Fluor Plus 555		Invitrogen	Cat#A-32794
Goat anti-Mouse IgG (H+L) Cross-Adsorbed Secondary Antibody, Alexa Fluor 647		Invitrogen	Cat#A-21235
Goat anti-Chicken IgY (H+L) Cross-Adsorbed Secondary Antibody, Alexa Fluor Plus 555		Invitrogen	Cat#A-32932
Goat anti-Rabbit IgG (H+L) Highly Cross-Adsorbed Secondary Antibody, Alexa Fluor Plus 647		Invitrogen	Cat#A-32733
Donkey anti-Mouse IgG (H+L) Highly Cross-Adsorbed Secondary Antibody, Alexa Fluor Plus 555		Invitrogen	Cat#A-32773
IgG Donkey anti-Rabbit, Biotin, Polyclonal, Secondary Antibody		MilliporeSigma	Cat#AP182B
IgG Goat anti-Mouse, Biotin, Polyclonal, Secondary Antibody		MilliporeSigma	Cat#AP181B
IgG Goat anti-Rat, Biotin, Polyclonal, Secondary Antibody		MilliporeSigma	Cat#AP183B
Mouse anti-Rabbit Light Chain Only HRP-conjugated		Cell Signaling	Cat# CS93702
Goat anti-Mouse HRP-conjugated		ThermoFisher	Cat# 31430
Goat anti-Rabbit HRP-conjugated		Pierce	Cat# 31460

Appendix B : List of Pathways Altered in YAP1 KO Mice and/or YAP1 KO/TAZ HET Mice Compared to WT

Table 4. List of IPA Canonical Pathways Altered only in YAP1 KO vs WT (not YAP KO/TAZ HET vs WT)

Ingenuity Canonical Pathways: Significantly altered only in YAP1 KO vs WT	Z score	pval
Coronavirus Pathogenesis Pathway	3.244	0.02398833
Coronavirus Replication Pathway	2.673	0.02951209
Netrin Signaling	2.524	0.02454709
Calcium Signaling	2.401	0.03548134
Prostanoid Biosynthesis	2.236	0.02398833
UVA-Induced MAPK Signaling	2.041	0.00010965
Trehalose Degradation II (Trehalase)	2	0.02570396
SPINK1 General Cancer Pathway	1.606	0.02344229
Role of BRCA1 in DNA Damage Response	1.604	0.00891251
GDNF Family Ligand-Receptor Interactions	1.414	0.03388442
Ovarian Cancer Signaling	1.4	0.00218776
Mouse Embryonic Stem Cell Pluripotency	1.177	0.03467369
Antiproliferative Role of TOB in T Cell Signaling	1.155	0.01995262
Bladder Cancer Signaling	1	0.00457088
Inhibition of Angiogenesis by TSP1	1	0.0057544
Gglutamyl Cycle	0.447	0.03801894
GPCR-Mediated Integration of Enteroendocrine Signaling Exemplified by an L Cell	0.447	0.04168694
Glycogen Biosynthesis II (from UDP-D-Glucose)	0	0.0128825
Apelin Pancreas Signaling Pathway	0	0.02454709
Colanic Acid Building Blocks Biosynthesis	0	0.03162278
Pyrimidine Ribonucleotides Interconversion	-0.302	0.03090295
Pyrimidine Ribonucleotides De Novo Biosynthesis	-0.302	0.04677351
Dermatan Sulfate Biosynthesis (Late Stages)	-0.535	0.03548134
Role of p14/p19ARF in Tumor Suppression	-1.265	0.03090295
Extrinsic Prothrombin Activation Pathway	-1.342	0.01819701
Retinol Biosynthesis	-1.807	0.01047129
Leucine Degradation I	-2.236	0.0144544
Apelin Cardiac Fibroblast Signaling Pathway	-2.53	0.00512861

Table 4 continued

Ephrin A Signaling		0.00040738
Docosahexaenoic Acid (DHA) Signaling		0.00213796
Tyrosine Biosynthesis IV		0.00645654
Branched-chain _-keto acid Dehydrogenase Complex		0.02187762
Sulfate Activation for Sulfonation		0.03467369
Arsenate Detoxification I (Glutaredoxin)		0.04786301
Proline Biosynthesis II (from Arginine)		0.04786301
"Tetrahydrofolate Salvage from 5,10-methenyltetrahydrofolate"		0.04786301
Tetrapyrrole Biosynthesis II		0.04786301
CMP-N-acetylneuraminate Biosynthesis I (Eukaryotes)		0.04786301
Myo-inositol Biosynthesis		0.04786301
Folate Polyglutamylation		0.04786301
Polyamine Regulation in Colon Cancer		0.04897788

Table 5. List of IPA Canonical Pathways altered only in YAP KO/TAZ HET vs WT (not YAP1 KO vs WT)

Ingenuity Canonical Pathways: Significantly altered only in YAP KO/TAZ HET vs WT	Z score	pval
Crosstalk between Dendritic Cells and Natural Killer Cells	4.264	0.00851138
IL-15 Signaling	2.558	0.02454709
UVC-Induced MAPK Signaling	2.183	0.0128825
SAPK/JNK Signaling	1.89	0.01698244
Androgen Signaling	1.706	0.02570396
Factors Promoting Cardiogenesis in Vertebrates	1.543	0.00363078
Regulation Of The Epithelial Mesenchymal Transition In Development Pathway	1.528	0.04570882
Synaptic Long Term Potentiation	1.48	0.00363078
GDP-glucose Biosynthesis	1.342	0.04466836
Systemic Lupus Erythematosus In T Cell Signaling Pathway	1.238	0.02089296
cAMP-mediated signaling	1.033	0.00162181
Nur77 Signaling in T Lymphocytes	0.894	0.03019952
Glucose and Glucose-1-phosphate Degradation	0.816	0.01659587
Cardiac β-adrenergic Signaling	0.577	0.01905461
Tumoricidal Function of Hepatic Natural Killer Cells	0.378	0.00288403
Wnt/β-catenin Signaling	0.316	0.0074131
Wnt/Ca+ pathway	0.218	0.00489779
Cholesterol Biosynthesis I	0	0.02570396
"Cholesterol Biosynthesis II (via 24,25-dihydrolanosterol)"	0	0.02570396
Cholesterol Biosynthesis III (via Desmosterol)	0	0.02570396
UDP-N-acetyl-D-glucosamine Biosynthesis II	-0.447	0.00134896
tRNA Splicing	-0.5	0.00234423
"Tryptophan Degradation X (Mammalian, via Tryptamine)"	-0.632	0.0042658
Triacylglycerol Biosynthesis	-0.775	0.00616595
Histamine Degradation	-1.134	0.03162278
Fatty Acid β-oxidation	-1.414	0.02630268
BAG2 Signaling Pathway	-1.604	0.02754229
Glycine Betaine Degradation	-1.633	0.00537032
"Phenylalanine Degradation IV (Mammalian, via Side Chain)"	-1.633	0.03801894
Dopamine Degradation	-1.732	0.00724436
Androgen Biosynthesis	-1.89	0.02238721
Tryptophan Degradation to 2-amino-3-carboxymuconate Semialdehyde	-2	0.01513561
Triacylglycerol Degradation	-3.3	0.0042658
TCA Cycle II (Eukaryotic)	-3.464	0.00070795
Circadian Rhythm Signaling		0.00199526
Mechanisms of Viral Exit from Host Cells		0.0074131
Gustation Pathway		0.01862087
Phenylethylamine Degradation I		0.02454709

Table 5 continued

Spermidine Biosynthesis I		0.03715352
Phagosome Maturation		0.04677351

Appendix C : Potential TEAD Targets Regulated by TAZ in YAP1 KO Mice

Table 6. List of genes which are significantly upregulated in female YAP1 KO vs WT (FC>2, q < 0.05) but either downregulated or unaltered in female YAP KO/TAZ HET vs WT (q>0.05 OR q<0.05, FC<0)

Gene Name	Potential TEAD Target	Gene Name	Potential TEAD Target	Gene Name	Potential TEAD Target
Ptgs2		Zbtb16		Fbln7	YES
Hesx1		Nptx1		Gpc3	YES
Fcrls		Cenpi		Pla2g4a	
Thbs4		H1f4		Trip13	
Omd		Cfap69		Hells	YES
Tubb2b		Edn1	YES	Sestd1	
Trpc2		Nectin4		Pole	
Ms4a4a		BC055324		AA986860	YES
Pex5l		Epb41l4a		Cd83	
Casq2		Il7		Tiparp	YES
Ldb3		Rad51ap1		Hspa1a	
Nxpe5		Ccn1	YES	Cacng7	
Flrt3		Zfp36		Prelid2	YES
Gdf3		Col6a6		Brca1	
Gdf15	YES	Cytip		Cidec	
Ms4a14		Tmem100		Tacc3	YES
Trem1		Dlg2	YES	Rad54b	YES
Lmtk3		Lrrc27		Mmp9	YES
Fjx1		Cep55		Ncaph	
Arsi		Slamf9		Jdp2	
Pcdhga10		Gpr132		Clec4a3	
A530064D06Rik		Corin		Cd248	
Fgf7		Zik1		Chrna4	
Nr4a1	YES	Shcbp1	YES	Cnnm4	
Zbtb8b		Foxc2		Gas2	YES
Stc1		Tlr8		Sept6	
Actc1		Galnt12		Fbxo44	
Osm		Runx2	YES	Pakap_2	
2210407C18Rik		Fanci		Ect2	YES
Tnfaip6		Maff		Adamtsl1	
Cacna1g		Otud1	YES	Ptpn22	
Kntc1		Lpar1		Tceal1	
Tmem139		Gab3		Glt28d2	
Il1r2	YES	Sytl2		Fmod	
Ska1		Flnc		Klf4	YES
H2-Q1		Prdm1		Gm13889	
Rasd1		Rem1		Tspan18	
Kif15		Kif23		St8sia4	
Gxylt2	YES	F2rl1	YES	Pik3cg	
Nat8l		Fam222a	YES	Fam102b	
Gadd45b	YES	Cpxm2		Mms22l	

Table 6 continued

Eno2		Fzd3		H4c9	
AL935121.1		Twist1		Dpysl3	
Klc3		Card9		E2f1	YES
Fkbp1b		Npnt		Oas3	
Dlgap5	YES	Camkk1		Smc2	
Misp3		B9d1		Ift81	
Retnlg		Slc14a1		Il1b	
BC030867		Lat2	YES	Vars	
Sap25		Mt2		Cttnbp2nl	
Cldn4	YES	Krt23	YES	Cbarp	
Mfap2		Gabrb3		Parp8	
Ncapg		Rnf180		Rgs19	
Adam32	YES	Large2		Pmepa1	
Celsr3		Dclk1		Eda	
Ttk		Olig1		Hspbap1	YES
Gm5150		Fbn2		Nuak1	YES
Chrm3		Tnfrsf23		Stk17b	YES
Themis		Pdk3		Plk2	YES
Itgbl1		Arg2		Cyp21a1	
Abca4	YES	Ms4a4c		Hspa2	
Tmem28		Tmem178		P3h3	
Apcdd1		Sorl1	YES	Arl4a	
Sirpb1b		Apba1		Cdon	
Ereg		Fam217b		Akap12	YES
Cdh15		Lxn		Bmper	YES
Sgo1		Fignl1		Cd34	
Car13		Ust	YES	Sccpdh	
Apold1		Kif4		Arl4d	YES
Cenph		Plin4	YES	Tagln	
Gm38392		Kif11	YES	Zfand2a	YES
Egr3	YES	Ptgds		Abcb1a	YES
Slc44a4	YES	Nusap1		Clec4a2	
Ch25h		Wfdc2		Ddit3_1	
Ier2	YES	Cdca7l		Zfp36l1	YES
Dusp1	YES	Pkia		Ifrd1	YES
Ntrk2	YES	Ccne1	YES	Ifi211	
Thsd7a		H3f3b		Mcm5	
Abhd1		Gpr65		Dbf4	
Slc10a6		H2-Q2		Clec1a	
Tox3	YES	Csrnp1		Chml	
Stil		Ptger4		Pdzk1ip1	
Lca5		Lmcd1		Vcpkmt	
Pkp1		Mid1		Fmnl1	
H1f10		Pf4		Aqp8	
Hivep3	YES	Fam177a		Gabra3	
Ercc6l		Ccn2	YES	Tmem218	
B4galt2		Ms4a6b		Rad9a	
Zbtb9		Igsf3		Ophn1	
Galnt17		Pask		Scd1	
H2-M2		Gpx8		Dynlt1f	
Sema3b	YES	Ppp1r15a	YES	Mcm3	
Cd244a		Anks6	YES	Ccdc34	
Slit3		Orm3		Hes1	YES
Mcub		Serpine2	YES	Nfkbia	YES
Exo1		Atp10a		Hk1	YES
Polq		Epha3		Plk3	YES
Fam83a		Spon1	YES	Abca9	YES

Table 6 continued

Rad18	YES	Prkar2b		Clstn3	
Slc25a25	YES				

Appendix D : Table of Patient Demographics (Chapter 5)

Table 7. Patient demographics for all subjects used in the study of LCN2 expression in Hepatoblastoma Tumors (Chapter 5), from Children's Hospital of Pittsburgh.

Patient demographics included age at diagnosis, number of histological subtypes in each tumor sample, whether the sample was collected before or after treatment, and additional relevant information on all HB cases. BWS, Beckwith-Wiedeman Syndrome; GS, Gardner Syndrome; FAP, Familial Adenomatous Polyposis; HCC, Hepatocellular Carcinoma. *Tumor histology; F, fetal; E, embryonal; CF, crowded fetal; B, blastema; SCU, small cell undifferentiated; MT, mesenchymal transition. † Follow up; AWOD, alive without disease; DOD, dead of disease. ‡ Risk factor. §Born premature.

Sample	Tumor Histology *	Age (m)	Sex	Serum AFP (ng/ml)	Stage	Pre- or Post-Treatment Samples	Surgery	Follow Up†	Risk Factors‡
HB2B	E			90,630		Post	Resection	AWOD 11yrs	
HB3C	F	1		250,670	IV	Post	Transplant	AWOD 2013	
HB 6A	E, CF, SCU				Recurrence, IV	Pre	Resection	DOD	
HB6B	F					Post			
HB6C	E, SCU, MT			744		Post			
HB6F	SCU					Post			
HB 6G	E, CF, SCU			5		Post			
HB9A	F+E+MT	8			IV	Pre	Resection	AWOD at 4 years	
HB10	F+E	5		112,500		Post	Resection	AWOD 11 years	25 wk §
HB 13	F, CF	1		868,100		Post	Resection	AWOD 4 months	
HB14	F, HCC-like	08				Post	Resection	Mets to pelvis at 3 mo.	
HB16	CF+E	2				Post	Resection	AWOD	

Table 7 continued

HB 17A	F, CF					Pre	Resection	AWOD 6 months	
HB17B	F+MT					Post			
HB21	CF/E F, MT	6			I	Pre	Resection	AWOD	
HB22	F, CF/E,					Post			
HB24	B, HCC-like	08				Post	Resection	AWOD 23 yrs	
HB25	F	56				Post	Resection	Lost to FU	
HB28 (26)	F			11,000		Post	Resection	AWOD at 4 years	
HB29	CF, EMT	4		162,100		Pre	Resection	AWOD at 17 yrs	
HB30	E, SCU, CF, Teratoid	2				Pre	Resection	AWOD at 9 years	BWS
HB31	CF, E, B	4			III	Post	Resection	DOD 2 years	
HB32B	CF, E	2		120,070		Post	Resection	AWOD at 9 years	
HB34	M, Giant Cell, E, CF, SCU	6				Post	Transplant	AWOD at 13 yrs	
HB35	F+ CF+E	4		9,022		Post	Resection		
HB36	F	8				Post	Resection	AWOD 23 yrs	GS
HB37B	CF	8		419,000		Post	Resection	AWOD at 5 yrs	
HB39	E, CF	6		8,151	III	Post	Transplant	AWOD at 5 yrs	
HB41A	CF	2		1,938	III	Pre	Transplant	AWOD at 3 yrs	
HB41B	CF, Giant Cell, focal E					Post			
HB44	CF, E	4		2,605		Post	Resection	F/U 6 mths lost	
HB49	B, teratoid	4		1,973,536	III	Post	Resection	AWOD at 6 yrs	
HB52	CF/GC	2		223,728	III	Post	Transplant	AWOD at 5 yrs	FAP, 24 wk §
HB 53A	E, CF, WDf, SCU			613,026		Pre	Resection	AWOD at 1 yr	
HB53B	CF					Post			
HB55	CF, F	1		1,166,092	III	Post	Transplant	AWOD at 4 yrs	
HB56	CF, E	4				Post	Resection	AWOD	

Table 7 continued

HB 57A	WDF, CF	2		3,450		Pre	Trans plant	AWOD at 5 yrs	APC
HB57B	CF, B					Post			
HB58 (69)	E, CF	4		>100,000	Recurrenc e, III	Post	Resection, then Transplant	AWOD at 4 yrs	
HB59	F	4		600,000		Post	Transplant	AWOD at 5 yrs	
HB60A	E, CF, B	2		123,751	III	Pre	Resection	AWOD at 5 yrs	27 wk §
HB60B	CF, E					Post			
HB61 (64)	CF	2				Post	Resection	AWOD	
HB63	CF	0		721,500	IV	Post	Transplant	AWOD at 12 yrs	
HB65	E, CF	8		402,400		Pre	Resection	AWOD at 13 yrs	
HB66 (73)	CF, E	4		1,260,000	IV	Post	Transplant	AWOD at 5 yrs	
HB73 (66)	E, CF (lung met)					Post			
HB67B	B, E, CF, MT, ?SCU	1		580,000	IV	Post	Resection	AWOD at 2.5 yrs	
HB68B	Teratoid (glandular) , CF	6		3,183		Post	Resection	AWOD at 6 yrs	BWS
HB 70A	E	4		88,774		Pre	Resection	AWOD at 3 yrs	27 wk §
HB70B	E, CF					Post			
HB71	CF, E	6		51,000		Post	Transplant	AWOD at 4 yrs	
HB74	F	2			I	Post	Resection	Lost to FU	
HB75	mainly E, SCU, CF	4			III	Post	Transplant	AWOD 16 yrs	
HB 76	CF ,E, B	2		582,000	III	Post	Transplant	AWOD 6 yrs	
HB79	CF, B	2				Post	Transplant	Died of sepsis at 3yrs	
HB 81 A	E,	2		470,000		Pre	Resection	AWOD at 2 yrs	33 wk §
HB81B	CF					Post			
HB82B	E, CF, F, B, ?SCU	4		36,737	Recurrenc e	Post	Transplant	AWD in 2012	
HB82D	E, CF				IV	Post			28 wk §
HB83B	E			199,900	III	Post	Resection	AWOD 4 mths	28 wk §
HB85	E, SCU, CF	2		3,687		Pre	Resection	AWOD 3 years	28 wk §, BWS

Table 7 continued

HB87B	E (mainly) SCU, CF	4		140,000		Post	Transplant	AWOD at 3 yrs	
HB88B	CF	0		278? On Rx		Post	Resection	AWOD	
HB89B	CF	2		2,000,000	Recurrence, IV	Post	Transplant		
HB91B	CF, B	2		468,590		Post	Transplant	AWOD	25 wk §
HB UK	E, CF, B					Post			
HB96	CF, E, B	6				Pre	Resection		
HB95	CF,	8		994		Pre	Resection	AWOD 3 mths	
B104B	CF, MT, B	2		538,000		Post	Transplant	AWOD	
HB 47	CF, E, M, B	4		398,035	IV	Pre		Lost to FU 3 cycles	BWS
HB 48	teratoid, E, B	6		262,566	III	Post		AWOD at 6 yrs	
HB 102	E, CF, B	0		3,054		Pre	Resection	AWOD	32 wk §

Bibliography

[1] Zanconato F, Forcato M, Battilana G, Azzolin L, Quaranta E, Bodega B, Rosato A, Bicciato S, Cordenonsi M, Piccolo S: Genome-wide association between YAP/TAZ/TEAD and AP-1 at enhancers drives oncogenic growth. Nat Cell Biol 2015, 17:1218-27.

[2] Galli GG, Carrara M, Yuan W-C, Valdes-Quezada C, Gurung B, Pepe-Mooney B, Zhang T, Geeven G, Gray NS, de Laat W, Calogero RA, Camargo FD: YAP Drives Growth by Controlling Transcriptional Pause Release from Dynamic Enhancers. Mol Cell 2015, 60:328-37.

[3] Stein C, Bardet AF, Roma G, Bergling S, Clay I, Ruchti A, Agarinis C, Schmelzle T, Bouwmeester T, Schübeler D, Bauer A: YAP1 Exerts Its Transcriptional Control via TEAD-Mediated Activation of Enhancers. PLoS Genet 2015, 11:e1005465.

[4] Zhao B, Ye X, Yu J, Li L, Li W, Li S, Yu J, Lin JD, Wang C-Y, Chinnaiyan AM, Lai Z-C, Guan K-L: TEAD mediates YAP-dependent gene induction and growth control. Genes Dev 2008, 22:1962-71.

[5] Patel SH, Camargo FD, Yimlamai D: Hippo Signaling in the Liver Regulates Organ Size, Cell Fate, and Carcinogenesis. Gastroenterology 2017, 152:533-45.

[6] Zhou D, Conrad C, Xia F, Park J-S, Payer B, Yin Y, Lauwers GY, Thasler W, Lee JT, Avruch J, Bardeesy N: Mst1 and Mst2 maintain hepatocyte quiescence and suppress hepatocellular carcinoma development through inactivation of the Yap1 oncogene. Cancer Cell 2009, 16:425-38.

[7] Zhao B, Li L, Tumaneng K, Wang C-Y, Guan K-L: A coordinated phosphorylation by Lats and CK1 regulates YAP stability through SCF(beta-TRCP). Genes Dev 2010, 24:72-85.

[8] Moleirinho S, Hoxha S, Mandati V, Curtale G, Troutman S, Ehmer U, Kissil JL: Regulation of localization and function of the transcriptional co-activator YAP by angiomotin. elife 2017, 6.

[9] Robinson BS, Moberg KH: Cell-cell junctions: α-catenin and E-cadherin help fence in Yap1. Curr Biol 2011, 21:R890-2.

[10] Sugihara T, Werneburg NW, Hernandez MC, Yang L, Kabashima A, Hirsova P, Yohanathan L, Sosa C, Truty MJ, Vasmatzis G, Gores GJ, Smoot RL: YAP Tyrosine Phosphorylation and Nuclear Localization in Cholangiocarcinoma Cells is Regulated by LCK and Independent of LATS Activity. Mol Cancer Res 2018.

[11] Panciera T, Azzolin L, Cordenonsi M, Piccolo S: Mechanobiology of YAP and TAZ in physiology and disease. Nat Rev Mol Cell Biol 2017, 18:758-70.

[12] Gumbiner BM, Kim N-G: The Hippo-YAP signaling pathway and contact inhibition of growth. J Cell Sci 2014, 127:709-17.

[13] Heng BC, Zhang X, Aubel D, Bai Y, Li X, Wei Y, Fussenegger M, Deng X: An overview of signaling pathways regulating YAP/TAZ activity. Cell Mol Life Sci 2021, 78:497-512.

[14] Moya IM, Halder G: Hippo-YAP/TAZ signalling in organ regeneration and regenerative medicine. Nat Rev Mol Cell Biol 2019, 20:211-26.

[15] Yin F, Yu J, Zheng Y, Chen Q, Zhang N, Pan D: Spatial organization of Hippo signaling at the plasma membrane mediated by the tumor suppressor Merlin/NF2. Cell 2013, 154:1342-55.

[16] Zhang S, Wang J, Wang H, Fan L, Fan B, Zeng B, Tao J, Li X, Che L, Cigliano A, Ribback S, Dombrowski F, Chen B, Cong W, Wei L, Calvisi DF, Chen X: Hippo cascade controls lineage commitment of liver tumors in mice and humans. Am J Pathol 2018, 0:995-1006.

[17] Wang J, Dong M, Xu Z, Song X, Zhang S, Qiao Y, Che L, Gordan J, Hu K, Liu Y, Calvisi DF, Chen X: Notch2 controls hepatocyte-derived cholangiocarcinoma formation in mice. Oncogene 2018.

[18] Kim W, Khan SK, Gvozdenovic-Jeremic J, Kim Y, Dahlman J, Kim H, Park O, Ishitani T, Jho E-H, Gao B, Yang Y: Hippo signaling interactions with Wnt/β-catenin and Notch signaling repress liver tumorigenesis. The Journal of Clinical Investigation 2017, 127:137-52.

[19] Kim W, Khan SK, Yang Y: Interacting network of Hippo, Wnt/beta-catenin and Notch signaling represses liver tumor formation. BMB Rep 2017, 50:1-2.

[20] Kriz V, Korinek V: Wnt, RSPO and hippo signalling in the intestine and intestinal stem cells. Genes (Basel) 2018, 9.

[21] Taniguchi K, Moroishi T, de Jong PR, Krawczyk M, Grebbin BM, Luo H, Xu R-H, Golob-Schwarzl N, Schweiger C, Wang K, Di Caro G, Feng Y, Fearon ER, Raz E, Kenner L, Farin HF, Guan K-L, Haybaeck J, Datz C, Zhang K, Karin M: YAP-IL-6ST autoregulatory loop activated on APC loss controls colonic tumorigenesis. Proceedings of the National Academy of Sciences of the United States of America 2017, 114:1643-8.

[22] Chang L, Azzolin L, Di Biagio D, Zanconato F, Battilana G, Lucon Xiccato R, Aragona M, Giulitti S, Panciera T, Gandin A, Sigismondo G, Krijgsveld J, Fassan M, Brusatin G, Cordenonsi M, Piccolo S: The SWI/SNF complex is a mechanoregulated inhibitor of YAP and TAZ. Nature 2018, 563:265-9.

[23] Cox AG, Hwang KL, Brown KK, Evason KJ, Beltz S, Tsomides A, O'Connor K, Galli GG, Yimlamai D, Chhangawala S, Yuan M, Lien EC, Wucherpfennig J, Nissim S, Minami A, Cohen DE, Camargo FD, Asara JM, Houvras Y, Stainier DYR, Goessling W: Yap reprograms glutamine metabolism to increase nucleotide biosynthesis and enable liver growth. Nat Cell Biol 2016, 18:886-96.

[24] Septer S, Edwards G, Gunewardena S, Wolfe A, Li H, Daniel J, Apte U: Yes-associated protein is involved in proliferation and differentiation during postnatal liver development. Am J Physiol Gastrointest Liver Physiol 2012, 302:G493-503.

[25] Ibar C, Irvine KD: Integration of Hippo-YAP Signaling with Metabolism. Dev Cell 2020, 54:256-67.

[26] Nguyen Q, Anders RA, Alpini G, Bai H: Yes-associated protein in the liver: Regulation of hepatic development, repair, cell fate determination and tumorigenesis. Dig Liver Dis 2015, 47:826-35.

[27] Alder O, Cullum R, Lee S, Kan AC, Wei W, Yi Y, Garside VC, Bilenky M, Griffith M, Morrissy AS, Robertson GA, Thiessen N, Zhao Y, Chen Q, Pan D, Jones SJM, Marra MA, Hoodless PA: Hippo signaling influences HNF4A and FOXA2 enhancer switching during hepatocyte differentiation. Cell Rep 2014, 9:261-71.

[28] Fitamant J, Kottakis F, Benhamouche S, Tian HS, Chuvin N, Parachoniak CA, Nagle JM, Perera RM, Lapouge M, Deshpande V, Zhu AX, Lai A, Min B, Hoshida Y, Avruch J, Sia D, Camprecións G, McClatchey AI, Llovet JM, Morrissey D, Raj L, Bardeesy N: YAP inhibition restores hepatocyte differentiation in advanced HCC, leading to tumor regression. Cell Rep 2015.

[29] Yuan WC, Pepe-Mooney B, Galli GG, Dill MT, Huang HT, Hao M, Wang Y, Liang H, Calogero RA, Camargo FD: NUAK2 is a critical YAP target in liver cancer. Nat Commun 2018, 9:4834.

[30] Pepe-Mooney BJ, Dill MT, Alemany A, Ordovas-Montanes J, Matsushita Y, Rao A, Sen A, Miyazaki M, Anakk S, Dawson PA, Ono N, Shalek AK, van Oudenaarden A, Camargo FD: Single-Cell Analysis of the Liver Epithelium Reveals Dynamic Heterogeneity and an Essential Role for YAP in Homeostasis and Regeneration. Cell Stem Cell 2019, 25:23-38 e8.

[31] Mooring M, Fowl BH, Lum SZC, Liu Y, Yao K, Softic S, Kirchner R, Bernstein A, Singhi AD, Jay DG, Kahn CR, Camargo FD, Yimlamai D: Hepatocyte Stress Increases Expression of Yes-Associated Protein and Transcriptional Coactivator With PDZ-Binding Motif in Hepatocytes to Promote Parenchymal Inflammation and Fibrosis. Hepatology 2020, 71:1813-30.

[32] Reggiani F, Gobbi G, Ciarrocchi A, Sancisi V: YAP and TAZ Are Not Identical Twins. Trends Biochem Sci 2021, 46:154-68.

[33] van Soldt BJ, Cardoso WV: Hippo-Yap/Taz signaling: Complex network interactions and impact in epithelial cell behavior. Wiley Interdiscip Rev Dev Biol 2020, 9:e371.

[34] Hansen CG, Moroishi T, Guan K-L: YAP and TAZ: a nexus for Hippo signaling and beyond. Trends Cell Biol 2015, 25:499-513.

[35] Wang W, Li X, Huang J, Feng L, Dolinta KG, Chen J: Defining the protein-protein interaction network of the human hippo pathway. Mol Cell Proteomics 2014, 13:119-31.

[36] Moroishi T, Park HW, Qin B, Chen Q, Meng Z, Plouffe SW, Taniguchi K, Yu F-X, Karin M, Pan D, Guan K-L: A YAP/TAZ-induced feedback mechanism regulates Hippo pathway homeostasis. Genes Dev 2015, 29:1271-84.

[37] Kaan HYK, Chan SW, Tan SKJ, Guo F, Lim CJ, Hong W, Song H: Crystal structure of TAZ-TEAD complex reveals a distinct interaction mode from that of YAP-TEAD complex. Sci Rep 2017, 7:2035.

[38] Hau JC, Erdmann D, Mesrouze Y, Furet P, Fontana P, Zimmermann C, Schmelzle T, Hofmann F, Chene P: The TEAD4-YAP/TAZ protein-protein interaction: expected similarities and unexpected differences. Chembiochem 2013, 14:1218-25.

[39] Cai J, Maitra A, Anders RA, Taketo MM, Pan D: β-Catenin destruction complex-independent regulation of Hippo-YAP signaling by APC in intestinal tumorigenesis. Genes Dev 2015, 29:1493-506.

[40] Azzolin L, Panciera T, Soligo S, Enzo E, Bicciato S, Dupont S, Bresolin S, Frasson C, Basso G, Guzzardo V, Fassina A, Cordenonsi M, Piccolo S: YAP/TAZ incorporation in the β-catenin destruction complex orchestrates the Wnt response. Cell 2014, 158:157-70.

[41] Azzolin L, Zanconato F, Bresolin S, Forcato M, Basso G, Bicciato S, Cordenonsi M, Piccolo S: Role of TAZ as mediator of Wnt signaling. Cell 2012, 151:1443-56.

[42] Morin-Kensicki EM, Boone BN, Howell M, Stonebraker JR, Teed J, Alb JG, Magnuson TR, O'Neal W, Milgram SL: Defects in yolk sac vasculogenesis, chorioallantoic fusion, and embryonic axis elongation in mice with targeted disruption of Yap65. Mol Cell Biol 2006, 26:77-87.

[43] Makita R, Uchijima Y, Nishiyama K, Amano T, Chen Q, Takeuchi T, Mitani A, Nagase T, Yatomi Y, Aburatani H, Nakagawa O, Small EV, Cobo-Stark P, Igarashi P, Murakami M, Tominaga J, Sato T, Asano T, Kurihara Y, Kurihara H: Multiple renal cysts, urinary concentration defects, and pulmonary emphysematous changes in mice lacking TAZ. Am J Physiol Renal Physiol 2008, 294:F542-53.

[44] Hossain Z, Ali SM, Ko HL, Xu J, Ng CP, Guo K, Qi Z, Ponniah S, Hong W, Hunziker W: Glomerulocystic kidney disease in mice with a targeted inactivation of Wwtr1. Proc Natl Acad Sci U S A 2007, 104:1631-6.

[45] Heng BC, Zhang X, Aubel D, Bai Y, Li X, Wei Y, Fussenegger M, Deng X: Role of YAP/TAZ in Cell Lineage Fate Determination and Related Signaling Pathways. Front Cell Dev Biol 2020, 8:735.

[46] Wang H, Wang J, Zhang S, Jia J, Liu X, Zhang J, Wang P, Song X, Che L, Liu K, Ribback S, Cigliano A, Evert M, Wu H, Calvisi DF, Zeng Y, Chen X: Distinct and Overlapping Roles of Hippo Effectors YAP and TAZ During Human and Mouse Hepatocarcinogenesis. Cell Mol Gastroenterol Hepatol 2020.

[47] Van Haele M, Moya IM, Karaman R, Rens G, Snoeck J, Govaere O, Nevens F, Verslype C, Topal B, Monbaliu D, Halder G, Roskams T: YAP and TAZ Heterogeneity in Primary Liver Cancer: An Analysis of Its Prognostic and Diagnostic Role. Int J Mol Sci 2019, 20.

[48] Lee D-H, Park JO, Kim T-S, Kim S-K, Kim T-H, Kim M-C, Park GS, Kim J-H, Kuninaka S, Olson EN, Saya H, Kim S-Y, Lee H, Lim D-S: LATS-YAP/TAZ controls lineage specification by regulating TGFβ signaling and Hnf4α expression during liver development. Nat Commun 2016, 7:11961.

[49] Yimlamai D, Christodoulou C, Galli GG, Yanger K, Pepe-Mooney B, Gurung B, Shrestha K, Cahan P, Stanger BZ, Camargo FD: Hippo pathway activity influences liver cell fate. Cell 2014, 157:1324-38.

[50] Dong J, Feldmann G, Huang J, Wu S, Zhang N, Comerford SA, Gayyed MF, Anders RA, Maitra A, Pan D: Elucidation of a universal size-control mechanism in Drosophila and mammals. Cell 2007, 130:1120-33.

[51] Gordillo M, Evans T, Gouon-Evans V: Orchestrating liver development. Development 2015, 142:2094-108.

[52] Ober EA, Lemaigre FP: Development of the liver: Insights into organ and tissue morphogenesis. J Hepatol 2018, 68:1049-62.

[53] Shin D, Monga SPS: Cellular and molecular basis of liver development. Compr Physiol 2013, 3:799-815.

[54] Lemaigre FP: Development of the Intrahepatic and Extrahepatic Biliary Tract: A Framework for Understanding Congenital Diseases. Annu Rev Pathol 2020, 15:1-22.

[55] Su X, Shi Y, Zou X, Lu Z-N, Xie G, Yang JYH, Wu C-C, Cui X-F, He K-Y, Luo Q, Qu Y-L, Wang N, Wang L, Han Z-G: Single-cell RNA-Seq analysis reveals dynamic trajectories during mouse liver development. BMC Genomics 2017, 18:946.

[56] Yang L, Wang W-H, Qiu W-L, Guo Z, Bi E, Xu C-R: A single-cell transcriptomic analysis reveals precise pathways and regulatory mechanisms underlying hepatoblast differentiation. Hepatology 2017, 66:1387-401.

[57] Tan X, Yuan Y, Zeng G, Apte U, Thompson MD, Cieply B, Stolz DB, Michalopoulos GK, Kaestner KH, Monga SPS: Beta-catenin deletion in hepatoblasts disrupts hepatic morphogenesis and survival during mouse development. Hepatology 2008, 47:1667-79.

[58] Gérard C, Tys J, Lemaigre FP: Gene regulatory networks in differentiation and direct reprogramming of hepatic cells. Semin Cell Dev Biol 2017, 66:43-50.

[59] Tanimizu N, Miyajima A: Notch signaling controls hepatoblast differentiation by altering the expression of liver-enriched transcription factors. J Cell Sci 2004, 117:3165-74.

[60] Clotman F, Jacquemin P, Plumb-Rudewiez N, Pierreux CE, Van der Smissen P, Dietz HC, Courtoy PJ, Rousseau GG, Lemaigre FP: Control of liver cell fate decision by a gradient of TGF beta signaling modulated by Onecut transcription factors. Genes Dev 2005, 19:1849-54.

[61] Takayama K, Kawabata K, Nagamoto Y, Inamura M, Ohashi K, Okuno H, Yamaguchi T, Tashiro K, Sakurai F, Hayakawa T, Okano T, Furue MK, Mizuguchi H: CCAAT/enhancer binding protein-mediated regulation of TGFbeta receptor 2 expression determines the hepatoblast fate decision. Development 2014, 141:91-100.

[62] Benhamouche-Trouillet S, O'Loughlin E, Liu C-H, Polacheck W, Fitamant J, McKee M, El-Bardeesy N, Chen CS, McClatchey AI: Proliferation-independent role of NF2 (merlin) in limiting biliary morphogenesis. Development 2018, 145.

[63] Tanimizu N, Kaneko K, Itoh T, Ichinohe N, Ishii M, Mizuguchi T, Hirata K, Miyajima A, Mitaka T: Intrahepatic bile ducts are developed through formation of homogeneous continuous luminal network and its dynamic rearrangement in mice. Hepatology 2016, 64:175-88.

[64] Tanimizu N, Kikkawa Y, Mitaka T, Miyajima A: alpha1- and alpha5-containing laminins regulate the development of bile ducts via beta1 integrin signals. J Biol Chem 2012, 287:28586-97.

[65] Carpentier R, Suñer RE, van Hul N, Kopp JL, Beaudry J-B, Cordi S, Antoniou A, Raynaud P, Lepreux S, Jacquemin P, Leclercq IA, Sander M, Lemaigre FP: Embryonic ductal plate cells give rise to cholangiocytes, periportal hepatocytes, and adult liver progenitor cells. Gastroenterology 2011, 141:1432-8, 8.e1.

[66] Font-Burgada J, Shalapour S, Ramaswamy S, Hsueh B, Rossell D, Umemura A, Taniguchi K, Nakagawa H, Valasek MA, Ye L, Kopp JL, Sander M, Carter H, Deisseroth K, Verma IM, Karin M: Hybrid Periportal Hepatocytes Regenerate the Injured Liver without Giving Rise to Cancer. Cell 2015, 162:766-79.

[67] Walter TJ, Cast AE, Huppert KA, Huppert SS: Epithelial VEGF signaling is required in the mouse liver for proper sinusoid endothelial cell identity and hepatocyte zonation in vivo. Am J Physiol Gastrointest Liver Physiol 2014, 306:G849-62.

[68] Fabris L, Cadamuro M, Libbrecht L, Raynaud P, Spirlì C, Fiorotto R, Okolicsanyi L, Lemaigre F, Strazzabosco M, Roskams T: Epithelial expression of angiogenic growth factors modulate arterial vasculogenesis in human liver development. Hepatology 2008, 47:719-28.

[69] Kietzmann T: Metabolic zonation of the liver: The oxygen gradient revisited. Redox Biol 2017, 11:622-30.

[70] Russell JO, Monga SS: Wnt/β-Catenin Signaling in Liver Development, Homeostasis, and Pathobiology. Annu Rev Pathol 2017, 13.

[71] Villasenor A, Stainier DYR: On the development of the hepatopancreatic ductal system. Semin Cell Dev Biol 2017, 66:69-80.

[72] Spence JR, Lange AW, Lin SC, Kaestner KH, Lowy AM, Kim I, Whitsett JA, Wells JM: Sox17 regulates organ lineage segregation of ventral foregut progenitor cells. Dev Cell 2009, 17:62-74.

[73] Uemura M, Higashi M, Pattarapanawan M, Takami S, Ichikawa N, Higashiyama H, Furukawa T, Fujishiro J, Fukumura Y, Yao T, Tajiri T, Kanai-Azuma M, Kanai Y: Gallbladder wall abnormality in biliary atresia of mouse Sox17 (+/-) neonates and human infants. Dis Model Mech 2020, 13.

[74] Higashiyama H, Ozawa A, Sumitomo H, Uemura M, Fujino K, Igarashi H, Imaimatsu K, Tsunekawa N, Hirate Y, Kurohmaru M, Saijoh Y, Kanai-Azuma M, Kanai Y: Embryonic cholecystitis and defective gallbladder contraction in the Sox17-haploinsufficient mouse model of biliary atresia. Development 2017, 144:1906-17.

[75] Uemura M, Ozawa A, Nagata T, Kurasawa K, Tsunekawa N, Nobuhisa I, Taga T, Hara K, Kudo A, Kawakami H, Saijoh Y, Kurohmaru M, Kanai-Azuma M, Kanai Y: Sox17 haploinsufficiency results in perinatal biliary atresia and hepatitis in C57BL/6 background mice. Development 2013, 140:639-48.

[76] Uemura M, Hara K, Shitara H, Ishii R, Tsunekawa N, Miura Y, Kurohmaru M, Taya C, Yonekawa H, Kanai-Azuma M, Kanai Y: Expression and function of mouse Sox17 gene in the

specification of gallbladder/bile-duct progenitors during early foregut morphogenesis. Biochem Biophys Res Commun 2010, 391:357-63.

[77] Sumazaki R, Shiojiri N, Isoyama S, Masu M, Keino-Masu K, Osawa M, Nakauchi H, Kageyama R, Matsui A: Conversion of biliary system to pancreatic tissue in Hes1-deficient mice. Nat Genet 2004, 36:83-7.

[78] Villasenor A, Gauvrit S, Collins MM, Maischein HM, Stainier DYR: Hhex regulates the specification and growth of the hepatopancreatic ductal system. Dev Biol 2020, 458:228-36.

[79] Dong PD, Munson CA, Norton W, Crosnier C, Pan X, Gong Z, Neumann CJ, Stainier DY: Fgf10 regulates hepatopancreatic ductal system patterning and differentiation. Nat Genet 2007, 39:397-402.

[80] Thestrup MI, Caviglia S, Cayuso J, Heyne RLS, Ahmad R, Hofmeister W, Satriano L, Wilkinson DG, Andersen JB, Ober EA: A morphogenetic EphB/EphrinB code controls hepatopancreatic duct formation. Nat Commun 2019, 10:5220.

[81] Brandt ZJ, Echert AE, Bostrom JR, North PN, Link BA: Core Hippo pathway components act as a brake on Yap and Taz in the development and maintenance of the biliary network. Development 2020, 147.

[82] Wei W, Lotto J, Hoodless PA: Expression patterns of Yes-associated protein 1 in the developing mouse liver. Gene Expr Patterns 2018, 29:10-7.

[83] Min Q, Molina L, Li J, Adebayo Michael AO, Russell JO, Preziosi ME, Singh S, Poddar M, Matz-Soja M, Ranganathan S, Bell AW, Gebhardt R, Gaunitz F, Yu J, Tao J, Monga SP: beta-Catenin and Yes-Associated Protein 1 Cooperate in Hepatoblastoma Pathogenesis. Am J Pathol 2019, 189:1091-104.

[84] Liu P, Calvisi DF, Kiss A, Cigliano A, Schaff Z, Che L, Ribback S, Dombrowski F, Zhao D, Chen X: Central role of mTORC1 downstream of YAP/TAZ in hepatoblastoma development. Oncotarget 2017, 8:73433-47.

[85] Tao J, Calvisi DF, Ranganathan S, Cigliano A, Zhou L, Singh S, Jiang L, Fan B, Terracciano L, Armeanu-Ebinger S, Ribback S, Dombrowski F, Evert M, Chen X, Monga SPS: Activation of β-catenin and Yap1 in human hepatoblastoma and induction of hepatocarcinogenesis in mice. Gastroenterology 2014, 147:690-701.

[86] Zhang N, Bai H, David KK, Dong J, Zheng Y, Cai J, Giovannini M, Liu P, Anders RA, Pan D: The Merlin/NF2 tumor suppressor functions through the YAP oncoprotein to regulate tissue homeostasis in mammals. Dev Cell 2010, 19:27-38.

[87] Oh S-H, Swiderska-Syn M, Jewell ML, Premont RT, Diehl AM: Liver regeneration requires Yap1-TGFβ-dependent epithelial-mesenchymal transition in hepatocytes. J Hepatol 2018.

[88] Schaub JR, Huppert KA, Kurial SNT, Hsu BY, Cast AE, Donnelly B, Karns RA, Chen F, Rezvani M, Luu HY, Mattis AN, Rougemont A-L, Rosenthal P, Huppert SS, Willenbring H: De novo formation of the biliary system by TGFβ-mediated hepatocyte transdifferentiation. Nature 2018, 557:247-51.

[89] Verboven E, Moya IM, Sansores-Garcia L, Xie J, Hillen H, Kowalczyk W, Vella G, Verhulst S, Castaldo SA, Alguero-Nadal A, Romanelli L, Mercader-Celma C, Souza NA, Soheily S, Van Huffel L, Van Brussel T, Lambrechts D, Roskams T, Lemaigre FP, Bergers G, van Grunsven LA, Halder G: Regeneration Defects in Yap and Taz Mutant Mouse Livers Are Caused by Bile Duct Disruption and Cholestasis. Gastroenterology 2021, 160:847-62.

[90] Xu X, Kobayashi S, Qiao W, Li C, Xiao C, Radaeva S, Stiles B, Wang RH, Ohara N, Yoshino T, LeRoith D, Torbenson MS, Gores GJ, Wu H, Gao B, Deng CX: Induction of intrahepatic cholangiocellular carcinoma by liver-specific disruption of Smad4 and Pten in mice. J Clin Invest 2006, 116:1843-52.

[91] Banales JM, Huebert RC, Karlsen T, Strazzabosco M, LaRusso NF, Gores GJ: Cholangiocyte pathobiology. Nat Rev Gastroenterol Hepatol 2019, 16:269-81.

[92] Sato K, Meng F, Giang T, Glaser S, Alpini G: Mechanisms of cholangiocyte responses to injury. Biochim Biophys Acta Mol Basis Dis 2018, 1864:1262-9.

[93] Sato K, Marzioni M, Meng F, Francis H, Glaser S, Alpini G: Ductular Reaction in Liver Diseases: Pathological Mechanisms and Translational Significances. Hepatology 2019, 69:420-30.

[94] Kamimoto K, Nakano Y, Kaneko K, Miyajima A, Itoh T: Multidimensional imaging of liver injury repair in mice reveals fundamental role of the ductular reaction. Commun Biol 2020, 3:289.

[95] Ko S, Russell JO, Molina LM, Monga SP: Liver Progenitors and Adult Cell Plasticity in Hepatic Injury and Repair: Knowns and Unknowns. Annu Rev Pathol 2020, 15:23-50.

[96] Clerbaux LA, Manco R, Van Hul N, Bouzin C, Sciarra A, Sempoux C, Theise ND, Leclercq IA: Invasive Ductular Reaction Operates Hepatobiliary Junctions upon Hepatocellular Injury in Rodents and Humans. Am J Pathol 2019, 189:1569-81.

[97] Sun T, Annunziato S, Tchorz JS: Hepatic ductular reaction: a double-edged sword. Aging (Albany NY) 2019, 11:9223-4.

[98] Wilson DB, Rudnick DA: Invasive Ductular Reaction: Form and Function. Am J Pathol 2019, 189:1501-4.

[99] Jin L, Huang H, Ni J, Shen J, Liu Z, Li L, Fu S, Yan J, Hu B: Shh-Yap signaling controls hepatic ductular reactions in CCl4 -induced liver injury. Environ Toxicol 2021, 36:194-203.

[100] Planas-Paz L, Sun T, Pikiolek M, Cochran NR, Bergling S, Orsini V, Yang Z, Sigoillot F, Jetzer J, Syed M, Neri M, Schuierer S, Morelli L, Hoppe PS, Schwarzer W, Cobos CM, Alford JL, Zhang L, Cuttat R, Waldt A, Carballido-Perrig N, Nigsch F, Kinzel B, Nicholson TB, Yang Y, Mao X, Terracciano LM, Russ C, Reece-Hoyes JS, Gubser Keller C, Sailer AW, Bouwmeester T, Greenbaum LE, Lugus JJ, Cong F, McAllister G, Hoffman GR, Roma G, Tchorz JS: YAP, but Not RSPO-LGR4/5, Signaling in Biliary Epithelial Cells Promotes a Ductular Reaction in Response to Liver Injury. Cell Stem Cell 2019, 25:39-53 e10.

[101] Pi L, Robinson PM, Jorgensen M, Oh S-H, Brown AR, Weinreb PH, Trinh TL, Yianni P, Liu C, Leask A, Violette SM, Scott EW, Schultz GS, Petersen BE: Connective tissue growth factor and integrin αvβ6: a new pair of regulators critical for ductular reaction and biliary fibrosis in mice. Hepatology 2015, 61:678-91.

[102] Bai H, Zhang N, Xu Y, Chen Q, Khan M, Potter JJ, Nayar SK, Cornish T, Alpini G, Bronk S, Pan D, Anders RA: Yes-associated protein regulates the hepatic response after bile duct ligation. Hepatology 2012, 56:1097-107.

[103] Yokoda RT, Rodriguez EA: Review: Pathogenesis of cholestatic liver diseases. World J Hepatol 2020, 12:423-35.

[104] Lazaridis KN, LaRusso NF: The Cholangiopathies. Mayo Clin Proc 2015, 90:791-800.

[105] Alvaro D, Mancino MG, Glaser S, Gaudio E, Marzioni M, Francis H, Alpini G: Proliferating cholangiocytes: a neuroendocrine compartment in the diseased liver. Gastroenterology 2007, 132:415-31.

[106] Meng L, Quezada M, Levine P, Han Y, McDaniel K, Zhou T, Lin E, Glaser S, Meng F, Francis H, Alpini G: Functional role of cellular senescence in biliary injury. Am J Pathol 2015, 185:602-9.

[107] Tabibian JH, O'Hara SP, Splinter PL, Trussoni CE, LaRusso NF: Cholangiocyte senescence by way of N-ras activation is a characteristic of primary sclerosing cholangitis. Hepatology 2014, 59:2263-75.

[108] Li Z-Q, Wu W-R, Zhao C, Zhao C, Zhang X-L, Yang Z, Pan J, Si W-K: CCN1/Cyr61 enhances the function of hepatic stellate cells in promoting the progression of hepatocellular carcinoma. Int J Mol Med 2017.

[109] Kim KH, Chen CC, Alpini G, Lau LF: CCN1 induces hepatic ductular reaction through integrin alphavbeta(5)-mediated activation of NF-kappaB. J Clin Invest 2015, 125:1886-900.

[110] Xia X, Demorrow S, Francis H, Glaser S, Alpini G, Marzioni M, Fava G, Lesage G: Cholangiocyte injury and ductopenic syndromes. Semin Liver Dis 2007, 27:401-12.

[111] Michalopoulos GK, Barua L, Bowen WC: Transdifferentiation of rat hepatocytes into biliary cells after bile duct ligation and toxic biliary injury. Hepatology 2005, 41:535-44.

[112] Sekiya S, Suzuki A: Hepatocytes, rather than cholangiocytes, can be the major source of primitive ductules in the chronically injured mouse liver. Am J Pathol 2014, 184:1468-78.

[113] Yanger K, Zong Y, Maggs LR, Shapira SN, Maddipati R, Aiello NM, Thung SN, Wells RG, Greenbaum LE, Stanger BZ: Robust cellular reprogramming occurs spontaneously during liver regeneration. Genes Dev 2013, 27:719-24.

[114] Okabe H, Yang J, Sylakowski K, Yovchev M, Miyagawa Y, Nagarajan S, Chikina M, Thompson M, Oertel M, Baba H, Monga SP, Nejak-Bowen KN: Wnt signaling regulates hepatobiliary repair following cholestatic liver injury in mice. Hepatology 2016, 64:1652-66.

[115] Lin S, Nascimento EM, Gajera CR, Chen L, Neuhöfer P, Garbuzov A, Wang S, Artandi SE: Distributed hepatocytes expressing telomerase repopulate the liver in homeostasis and injury. Nature 2018, 556:244-8.

[116] Tarlow BD, Pelz C, Naugler WE, Wakefield L, Wilson EM, Finegold MJ, Grompe M: Bipotential adult liver progenitors are derived from chronically injured mature hepatocytes. Cell Stem Cell 2014, 15:605-18.

[117] Andersson ER, Chivukula IV, Hankeova S, Sjoqvist M, Tsoi YL, Ramskold D, Masek J, Elmansuri A, Hoogendoorn A, Vazquez E, Storvall H, Netusilova J, Huch M, Fischler B, Ellis E, Contreras A, Nemeth A, Chien KC, Clevers H, Sandberg R, Bryja V, Lendahl U: Mouse Model of Alagille Syndrome and Mechanisms of Jagged1 Missense Mutations. Gastroenterology 2018, 154:1080-95.

[118] Thakurdas SM, Lopez MF, Kakuda S, Fernandez-Valdivia R, Zarrin-Khameh N, Haltiwanger RS, Jafar-Nejad H: Jagged1 heterozygosity in mice results in a congenital cholangiopathy which is reversed by concomitant deletion of one copy of Poglut1 (Rumi). Hepatology 2016, 63:550-65.

[119] Mitchell E, Gilbert M, Loomes KM: Alagille Syndrome. Clin Liver Dis 2018, 22:625-41.

[120] Tschaharganeh DF, Chen X, Latzko P, Malz M, Gaida MM, Felix K, Ladu S, Singer S, Pinna F, Gretz N, Sticht C, Tomasi ML, Delogu S, Evert M, Fan B, Ribback S, Jiang L,

Brozzetti S, Bergmann F, Dombrowski F, Schirmacher P, Calvisi DF, Breuhahn K: Yes-associated protein up-regulates Jagged-1 and activates the Notch pathway in human hepatocellular carcinoma. Gastroenterology 2013, 144:1530-42.e12.

[121] Claudel T, Zollner G, Wagner M, Trauner M: Role of nuclear receptors for bile acid metabolism, bile secretion, cholestasis, and gallstone disease. Biochim Biophys Acta 2011, 1812:867-78.

[122] Wagner M, Zollner G, Trauner M: Nuclear receptor regulation of the adaptive response of bile acid transporters in cholestasis. Semin Liver Dis 2010, 30:160-77.

[123] Nuno-Lambarri N, Barbero-Becerra VJ, Uribe M, Chavez-Tapia NC: Elevated cholesterol levels have a poor prognosis in a cholestasis scenario. J Biochem Mol Toxicol 2017, 31:1-6.

[124] Chisholm JW, Nation P, Dolphin PJ, Agellon LB: High plasma cholesterol in drug-induced cholestasis is associated with enhanced hepatic cholesterol synthesis. Am J Physiol 1999, 276:G1165-73.

[125] Arab JP, Cabrera D, Arrese M: Bile Acids in Cholestasis and its Treatment. Ann Hepatol 2017, 16:s53-s7.

[126] Schaap FG, Trauner M, Jansen PL: Bile acid receptors as targets for drug development. Nat Rev Gastroenterol Hepatol 2014, 11:55-67.

[127] Chiang JYL: Bile acid metabolism and signaling in liver disease and therapy. Liver Research 2017, 1:3-9.

[128] Zhao Q, Yang R, Wang J, Hu DD, Li F: PPARalpha activation protects against cholestatic liver injury. Sci Rep 2017, 7:9967.

[129] Ghonem NS, Assis DN, Boyer JL: Fibrates and cholestasis. Hepatology 2015, 62:635-43.

[130] Zollner G, Trauner M: Nuclear receptors as therapeutic targets in cholestatic liver diseases. Br J Pharmacol 2009, 156:7-27.

[131] Mia MM, Cibi DM, Abdul Ghani SAB, Song W, Tee N, Ghosh S, Mao J, Olson EN, Singh MK: YAP/TAZ deficiency reprograms macrophage phenotype and improves infarct healing and cardiac function after myocardial infarction. PLoS Biol 2020, 18:e3000941.

[132] Kosters A, Karpen SJ: The role of inflammation in cholestasis: clinical and basic aspects. Semin Liver Dis 2010, 30:186-94.

[133] Katzenellenbogen M, Pappo O, Barash H, Klopstock N, Mizrahi L, Olam D, Jacob-Hirsch J, Amariglio N, Rechavi G, Mitchell LA, Kohen R, Domany E, Galun E, Goldenberg D: Multiple adaptive mechanisms to chronic liver disease revealed at early stages of liver carcinogenesis in the Mdr2-knockout mice. Cancer Res 2006, 66:4001-10.

[134] Lanton T, Shriki A, Nechemia-Arbely Y, Abramovitch R, Levkovitch O, Adar R, Rosenberg N, Paldor M, Goldenberg D, Sonnenblick A, Peled A, Rose-John S, Galun E, Axelrod JH: Interleukin 6-dependent genomic instability heralds accelerated carcinogenesis following liver regeneration on a background of chronic hepatitis. Hepatology 2017, 65:1600-11.

[135] Barash H, E RG, Edrei Y, Ella E, Israel A, Cohen I, Corchia N, Ben-Moshe T, Pappo O, Pikarsky E, Goldenberg D, Shiloh Y, Galun E, Abramovitch R: Accelerated carcinogenesis following liver regeneration is associated with chronic inflammation-induced double-strand DNA breaks. Proc Natl Acad Sci U S A 2010, 107:2207-12.

[136] Katzenellenbogen M, Mizrahi L, Pappo O, Klopstock N, Olam D, Jacob-Hirsch J, Amariglio N, Rechavi G, Domany E, Galun E, Goldenberg D: Molecular mechanisms of liver carcinogenesis in the mdr2-knockout mice. Mol Cancer Res 2007, 5:1159-70.

[137] Katzenellenbogen M, Mizrahi L, Pappo O, Klopstock N, Olam D, Barash H, Domany E, Galun E, Goldenberg D: Molecular mechanisms of the chemopreventive effect on hepatocellular carcinoma development in Mdr2 knockout mice. Mol Cancer Ther 2007, 6:1283-91.

[138] Anakk S, Bhosale M, Schmidt VA, Johnson RL, Finegold MJ, Moore DD: Bile acids activate YAP to promote liver carcinogenesis. Cell Rep 2013, 5:1060-9.

[139] Sokol RJ, Stall C: Anthropometric evaluation of children with chronic liver disease. Am J Clin Nutr 1990, 52:203-8.

[140] Subramaniam P, Knisely A, Portmann B, Qureshi SA, Aclimandos WA, Karani JB, Baker AJ: Diagnosis of Alagille syndrome-25 years of experience at King's College Hospital. J Pediatr Gastroenterol Nutr 2011, 52:84-9.

[141] Kamath BM, Ye W, Goodrich NP, Loomes KM, Romero R, Heubi JE, Leung DH, Spinner NB, Piccoli DA, Alonso EM, Guthery SL, Karpen SJ, Mack CL, Molleston JP, Murray KF, Rosenthal P, Squires JE, Teckman J, Wang KS, Thompson RJ, Magee JC, Sokol RJ, (ChiLDReN) ftCLDRN: Outcomes of Childhood Cholestasis in Alagille Syndrome: Results of a Multicenter Observational Study. Hepatology Communications 2020, 4:387-98.

[142] Emerick KM, Rand EB, Goldmuntz E, Krantz ID, Spinner NB, Piccoli DA: Features of Alagille syndrome in 92 patients: frequency and relation to prognosis. Hepatology 1999, 29:822-9.

[143] Lykavieris P, Hadchouel M, Chardot C, Bernard O: Outcome of liver disease in children with Alagille syndrome: a study of 163 patients. Gut 2001, 49:431-5.

[144] Kamath BM, Munoz PS, Bab N, Baker A, Chen Z, Spinner NB, Piccoli DA: A longitudinal study to identify laboratory predictors of liver disease outcome in Alagille syndrome. J Pediatr Gastroenterol Nutr 2010, 50:526-30.

[145] Spinner NB, Colliton RP, Crosnier C, Krantz ID, Hadchouel M, Meunier-Rotival M: Jagged1 mutations in alagille syndrome. Hum Mutat 2001, 17:18-33.

[146] Crosnier C, Driancourt C, Raynaud N, Dhorne-Pollet S, Pollet N, Bernard O, Hadchouel M, Meunier-Rotival M: Mutations in JAGGED1 gene are predominantly sporadic in Alagille syndrome. Gastroenterology 1999, 116:1141-8.

[147] Ryan MJ, Bales C, Nelson A, Gonzalez DM, Underkoffler L, Segalov M, Wilson-Rawls J, Cole SE, Moran JL, Russo P, Spinner NB, Kusumi K, Loomes KM: Bile duct proliferation in Jag1/fringe heterozygous mice identifies candidate modifiers of the Alagille syndrome hepatic phenotype. Hepatology 2008, 48:1989-97.

[148] Tsai EA, Gilbert MA, Grochowski CM, Underkoffler LA, Meng H, Zhang X, Wang MM, Shitaye H, Hankenson KD, Piccoli D, Lin H, Kamath BM, Devoto M, Spinner NB, Loomes KM: THBS2 Is a Candidate Modifier of Liver Disease Severity in Alagille Syndrome. Cell Mol Gastroenterol Hepatol 2016, 2:663-75 e2.

[149] Bell D, Ranganathan S, Tao J, Monga SP: Novel Advances in Understanding of Molecular Pathogenesis of Hepatoblastoma: A Wnt/β-Catenin Perspective. Gene Expr 2017, 17:141-54.

[150] Czauderna P, Lopez-Terrada D, Hiyama E, Häberle B, Malogolowkin MH, Meyers RL: Hepatoblastoma state of the art: pathology, genetics, risk stratification, and chemotherapy. Curr Opin Pediatr 2014, 26:19-28.

[151] Feng J, Polychronidis G, Heger U, Frongia G, Mehrabi A, Hoffmann K: Incidence trends and survival prediction of hepatoblastoma in children: a population-based study. Cancer Commun (Lond) 2019, 39:62.

[152] López-Terrada D, Alaggio R, de Dávila MT, Czauderna P, Hiyama E, Katzenstein H, Leuschner I, Malogolowkin M, Meyers R, Ranganathan S, Tanaka Y, Tomlinson G, Fabrè M, Zimmermann A, Finegold MJ, Children's Oncology Group Liver Tumor C: Towards an international pediatric liver tumor consensus classification: proceedings of the Los Angeles COG liver tumors symposium. Mod Pathol 2014, 27:472-91.

[153] Ranganathan S, Lopez-Terrada D, Alaggio R: Hepatoblastoma and Pediatric Hepatocellular Carcinoma: An Update. Pediatr Dev Pathol 2020, 23:79-95.

[154] Hafberg E, Borinstein SC, Alexopoulos SP: Contemporary management of hepatoblastoma. Curr Opin Organ Transplant 2019, 24:113-7.

[155] Sunil BJ, Palaniappan R, Venkitaraman B, Ranganathan R: Surgical Resection for Hepatoblastoma-Updated Survival Outcomes. J Gastrointest Cancer 2017.

[156] Trobaugh-Lotrario AD, Meyers RL, Tiao GM, Feusner JH: Pediatric liver transplantation for hepatoblastoma. Transl Gastroenterol Hepatol 2016, 1:44.

[157] Meyers RL, Maibach R, Hiyama E, Haberle B, Krailo M, Rangaswami A, Aronson DC, Malogolowkin MH, Perilongo G, von Schweinitz D, Ansari M, Lopez-Terrada D, Tanaka Y, Alaggio R, Leuschner I, Hishiki T, Schmid I, Watanabe K, Yoshimura K, Feng Y, Rinaldi E, Saraceno D, Derosa M, Czauderna P: Risk-stratified staging in paediatric hepatoblastoma: a unified analysis from the Children's Hepatic tumors International Collaboration. Lancet Oncol 2017, 18:122-31.

[158] Czauderna P, Haeberle B, Hiyama E, Rangaswami A, Krailo M, Maibach R, Rinaldi E, Feng Y, Aronson D, Malogolowkin M, Yoshimura K, Leuschner I, Lopez-Terrada D, Hishiki T, Perilongo G, von Schweinitz D, Schmid I, Watanabe K, Derosa M, Meyers R: The Children's Hepatic tumors International Collaboration (CHIC): Novel global rare tumor database yields new prognostic factors in hepatoblastoma and becomes a research model. Eur J Cancer 2016, 52:92-101.

[159] Cairo S, Armengol C, Maibach R, Haberle B, Becker K, Carrillo-Reixach J, Guettier C, Vokuhl C, Schmid I, Buendia MA, Branchereau S, von Schweinitz D, Kappler R: A combined clinical and biological risk classification improves prediction of outcome in hepatoblastoma patients. Eur J Cancer 2020, 141:30-9.

[160] Buendia MA, Armengol C, Cairo S: Molecular classification of hepatoblastoma and prognostic value of the HB 16-gene signature. Hepatology 2017, 66:1351-2.

[161] Eichenmüller M, Trippel F, Kreuder M, Beck A, Schwarzmayr T, Häberle B, Cairo S, Leuschner I, von Schweinitz D, Strom TM, Kappler R: The genomic landscape of hepatoblastoma and their progenies with HCC-like features. J Hepatol 2014, 61:1312-20.

[162] Cairo S, Armengol C, De Reyniès A, Wei Y, Thomas E, Renard C-A, Goga A, Balakrishnan A, Semeraro M, Gresh L, Pontoglio M, Strick-Marchand H, Levillayer F, Nouet Y, Rickman D, Gauthier F, Branchereau S, Brugières L, Laithier V, Bouvier R, Boman F, Basso G, Michiels J-F, Hofman P, Arbez-Gindre F, Jouan H, Rousselet-Chapeau M-C, Berrebi D, Marcellin L, Plenat F, Zachar D, Joubert M, Selves J, Pasquier D, Bioulac-Sage P, Grotzer M, Childs M, Fabre M, Buendia M-A: Hepatic stem-like phenotype and interplay of Wnt/beta-catenin and Myc signaling in aggressive childhood liver cancer. Cancer Cell 2008, 14:471-84.

[163] Sumazin P, Chen Y, Trevino LR, Sarabia SF, Hampton OA, Patel K, Mistretta TA, Zorman B, Thompson P, Heczey A, Comerford S, Wheeler DA, Chintagumpala M, Meyers R, Rakheja D, Finegold MJ, Tomlinson G, Parsons DW, Lopez-Terrada D: Genomic analysis of hepatoblastoma identifies distinct molecular and prognostic subgroups. Hepatology 2017, 65:104-21.

[164] Molina L, Bell D, Tao J, Preziosi M, Pradhan-Sundd T, Singh S, Poddar M, Luo J, Ranganathan S, Chikina M, Monga SP: Hepatocyte-Derived Lipocalin 2 Is a Potential Serum Biomarker Reflecting Tumor Burden in Hepatoblastoma. Am J Pathol 2018.

[165] Adebayo Michael AO, Ko S, Tao J, Moghe A, Yang H, Xu M, Russell JO, Pradhan-Sundd T, Liu S, Singh S, Poddar M, Monga JS, Liu P, Oertel M, Ranganathan S, Singhi A, Rebouissou S, Zucman-Rossi J, Ribback S, Calvisi D, Qvartskhava N, Gorg B, Haussinger D, Chen X, Monga SP: Inhibiting Glutamine-Dependent mTORC1 Activation Ameliorates Liver Cancers Driven by beta-Catenin Mutations. Cell Metab 2019.

[166] Park Y-Y, Sohn BH, Johnson RL, Kang M-H, Kim SB, Shim J-J, Mangala LS, Kim JH, Yoo JE, Rodriguez-Aguayo C, Pradeep S, Hwang JE, Jang H-J, Lee H-S, Rupaimoole R, Lopez-Berestein G, Jeong W, Park IS, Park YN, Sood AK, Mills GB, Lee J-S: Yes-associated protein 1 and transcriptional coactivator with PDZ-binding motif activate the mammalian target of rapamycin complex 1 pathway by regulating amino acid transporters in hepatocellular carcinoma. Hepatology 2016, 63:159-72.

[167] Tumaneng K, Schlegelmilch K, Russell RC, Yimlamai D, Basnet H, Mahadevan N, Fitamant J, Bardeesy N, Camargo FD, Guan K-L: YAP mediates crosstalk between the Hippo and PI(3)K–TOR pathways by suppressing PTEN via miR-29. Nat Cell Biol 2012, 14:1322-9.

[168] Molina L, Yang H, Adebayo Michael AO, Oertel M, Bell A, Singh S, Chen X, Tao J, Monga SPS: mTOR inhibition affects Yap1-beta-catenin-induced hepatoblastoma growth and development. Oncotarget 2019, 10:1475-90.

[169] Tharehalli U, Svinarenko M, Kraus JM, Kuhlwein SD, Szekely R, Kiesle U, Scheffold A, Barth TFE, Kleger A, Schirmbeck R, Kestler HA, Seufferlein T, Oswald F, Katz SF, Lechel A: YAP Activation Drives Liver Regeneration after Cholestatic Damage Induced by Rbpj Deletion. Int J Mol Sci 2018, 19.

[170] Reginensi A, Scott RP, Gregorieff A, Bagherie-Lachidan M, Chung C, Lim DS, Pawson T, Wrana J, McNeill H: Yap- and Cdc42-dependent nephrogenesis and morphogenesis during mouse kidney development. PLoS Genet 2013, 9:e1003380.

[171] Bray NL, Pimentel H, Melsted P, Pachter L: Near-optimal probabilistic RNA-seq quantification. Nat Biotechnol 2016, 34:525-7.

[172] Li H, Handsaker B, Wysoker A, Fennell T, Ruan J, Homer N, Marth G, Abecasis G, Durbin R, Genome Project Data Processing S: The Sequence Alignment/Map format and SAMtools. Bioinformatics 2009, 25:2078-9.

[173] La Manno G, Soldatov R, Zeisel A, Braun E, Hochgerner H, Petukhov V, Lidschreiber K, Kastriti ME, Lonnerberg P, Furlan A, Fan J, Borm LE, Liu Z, van Bruggen D, Guo J, He X, Barker R, Sundstrom E, Castelo-Branco G, Cramer P, Adameyko I, Linnarsson S, Kharchenko PV: RNA velocity of single cells. Nature 2018, 560:494-8.

[174] Stuart T, Butler A, Hoffman P, Hafemeister C, Papalexi E, Mauck WM, 3rd, Hao Y, Stoeckius M, Smibert P, Satija R: Comprehensive Integration of Single-Cell Data. Cell 2019, 177:1888-902 e21.

[175] Trapnell C, Cacchiarelli D, Grimsby J, Pokharel P, Li S, Morse M, Lennon NJ, Livak KJ, Mikkelsen TS, Rinn JL: The dynamics and regulators of cell fate decisions are revealed by pseudotemporal ordering of single cells. Nat Biotechnol 2014, 32:381-6.

[176] Qi M, Li W, Tsang IW, Yijun S: Principal Graph and Structure Learning Based on Reversed Graph Embedding. IEEE Trans Pattern Anal Mach Intell 2017, 39:2227-41.

[177] Schindelin J, Arganda-Carreras I, Frise E, Kaynig V, Longair M, Pietzsch T, Preibisch S, Rueden C, Saalfeld S, Schmid B, Tinevez JY, White DJ, Hartenstein V, Eliceiri K, Tomancak P, Cardona A: Fiji: an open-source platform for biological-image analysis. Nat Methods 2012, 9:676-82.

[178] Chung K, Wallace J, Kim SY, Kalyanasundaram S, Andalman AS, Davidson TJ, Mirzabekov JJ, Zalocusky KA, Mattis J, Denisin AK, Pak S, Bernstein H, Ramakrishnan C, Grosenick L, Gradinaru V, Deisseroth K: Structural and molecular interrogation of intact biological systems. Nature 2013, 497:332-7.

[179] Muntifering M, Castranova D, Gibson GA, Meyer E, Kofron M, Watson AM: Clearing for Deep Tissue Imaging. Curr Protoc Cytom 2018, 86:e38.

[180] Murray E, Cho JH, Goodwin D, Ku T, Swaney J, Kim SY, Choi H, Park YG, Park JY, Hubbert A, McCue M, Vassallo S, Bakh N, Frosch MP, Wedeen VJ, Seung HS, Chung K: Simple, Scalable Proteomic Imaging for High-Dimensional Profiling of Intact Systems. Cell 2015, 163:1500-14.

[181] Susaki EA, Tainaka K, Perrin D, Kishino F, Tawara T, Watanabe TM, Yokoyama C, Onoe H, Eguchi M, Yamaguchi S, Abe T, Kiyonari H, Shimizu Y, Miyawaki A, Yokota H, Ueda HR: Whole-brain imaging with single-cell resolution using chemical cocktails and computational analysis. Cell 2014, 157:726-39.

[182] Watson AM, Rose AH, Gibson GA, Gardner CL, Sun C, Reed DS, Lam LKM, St Croix CM, Strick PL, Klimstra WB, Watkins SC: Ribbon scanning confocal for high-speed high-resolution volume imaging of brain. PLoS One 2017, 12:e0180486.

[183] Tonsberg H, Holm R, Bjerregaard TG, Boll JB, Jacobsen J, Mullertz A: An updated and simplified method for bile duct cannulation of rats. Lab Anim 2010, 44:373-6.

[184] Plaa GL, Becker BA: Demonstration of bile stasis in the mouse by a direct and an indirect method. J Appl Physiol 1965, 20:534-7.

[185] Zhu J, Wang P, Shehu AI, Lu J, Bi H, Ma X: Identification of Novel Pathways in Idelalisib Metabolism and Bioactivation. Chem Res Toxicol 2018, 31:548-55.

[186] Jiang C, Xie C, Li F, Zhang L, Nichols RG, Krausz KW, Cai J, Qi Y, Fang ZZ, Takahashi S, Tanaka N, Desai D, Amin SG, Albert I, Patterson AD, Gonzalez FJ: Intestinal farnesoid X receptor signaling promotes nonalcoholic fatty liver disease. J Clin Invest 2015, 125:386-402.

[187] Pradhan-Sundd T, Vats R, Russell JO, Singh S, Michael AA, Molina L, Kakar S, Cornuet P, Poddar M, Watkins SC, Nejak-Bowen KN, Monga SP, Sundd P: Dysregulated Bile Transporters and Impaired Tight Junctions During Chronic Liver Injury in Mice. Gastroenterology 2018, 155:1218-32 e24.

[188] Subramanian A, Tamayo P, Mootha VK, Mukherjee S, Ebert BL, Gillette MA, Paulovich A, Pomeroy SL, Golub TR, Lander ES, Mesirov JP: Gene set enrichment analysis: a knowledge-based approach for interpreting genome-wide expression profiles. Proceedings of the National Academy of Sciences of the United States of America 2005, 102:15545-50.

[189] Kuleshov MV, Jones MR, Rouillard AD, Fernandez NF, Duan Q, Wang Z, Koplev S, Jenkins SL, Jagodnik KM, Lachmann A, McDermott MG, Monteiro CD, Gundersen GW, Ma'ayan A: Enrichr: a comprehensive gene set enrichment analysis web server 2016 update. Nucleic Acids Res 2016, 44:W90-7.

[190] Chen EY, Tan CM, Kou Y, Duan Q, Wang Z, Meirelles GV, Clark NR, Ma'ayan A: Enrichr: interactive and collaborative HTML5 gene list enrichment analysis tool. BMC Bioinformatics 2013, 14:128.

[191] Davis CA, Hitz BC, Sloan CA, Chan ET, Davidson JM, Gabdank I, Hilton JA, Jain K, Baymuradov UK, Narayanan AK, Onate KC, Graham K, Miyasato SR, Dreszer TR, Strattan JS, Jolanki O, Tanaka FY, Cherry JM: The Encyclopedia of DNA elements (ENCODE): data portal update. Nucleic Acids Res 2018, 46:D794-D801.

[192] Consortium EP: An integrated encyclopedia of DNA elements in the human genome. Nature 2012, 489:57-74.

[193] Bolger AM, Lohse M, Usadel B: Trimmomatic: a flexible trimmer for Illumina sequence data. Bioinformatics 2014, 30:2114-20.

[194] Li H, Durbin R: Fast and accurate short read alignment with Burrows-Wheeler transform. Bioinformatics 2009, 25:1754-60.

[195] Zhang Y, Liu T, Meyer CA, Eeckhoute J, Johnson DS, Bernstein BE, Nusbaum C, Myers RM, Brown M, Li W, Liu XS: Model-based analysis of ChIP-Seq (MACS). Genome Biol 2008, 9:R137.

[196] Zhu LJ, Gazin C, Lawson ND, Pages H, Lin SM, Lapointe DS, Green MR: ChIPpeakAnno: a Bioconductor package to annotate ChIP-seq and ChIP-chip data. BMC Bioinformatics 2010, 11:237.

[197] Zhu LJ: Integrative analysis of ChIP-chip and ChIP-seq dataset. Methods Mol Biol 2013, 1067:105-24.

[198] Yu G, Wang LG, He QY: ChIPseeker: an R/Bioconductor package for ChIP peak annotation, comparison and visualization. Bioinformatics 2015, 31:2382-3.

[199] Postic C, Magnuson MA: DNA excision in liver by an albumin-Cre transgene occurs progressively with age. Genesis 2000, 26:149-50.

[200] Lee CS, Friedman JR, Fulmer JT, Kaestner KH: The initiation of liver development is dependent on Foxa transcription factors. Nature 2005, 435:944-7.

[201] Mansini AP, Peixoto E, Thelen KM, Gaspari C, Jin S, Gradilone SA: The cholangiocyte primary cilium in health and disease. Biochim Biophys Acta Mol Basis Dis 2018, 1864:1245-53.

[202] Pablo Arab J, Cabrera D, Arrese M: Bile Acids in Cholestasis and its Treatment. Ann Hepatol 2017, 16 Suppl 1:S53-S7.

[203] Heuman DM: Quantitative estimation of the hydrophilic-hydrophobic balance of mixed bile salt solutions. J Lipid Res 1989, 30:719-30.

[204] Airik M, Schuler M, McCourt B, Weiss AC, Herdman N, Ludtke TH, Widmeier E, Stolz DB, Nejak-Bowen KN, Yimlamai D, Wu YL, Kispert A, Airik R, Hildebrandt F: Loss of Anks6 leads to YAP deficiency and liver abnormalities. Hum Mol Genet 2020, 29:3064-80.

[205] Wu N, Nguyen Q, Wan Y, Zhou T, Venter J, Frampton GA, DeMorrow S, Pan D, Meng F, Glaser S, Alpini G, Bai H: The Hippo signaling functions through the Notch signaling to regulate intrahepatic bile duct development in mammals. Lab Invest 2017, 97:843-53.

[206] Antoniou A, Raynaud P, Cordi S, Zong Y, Tronche F, Stanger BZ, Jacquemin P, Pierreux CE, Clotman F, Lemaigre FP: Intrahepatic bile ducts develop according to a new mode of tubulogenesis regulated by the transcription factor SOX9. Gastroenterology 2009, 136:2325-33.

[207] Walter TJ, Vanderpool C, Cast AE, Huppert SS: Intrahepatic bile duct regeneration in mice does not require Hnf6 or Notch signaling through Rbpj. Am J Pathol 2014, 184:1479-88.

[208] Li X, Tao J, Cigliano A, Sini M, Calderaro J, Azoulay D, Wang C, Liu Y, Jiang L, Evert K, Demartis MI, Ribback S, Utpatel K, Dombrowski F, Evert M, Calvisi DF, Chen X: Co-activation of PIK3CA and Yap promotes development of hepatocellular and cholangiocellular tumors in mouse and human liver. Oncotarget 2015, 6:10102-15.

[209] Paranjpe S, Bowen WC, Mars WM, Orr A, Haynes MM, DeFrances MC, Liu S, Tseng GC, Tsagianni A, Michalopoulos GK: Combined systemic elimination of MET and epidermal growth factor receptor signaling completely abolishes liver regeneration and leads to liver decompensation. Hepatology 2016, 64:1711-24.

[210] Brasen JH, Mederacke YS, Schmitz J, Diahovets K, Khalifa A, Hartleben B, Person F, Wiech T, Steenbergen E, Grosshennig A, Manns MP, Schmitt R, Mederacke I: Cholemic Nephropathy Causes Acute Kidney Injury and Is Accompanied by Loss of Aquaporin 2 in Collecting Ducts. Hepatology 2019, 69:2107-19.

[211] Fickert P, Krones E, Pollheimer MJ, Thueringer A, Moustafa T, Silbert D, Halilbasic E, Yang M, Jaeschke H, Stokman G, Wells RG, Eller K, Rosenkranz AR, Eggertsen G, Wagner CA, Langner C, Denk H, Trauner M: Bile acids trigger cholemic nephropathy in common bile-duct-ligated mice. Hepatology 2013, 58:2056-69.

[212] Mandorfer M, Hecking M: The Renaissance of Cholemic Nephropathy: A Likely Underestimated Cause of Renal Dysfunction in Liver Disease. Hepatology 2019, 69:1858-60.

[213] Krones E, Pollheimer MJ, Rosenkranz AR, Fickert P: Cholemic nephropathy - Historical notes and novel perspectives. Biochim Biophys Acta Mol Basis Dis 2018, 1864:1356-66.

[214] Sood V, Lal BB, Lata S, Rastogi A, Alam S: Cholemic or Bile Cast Nephropathy in a Child with Liver Failure. J Clin Exp Hepatol 2017, 7:373-5.

[215] Power RM, Huisken J: A guide to light-sheet fluorescence microscopy for multiscale imaging. Nat Methods 2017, 14:360-73.

[216] Watson AM, Watkins SC: Massive volumetric imaging of cleared tissue: The necessary tools to be successful. Int J Biochem Cell Biol 2019, 112:76-8.

[217] Renier N, Wu Z, Simon DJ, Yang J, Ariel P, Tessier-Lavigne M: iDISCO: a simple, rapid method to immunolabel large tissue samples for volume imaging. Cell 2014, 159:896-910.

[218] Yang B, Treweek JB, Kulkarni RP, Deverman BE, Chen CK, Lubeck E, Shah S, Cai L, Gradinaru V: Single-cell phenotyping within transparent intact tissue through whole-body clearing. Cell 2014, 158:945-58.

[219] Hama H, Kurokawa H, Kawano H, Ando R, Shimogori T, Noda H, Fukami K, Sakaue-Sawano A, Miyawaki A: Scale: a chemical approach for fluorescence imaging and reconstruction of transparent mouse brain. Nat Neurosci 2011, 14:1481-8.

[220] Richardson DS, Lichtman JW: Clarifying Tissue Clearing. Cell 2015, 162:246-57.

[221] Tainaka K, Kuno A, Kubota SI, Murakami T, Ueda HR: Chemical Principles in Tissue Clearing and Staining Protocols for Whole-Body Cell Profiling. Annu Rev Cell Dev Biol 2016, 32:713-41.

[222] Spalteholz W: Uber das Durchsichtigmachen von menschlichen und tierischen Praparaten: S. Hirzel, 1914.

[223] Dodt HU, Leischner U, Schierloh A, Jahrling N, Mauch CP, Deininger K, Deussing JM, Eder M, Zieglgansberger W, Becker K: Ultramicroscopy: three-dimensional visualization of neuronal networks in the whole mouse brain. Nat Methods 2007, 4:331-6.

[224] Erturk A, Lafkas D, Chalouni C: Imaging cleared intact biological systems at a cellular level by 3DISCO. J Vis Exp 2014.

[225] Damle-Vartak A, Begher-Tibbe B, Gunther G, Geisler F, Vartak N, Hengstler JG: Pipe-3D: A Pipeline Based on Immunofluorescence, 3D Confocal Imaging, Reconstructions, and Morphometry for Biliary Network Analysis in Cholestasis. Methods Mol Biol 2019, 1981:25-53.

[226] Oren R, Fellus-Alyagor L, Addadi Y, Bochner F, Gutman H, Blumenreich S, Dafni H, Dekel N, Neeman M, Lazar S: Whole Organ Blood and Lymphatic Vessels Imaging (WOBLI). Sci Rep 2018, 8:1412.

[227] Lee H, Park JH, Seo I, Park SH, Kim S: Improved application of the electrophoretic tissue clearing technology, CLARITY, to intact solid organs including brain, pancreas, liver, kidney, lung, and intestine. BMC Dev Biol 2014, 14:48.

[228] Khoradmehr A, Mazaheri F, Anvari M, Tamadon A: A Simple Technique for Three-Dimensional Imaging and Segmentation of Brain Vasculature U sing Fast Free-of-Acrylamide Clearing Tissue in Murine. Cell J 2019, 21:49-56.

[229] Epp JR, Niibori Y, Liz Hsiang HL, Mercaldo V, Deisseroth K, Josselyn SA, Frankland PW: Optimization of CLARITY for Clearing Whole-Brain and Other Intact Organs. eNeuro 2015, 2.

[230] Tainaka K, Murakami TC, Susaki EA, Shimizu C, Saito R, Takahashi K, Hayashi-Takagi A, Sekiya H, Arima Y, Nojima S, Ikemura M, Ushiku T, Shimizu Y, Murakami M, Tanaka KF, Iino M, Kasai H, Sasaoka T, Kobayashi K, Miyazono K, Morii E, Isa T, Fukayama M, Kakita A, Ueda HR: Chemical Landscape for Tissue Clearing Based on Hydrophilic Reagents. Cell Rep 2018, 24:2196-210 e9.

[231] Seglen PO: Preparation of isolated rat liver cells. Methods Cell Biol 1976, 13:29-83.

[232] Gores GJ, Kost LJ, LaRusso NF: The isolated perfused rat liver: conceptual and practical considerations. Hepatology 1986, 6:511-7.

[233] Zhan N, Adebayo Michael A, Wu K, Zeng G, Bell A, Tao J, Monga SP: THE EFFECT OF SELECTIVE C-MET INHIBITOR ON HCC IN THE MET-ACTIVE, β-CATENIN MUTATED MOUSE MODEL. Gene Expr 2018.

[234] Puliga E, Min Q, Tao J, Zhang R, Pradhan-Sundd T, Poddar M, Singh S, Columbano A, Yu J, Monga SP: Thyroid Hormone Receptor-beta Agonist GC-1 Inhibits Met-beta-Catenin-Driven Hepatocellular Cancer. Am J Pathol 2017, 187:2473-85.

[235] Tao J, Xu E, Zhao Y, Singh S, Li X, Couchy G, Chen X, Zucman-Rossi J, Chikina M, Monga SPS: Modeling a human hepatocellular carcinoma subset in mice through coexpression of met and point-mutant β-catenin. Hepatology 2016, 64:1587-605.

[236] Linabery AM, Ross JA: Trends in childhood cancer incidence in the U.S. (1992-2004). Cancer 2008, 112:416-32.

[237] Garber JE, Li FP, Kingston JE, Krush AJ, Strong LC, Finegold MJ, Bertario L, Bulow S, Filippone A, Jr., Gedde-Dahl T, Jr., et al.: Hepatoblastoma and familial adenomatous polyposis. J Natl Cancer Inst 1988, 80:1626-8.

[238] Cohen MM, Jr.: Beckwith-Wiedemann syndrome: historical, clinicopathological, and etiopathogenetic perspectives. Pediatr Dev Pathol 2005, 8:287-304.

[239] Kremer N, Walther AE, Tiao GM: Management of hepatoblastoma: an update. Curr Opin Pediatr 2014, 26:362-9.

[240] Armengol C, Cairo S, Fabre M, Buendia MA: Wnt signaling and hepatocarcinogenesis: the hepatoblastoma model. Int J Biochem Cell Biol 2011, 43:265-70.

[241] Koch A, Denkhaus D, Albrecht S, Leuschner I, von Schweinitz D, Pietsch T: Childhood hepatoblastomas frequently carry a mutated degradation targeting box of the beta-catenin gene. Cancer Res 1999, 59:269-73.

[242] Rebouissou S, Franconi A, Calderaro J, Letouzé E, Imbeaud S, Pilati C, Nault J-C, Couchy G, Laurent A, Balabaud C, Bioulac-Sage P, Zucman-Rossi J: Genotype-phenotype correlation of CTNNB1 mutations reveals different ß-catenin activity associated with liver tumor progression. Hepatology 2016, 64:2047-61.

[243] Hartmann W, Kuchler J, Koch A, Friedrichs N, Waha A, Endl E, Czerwitzki J, Metzger D, Steiner S, Wurst P, Leuschner I, von Schweinitz D, Buettner R, Pietsch T: Activation of phosphatidylinositol-3'-kinase/AKT signaling is essential in hepatoblastoma survival. Clin Cancer Res 2009, 15:4538-45.

[244] Wagner F, Henningsen B, Lederer C, Eichenmuller M, Godeke J, Muller-Hocker J, von Schweinitz D, Kappler R: Rapamycin blocks hepatoblastoma growth in vitro and in vivo implicating new treatment options in high-risk patients. Eur J Cancer 2012, 48:2442-50.

[245] McCormack FX, Inoue Y, Moss J, Singer LG, Strange C, Nakata K, Barker AF, Chapman JT, Brantly ML, Stocks JM, Brown KK, Lynch JP, 3rd, Goldberg HJ, Young LR, Kinder BW, Downey GP, Sullivan EJ, Colby TV, McKay RT, Cohen MM, Korbee L, Taveira-DaSilva AM, Lee HS, Krischer JP, Trapnell BC, National Institutes of Health Rare Lung Diseases C, Group MT: Efficacy and safety of sirolimus in lymphangioleiomyomatosis. N Engl J Med 2011, 364:1595-606.

[246] Zaza G, Granata S, Caletti C, Signorini L, Stallone G, Lupo A: mTOR Inhibition Role in Cellular Mechanisms. Transplantation 2018, 102:S3-S16.

[247] Gautier L, Cope L, Bolstad BM, Irizarry RA: affy--analysis of Affymetrix GeneChip data at the probe level. Bioinformatics 2004, 20:307-15.

[248] Sandberg R, Larsson O: Improved precision and accuracy for microarrays using updated probe set definitions. BMC Bioinformatics 2007, 8:48.

[249] Wu JaI, Rafael, with contributions from James MacDonald and Jeff Gentry: gcrma: Background Adjustment Using Sequence Information. R package version 2.54.0 ed, 2018.

[250] Gentleman R CV, Huber W, Hahne F: genefilter: methods for filtering genes from high-throughput experiments. R package version 1.64.0 ed, 2018.

[251] Gentleman R: annotate: Annotation for microarrays. R package version 1.60.0 ed, 2018.

[252] Carlson M: mouse4302.db: Affymetrix Mouse Genome 430 2.0 Array annotation data (chip mouse4302). R package version 3.2.3 ed, 2016.

[253] Wickham H: ggplot2: Elegant Graphics for Data Analysis. Springer-Verlag New York, 2016.

[254] Tang Y HM, Li W: ggfortify: Unified Interface to Visualize Statistical Result of Popular R Packages. The R Journal 82 2016:478-89.

[255] Ritchie ME, Phipson B, Wu D, Hu Y, Law CW, Shi W, Smyth GK: limma powers differential expression analyses for RNA-sequencing and microarray studies. Nucleic Acids Res 2015, 43:e47.

[256] Kupershmidt I, Su QJ, Grewal A, Sundaresh S, Halperin I, Flynn J, Shekar M, Wang H, Park J, Cui W, Wall GD, Wisotzkey R, Alag S, Akhtari S, Ronaghi M: Ontology-based meta-analysis of global collections of high-throughput public data. PLoS One 2010, 5.

[257] Liberzon A, Subramanian A, Pinchback R, Thorvaldsdottir H, Tamayo P, Mesirov JP: Molecular signatures database (MSigDB) 3.0. Bioinformatics 2011, 27:1739-40.

[258] Subramanian A, Tamayo P, Mootha VK, Mukherjee S, Ebert BL, Gillette MA, Paulovich A, Pomeroy SL, Golub TR, Lander ES, Mesirov JP: Gene set enrichment analysis: a knowledge-based approach for interpreting genome-wide expression profiles. Proc Natl Acad Sci U S A 2005, 102:15545-50.

[259] Hooks KB, Audoux J, Fazli H, Lesjean S, Ernault T, Dugot-Senant N, Leste-Lasserre T, Hagedorn M, Rousseau B, Danet C, Branchereau S, Brugieres L, Taque S, Guettier C, Fabre M, Rullier A, Buendia MA, Commes T, Grosset CF, Raymond AA: New insights into diagnosis and therapeutic options for proliferative hepatoblastoma. Hepatology 2018, 68:89-102.

[260] Hsiao LL, Dangond F, Yoshida T, Hong R, Jensen RV, Misra J, Dillon W, Lee KF, Clark KE, Haverty P, Weng Z, Mutter GL, Frosch MP, MacDonald ME, Milford EL, Crum CP, Bueno R, Pratt RE, Mahadevappa M, Warrington JA, Stephanopoulos G, Stephanopoulos G, Gullans SR: A compendium of gene expression in normal human tissues. Physiol Genomics 2001, 7:97-104.

[261] Chiarini F, Evangelisti C, McCubrey JA, Martelli AM: Current treatment strategies for inhibiting mTOR in cancer. Trends Pharmacol Sci 2015, 36:124-35.

[262] Carew JS, Kelly KR, Nawrocki ST: Mechanisms of mTOR inhibitor resistance in cancer therapy. Target Oncol 2011, 6:17-27.

[263] McLaughlin CC, Baptiste MS, Schymura MJ, Nasca PC, Zdeb MS: Maternal and infant birth characteristics and hepatoblastoma. Am J Epidemiol 2006, 163:818-28.

[264] Darbari A, Sabin KM, Shapiro CN, Schwarz KB: Epidemiology of primary hepatic malignancies in U.S. children. Hepatology 2003, 38:560-6.

[265] Perilongo G, Brown J, Shafford E, Brock P, De Camargo B, Keeling JW, Vos A, Philips A, Pritchard J, Plaschkes J: Hepatoblastoma presenting with lung metastases: treatment results of the first cooperative, prospective study of the International Society of Paediatric Oncology on childhood liver tumors. Cancer 2000, 89:1845-53.

[266] Meyers RL, Rowland JR, Krailo M, Chen Z, Katzenstein HM, Malogolowkin MH: Predictive power of pretreatment prognostic factors in children with hepatoblastoma: a report from the Children's Oncology Group. Pediatr Blood Cancer 2009, 53:1016-22.

[267] Cairo S, Armengol C, De Reynies A, Wei Y, Thomas E, Renard CA, Goga A, Balakrishnan A, Semeraro M, Gresh L, Pontoglio M, Strick-Marchand H, Levillayer F, Nouet Y, Rickman D, Gauthier F, Branchereau S, Brugieres L, Laithier V, Bouvier R, Boman F, Basso G, Michiels JF, Hofman P, Arbez-Gindre F, Jouan H, Rousselet-Chapeau MC, Berrebi D, Marcellin L, Plenat F, Zachar D, Joubert M, Selves J, Pasquier D, Bioulac-Sage P, Grotzer M, Childs M, Fabre M, Buendia MA: Hepatic stem-like phenotype and interplay of Wnt/beta-catenin and Myc signaling in aggressive childhood liver cancer. Cancer Cell 2008, 14:471-84.

[268] Dan YY, Riehle KJ, Lazaro C, Teoh N, Haque J, Campbell JS, Fausto N: Isolation of multipotent progenitor cells from human fetal liver capable of differentiating into liver and mesenchymal lineages. Proc Natl Acad Sci U S A 2006, 103:9912-7.

[269] Koch A, Weber N, Waha A, Hartmann W, Denkhaus D, Behrens J, Birchmeier W, von Schweinitz D, Pietsch T: Mutations and elevated transcriptional activity of conductin (AXIN2) in hepatoblastomas. J Pathol 2004, 204:546-54.

[270] Aretz S, Koch A, Uhlhaas S, Friedl W, Propping P, von Schweinitz D, Pietsch T: Should children at risk for familial adenomatous polyposis be screened for hepatoblastoma and children with apparently sporadic hepatoblastoma be screened for APC germline mutations? Pediatr Blood Cancer 2006, 47:811-8.

[271] Cairo S, Armengol C, Buendia MA: Activation of Wnt and Myc signaling in hepatoblastoma. Front Biosci (Elite Ed) 2012, 4:480-6.

[272] Li H, Wolfe A, Septer S, Edwards G, Zhong X, Abdulkarim AB, Ranganathan S, Apte U: Deregulation of Hippo kinase signalling in human hepatic malignancies. Liver Int 2012, 32:38-47.

[273] Camargo FD, Gokhale S, Johnnidis JB, Fu D, Bell GW, Jaenisch R, Brummelkamp TR: YAP1 increases organ size and expands undifferentiated progenitor cells. Curr Biol 2007, 17:2054-60.

[274] Tan X, Behari J, Cieply B, Michalopoulos GK, Monga SP: Conditional deletion of beta-catenin reveals its role in liver growth and regeneration. Gastroenterology 2006, 131:1561-72.

[275] Monga SP, Pediaditakis P, Mule K, Stolz DB, Michalopoulos GK: Changes in WNT/beta-catenin pathway during regulated growth in rat liver regeneration. Hepatology 2001, 33:1098-109.

[276] Tao J, Calvisi DF, Ranganathan S, Cigliano A, Zhou L, Singh S, Jiang L, Fan B, Terracciano L, Armeanu-Ebinger S, Ribback S, Dombrowski F, Evert M, Chen X, Monga SP: Activation of beta-catenin and Yap1 in human hepatoblastoma and induction of hepatocarcinogenesis in mice. Gastroenterology 2014, 147:690-701.

[277] Bauer M, Eickhoff JC, Gould MN, Mundhenke C, Maass N, Friedl A: Neutrophil gelatinase-associated lipocalin (NGAL) is a predictor of poor prognosis in human primary breast cancer. Breast Cancer Res Treat 2008, 108:389-97.

[278] Candido S, Maestro R, Polesel J, Catania A, Maira F, Signorelli SS, McCubrey JA, Libra M: Roles of neutrophil gelatinase-associated lipocalin (NGAL) in human cancer. Oncotarget 2014, 5:1576-94.

[279] Rodvold JJ, Mahadevan NR, Zanetti M: Lipocalin 2 in cancer: when good immunity goes bad. Cancer Lett 2012, 316:132-8.

[280] Roli L, Pecoraro V, Trenti T: Can NGAL be employed as prognostic and diagnostic biomarker in human cancers? A systematic review of current evidence. Int J Biol Markers 2017, 32:e53-e61.

[281] Goetz DH, Holmes MA, Borregaard N, Bluhm ME, Raymond KN, Strong RK: The neutrophil lipocalin NGAL is a bacteriostatic agent that interferes with siderophore-mediated iron acquisition. Mol Cell 2002, 10:1033-43.

[282] Wheeler DS, Devarajan P, Ma Q, Harmon K, Monaco M, Cvijanovich N, Wong HR: Serum neutrophil gelatinase-associated lipocalin (NGAL) as a marker of acute kidney injury in critically ill children with septic shock. Crit Care Med 2008, 36:1297-303.

[283] Mishra J, Ma Q, Kelly C, Mitsnefes M, Mori K, Barasch J, Devarajan P: Kidney NGAL is a novel early marker of acute injury following transplantation. Pediatr Nephrol 2006, 21:856-63.

[284] Devarajan P: NGAL in acute kidney injury: from serendipity to utility. Am J Kidney Dis 2008, 52:395-9.

[285] Yang J, Bielenberg DR, Rodig SJ, Doiron R, Clifton MC, Kung AL, Strong RK, Zurakowski D, Moses MA: Lipocalin 2 promotes breast cancer progression. Proc Natl Acad Sci U S A 2009, 106:3913-8.

[286] Fernandez CA, Yan L, Louis G, Yang J, Kutok JL, Moses MA: The matrix metalloproteinase-9/neutrophil gelatinase-associated lipocalin complex plays a role in breast tumor growth and is present in the urine of breast cancer patients. Clin Cancer Res 2005, 11:5390-5.

[287] Wang Y, Zeng T: Neutrophil gelatinase-associated lipocalin protein as a biomarker in the diagnosis of breast cancer: A meta-analysis. Biomed Rep 2013, 1:479-83.

[288] Tong Z, Kunnumakkara AB, Wang H, Matsuo Y, Diagaradjane P, Harikumar KB, Ramachandran V, Sung B, Chakraborty A, Bresalier RS, Logsdon C, Aggarwal BB, Krishnan S, Guha S: Neutrophil gelatinase-associated lipocalin: a novel suppressor of invasion and angiogenesis in pancreatic cancer. Cancer Res 2008, 68:6100-8.

[289] Xu B, Jin DY, Lou WH, Wang DS: Lipocalin-2 is associated with a good prognosis and reversing epithelial-to-mesenchymal transition in pancreatic cancer. World J Surg 2013, 37:1892-900.

[290] Iannetti A, Pacifico F, Acquaviva R, Lavorgna A, Crescenzi E, Vascotto C, Tell G, Salzano AM, Scaloni A, Vuttariello E, Chiappetta G, Formisano S, Leonardi A: The neutrophil gelatinase-associated lipocalin (NGAL), a NF-kappaB-regulated gene, is a survival factor for thyroid neoplastic cells. Proc Natl Acad Sci U S A 2008, 105:14058-63.

[291] Mahadevan NR, Rodvold J, Almanza G, Perez AF, Wheeler MC, Zanetti M: ER stress drives Lipocalin 2 upregulation in prostate cancer cells in an NF-kappaB-dependent manner. BMC Cancer 2011, 11:229.

[292] Kim HJ, Ohk B, Kang WY, Seong SJ, Suk K, Lim MS, Kim SY, Yoon YR: Deficiency of Lipocalin-2 Promotes Proliferation and Differentiation of Osteoclast Precursors via Regulation of c-Fms Expression and Nuclear Factor-kappa B Activation. J Bone Metab 2016, 23:8-15.

[293] Tang HC, Chang PC, Chen YC: Iron depletion strategy for targeted cancer therapy: utilizing the dual roles of neutrophil gelatinase-associated lipocalin protein. J Mol Model 2016, 22:32.

[294] Lachmann A, Xu H, Krishnan J, Berger SI, Mazloom AR, Ma'ayan A: ChEA: transcription factor regulation inferred from integrating genome-wide ChIP-X experiments. Bioinformatics 2010, 26:2438-44.

[295] Heinz S, Benner C, Spann N, Bertolino E, Lin YC, Laslo P, Cheng JX, Murre C, Singh H, Glass CK: Simple combinations of lineage-determining transcription factors prime cis-regulatory elements required for macrophage and B cell identities. Mol Cell 2010, 38:576-89.

[296] Nejak-Bowen K, Moghe A, Cornuet P, Preziosi M, Nagarajan S, Monga SP: Role and Regulation of p65/beta-Catenin Association During Liver Injury and Regeneration: A "Complex" Relationship. Gene Expr 2017, 17:219-35.

[297] Lopez-Terrada D, Alaggio R, de Davila MT, Czauderna P, Hiyama E, Katzenstein H, Leuschner I, Malogolowkin M, Meyers R, Ranganathan S, Tanaka Y, Tomlinson G, Fabre M, Zimmermann A, Finegold MJ, Children's Oncology Group Liver Tumor C: Towards an international pediatric liver tumor consensus classification: proceedings of the Los Angeles COG liver tumors symposium. Mod Pathol 2014, 27:472-91.

[298] Guo H, Jin D, Chen X: Lipocalin 2 is a regulator of macrophage polarization and NF-kappaB/STAT3 pathway activation. Mol Endocrinol 2014, 28:1616-28.

[299] Wang Y, Zeng TT: Clinical significance of neutrophil gelatinase-associated lipocalin (NGAL) in colorectal cancer: a meta-analysis. Genet Mol Res 2014, 13:7102-12.

[300] Ozemir IA, Aslan S, Eren T, Bayraktar B, Bilgic C, Isbilen B, Yalman H, Yigitbasi R, Alimoglu O: The Diagnostic and Prognostic Significance of Serum Neutrophil Gelatinase-Associated Lipocalin Levels in Patients with Colorectal Cancer. Chirurgia (Bucur) 2016, 111:414-21.

[301] Asimakopoulou A, Weiskirchen S, Weiskirchen R: Lipocalin 2 (LCN2) Expression in Hepatic Malfunction and Therapy. Front Physiol 2016, 7:430.

[302] Zhou F, Luo Q, Wang L, Han L: Diagnostic value of neutrophil gelatinase-associated lipocalin for early diagnosis of cardiac surgery-associated acute kidney injury: a meta-analysis. Eur J Cardiothorac Surg 2016, 49:746-55.

[303] Bell D, Ranganathan S, Tao J, Monga SP: Novel Advances in Understanding of Molecular Pathogenesis of Hepatoblastoma: A Wnt/beta-Catenin Perspective. Gene Expr 2017, 17:141-54.

[304] Kienzl-Wagner K, Moschen AR, Geiger S, Bichler A, Aigner F, Brandacher G, Pratschke J, Tilg H: The role of lipocalin-2 in liver regeneration. Liver Int 2015, 35:1195-202.

[305] Xu MJ, Feng D, Wu H, Wang H, Chan Y, Kolls J, Borregaard N, Porse B, Berger T, Mak TW, Cowland JB, Kong X, Gao B: Liver is the major source of elevated serum lipocalin-2 levels after bacterial infection or partial hepatectomy: a critical role for IL-6/STAT3. Hepatology 2015, 61:692-702.

[306] Kim SL, Lee ST, Min IS, Park YR, Lee JH, Kim DG, Kim SW: Lipocalin 2 negatively regulates cell proliferation and epithelial to mesenchymal transition through changing metabolic gene expression in colorectal cancer. Cancer Sci 2017, 108:2176-86.

[307] Feng M, Feng J, Chen W, Wang W, Wu X, Zhang J, Xu F, Lai M: Lipocalin2 suppresses metastasis of colorectal cancer by attenuating NF-kappaB-dependent activation of snail and epithelial mesenchymal transition. Mol Cancer 2016, 15:77.

[308] Wang YP, Yu GR, Lee MJ, Lee SY, Chu IS, Leem SH, Kim DG: Lipocalin-2 negatively modulates the epithelial-to-mesenchymal transition in hepatocellular carcinoma through the epidermal growth factor (TGF-beta1)/Lcn2/Twist1 pathway. Hepatology 2013, 58:1349-61.

[309] Preziosi ME, Monga SP: Update on the mechanisms of liver regeneration. Semin Liver Dis 2017, 37:141-51.

[310] Grijalva JL, Huizenga M, Mueller K, Rodriguez S, Brazzo J, Camargo F, Sadri-Vakili G, Vakili K: Dynamic alterations in Hippo signaling pathway and YAP activation during liver regeneration. Am J Physiol Gastrointest Liver Physiol 2014, 307:G196-204.

[311] Thompson BJ: YAP/TAZ: Drivers of Tumor Growth, Metastasis, and Resistance to Therapy. Bioessays 2020, 42:e1900162.

[312] Totaro A, Castellan M, Battilana G, Zanconato F, Azzolin L, Giulitti S, Cordenonsi M, Piccolo S: YAP/TAZ link cell mechanics to Notch signalling to control epidermal stem cell fate. Nat Commun 2017, 8:15206.

[313] Shikai Hu LM, Junyan Tao, Silvia Liu, Mohammed Hassan, Sucha Singh, Minakshi Poddar, Aaron Bell, Daniela Sia, Michael Oertel, Reben Raeman, Kari Nejak-Bowen, Aatur Singhi, Jianhua Luo, Satdarshan P. Monga, Sungjin Ko: NOTCH-YAP1/TEAD-DNMT1 axis regulates hepatocyte reprogramming into intrahepatic cholangiocarcinoma. BioRXiv, 2020.

[314] Azar WJ, Christie EL, Mitchell C, Liu DS, Au-Yeung G, Bowtell DDL: Noncanonical IL6 Signaling-Mediated Activation of YAP Regulates Cell Migration and Invasion in Ovarian Clear Cell Cancer. Cancer Res 2020, 80:4960-71.

[315] Michalopoulos GK, Bhushan B: Liver regeneration: biological and pathological mechanisms and implications. Nat Rev Gastroenterol Hepatol 2021, 18:40-55.

[316] Tsagianni A, Mars WM, Bhushan B, Bowen WC, Orr A, Stoops J, Paranjpe S, Tseng GC, Liu S, Michalopoulos GK: Combined Systemic Disruption of MET and Epidermal Growth Factor Receptor Signaling Causes Liver Failure in Normal Mice. Am J Pathol 2018, 188:2223-35.

[317] Woodfield SE, Shi Y, Patel RH, Jin J, Major A, Sarabia SF, Starosolski Z, Zorman B, Gupta SS, Chen Z, Ibarra AM, Bissig KD, Ghaghada KB, Sumazin P, Lopez-Terrada D, Vasudevan SA: A Novel Cell Line Based Orthotopic Xenograft Mouse Model That Recapitulates Human Hepatoblastoma. Sci Rep 2017, 7:17751.

[318] Mokkapati S, Niopek K, Huang L, Cunniff KJ, Ruteshouser EC, deCaestecker M, Finegold MJ, Huff V: β-catenin activation in a novel liver progenitor cell type is sufficient to cause hepatocellular carcinoma and hepatoblastoma. Cancer Res 2014, 74:4515-25.

[319] Imajo M, Miyatake K, Iimura A, Miyamoto A, Nishida E: A molecular mechanism that links Hippo signalling to the inhibition of Wnt/β-catenin signalling. EMBO J 2012, 31:1109-22.

[320] Pan X, Wu B, Fan X, Xu G, Ou C, Chen M: YAP accelerates vascular senescence via blocking autophagic flux and activating mTOR. J Cell Mol Med 2021, 25:170-83.

[321] Theo Hirsch JP, Guillaume Morcrette, Amélie Roehrig, Benedict Monteiro, Laura Molina, Quentin Bayard, Eric Trépo, Léa Meunier, Stefano Caruso, Victor Renault, Jean-François Deleuze, Brice Fresneau, Christophe Chardot, Emmanuel Gonzales, Emmanuel Jacquemin, Florent Guerin, Monique Fabre, Isabelle Aerts, Sophie Taque, Véronique Laithier, Sophie Branchereau, Catherine Guettier, Laurence Brugières, Sandra Rebouissou, Eric Letouzé, Jessica Zucman-Rossi: Integrated genomic analysis identifies driver genes and cisplatin-resistant progenitor phenotype in pediatric liver cancer. Cancer discovery (in press) 2021.